Molecular Simulation Studies on Selective Capture of CO_2 from Gas Mixtures using Pure and Modified Mesoporous and Microporous Adsorbents

A Thesis Submitted in Partial Fulfillment of the

Requirements for the Degree of

Doctor of Philosophy

by

Kishant Kumar

Roll No: 126107006

Department of Chemical Engineering

Indian Institute of Technology Guwahati, Guwahati, India

June, 2018

CERTIFICATE

It is certified that the work reported in this thesis entitled "**Molecular Simulation Studies on Selective Capture of CO_2 from Gas Mixtures using Pure and Modified Mesoporous and Microporous Adsorbents**", by Kishant Kumar, has been carried out under my supervision and that this work has not been submitted elsewhere for a degree.

June 2018
IIT Guwahati

Dr. Amit Kumar
Associate Professor
Department of Chemical Engineering
Indian Institute of Technology Guwahati

Dedicated to My Parents

Acknowledgements

I would like to take this opportunity to express my heartiest gratitude to all who were by my side during my PhD study. First of all, I would like to thank my supervisor, Dr. Amit Kumar. His continuous encouraging guidance led me to accomplish my research during the stay at IIT Guwahati. I am grateful and honored to have the opportunity to learn and work with him.

I am thankful to my doctoral committee members, Dr. Anki Reddy Katha, Dr. Mahuya De, Prof. Sasidhar Gumma, Department of Chemical Engineering and Prof. Gopal Das, Department of Chemistry, for their valuable suggestions during my research period.

I would like to thank Department of Chemical Engineering, IIT Guwahati for providing the friendly environment which always motivated me. I also thank DST, India for the providing computing facility to conduct the simulation work. I also thank Prof. Bishnupada Mandal, Head, Department of Chemical Engineering, for his administrative support. Furthermore, I would like to thank other Faculty and Staff members of the Department of Chemical Engineering for their valuable support during my research.

I deeply acknowledge my research group members Dr. Sravanthi Loganathan, Dr. Kamal Kumar Bhatluri, Dr. Mriganka Manna, Dr. Manish Kamal, Dr. Rupak Kishor, and Abhik Bhattacharjee for providing a cooperative research environment.

I would like to thank Dr. Prashant Mishra for helping me in IAST calculations and Dr. Anand Bharti in calculation of charge from Gaussian software. I would also like to thank Mr. Mood

Mohan for helping me in formatting the thesis. I would like to especially thank Mr**.** Prudhvi Raj for fruitful discussion prior to my study of adsorption on functionalized Cu-BTC.

My sincere thanks to friends Mr. Bisweswar Das, Mr. Binay Deogam, Mr. Satnarayan Edubilli, Mr. Badri Vishal, Mr. Sujit, Mr. Jitendra Singh Rawat, Mr. Ranjeet Kumar Mishra, Mr. Proloy Das, Mr. Kulbhusan Samal, Mr. Deosashish Kundu, Dr. Suresh Kanchapogu, Mr. Kolethu Suresh, Siddharth Bhasney, Abhishek Kumar, Lalit Gosawami, Arun Kumar, Amit Pandey, and many more for making my stay at IIT Guwahati memorable.

Above all, I would like to thank my father, mother, brothers, and sister for their love and support which kept my morale high during the PhD.

Kishant Kumar

ABSTRACT

Rise in the atmospheric concentration of carbon dioxide is believed to play a significant role in global warming through the greenhouse effect. Separation of CO_2 from the flue gas emissions from power plants is important to reduce the amount of CO_2 released into the atmosphere. 'Sweetening' of natural gas is another important industrial operation involving the separation of CO_2 from a gas mixture. Adsorptive separation of CO_2 using porous materials such as zeolites, mesoporous silicas, metal organic frameworks (MOFs), porous carbons etc. is an attractive alternative to conventional amine scrubbing due to lower regeneration energy requirements. Mesoporous silica such as MCM-41 and SBA-15 are an important class of adsorbents that can be readily modified through functionalization or other means due to their large, regularly arranged pores. Microporous metal-organic frameworks (MOFs) represent another class of adsorbents that can be modified through functionalization of the organic linker groups.

In this work, realistic molecular models of pure and modified MCM-41 and representative models of SBA-15 have been developed to study CO_2 separation on mesoporous silica using grand canonical Monte Carlo (GCMC) simulations. Structural characterization of the developed MCM-41 models compared favorably with experimental data available in literature. Further, the simulated adsorption isotherm and calculated isosteric heat of adsorption of pure CO_2 showed good agreement with reported experimental values. Simulations of CO_2/N_2 mixture adsorption showed selectivities of CO_2 over N_2 to be in the range 4–10. Further studies on adsorption of ternary and quaternary bulk gas mixtures containing water vapor and O_2 did not reveal any significant effect on CO_2 adsorption and CO_2-N_2 selectivity. Next, to study the effect of pore size and microporosity of pore walls, models having larger mesopore diameter of ~75 Å were developed, and representative models of SBA-15 were generated by carving different numbers of

micropores across the pore walls. GCMC simulations were used to study the adsorption of pure gases as well as gas mixtures of CO_2, N_2 and CH_4. Increase in mesopore size resulted in reduced specific surface area and CO_2 uptake, whereas with increase in wall microporosity, the uptake of CO_2 was observed to first decrease and then increase. The SBA-15 models are more selective toward CO_2 over CH_4 and N_2. At low pressures, the selectivities were higher for models with wall microporosity. The MCM-41 models were modified by incorporation of the ionic liquid (IL) 1-methyl-1-butyl-pyrrolidinium bis(trifluoromethanesulfonyl)imide $[C4PYR^+][TF2N^-]$ at two different loadings. The MCM-41 model with lower loading of IL showed significantly higher adsorption of pure CO_2 than pristine MCM-41. Molecular dynamics simulation of pure CO_2 in IL-loaded MCM-41 models revealed that CO_2 molecules prefer locations near the pore walls as well as in the pore interior around IL molecules. The CO_2/N_2 and CO_2/CH_4 selectivities were highest for the MCM-41 with larger IL loading, with values almost twice that for pure MCM-41. Thus, modifying the mesopores of MCM-41 with IL can result in significant enhancement in CO_2 adsorption and selectivity.

For studies on adsorptive separation of CO_2 on MOFs using GCMC simulations, zirconium-based UiO-66 and UiO-67, and functionalized copper-based Cu-BTC have been considered. The two Zr-based MOFs studied are topologically similar but have channels and cages of different sizes. The amount of gas adsorbed as well as the isosteric heats of adsorption show the order $CO_2 > CH_4 > CO > N_2$ on both UiO-66 and UiO-67. Isosteric heats of adsorption and gas uptake at low pressures were higher in the case of UiO-66 due to the presence of smaller cages leading to stronger interactions. At higher pressures, gas uptake in UiO-67 was larger because of larger cages and greater surface area. CO_2 was observed to preferentially adsorp near the organic linkers in the smaller cages of the MOFs. The binary mixture selectivity of CO_2 over CH_4 and N_2 was

significantly higher for adsorption in UiO-66 than in UiO-67 because of the narrow window size and smaller cages in UiO-66. Finally, the effect of pore modification on CO_2 adsorption was studied using different functionalized Cu-BTC MOFs having iodo-, single methyl and two methyl functional groups grafted to the organic linkers. At low pressures (< 1 bar), adsorption of CO_2 was seen to be higher for the iodo-functionalized Cu-BTC. However, at higher pressures, CO_2 uptake was highest for the unmodified Cu-BTC because of its larger pore volume. Moreover, selectivity of CO_2 over CH_4 and N_2 was found to be higher for the iodo-functionalized Cu-BTC at high pressures (> 2 bar). In the low-pressure regime, Cu-BTC functionalized with two methyl groups showed higher selectivity of CO_2 over N_2. The geometric characteristics of the pore such as pore size, surface area and volume, and the interaction environment within the pores strongly affect CO_2 adsorption and hence, can be tuned to enhance CO_2 uptake and selectivity.

Table of Contents

List of Figures

List of Tables

CHAPTER 1

Introduction

1.1 Introduction

Increased consumption of carbon-containing fossil fuels, to meet the rising demands in the power generation and transportation sector, has led to increased emission of carbon dioxide in the atmosphere. The rise in the atmospheric concentration of carbon dioxide is believed to play a significant role in global warming through the greenhouse effect. Economic reforms and increasing urbanization in India has resulted in an increase in the energy consumption from 191 million tons of oil equivalent (MTOE) in 1991 to 595 MTOE in 2013 [1]. Coal is primarily used in power plants for electricity generation and accounts for over 50% of the total energy consumption in India. The three major energy sources viz. coal, crude oil and natural gas accounted for energy consumption of 289.3, 171.6 and 49.1 MTOE respectively in India during the year 2012. CO_2 emissions in India have almost tripled between 1990 and 2013 increasing at a compounded annual growth rate of 5%, with coal contributing more than 60% of the total CO_2 emissions in 2013. Electricity generation (primarily using coal) accounted for about 48% CO_2 emissions in 2013 followed by transport at over 10%. Therefore, existing CO_2 separation technology must be improved in order to cope with the increasing CO_2 emissions from coal-based and other fossil fuel sources. Existing amine-based carbon capture technology is expensive and energy intensive, and is prohibitive when applied to large-scale power plants. Composition of flue gas from power plants depends on the design of the power plants and the source of fuel used such as coal or natural gas. However, irrespective of the fuel used, flue gas contains significant amount of CO_2 which has been identified as an important cause of global warming. To prevent the release of large amount so CO_2 in the atmosphere, it needs to be captured from the flue gas stream for storage and sequestration. The separation of CO_2 from flue gas constitutes post-combustion carbon capture as CO_2 is captured after the combustion of

fuel. CO_2 can also be captured before the combustion of fuel in the power plant takes place; such an operation is referred to as pre-combustion carbon capture and is described in section 1.2.2.

Apart from flue gas separation, 'sweetening' of natural gas is another important industrial operation that involves the separation of CO_2 from a gas mixture. Natural gas accounted for ~9% of the total energy demand in India in 2012 and its consumption has increased from 0.6 MTOE in 1971 to 49.1 MTOE in 2012 [2]. Petroleum Planning and Analysis Cell (PPAC) of India [3] keeps the record for the total consumption, export and import of natural gas. The consumption of natural gas in India during the past 10 years is summarized in Table 1.1. Removal of CO_2 is an important step in the purification of natural gas (which primarily contains methane).

Table 1.1 Total natural gas consumption during last 10 years. Data were obtained from the PPAC of India [3]**.**

Year	Natural Gas consumption (BCM*)
2007–08	37.90
2008–09	37.60
2009–10	52.65
2010–11	58.93
2011–12	58.75
2012–13	51.68
2013–14	46.18
2014–15	45.32
2015–16	46.68
2016–17	49.67
2017–18	52.26

*BCM: billion cubic meter

Thus, the separation of CO_2 from gases such as N_2 and CH_4 is of great interest. Post-combustion CO_2 capture, pre-combustion CO_2 capture and CO_2 removal from natural gas constitute three key operations where separation of CO_2 from other gases is required. Composition of gas mixtures present in these processes is summarized in Table 1.2. Removal of CO_2 from natural gas is necessary to enhance the calorific efficiency and prevent corrosion of pipeline, as CO_2 can form acid in the presence of water. Natural gas mainly contains methane, which has good calorific value and is considered a clean fuel for domestic as well as commercial purpose.

Table 1.2 Typical conditions for post-combustion [4–5] capture, pre-combustion [4] capture and the natural gas sweetening [6–7] processes.

Gas	Post-combustion carbon capture at 40–75 °C and 1 bar (mole %)	Pre-combustion carbon capture at 40 °C and 30 bar (mole %)	Natural gas sweetening at 30–40 °C and 5–120 bar (mole %)
CO_2	10–15	37.7	0.1–8
H_2O	5–10	0.14	
H_2		55.5	
O_2	3–4		
CO	20ppm	1.7	
N_2	70–75	3.9	0–0.2
NOx	<800 ppm		
SOx	<500 ppm		
H_2S		0.4	0–15
CH_4			70–95
C2+			0–15

Traces of H_2S, CO_2 and other heavier paraffin present in the natural gas seriously reduce its calorific value and make it less environment-friendly [8–10]. In addition, CO_2 separation from blast furnace gas [11] containing CO_2, CO, C_xH_y, H_2S, N_2, O_2, and NOx, and production and

separation of CO_2 from landfill gas containing CO_2 and CH_4 are also some relevant operations requiring CO_2 separation [12].

1.2 Pathways for CO_2 Capture and Separation

In the current scenario, researchers throughout the world are mainly devoted to finding alternative techniques for capturing anthropogenic CO_2 emissions. Pathways for CO_2 capture from processes involving combustion of fossil fuels can be classified into three types, as discussed next.

1.2.1. Post-combustion Capture

This method is widely used in fossil fuel-based power plants which contribute a major part of total anthropogenic CO_2 emission. Thermal power plants generate electricity by burning fossil fuels such as coal to produce heat, which in turn is used to generate high-pressure steam. The high-pressure steam is subsequently used to drive the turbine in order to generate electricity using a high capacity generator. Under the post-combustion process, fossil fuel is burnt in the presence of air to produce a mixture of CO_2, N_2, H_2O, sulphur, NO_X, SO_X and particulate matter. Typical composition of the gas mixture obtained after the combustion process is summarized in Table 1.2. The particulate matter being heavier can be separated out using filtration and electrostatic precipitator. Sulphur present in the flue gas is scrubbed by limestone slurry to form a useful product gypsum, which is mainly used in cement industry. Finally, flue gas contains lighter molecules such as N_2 (73–77%), CO_2 (10–16%) and traces of SO_X, NO_X and water vapor. As CO_2 is responsible for the greenhouse effect, it must be separated using an appropriate separation technique before the gas is released in the atmosphere. A schematic diagram for post-combustion carbon capture is shown in Figure 1.1. The main separation operation of interest in this process is CO_2/N_2 separation.

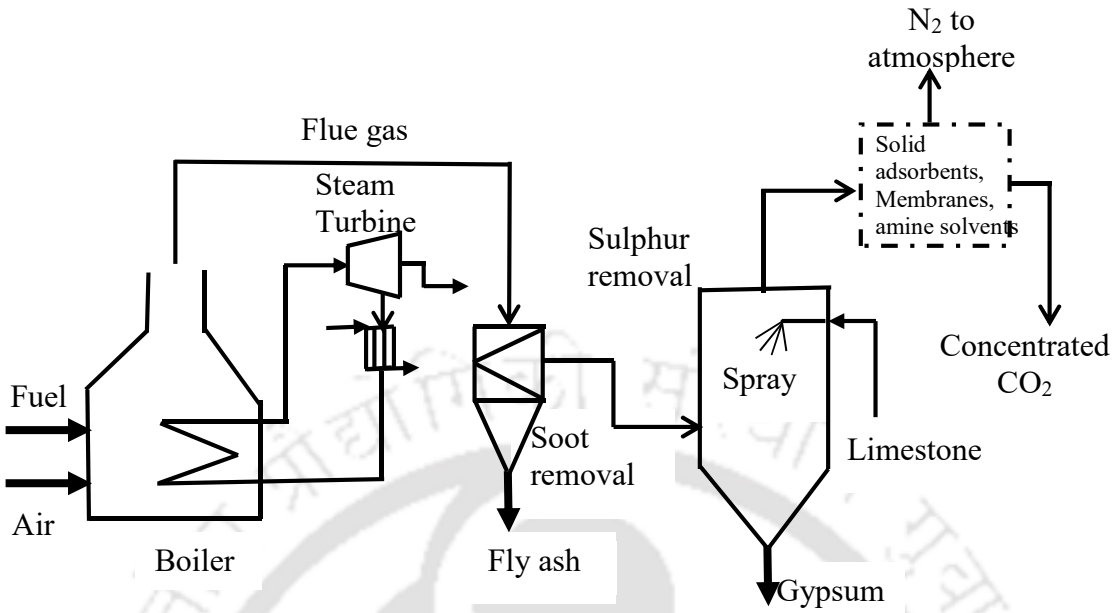

Figure 1.1 Schematic diagram of post-combustion CO_2 capture process in industry (adapted from [13] **)**

1.2.2. Pre-combustion Capture

The pre-combustion CO_2 capture process is typically associated with integrated gasification combined cycle (IGCC), which requires higher operating cost and equipment cost. In this process, the fossil fuel is gasified in the presence of pure oxygen and steam to produce synthesis gas (CO and H_2). Thereafter, synthesis gas is fed to water-gas-shift (WGS) reactor after passing it through desulphurization unit to remove any unwanted sulfur. In the WGS reactor, steam is passed through the syngas in order to convert CO into CO_2. Figure 1.2 shows the process diagram for the pre-combustion carbon capture. The main separation operation needed in this process is CO_2/H_2 separation.

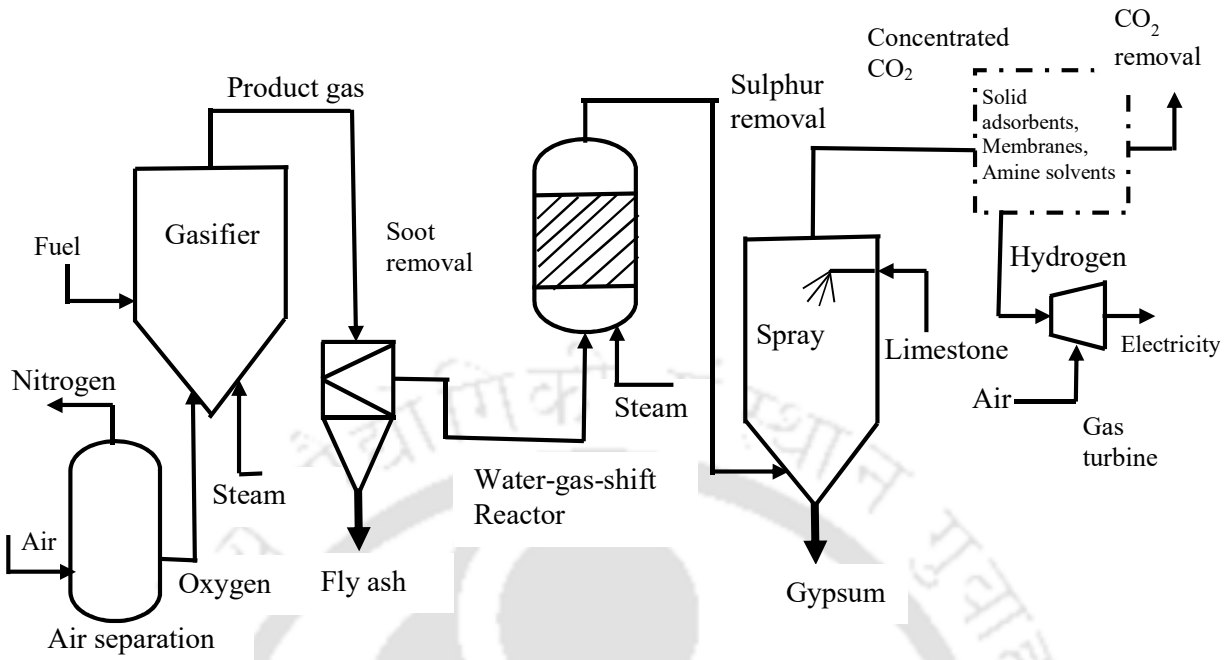

Figure 1.2 Schematic diagram of pre-combustion CO_2 capture process in industry (adapted from [13] **)**

1.2.3. Oxyfuel Combustion Capture

Oxyfuel combustion process is a promising technique, and presently an active research area of interest. A schematic process diagram for the said process is shown in Figure 1.3. In this process, pure oxygen is used to burn the fuel for heat generation. In power generation unit, the released heat produces high-pressure steam to rotate the turbine for electricity generation. The result is mainly water vapor and CO_2 gas with some amount of heavy particles and sulfur. Water vapor is condensed in the condensation chamber and heavier particulate such as fly ash is removed in the soot removal chamber. Finally, the flue gas is fed to a desulphurization unit for scrubbing sulfur to get concentrated CO_2 gas which may then be stored beneath earth's surface.

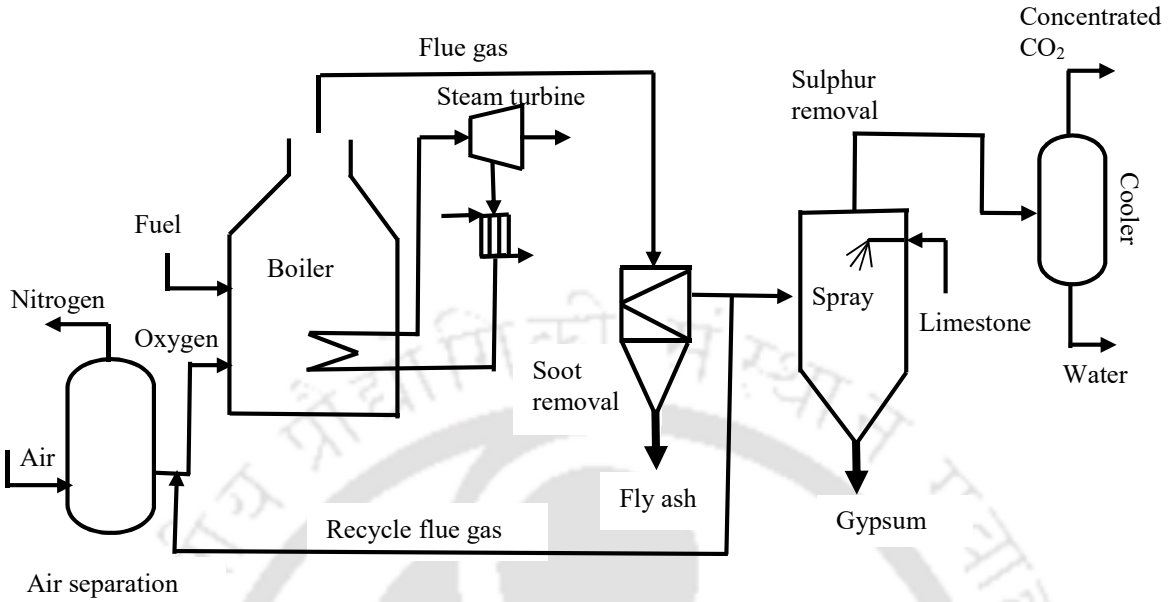

Figure 1.3 Schematic diagram for oxyfuel combustion process in industry (adapted from [13] **)**

1.3 Natural Gas Sweetening

Capture and separation of CO_2 gas is not only important during flue gas treatment but also is of industrial relevance in sweetening of natural gas prior to liquefaction and transportation. Demand for natural gas is increasing per year at a rate of 1.4%. Natural gas mainly comprises CH_4 with traces of other lighter hydrocarbons, and CO_2 and H_2S. Among the other components of natural gas, CO_2 and H_2S are necessary to separate from the natural gas prior to further processing. Even traces of CO_2 may form dry ice or formation of gas hydrate, which will retard the liquefaction process upon clogging into the system. Moreover, CO_2 and H_2S show corrosive nature in the presence of water vapor and presence of CO_2 in the natural gas lowers the calorific value. The important technologies that can be used for separation of carbon dioxide are absorption, adsorption and membrane gas separation. Absorption using aqueous amine solutions is energy-intensive due

to the large energy required for amine regeneration. Adsorptive separation of CO_2 using porous materials such as zeolites, mesoporous silicas, metal organic frameworks, porous carbons etc. is an attractive alternative to conventional amine scrubbing due to lower regeneration energy requirements. A brief description of the adsorption process along with details of promising adsorbent materials for CO_2 separation is provided next.

1.4 Adsorption

When the number density of fluids increases near the vicinity of the solid surface due to either van der Waals interaction, electrostatic forces or by formation of covalent bonds between the fluid and solid surface, the surface phenomenon is referred to as adsorption. The fluid is called adsorbate while the solid material is called adsorbent. Phenomenon of adsorption was first coined by Scheele and Fontana [14] in the eighteenth century. The adsorption process has been employed in several industries, and research and development organizations for gas storage and separation application. In the earlier decades, adsorption process was most commonly used to remove traces of moisture from natural gas. Water vapor needs to be removed when experiments are to be carried out in controlled moisture-free environment. Silica gel is one of the most common adsorbents and has wide range of industrial applications including the control of humidity in a closed atmosphere [15]. Almost every electronics equipment comes with the packet of silica gel inside in order to keep the level of moisture low. Adsorption can be broadly categorized into two types:

1.4.1. Physisorption

Adsorption that takes place specifically due to van der Waals and electrostatic forces between the adsorbate and the adsorbent is known as physisorption. Van der Waals contribution plays an

important role in every kind of adsorbate-adsorbent system while the electrostatic interaction is significant when adsorbate possess some polarity (dipole, quadrupole etc.). The reversibility of physical adsorption depends on the strength of acting forces between adsorbate and adsorbent [16,17]. Binding energy for nonpolar molecules is in the range of a few kilojoules while polar molecules such as H_2O possess a high (80–160 kJ mol^{-1}) value [18]. Multilayer adsorption is also possible in mesoporous materials when adsorbate molecules completely occupy all the available sites on the solid surface and start depositing over an already adsorbed layer of adsorbates.

1.4.2. Chemisorption:

In this type of adsorption, adsorbate molecules associate with the surface of adsorbent through formation of covalent bond(s). It is a specific process which depends on the chemical nature of adsorbent [18]. As chemisorption involves the formation of bond(s), a high amount (100–1000 kJ mol^{-1}) of energy is released during this process.

1.5 Key Considerations for Adsorbent Selection

1.5.1. Surface Polarity

The concept arises from the fact that “polar dissolves polar”. As we know that adsorption is a surface phenomenon, pore surfaces that are well decorated with functional groups such as hydroxyl, halide, carboxylic, amine, alkoxide etc. polarize other guest (adsorbate) molecules resulting to a higher concentration of guest molecules at the solid surface. Polar adsorbents such as silica gel, zeolites and activated alumina are considered hydrophilic in nature due to the presence of polarity at the adsorbent surface. On the other hand, activated carbon exhibits non-polar surface

and hence it is considered as hydrophobic and organophilic nature. These surface features of the pores can be utilized beneficially for several separation processes and catalytic activity.

1.5.2. Porosity

Porosity, also referred to as void fraction, is one of the important characteristics of a good adsorbent. The adsorption capacity depends strongly on the accessible surface area and available pore volume to achieve higher saturation loading. Thus, higher porosity is generally desirable for higher amount of adsorbate loading inside the adsorbent. Highly porous adsorbents usually have low volumetric uptake up to the saturation pressure, which necessitates larger adsorbent bed size. Therefore, a balance between volumetric uptake and bed size must be maintained in order to achieve minimum possible installation and maintenance cost in adsorption and separation-based industries.

1.5.3. Uptake Capacity

A high uptake capacity of an adsorbent is desirable in the process condition, which reduces the bed size and helps in achieving low operating and fixed cost of the entire adsorption plant. Uptake capacity may be expressed in several ways such as moles of adsorbate per kg of adsorbent, grams of adsorbate per gram of adsorbent, cm^3 of adsorbate per gram of adsorbent, number of molecule of adsorbate per unit cell of a crystalline adsorbent, etc.

1.5.4. Selectivity

Selectivity is one of the important parameters in adsorption-based separation. It is a measure of the extent to which an adsorbent selectively adsorbs a particular component over the other components of the mixture. Higher the selectivity of one species over the others, better will be the separation efficiency.

1.5.5. Adsorbent Regeneration

Adsorbents that can be easily regenerated on applying higher temperature or vacuum is said to be an ideal adsorbent. Regeneration at high temperature and high vacuum must be tolerable with operational cost. Enthalpy of adsorption is directly related to the difficulty of regeneration. Higher the enthalpy value, more difficult will regeneration of any adsorbent be. Enthalpy value also affects the adsorption capacity; therefore, enthalpy value and regeneration difficulty must be optimized while selecting an adsorbent.

1.5.6. Stability of Adsorbent

During the different applications, the adsorbent has to suffer the processing conditions including high pressure, temperature, moisture, harsh chemical environment etc. The selected adsorbent should therefore be thermally, mechanically and chemically stable.

1.6 Types of Adsorbents

Choice of an adsorbent in purification and separation industry requires important attention. Among a large number of adsorbents reported in literature, few such as silica gel, activated carbon, carbon molecular sieve, activated alumina, zeolites etc. have found applications in industries and serve as widely used materials. Based on the elemental composition, the adsorbents can be divided into two broad categories.

1.6.1. Organic Adsorbents:

Activated carbon [19] is a widely used adsorbent that falls under this category. These porous carbon materials are generally synthesized by the pyrolysis of carbon-rich materials and possess high pore volume, and large saturation loading of adsorbate. However, the structure of these

materials is disordered and the porosity is irregular with a broad pore size distribution due to which selectivity is not very high. In order to overcome the poor selectivities, carbon adsorbents with narrow pore channels have been synthesized through proper activation procedure. These carbon materials containing a very narrow pore size distribution are known as carbon molecular sieves with pore diameters ranging from 4 to 9 Å. However, carbon molecular sieves do not possess very high porosity and exhibit relatively low saturation loadings. Graphene sheets and carbon nanotubes also belong to the organic family of adsorbent, and these materials have been extensively investigated for hydrogen storage and separation of CO_2/N_2 mixtures. Molecular structure of graphene sheets and carbon nanotubes are shown in Figure 1.4.

Metal-organic frameworks (MOFs) are a relatively new class of materials that are actively being investigated for a variety of applications including gas storage and separation. MOFs consist of metal atoms or clusters coordinated by several organic linker groups, forming a three-dimensional ordered, porous network. These materials possess many desirable properties such as very large surface areas and pore volumes, tunable pore size, ease of functionalization etc. In fact, certain MOFs display ultrahigh porosities of the order of ~90% and Brunauer-Emmett-Teller (BET) surface areas above 7000 m^2g^{-1} [20–21]. MOFs have huge potential in applications such as storage of small gases (e.g. hydrogen, methane and other small organic alkanes), in the separation and purification industry, in catalysis, membrane science and thin film devices [22]. The CO_2 adsorption capacity of some of the popular MOFs such as Cu-BTC, DABCO, UiO-66 etc. are summarized in Table 1.3. Figure 1.5 shows the structure of Cu-BTC (also known as HKUST-1) which consists of copper coordinated with benzene tricarboxylic acid linkers. It possesses high CO_2 storage capacity as shown in Table 1.3. Due to the desirable properties of these materials,

such as high surface areas and pore volumes, tunable pore sizes, ease of pore modification etc., adsorption behavior of CO_2 and capture of CO_2 from gas mixtures using MOFs is the focus of the latter half of this thesis.

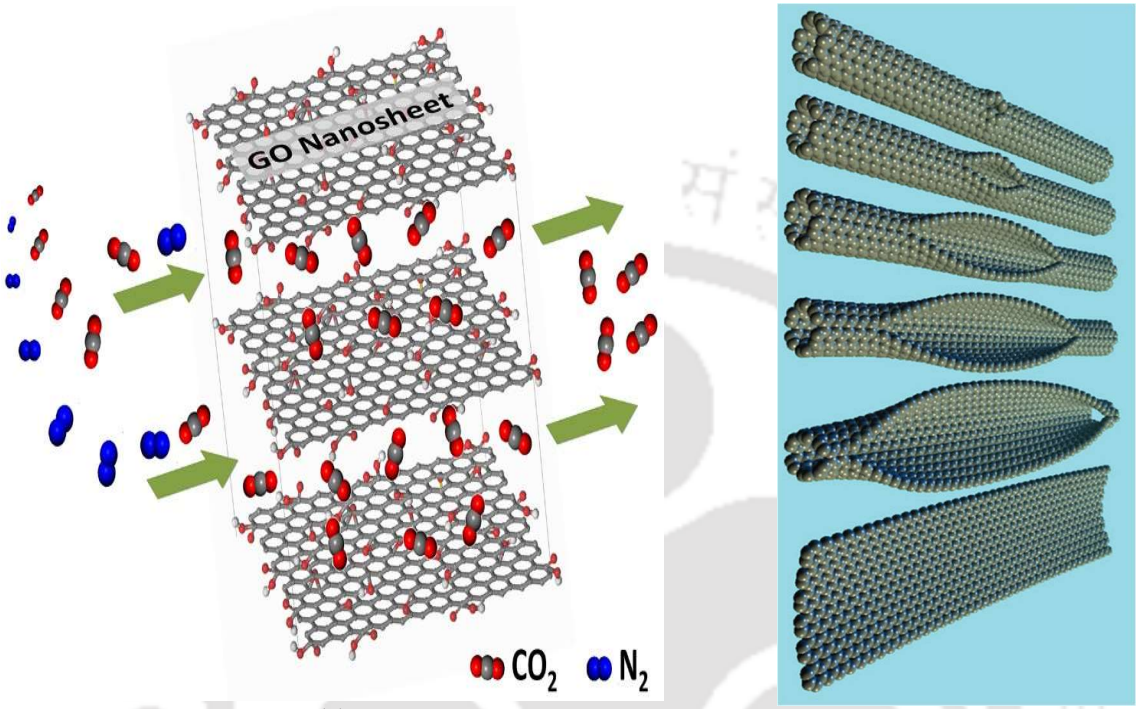

(a) (b)

Figure 1.4 (a) Graphene sheet (taken from [23]**) (b) Carbon nanotube (taken from** [24]**)**

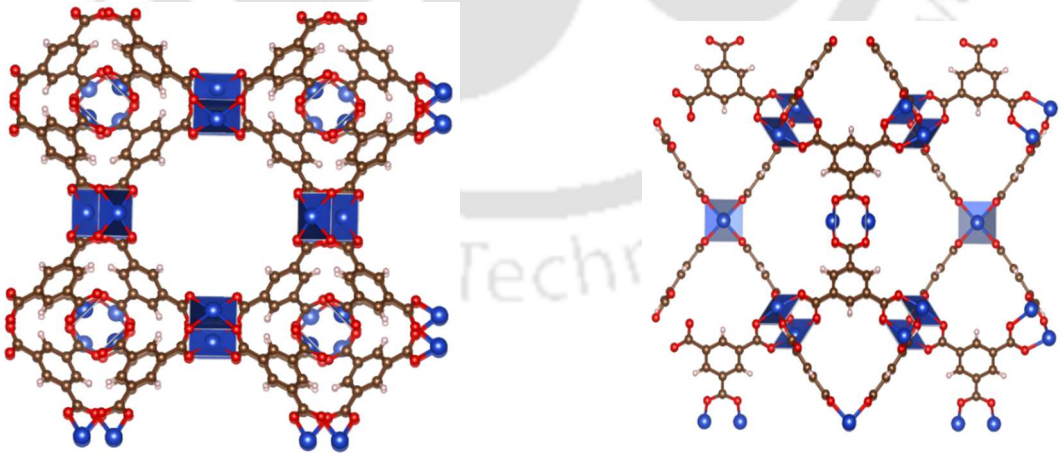

(a) X-Y, Y-Z, Z-X view (b) Tilted view

Figure 1.5 Axial View of Cu-BTC

Table 1.3 CO_2 loading in various Metal-Organic Frameworks in the low-pressure regime and over the temperature range 293–319 K

Chemical Formula	Common Name	BET Surface area (m^2g^{-1})	Temperature (K)	Pressure (bar)	Capacity (mmol g^{-1})	Ref.
$Mg_2(dobdc)$	Mg-MOF-74, CPO-27-Mg	1174	298	1	8.61	[25]
$Ni_2(dobdc)$	Ni-MOF-74, CPO-27-Ni	936	298	1	7.084	[26]
$Zn_2(dobdc)$	Zn-MOF-74, CPO-27-Zn		296	1	5.61	[26]
$Cu_3(BTC)_2$	HKUST-1	1492[a]	298	1	4.97	[27]
$H_3[(Cu_4Cl)_3(BTTri)_8(mmen)_{12}]$	mmen-Cu-BTTri	870	298	1	4.2	[28]
H3[(Cu4Cl)3(BTTri)8	CuBTTri	1770	298	1	3.68	[28]
Zn(nbIm)(nIm)	ZIF-78	620	298	1	2.23	[29]
$Zn(cyanIm)_2$	ZIF-96	960	298	1.06	2.18	[30]
$Zn_4O(BDC)_3$	MOF-5, IRMOF-1	2304	296	1	1.95	[31]
Cr(OH)(BDC)	MIL-53(Cr)		304	1	2.17	[32]
$Zn(almeIm)_2$	ZIF-93	864	298	1	1.65	[30]
$Zn_4O(BDC\text{-}NH_2)_3$	IRMOF-3	2160	298	1.1	1.2	[33]
$Cu_2(TP)_3(OH)$	Cu-TP-1	258	298	1	1.1	[34]
$Zn_4O(BDC\text{-}C_2H_4)_3$	IRMOF-6	2516	298	1.2	1.1	[33]
	UiO-66	940	298	1	1.5	[35]

[a] denotes the Langmuir surface area

1.6.2. Inorganic Frameworks:

The widely used adsorbents in this category are activated alumina, silica gel and zeolites. Mesoporous silica are form an important class of inorganic adsorbents.

Activated alumina

It is a highly porous form of aluminium oxide having a surface area of up to 200 m^2g^{-1}. This material has a polar surface having both acidic and basic nature (amphoteric). Due to the polar nature of the surface, this kind of material was used as a desiccant before its replacement by molecular sieve [36].

Zeolite

Zeolites are crystalline aluminosilicates with alkali and alkaline cations such as sodium, potassium and calcium present in their framework. The chemical composition for the zeolite can be represented by the formula [37]

$$M_{Z_1/n}\left[(AlO_2)_{Z_1}(SiO_2)_{Z_2}\right].z_3H_2O$$

where z_1 and z_2 are integers such that z_2/z_1 is equal to or greater than 1, metal cation is represented by *M* with *n* as its valence, and z_3 represents the number of water molecules present in the unit cell. Silicon and aluminium are connected to shared oxygen atom in a tetrahedral arrangement to form a fixed crystal lattice. Further, varying the silicon-to-aluminium ratio leads to change in the adsorption behavior of the material. Zeolites rich in aluminum content are said to be hydrophilic and possess a good affinity towards polar molecule such as water vapor while silico- rich zeolites are less hydrophilic in nature. A typical atomistic model of zeolite is shown in Figure 1.6 (grey region shows the accessible surface area and hollow part shows the free volume).

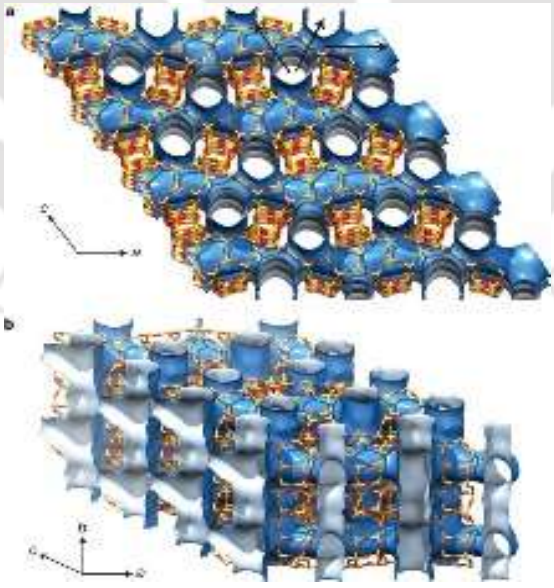

Figure 1.6 Zeolite structure (grey region showing accessible surface area, taken from [38]**)**

Silica Gel

It is a granular, colloidal, porous and vitreous form of silicon dioxide ($SiO_2.nH_2O$), which is synthesized from silica sources such as tetraethyl orthosilicate (TEOS), silica fume etc. Due to the presence of hydroxyl group in the micropores, it possesses high affinity towards polar molecules, due to which it is used as a commercial desiccant to maintain low humidity.

Mesoporous Silica

Mesoporous silica was first synthesized in 1990 by researchers from Japan [39]. The material was synthesized in the Mobil Corporation laboratories and named molecular 41 sieves (M41S) [40]. The material consists of regular cylindrical pores of tunable diameter in the range from 2 to 30 *nm*. These materials possess desirable properties such as tunable pore size, high thermal stability, ease of functionalization (with even large moieties) at their pore surface and high surface area in the range of 700–1500 m^2g^{-1}. Therefore, due to their several remarkable properties, these materials are applied in the fields of adsorption, separation, catalysis, and in biotechnology devices. MCM-41, MCM-48, and MCM-50 are the most widely known among the M41S family of adsorbents with pores arranged in regular hexagonal array, cubic (double gyroid) and lamellar structure, respectively [41]. A hexagonal array of pores contained in the mesoporous silica MCM-41 are shown in Figure 1.7. The adsorption capacity of CO_2 in various unmodified and amine-functionalized/impregnated mesoporous silica materials, as reported in literature, are listed in Table 1.4. Due to the attractive properties of these materials, especially regularly arranged, large tunable pores than can be readily modified, CO_2 adsorption and separation in mesoporous silica is the focus of the first half of this thesis.

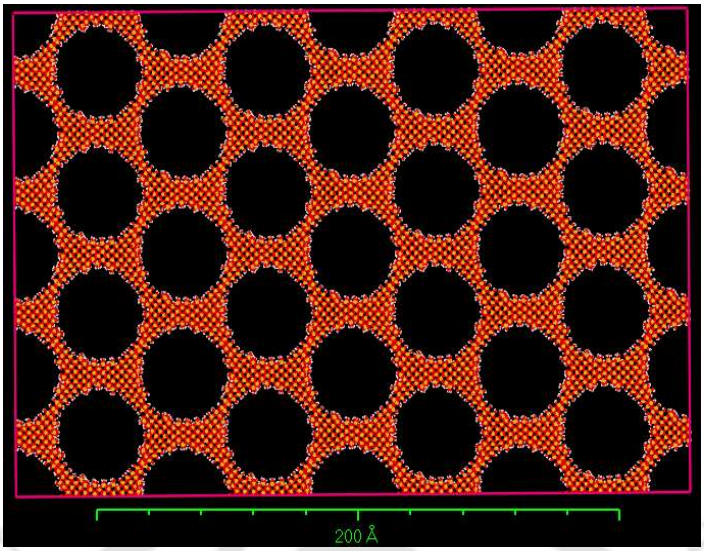

Figure 1.7 Atomistic model for hexagonal array of mesoporous silica, MCM-41

1.7 CO_2 Separation in Mesoporous Silica and MOFs

Currently, capture of CO_2 from flue gas or for natural gas sweetening involves absorption in solvents such as monoethanolamine (MEA), methyldiethanolamine and diethanolamine (DEA), which results in the formation of carbamate intermediate with CO_2 molecules (chemical absorption). Further the conversion into bicarbonate or carbonate takes place in water [42–43]. However, current method has several drawbacks such as the issue of equipment corrosion and high consumption of energy in regenerating the solvent. So, in order to address these issues, functionalization or impregnation of amine groups onto the porous surface led to an attractive and environment-friendly alternative to overcome the major disadvantages of amine-based absorption [51]. For this purpose, various ordered mesoporous materials such as MCM-41 [44,52], SBA-15 [47,48], KIT-6 [49] and MCM-48 [46] have been explored to anchor the amine-containing compounds on the porous surface.

Table 1.4 CO_2 adsorption capacity on pure and modified mesoporous silica adsorbents at ambient temperature and pressure condition.

Adsorbent	Functionalization/ Impregnation	BET surface area	Pressure (bar)	Temperature (K)	Adsorption Capacity (mmol g-1)	Ref.
MCM-41		856	1	303.15	0.50	[44]
MCM-41	3-aminopropyl triethoxysilane (APTES) (3.46 mmol of N /g)	27.1	1	298.15	1.74	[45]
MCM-48	APTES (2.3 mmol g-1 adsorbent)	1389 (pure MCM-48)	1	298.15	1.136	[46]
SBA-15		588.5	1	303.15	0.51	[47]
SBA-15	PEHA-50% of the total weight	10	1	298.15	2.37	[48]
KIT-6		857	1	303.15	0.65	[49]
KIT-6	PEHA (40%)	100	1	303.15	3.0	[49]
SBA-12	APTES	310	1	298	1.03	[50]

These mesoporous materials were found to be good candidate for potential application of CO_2 capture because of the relative ease of regeneration, large surface area and high pore volume. Zelenaka et al. [50] synthesized three different mesoporous materials namely MCM-41, SBA-12 and SBA-15 having average pore diameters of 33 Å, 38 Å and 71 Å respectively, to examine the potential of CO_2 capture upon grafting the porous surface with 3-aminopropyl triethoxysilane (APTES). They found that the adsorption capacity depends on the pore size and different amine groups at the pore surface. Thus, modification of the pores of these mesoporous silica materials is a promising way to improve CO_2 separation behavior. Due to the presence of large, regularly arranged pores, even large molecules/functional groups can be incorporated in the mesopores.

Most of the studies on selective CO_2 capture have been on zeolites, functionalized mesoporous silica and activated carbon. However, metal-organic frameworks have recently emerged as promising candidates over other traditional adsorbents. Zongbi et al. [25] successfully synthesized a MOF named as Mg-MOF-74, and reported a median pore width and surface area of 10.2 Å and 1174 m^2g^{-1} respectively. They found the adsorption capacity of pure CO_2 and CH_4 gases to be 8.61 $mmolg^{-1}$ and 1.05 mmol g^{-1} respectively, at 298 K and 1 bar, which is higher than the uptake in zeolite 13 X adsorbent under same condition of temperature and pressure. Several other MOFs such as Cu-BTC also show remarkably high CO_2 loadings (see Table 1.3). Thus, MOFs are ideally suited for detailed investigation of the effect of pore size, topology and functionalization on the CO_2 separation behavior to identify strategies for improved performance.

1.8 Objectives of the Thesis

The overall objective of this thesis is the computational study of mesoporous silica and microporous MOFs as candidates for adsorptive CO_2 capture from gas mixtures and the effect of adsorbent modifications such as chemical functionalization and physical impregnation on improvement of CO_2-capture performance. The specific objectives addressed in the thesis are outlined below:

- *Development and Evaluation of Molecular Models of Mesoporous Silica MCM-41 for Adsorption of CO_2, N_2, H_2O, CH_4 and C_2H_6 and Separation of CO_2 from Gas Mixtures*: MCM-41, a mesoporous silica material, is considered as promising material in the field of gas separation, drug delivery and catalysis. Thus, the objective is to develop realistic atomistic models of MCM-41 and study the selective physical adsorption of gases present

in representative flue gas compositions, relevant to post-combustion carbon capture using GCMC simulations.

- *Investigation of the Effect of Pore Size and Wall Microporosity of Mesoporous Silica on Adsorption and Separation of CO_2 from Gas Mixtures*: SBA-15 is a mesoporous silica material that possesses larger mesopores than MCM-41 and has micropores in the silica walls. This objective deals with the effect of pore size and presence of micropores inside the silica walls as well as the ratio of micropore-to-mesopore surface area and volume on CO_2 adsorption and separation, from the perspective of flue gas and natural gas purification.
- *Modification of Mesoporous Silica by Ionic Liquid Impregnation inside the Mesopores for Enhanced CO_2 Selectivity over N_2 and CH_4*: IL-impregnated porous adsorbents materials have been investigated for potential application in selective CO_2 adsorption. Here we aim to investigate in detail the separation of CO_2 from gas mixtures using ILs loaded in the regular cylindrical pores of mesoporous silica materials. Two different loadings of ILs confined in the pores of MCM-41 are considered to examine the effect on CO_2 adsorption and selectivity over CH_4 and N_2. GCMC as well as MD simulations are used to study the effect of IL confined inside the MCM-41 pores.
- *Comparative Study of CO_2 Adsorption and Separation from Gas Mixtures on Zirconium-based MOFs UiO-66 and UiO-67*: To understand the adsorption behavior in cages and windows present in MOFs and to evaluate the effect of pore and channel size, we have selected two different zirconium-based MOFs of the same UiO series. Adsorption of CO_2, CH_4, CO and N_2 and separation of CO_2 from binary gas mixtures has been studied on UiO-66 and UiO-67, using GCMC simulations. The two Zr-based MOFs studied in this work,

although topologically similar, have channels and cages of different sizes, allowing the effect of pore size on the adsorption and separation of gas mixtures to be explored.

- *Evaluation of Functionalized Cu-BTC MOFs for CO_2 Adsorption and Separation*: This objective focuses on the tailoring of MOF linkers by attaching different functional groups and evaluating the effect on adsorptive separation of CO_2. Cu-BTC was modified by grafting different functional groups (-I, -CH_3) to the linker and effect on CO_2 uptake and its selectivity over other gases such as CH_4 and N_2 was studied using GCMC simulations.

1.9 Organization of the Thesis

Brief introduction on research objectives will be discussed in the individual chapters of the thesis. The thesis can be broadly divided into three parts. In the first part, unmodified mesoporous silica such as MCM-41 and SBA-15 were modeled and gas adsorption was studied to understand the adsorption behavior of different guest molecules, in particular CO_2. In the second part, modified MCM-41 was modeled by confinement of ionic liquid inside the MCM-41 pores in order to achieve higher adsorption capacity of CO_2 as well as improved selectivity of CO_2 towards other gases. Effect of pore size and linker functionalization in microporous metal-organic frameworks on CO_2 adsorption and separation constitute the third part of the work. The thesis is organized in eight chapters namely:

1. Introduction
2. Theory and Simulation Methods
3. CO_2 Adsorption and Separation from Multicomponent Gas Mixtures using Developed Models of Mesoporous Silica MCM-41

4. Effect of Pore Size and Wall Microporosity on CO_2 Adsorption and Separation in Mesoporous Silica
5. Pore Modification of Mesoporous Silica by Ionic Liquid Impregnation for Enhanced CO_2 Separation
6. CO_2 Adsorption and Separation on Zirconium-based Metal-Organic Frameworks
7. Effect of Functional Groups on CO_2 Loading and Selectivity in Functionalized Cu-BTC Metal-Organic Frameworks
8. Conclusions and Future Directions

A schematic outline of the thesis is shown in Figure 1.8. A brief overview of the thesis chapters is presented next.

In Chapter 1, adsorption and separation of CO_2 using different adsorbents is discussed, having relevance to post combustion CO_2 capture and natural gas sweetening. This chapter also includes relevant literature survey and a statement of the thesis objectives.

In Chapter 2, the simulation methods and computational tools employed in the remainder of the thesis for conducting the various simulations and analyzing their results are discussed. The theory behind some of the techniques is also highlighted.

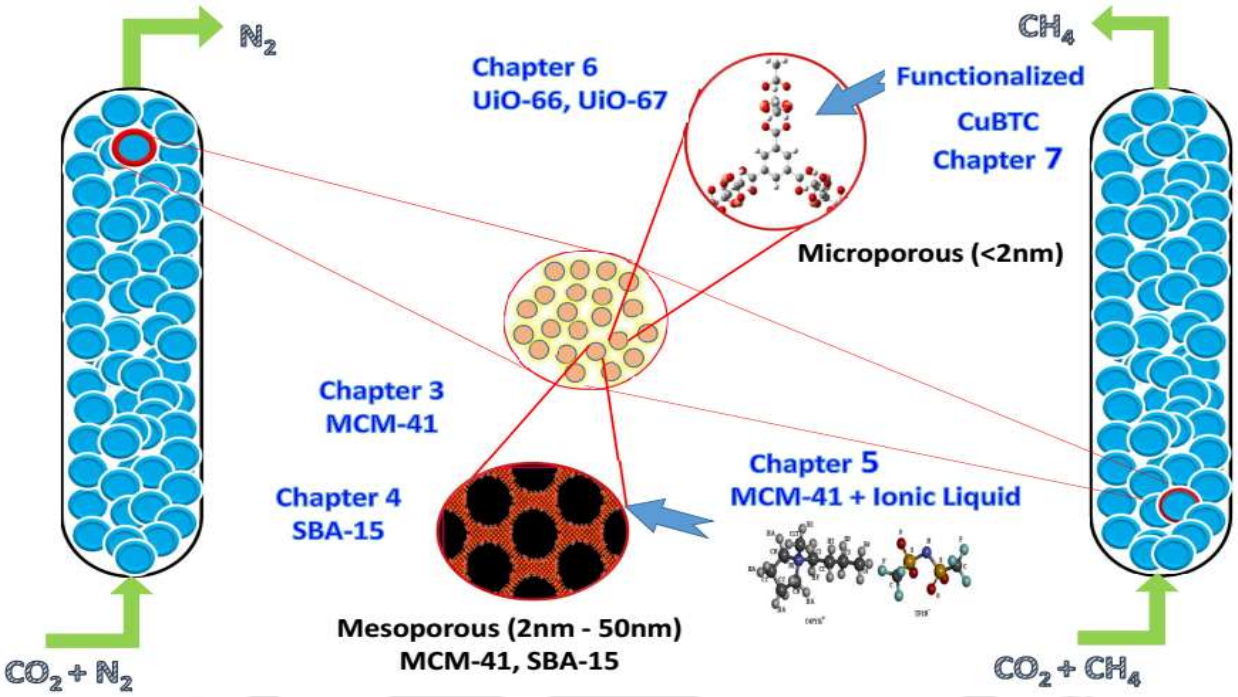

Figure 1.8: Schematic Outline of the Thesis

In Chapter 3, a detailed adsorption study of CO_2, N_2, O_2, water vapor and their mixtures has been reported on three different realistic molecular models of MCM-41 using grand canonical Monte Carlo (GCMC) simulations. Adsorption of pure gases, binary, ternary and quaternary mixtures has been studied at different temperatures and mixture compositions to determine the effect of the presence of water vapor and oxygen in flue gas mixtures on CO_2 adsorption and CO_2/N_2 separation in mesoporous silica adsorbents.

In Chapter 4, representative atomistic models of SBA-15 have been generated with varying wall microporosity and the effect of the micropore-to-mesopore surface area and volume ratios on the adsorption and selectivity of CO_2 has been studied. The adsorption behavior on SBA-15 has also been compared with that on MCM-41 to explore the effect of pore size and wall microporosity.

In Chapter 5, adsorption and separation of CO_2 has been studied in MCM-41 impregnated with a pyrrolidinium-based ionic liquid (IL) at different loadings. Several studies exist in the literature on amine-functionalization at the surface –OH groups of MCM-41 for enhanced CO_2 selectivity towards other gases. Further, CO_2 separation using IL solvents is also an active area of research. As only few reports are available on CO_2 adsorption using IL confined to mesoporous silica pores, there is ample scope for further work in this area which motivated the studies reported in this chapter.

In Chapter 6, adsorption of CO_2, CH_4, CO and N_2 and separation of CO_2 from binary gas mixtures has been studied on two different zirconium-based metal organic frameworks (MOFs), namely UiO-66 and UiO-67, using GCMC simulations. The two Zr-based MOFs studied in this work, although topologically similar, have channels and cages of different sizes, allowing the effect of pore size on the adsorption and separation of gas mixtures to be explored.

In Chapter 7, three different functionalized Cu-BTC MOFs having iodo-, single methyl and two methyl functional groups on the linker have been studied for selectivity of CO_2 over CH_4 and N_2, and compared with the results for pure CuBTC. Thus, the effect of functionalization on the adsorptive separation of CO_2 in Cu-BTC is discussed.

In Chapter 8, overall conclusions of the thesis are summarized and suggestions for future work in this area are presented.

CHAPTER 2

Theory and Simulation Methods

2.1 Introduction

This chapter discusses the details of the various computational tools and techniques employed in this thesis. A brief introduction to the grand canonical Monte Carlo simulation technique for studying gas adsorption is provided. In addition, methods to calculate other quantities relevant to gas adsorption such as excess adsorbed amount, Henry's constant, adsorption enthalpy, and selectivity are described. The ideal adsorbed solution theory, used to predict mixture adsorption isotherms from pure species adsorption data, is discussed. An insight into molecular dynamics simulations is also presented, which has been used in this work primarily to equilibrate structures, and calculate properties such as radial distribution functions and adsorbate distribution in the porous frameworks.

2.2 Molecular Simulation

Molecular simulations can be employed to obtain fundamental understanding of physical processes and phenomena at the microscopic level. Such simulations can help us understand the processes occurring in real experiments at an atomistic level, and provide details that may be inaccessible via experiments. The term 'computer experiments' is also sometimes applied to molecular simulations. Computer simulations may be employed to qualitatively predict the outcome of a process at different conditions as a pre-screening tool in order to avoid conducting experiments that may not generate promising results. In general, to conduct a molecular simulation with sufficient level of confidence, a good structural model of the material(s) to be simulated is required along with a suitable force field that describes the various interactions (bonded and non-bonded) present in the system to an acceptable degree of accuracy. For example, to simulate the

phenomenon of gas adsorption, which involves interaction of gas molecules with a solid surface, various interactions such as those between adsorbate and adsorbent, adsorbate and adsorbate, and (for flexible porous materials) within the adsorbent (intramolecular) need to be described sufficiently accurately in order to predict the adsorption behavior. The common bonded interactions include bond stretching, angle bending and dihedral interactions whereas common non-bonded interactions are the van der Waals interaction (usually modeled by the 12-6 Lennard-Jones potential) and electrostatic interaction (usually modeled by assigning partial charges and using Coulomb's law). Molecular simulation techniques can broadly be classified into two categories: Monte Carlo (MC) and molecular dynamics (MD). The former technique is probabilistic is nature where physical time is not explicitly considered whereas the latter is deterministic and is well-suited to study dynamical properties of a system.

Generally, the number of molecules involved in real experiments for the bulk system is very large (of the order of ~10^{23} molecules/atoms/ions). In order to study the thermodynamic properties of bulk systems through computer simulation directly, the number of particle-particle interactions to be considered will be enormously large to handle through computer-based calculations. The computational power required to simulate such systems in a reasonable amount of time is well beyond the capabilities of the fastest supercomputers, making the calculations practically impossible. The typical system sizes tractable by regular computational clusters are of the order of a few thousands to a few tens of thousands of particles although powerful supercomputers can now readily simulate systems with millions of particles. In order to study the bulk properties of systems using only a small fraction of the actual number of particles, a small simulation box containing 10^3–10^4 particles (box size ~20 to 50 Å) is considered and is replicated in one or more directions

through periodic boundary conditions (PBCs). PBC is applied to the original simulation cell thereby surrounding it with imaginary replica of itself in the x, y and z directions, thus eliminating any surface effects and simulating bulk-like conditions. PBC applied on a particle in an orthogonal simulation cell (with box side lengths L_x, L_y and L_z) having coordinates x_{real}, y_{real}, z_{real} are related to the coordinates of image particle by the equation

$$x_{image} = x_{real} + n_x Lx \quad (2.1)$$

$$y_{image} = y_{real} + n_y Ly \quad (2.2)$$

$$z_{image} = z_{real} + n_z Lz \quad (2.3)$$

where x_{image}, y_{image} and z_{image} are the coordinates of particle in replica boxes and n_x, n_y and n_z are the integers including zero. On applying PBC, each particle will have an infinite number of images and in order to calculate the interactions, considering an infinite number of images is not feasible. For non-bonded interactions, a cutoff distance is usually employed (especially for short-range interactions) with particles separated by more than this distance considered not to be interacting with each other.

2.2.1. Statistical Mechanics

Statistical mechanics allows us to study the macroscopic behavior of a large collection of particles (around ~10^{23}) by examining the properties of a much smaller system (around ~10^4). MC and MD simulations are two different approaches to gain the detailed description of a microscopic system in a given thermodynamic condition. For example, particle positions and velocity distribution are the two important quantities obtained from MD simulation which are useful to predict macroscopic

properties such as diffusivity and thermal conductivity. Further, fluctuations in the number of particles and system energy can be related to properties such as the heat capacity. Thus, statistical mechanics forms the link that relates the information obtained from molecular simulation of microscopic systems to macroscopic thermodynamic properties of the system. Statistical mechanics works on two fundamental postulates: (i) given an isolated system in equilibrium, each accessible microstate corresponding to the same total energy can be found with equal probability, i.e. a system in equilibrium does not have any preference for any of its microstates, and (ii) the ensemble average of a thermodynamic property (i.e., average over the different possible microstates of the system) is equivalent to the time-averaged macroscopic value of the property for the real system. The second postulate is also referred to as the ergodic hypothesis, and enables the use of molecular simulation techniques to calculate macroscopic properties of a system.

Canonical Ensemble: In the canonical ensemble [53], number of particles (N), volume (V) and temperature (T) are constant for a particular molecular or atomic system. The partition function [53] $Q(N,V,T)$ is given by

$$Q(N,V,T) \equiv \frac{1}{\Lambda^{3N}N!}\int dr^N \, exp[-\beta U(r^N)] \qquad (2.4)$$

where $\Lambda = \sqrt{h^2/(2\pi m k_B T)}$ is the thermal de Broglie wavelength. β is related to temperature according to the equation $\beta = 1/(k_B T)$, k_B is the Boltzmann constant, $U(r^N)$ is the potential energy of the system with particle positions given by r^N. Canonical ensemble is also known as NVT ensemble, where sampling of system through MC simulation can be performed according to the following scheme:

1. A random particle is selected and energy of the configuration is calculated as $U(o)$.
2. A random displacement is given to the particle: $r(n) \rightarrow r(o) + \Delta(Ranf - 0.5)$

Here Δ denotes a very small displacement, and $Ranf$ is a random number between 0 and 1 (generated by appropriate random number generator).

3. The new configuration can be accepted according to a probability

$$acc(o \rightarrow n) = \min(1, exp[-\beta\{U(n) - U(o)\}]) \quad (2.5)$$

where $U(n)$ indicates the energy of the new configuration. If the move is rejected then the configuration of the system is reverted to its old configuration.

Isobaric Isothermal ensemble: Molecular simulations are frequently carried out in isobaric-isothermal ensemble (also known as NPT ensemble) as many experiments are conducted at controlled temperature and pressure. Further, if the system density is not known a priori, simulations in the NPT ensemble may drive the system to its correct density. MC simulation in the NPT ensemble was first carried by McDonald to calculate the excess properties of binary mixtures of liquids interacting by the Lennard-Jones (LJ) potential. In the NPT ensemble, simulation box size is free to relax according to applied pressure and temperature. For a cubic simulation box of volume V, and side length L, the real coordinate r^N is related to scaled coordinate s^N by

$$s_i = \frac{r_i}{L} \quad (2.6)$$

Partition function [53] for NPT ensemble is given by

$$Q(N,P,T) \equiv \frac{\beta P}{\Lambda^{3N} N!} \int d(\ln V) V^{N+1}\, exp[-\beta PV] \int ds^N \exp[-\beta U(s^N)] \qquad (2.7)$$

and the probability of finding the volume V of a simulation box is given by

$$\mathcal{N}(V; s^N) \;\alpha\; V^{N+1} \exp(-\beta PV) \exp[-\beta U(s^N; L)] \qquad (2.8)$$

The distribution can be sampled according to the acceptance rule

$$acc(o \to n) = \min\left(1, exp\left[-\beta\left\{U(s^N, V') - U(s^N, V) + P(V' - V) - (N+1)\beta^{-1} ln\left(\frac{V'}{V}\right)\right\}\right]\right) \qquad (2.9)$$

2.2.2. Grand Canonical Monte Carlo Simulation

Grand canonical Monte Carlo (GCMC) simulations [53] are often employed to study the adsorption of gases on atomistic models of different porous materials. In this thesis, GCMC simulations have been conducted using the Towhee [54] and RASPA software packages [55] to calculate the adsorbate loading inside the adsorbent pores as a function of the pressure of the bulk gas in equilibrium with the adsorbent.

GCMC is a MC simulation technique in which the chemical potential (μ), volume (V) and temperature (T) is fixed during the simulation. Four different moves are carried out on the adsorbate molecules for pure gas adsorption, *viz.* (i) translational, (ii) rotation, (iii) insertion and (iv) deletion. In the case of adsorption of gas mixtures, an identity exchange (or particle swap) move is also frequently used. Each type of move is accepted according to Metropolis scheme.

Translation and rotation moves are accepted when a random number between 0 and 1 is less than the calculated probability according to equation 2.10.

$$acc(c \rightarrow c') = \min(1, exp\{-\beta[U(c') - U(c)]\}) \quad (2.10)$$

For deletion, the acceptance criterion is

$$acc(c \rightarrow c') = \min\left(1, \frac{N}{V\beta P} exp\{\beta[U(c') - U(c)]\}\right) \quad (2.11)$$

and for insertion,

$$acc(c \rightarrow c') = \min\left(1, \frac{V\beta P}{(N+1)} exp\{-\beta[U(c') - U(c)]\}\right) \quad (2.12)$$

Here c and c' are the old and new configurations after each type of MC move respectively, V is the volume of simulation box, N is the original number of particle insides the box (before the move) and P is the pressure. The acceptance criteria for the insertion and deletion moves above are valid for ideal gases (i.e., at low pressures) for constant μ, V and T. For higher pressures, the species fugacity will have to considered instead of pressure. The fugacity coefficient can be obtained from an appropriate equation of state such as the Peng-Robinson equation of state. Value of β is directly dependent on the Boltzmann constant k_B and temperature T according to $\beta = 1/(k_B T)$.

For multicomponent adsorption, particle swap move [56,57] were taken into account in order to achieve faster equilibrium inspite of being a non physical move. Therefore, swap move was accepted with a probability (when component "*j*" changed to "*i*")

$$acc(c \rightarrow c') = \min\left(1, \frac{{N_j}^{old} z_i}{({N_i}^{old} + 1) z_j} exp\{-\beta[U(c') - U(c)]\}\right) \quad (2.13)$$

where N denotes the number of particles, z_i and z_j is the activity of species *i* and *j* respectively.

Activity of species is dependent upon the chemical potential of the species according to equation 2.14.

$$z_i = \frac{\exp\left(\frac{\mu_i}{k_b T}\right)}{{\Lambda_i}^3} \quad (2.14)$$

where $\Lambda_i = h/\sqrt{2\pi m_i k_b T}$ is the de Broglie wavelength.

Interaction Potentials

Mathematical functional form describing the interactions between atoms is referred to as interatomic potential. The proper selection of interatomic potential is necessary to describe the behavior of atomic system correctly and to mimic the real experiment theoretically. The non-bonded interactions between atoms is commonly described by the 12-6 Lennard-Jones potential (for van der Waals interaction) and Coulomb's law (for electrostatic interactions), as shown in equation 2.15

$$u_{ij}(r) = 4\varepsilon_{ij}\left[\left(\frac{\sigma_{ij}}{r_{ij}}\right)^{12} - \left(\frac{\sigma_{ij}}{r_{ij}}\right)^{6}\right] + \frac{q_i q_j}{4\pi\varepsilon_0 r_{ij}} \quad (2.15)$$

Here $u_{ij}(r)$, ε_{ij}, σ_{ij}, r_{ij}, q_i, q_j and ε_0 are the total non-bonded potential energy, LJ well depth, LJ size, distance between the two sites *i* and *j*, charges on i^{th} and j^{th} site and vacuum permittivity

respectively. Electrostatic interactions have been calculated in all the GCMC simulations in this thesis using the Ewald summation technique [58].

Intramolecular potentials describe the interactions between the bonded atoms within a molecule. Bonded potential includes bond stretch (2-body), bond angle bend (3 body), dihedral angle torsion (4-body) and inversion term (4-body). Bond stretching and angle bending are usually described using a simple harmonic oscillator, although the Morse potential and harmonic cosine form are also sometimes used (for bond stretching and angle bending respectively). Dihedral interactions are frequently described using a cosine functional form.

$$E_{bond} = K_b(r - r_0)^2 \quad (2.16)$$

$$E_{angle} = K_a(\theta - \theta_0)^2 \quad (2.17)$$

$$E^T{}_{abcd} = \frac{1}{2}V_{bc}[1 - cos\{n_{bc}(\varphi - \varphi^o_{bc})\}] \quad (2.18)$$

where $E^T{}_{abcd}$ is the dihedral interaction for two bonds *ab* and *cd* connected with a common bond *bc*, φ is the dihedral angle (between *abc* and *bcd*), φ^o_{bc} is the equilibrium dihedral angle and V_{bc} is the barrier to rotation. K_b is the harmonic force constant for stretching of bond. Where r_o is the equilibrium bond length. K_a is the bending constant and θ_0 stands for equilibrium angle.

2.2.3. Analysis Tools

a) Radial Distribution Function

Radial distribution function (RDF), also known as pair distribution function, is an important quantity used to characterize local order or correlations in the simulated structure.

The mathematical formulation for finding the RDF between pair of atoms *i* and *j* is

$$g_{ij}(r) = \frac{V}{4\pi r^2 \Delta r N_i N_j} \sum_{k=1}^{N_i} n_k(r, r + \Delta r) \qquad (2.19)$$

Here *Ni* and *Nj* are the total number of atoms of type *i* and *j* respectively constituting the system, *V* is the volume of the simulation box, subscript of g_{ij} indicates that the number of particles of type *j* are being counted within a spherical shell of radius r and thickness Δr, centered at particles of type *i*. Thus, $n_k(r, r + \Delta r)$ is the number of particles of type *j* between distance r and $r + \Delta r$ from particle number *k* of type *i*.

b) Coordination number

The coordination number (CN) is obtained from integration of the RDF peaks and provides an estimate of the number of molecules in the vicinity of the reference molecule. In the calculation of coordination number, density of the system is also accounted for, along with the height and width of the RDF peaks. Integration of gij(r) in the spherical coordinate to the first minimum of the RDF will give us the coordination number of a molecule in its first coordination shell.

$$CN = 4\pi\rho_N \int_{r_0}^{r_i} g_{ij}(r) r^2 dr \qquad (2.20)$$

Here, r_0 is the leftmost position starting from $r = 0$, where $g_{ij}(r)$ is zero, r_1 corresponds to the first minimum of g_{ij}, and ρ_N is the number density of the surrounding atom in a spherical shell.

c) 3D Spatial Distribution Plots:

The 3D spatial distribution plots give a visual three-dimensional representation of the different locations in the simulation box where the adsorbate molecules are present. These plots have been

constructed by considering the location of the adsorbate molecules in the adsorbent framework over a large number of snapshots (typically 100 or more) at a particular temperature and pressure.

d) Mean-squared Displacement:

Mean-squared displacement (MSD) describes the average of the square of the displacement of an atom from its initial position with respect to time (t). It is defined as,

$$MSD = \langle |\vec{r}_i(t) - \vec{r}_i(0)|^2 \rangle \tag{2.21}$$

where $\vec{r}_i(t)$ is the position vector of the i^{th} particle after time t. For d-dimensional motion, the diffusivity D can be estimated from the Einstein's equation (2.22)

$$D = \lim_{t\prime \to \infty} \frac{1}{2dNt} \langle \sum_{j=1}^{N} \left[\vec{r}_j(t + t') - \vec{r}_j(t)\right]^2 \rangle \tag{2.22}$$

Here, the expression within the angle brackets $\langle \cdots \rangle$ corresponds to the mean-squared displacement (MSD) of the molecule. Self-diffusion coefficients can be calculated from the slope of MSD vs. time curve.

2.3 Adsorption

Adsorption is the adhesion of molecules (typically gas or liquid) to the surface of a solid. It is a surface phenomenon which possess one extra degree of freedom in addition to bulk phase equilibrium.

2.3.1. Equilibrium Adsorption Isotherm

At equilibrium, amount of pure gas adsorbed (N) on any adsorbent is a function of pressure (P) and temperature (T),

$$N = I(P, T) \tag{2.23}$$

where N is the amount adsorbed, P is the pressure and T is the temperature. The adsorbed amount at constant temperature is then given by

$$N = I(P) \tag{2.24}$$

The above equation relating the amount adsorbed to the bulk gas pressure at constant temperature is commonly known as adsorption isotherm.

At high pressures, gaseous behavior deviates from ideality. In order to mimic the real (non-ideal) behavior of gases at high pressures, generally the pressure term is replaced by fugacity (f) which can be calculated using an equation of state such as the Peng-Robinson equation of state. Thus, the adsorption isotherm is given by equation

$$N = I(f) \tag{2.25}$$

Different adsorption isotherms are classified according to their IUPAC nomenclature, as shown in Figure 2.1. Type I adsorption isotherm represents the adsorption behavior on microporous adsorbent. The saturation loading in type I isotherm corresponds to the definite and complete filling of micropores. Non-porous adsorbent such as macroporous adsorbent shows type II, III and VI isotherms while type IV and V isotherms are exhibited by mesoporous adsorbents, on which multilayer adsorption may take place at high pressures.

2.3.2. Henry's Constant

Henry's constant is defined as the slope of adsorption isotherm in the limit of zero pressure. It can be related to amount adsorbed (N) and pressure (P) as shown in equation (2.26)

$$\beta = \left(\frac{N}{P}\right)_{P\to 0} \tag{2.26}$$

where β is the Henry's constant.

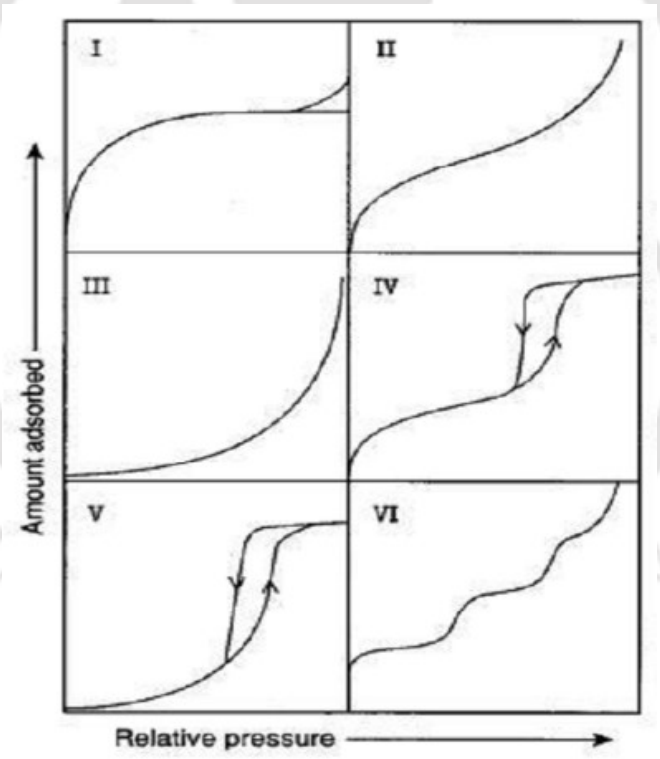

Figure 2.1 IUPAC classifications of adsorption isotherms (taken from [59]**).**

2.3.3. Models for Pure Gas Isotherms

The adsorption isotherm models used in this thesis are discussed next.

(a) Langmuir Isotherm [60]: This type of isotherm model is based on the following assumptions:

(i) Adsorption sites are fixed.

(ii) Each site corresponds to one adsorbate molecule.

(iii) All sites are energetically identical.

(iv) There are no lateral interactions between adsorbate molecules.

Based on the above assumption, the Langmuir equation is formulated as

$$N = \frac{N_1^{max} \beta P}{N_1^{max} + \beta P} \tag{2.27}$$

where N is the excess amount adsorbed, f is the fugacity, N_1^{max} is the saturation capacity, and β is Henry's constant. Saturation capacity is considered to be independent of temperature, and the temperature dependence for Henry's constant is expressed by

$$\beta = \beta_{10} \exp(\beta_{11}/T) \tag{2.28}$$

where T is absolute temperature. The two parameters β_{10} and β_{11} are related to entropy and enthalpy of adsorption at zero loading, respectively.

(b) Dual-Site Langmuir Isotherm

The dual-site Langmuir (DSL) model [60,61] is based on the assumption that there exist two different types of adsorption sites on the solid surface. Each site follows a Langmuir adsorption behavior but the two types of sites are energetically distinct. Thus, a DSL isotherm model is given by equation (2.29)

$$N = \frac{N_1^{max}\beta_1 P}{1+\beta_1 P} + \frac{N_2^{max}\beta_2 P}{1+\beta_2 P} \qquad (2.29)$$

where N is the amount adsorbed, P is the pressure, N_1^{max} and N_2^{max} are the saturation loadings for sites 1 and 2 respectively, and β_1 and β_2 represent affinity parameters for sites 1 and 2 respectively. N_1^{max} and N_2^{max} represent saturation loadings, and therefore are independent of temperature. However, the affinity parameter β_1 and β_2 are functions of temperature. Temperature dependence of the affinity parameters is given by the equation (2.30)

$$\beta_1 = \beta_{10}\exp(\beta_{11}/T)\,; \qquad \beta_2 = \beta_{20}\exp(\beta_{21}/T) \qquad (2.30)$$

where T is the absolute temperature. Henry's constant for the DSL model is given by equation (2.31)

$$\beta = \beta_1 N_1^{max} + \beta_2 N_2^{max} \qquad (2.31)$$

where β represents Henry's constant.

2.3.4. Calculation of Isosteric Heat of Adsorption

Enthalpy of adsorption plays an important role in determining the adsorbate-adsorbent strength and can be used to characterize the adsorptive behavior of an adsorbent towards different

adsorbates. Enthalpy of adsorption can be used to relate the adsorbate loading on different adsorbents at low coverage or in the low-pressure regime. It also dictates the regeneration capability of the adsorbent after successful selective capture of gaseous adsorbate. For example, lower adsorption enthalpy at zero coverage will lead to easier regeneration and will result in lower cost of regenerating the adsorbent. Two different approaches for obtaining the enthalpy of adsorption are discussed next.

a) The isosteric heat of adsorption can be calculated from GCMC simulation using fluctuations in the potential energy [62] and the number of particles according to the equation (2.32)

$$\Delta H_{ads} = \frac{\langle UN \rangle_\mu - \langle U \rangle_\mu \langle N \rangle_\mu}{\langle N^2 \rangle_\mu - \langle N \rangle_\mu \langle N \rangle_\mu} - \langle U_g \rangle - k_B T \qquad (2.32)$$

where ΔH_{ads} is the change in enthalpy upon adsorption of a single molecule, $\langle \cdots \rangle_\mu$ represents ensemble average in the grand canonical ensemble, U is the internal energy of the system containing all interactions between adsorbate-adsorbate and adsorbate-adsorbent, N is the total number of molecules in the system. Subscript g represents the gas phase, k_B is the Boltzmann constant and T is temperature of the system.

b) Enthalpy of adsorption can also be evaluated using the pure component adsorption isotherm data [61] obtained from the GCMC simulation in conjunction with the equation (2.33)

$$\Delta H_{ads} = -R \left. \frac{\partial (\ln f)}{\partial \left(\frac{1}{T}\right)} \right|_N \qquad (2.33)$$

where f is the fugacity and R is the universal gas constant. Adsorbate loading is a function of fugacity and can expressed as such using different isotherm models. The specific expressions for calculating enthalpy of adsorption for the Langmuir and DSL models are shown in equation (2.34) and (2.35) respectively.

$$\Delta H_{ads} = -R(\beta_{11}) \tag{2.34}$$

$$\Delta H_{ads} = -R\left(\frac{\beta_{10}N_1^{max}\beta_1(1+\beta_2 f)^2 + \beta_{20}N_2^{max}\beta_2(1+\beta_1 f)^2}{N_1^{max}\beta_1(1+\beta_2 f)^2 + N_2^{max}\beta_2(1+\beta_1 f)^2}\right) \tag{2.35}$$

2.3.5. Conversion of Absolute Adsorbed Amount to Excess Amount

Total number of adsorbate molecules obtained from GCMC simulations is the absolute adsorbed amount, which includes both adsorbed phase and bulk phase adsorbate molecules. In contrast, the number of molecules present only in the adsorbed phase is known as the excess amount adsorbed, which is what experiments measure. In order to compare the GCMC results and the experimental results, absolute amounts obtained from simulations must be converted to excess amounts. The number density of adsorbate gas molecules in the bulk phase at a given temperature and pressure is obtained either from an equation of state such as the Peng-Robinson equation of state or from MC simulations in the NPT ensemble at the process temperature and pressure. Thereafter, the excess amount adsorbed is obtained from the absolute amount according to the equation (2.36)

$$N_{ex} = N_{abs} - (\rho \times \epsilon \times V_{tot}) \tag{2.36}$$

where N_{ex} is the excess amount adsorbed, N_{abs} is the absolute amount from GCMC simulation, ρ is the number density of adsorbate molecules in the bulk gas, V_{tot} is the total volume of simulation box and ϵ is the helium void fraction for accessible volume present inside the unit cell of simulation

box. In this thesis, the helium void fraction is generally obtained from the surface and volume tool present in the Materials Studio 7.0 software package [63].

2.3.6. Ideal Adsorption Solution Theory

Ideal adsorbed solution theory (IAST) by Myers and Prausnitz [64] permits the theoretical prediction of multi-component adsorption isotherms and selectivities from adsorption equilibrium data of pure species. The adsorbed gas mixture is treated as an ideal solution and no energetic heterogeneity of adsorption sites is assumed to be present. The spreading pressure,

$$\pi = \frac{RT}{A}\int_{P=0}^{P=P_i^0} n_i^0(P) \times d\ln P \qquad (2.37)$$

where T is the temperature, R is the universal gas constant, A is the surface area of the adsorbent, P_i^0 is the pure component pressure and $n_i^0(P)$ is the amount of pure component adsorbed at pressure P. For binary mixtures, IAST gives a complete set of equations (2.38–2.40) that need to be solved together in order to find the amount of each component in the adsorbed phase.

$$\pi_1^0 = \varphi_1(P_1^0)\ , \pi_2^0 = \varphi_2(P_2^0) \qquad (2.38)$$

$$Py_1 = P_1^0 \times x_1\ , Py_2 = P_2^0 \times x_2 \qquad (2.39)$$

$$\pi_1^0 = \pi_2^0\ , \quad x_1 + x_2 = 1, \quad y_1 + y_2 = 1 \qquad (2.40\ \text{a, b, c})$$

In equations (2.40 a,b,c), x and y are the adsorbed and bulk gas phase mole fractions respectively, and the subscripts denote the species constituting the binary mixture. The parameters of the Langmuir/DSL model are determined by fitting the model to the pure species adsorption data (obtained from GCMC simulations). The resulting model equation is used to evaluate the integral

in equation (2.37); solving equations (2.38) and (2.39) simultaneously then gives the adsorbed phase mole fractions at any given temperature, pressure and bulk gas composition.

2.3.7. Selectivity

The adsorptive selectivity for binary mixture adsorption of species A and B is defined as

$$\alpha_{A/B} = \frac{\left({}^{x_A}/_{x_B}\right)}{\left({}^{y_A}/_{y_B}\right)} \tag{2.41}$$

where $\alpha_{A/B}$ is the selectivity of species A over species B, x represents the mole fraction in the adsorbed phase, y represents the mole fraction in the bulk gas phase, and subscripts A and B denote the corresponding species.

CHAPTER 3

CO_2 Adsorption and Separation from Multicomponent Gas Mixtures using Developed Models of Mesoporous Silica MCM-41

3.1 Introduction

Adsorptive separation of CO_2 using porous materials such as zeolites, mesoporous silicas, metal organic frameworks, porous carbons etc. is an attractive alternative to conventional amine scrubbing due to lower regeneration energy requirements. The surface area, pore texture, and pore size distribution of an adsorbent play a vital role in effective and efficient separation. The M41S family of mesoporous silica materials, discovered by researchers at Mobil Corporation in 1992, have large pores, uniform pore size and structure, and high surface area. MCM-41 belongs to M41S family of mesoporous silica materials and possesses high surface area, tunable pore size (by varying chain length of the surfactant during synthesis), uniformly aligned, ordered hexagonal arrangement of cylindrical pores, and considerable surface silanol groups. The surface area and pore volume are typically in the range of 700–1500 m^2g^{-1}, and 0.7–1.0 cm^3g^{-1} respectively [40,65,66]. The pore size of MCM-41 is highly tunable and ranges from 15–100 Å. The pore walls consist of disordered network of siloxane bridges having skeletal density of 2.2–2.4 g cm^{-3} [65]. These remarkable features of MCM-41 make it suitable for applications such as catalysis, gas adsorption and separation, drug delivery etc.

MCM-41 was first synthesized by Kresge et al. [40] using aluminosilicate gels in the presence of surfactants having ordered array of pores arranged in hexagonal fashion with pore size in the range of 16 Å–100 Å. BET surface area and pore volume were found to be ≥1000 m^2g^{-1} and 0.7–1.2 cm^3g^{-1} respectively [40]. Zhaohua et al. [67] prepared aluminosilicate molecular sieves by following a synthesis procedure similar to that used for MCM-41. Two different raw materials namely Catapal alumina or sodium aluminate and aluminum sulfate were used as aluminum source to achieve 6- and 4-coordination number of aluminum respectively. They showed through XRD

analysis and TEM images that hexagonal mesopore arrangement ceases to exist on increasing Si/Al ratio in the solid wall of the pore. They also confirmed that calcination at 550°C for 24 hours enhances the mesopore formation. Catalytic activity of pure MCM-41 can be enhanced by substituting the silicon sites in the pore walls of MCM-41 with metal atoms. For example, Placidus et al. [68] modified pure MCM-41 by substituting silicon sites with Fe metal to obtain Fe-MCM-41 which was used as a catalyst for the production of carbon nanotubes by acetylene pyrolysis.

Yun et al. [69] studied the adsorption of methane, ethane and their binary mixtures on MCM-41 through molecular simulation using a simple model for cylindrical MCM-41 pores. He and Seaton [65,66] conducted molecular simulation study of pure gas and mixture adsorption behavior of methane, ethane and carbon dioxide in MCM-41 using the same simple model. This model of MCM-41 consists of three concentric, cylindrical layers of oxygen atoms made infinitely long by applying periodic boundary condition in the axial direction of the cylinders. The simple model represented a single, isolated pore and was not a very realistic representation of the hexagonally arranged pore network observed in real MCM-41. Zhuo et al. [70] performed molecular simulation studies on binary adsorption of CO_2/N_2 mixtures in mimetic MCM-41 models at representative flue gas composition but did not consider the effect of the presence of other gases such as water vapor in the flue gas. Builes and Vega [71] investigated the adsorption of pure CO_2 on a realistic model of amine functionalized MCM-41 by simulation studies. Jing et al. [72] studied the adsorption of CO_2, N_2 and their mixtures on MCM-41 material but did not investigate the effect of water vapor on the adsorption behavior. Pajzderska et al. [73] studied the behavior of water confined in the pores of MCM-41 material using ^1H NMR and molecular dynamics simulation. They observed that at low filling, water molecules remained close to the pore surface and whereas

at higher fillings, water molecules were present away from the surface as well; however, the dynamics of water molecules was much slower than in bulk water. Coasne et al. [74] used grand canonical Monte Carlo (GCMC) simulations to study the solubility of CO_2, N_2 and CH_4 in water confined in pores of ZSM-5, MCM-41 and MIL-100. They observed significant enhancement in the solubility of the gases in confined water over that in bulk water. Mason et al. [75] studied the adsorption of gaseous mixture of CO_2, N_2 and H_2O in several microporous and mesoporous adsorbents, including amine-grafted MCM-41, using high-throughput analyzer. In amine-grafted MCM-41 samples, although the presence of water was observed to affect the amount of CO_2 adsorbed, the exact behavior depended on the type of amine.

In the present work, a detailed adsorption study of CO_2, N_2, O_2, water vapor and their mixtures has been carried out on three different realistic molecular models of MCM-41 using grand canonical Monte Carlo (GCMC) simulations. Adsorption of pure gases, binary, ternary and quaternary mixtures has been studied at different temperatures and mixture compositions to determine the effect of the presence of water vapor and oxygen in flue gas mixtures on CO_2 adsorption and CO_2/N_2 separation in mesoporous silica adsorbents.

3.2 Model and Simulation Details

Three different molecular models of MCM-41, henceforth referred to as model 1, model 2 and model 3, have been investigated in this work to study gas adsorption and separation. Model 1 was constructed by carving cylindrical pores (approximately 36 Å in diameter) in a block of amorphous silica matrix (taken from the database of structures available in the Materials Studio 7.0 software [63]) while maintaining the regular hexagonal arrangement of the pores, as shown in Figure 3.1

(d). Creation of pores resulted in unsaturated Si and O sites on the pore surface. In order to saturate these dangling bonds, a simple rule was followed which involved identifying the atoms having one or more dangling bond(s). Silicon atoms with exactly three dangling bonds were replaced with hydrogen atoms whereas those having less than three dangling bonds were saturated with appropriate number of hydroxyl (–OH) groups (one or two). Similarly, dangling bonds of oxygen atoms were saturated with H atoms. Si–O and O–H bond lengths were taken to be 1.61 Å and 1.1 Å respectively [76] for addition of H atoms and –OH groups. The geometry of the MCM-41 structure thus obtained was optimized. Figure 3.1 (a) shows the initial amorphous silica block, Figure 3.1 (b) shows the principal cylindrical pore, and Figure 3.1 (c) shows the simulation box containing the principal pore and four quarter pores, where the dangling bonds on the pore wall have been saturated and geometry has been optimized. Hexagonal arrangement of the cylindrical pores is obtained by application of periodic boundary condition in all three direction (x, y and z), as shown in Figure 3.1 (d) where the simulation box has been replicated three times in the x and y directions. Model 2 was derived from purely crystalline silica framework of cristobalite (structure taken from the crystallographic database [77]). The crystobalite unit cell was replicated 6x6x9 times in x, y and z direction to create a crystalline cuboidal block. Molecular dynamics (MD) simulations were carried out on the cristobalite block at high temperature using Materials Studio 7.0 software [63] to disrupt the crystalline structure and generate disorder in the regular arrangement. Cylindrical pores having diameter of approximately 36 Å were then carved in the framework, dangling bonds were saturated and geometry was optimized. The methodology used for saturating the dangling bonds was identical to that employed during generation of model 1.

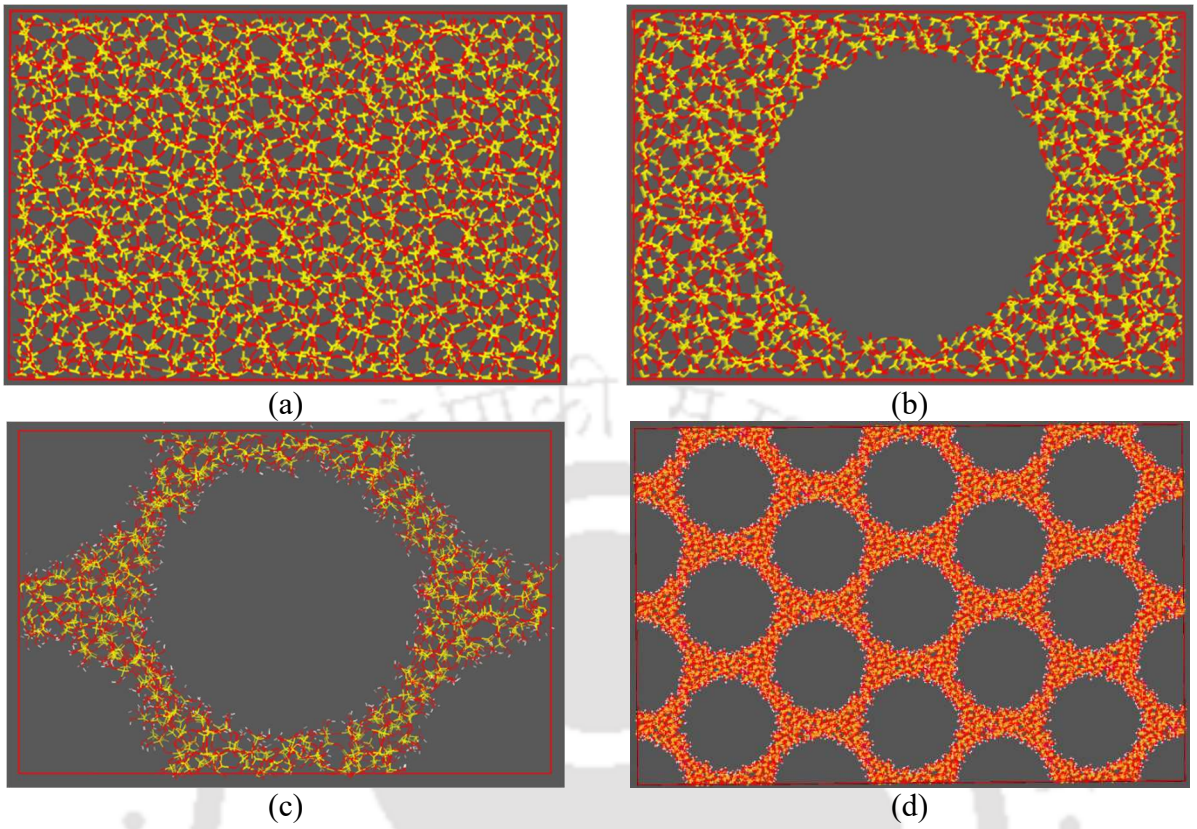

Figure 3.1 (a) Amorphous block of silica matrix, (b) principal pore, (c) unit simulation box with hydroxyl group attached after geometry optimization, (d) periodic replication to obtain hexagonal array of pores.

Model 3 of MCM-41 has been taken from the work of Ugliengo et al. [78], which was developed by inducing disorder in a hexagonal supercell of α-quartz through classical molecular dynamics at high temperature, cutting the pore, appropriately saturating the dangling bonds with H atoms or −OH groups, and optimizing the obtained structure using density functional theory (DFT). Pore diameters in all the models considered here lie in the range typically observed in real MCM-41 adsorbents [79]. Unit simulation boxes of the three models used in this work are shown in Figure 3.2. For models 1 and 2, Forcite module of Materials Studio 7.0 software [63] was used to carry out geometry optimization employing the DREIDING force field [80] which includes both bonded and non-bonded interaction terms. Non-bonded interactions were computed as the sum of Lennard-

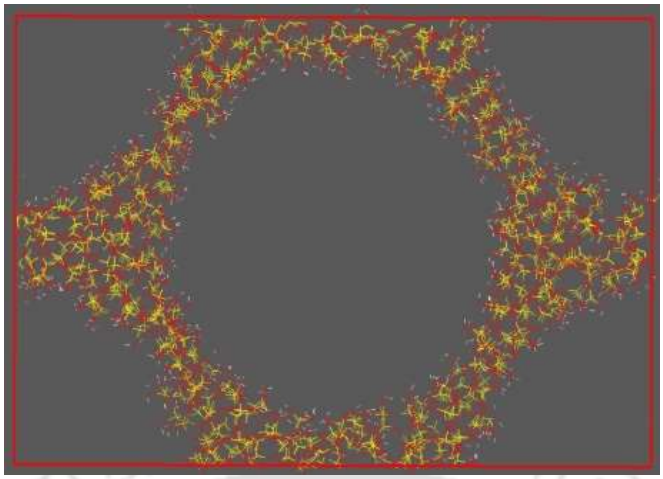

(a)

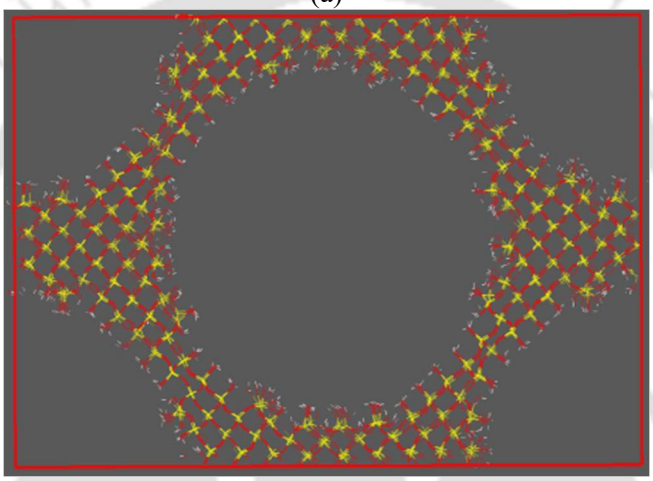

(b)

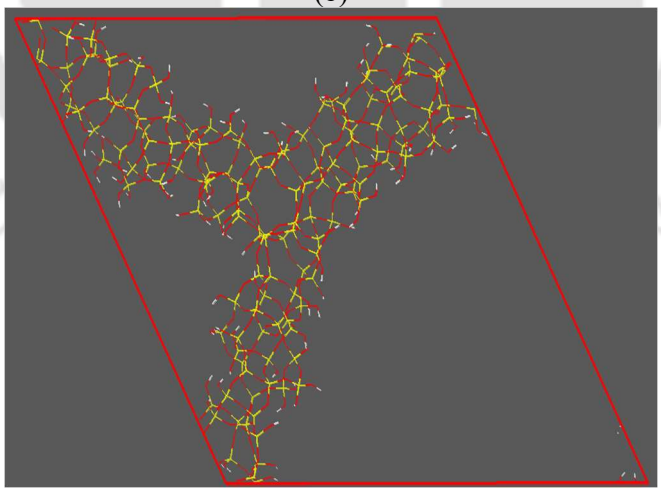

(c)

Figure 3.2 Simulation box of a) Model 1, b) Model 2, c) Model 3.

Jones (LJ) potential and Coulombic interaction. The van der Waals interactions were computed using a cutoff distance of 12.5 Å and the Coulombic interactions were calculated using the Ewald sum method [58]. Charges on individual atoms were estimated from the charge equilibration (QEq) method [81]. Geometry optimization was not carried out for model 3 because the structure taken from [78] was already optimized using DFT calculations.

The three MCM-41 models were characterized by determining the X-ray diffraction (XRD) pattern, surface area, accessible pore volume and radial distribution function (RDF). XRD pattern, Connolly surface area [82] and accessible pore volume for all the models were calculated using the Materials Studio 7.0 software. XRD patterns of MCM-41 models were simulated using Cu Kα (λ = 1.5406 Å) radiation. Diffraction data were recorded in the 2θ range of 1–8° with a step size of 0.05. Connolly surface area and accessible pore volume were calculated by rolling a spherical probe having a radius of 1.4 Å on the surface of the adsorbent pores. The accessible surface area was calculated using nitrogen probe of radius 1.82 Å. RDF is the probability distribution of finding particles/atoms of a certain type in a spherical region around another central particle/atom of same or different type. Thus Si–Si RDF in the MCM-41 framework provides a measure of how Si atoms are spatially distributed with respect to each other whereas Si–O RDF indicates how O atoms are distributed with respect to the Si atoms. The Si–Si, O–O, Si–O, O–H and H–H RDFs were calculated for all three MCM-41 models considered. In addition, the adsorbent-adsorbate (C_{CO2}–$O_{MCM\text{-}41}$) and adsorbate-adsorbate (C_{CO2}–C_{CO2}) RDFs were calculated to study the distribution of adsorbed CO_2 in the MCM-41 pores.

GCMC [83] simulations were performed using the Towhee software package [54] to study the adsorption of CO_2, N_2, O_2, H_2O and their mixtures in the MCM-41 models. In this work, N_2 [84]

and O_2 [85] were modeled as having two LJ interaction sites at the respective atom positions and three sites with partial charges (two sites at the two atom positions and one at the center of mass) to capture the effect of quadrupole moment of these small molecules. A three-site model was employed for CO_2, with the sites located at the respective atom positions and having an LJ interaction center and partial charge. The detailed force field parameters for the adsorbate gases as well as the adsorbent (MCM-41) have been taken from literature and are summarized in Table 3.1.

Table 3.1 LJ potential parameter, charges and bond lengths in adsorbent and adsorbate molecules

Molecule	Site	$\sigma(\text{Å})$	$\varepsilon(K)$	$q(e)$	Bond length (Å)
MCM-41 [72]	Si	3.804	155.858	0.1222	
	O	3.033	48.115	-0.0615	
	H	2.846	0.050	0.0318	
CO_2 [72]	C	3.473	47.813	0.6040	1.152 (C=O)
	O	3.033	48.115	-0.3020	
N_2 [84]	N	3.310	36.000	-0.4820	1.10 (N≡N)
	N(COM)†	0.000	0.000	0.9640	
O_2 [85]	O	3.020	49.000	-0.1130	1.210 (O=O)
	O(COM)†	0.000	0.000	0.2260	
H_2O [86]*	H	0.000	0.000	0.4238	1.0 (O–H)
	O	3.166	78.197	-0.8476	

†COM stands for center of mass; *H–O–H angle (water model SPCE [86]*) = 109.47°

The chemical potential values of the adsorbate gases, provided as input to the GCMC simulations, were calculated for each pure adsorbate species as well as mixture of adsorbate molecules by carrying out Monte Carlo (MC) simulations on the bulk gas (pure or mixture) in the isothermal-isobaric (constant NPT) ensemble using the Towhee software package at the appropriate

temperature and pressure. For this purpose, a simulation box containing only the gas molecules (of one or more type depending on whether pure gas or mixture is being considered) is first equilibrated at the desired temperature and pressure (at which we seek to obtain the adsorption loading) by carrying out MC simulations in the constant NPT ensemble. After the density of the simulation box becomes relatively constant, the gas or gas mixture in the box is representative of the bulk gas phase at the temperature and pressure of interest. The chemical potential of the gas (or gases, if we are studying mixtures) is then calculated using the Towhee software by performing several trial insertions of gas molecules in the box and averaging the values of chemical potential obtained for each insertion. The force field employed for the gas molecules during equilibration and calculation of chemical potential is identical to that employed during the subsequent GCMC simulations.

Framework of MCM-41 was maintained rigid and frozen during the GCMC simulations and thus, stretching, bending, torsion and inversion interactions were not considered within the framework. GCMC simulation was basically carried out by applying four different types of GCMC moves [83] viz. insertion, deletion, translation and rotation. Insertion and deletion moves were assigned equal probability of 0.3 each, and rotation and translation were given equal probability of 0.2 each. In the case of mixture of two or more adsorbate species, particle swap moves (or identity exchange moves) [56,57] were performed in addition to the other four types of move to achieve faster equilibrium. Identity exchange move was assigned a probability of 0.05; the probabilities for carrying out the insertion and deletion moves were changed to 0.275 each while keeping the probability of rotation and translation moves unchanged (at 0.2 each). Non-bonded interactions were computed as the sum of LJ potential and Coulombic interactions. A cutoff of 12 Å was used

the LJ potential along with tail correction. Lorentz-Berthelot mixing rules (equations 3.1 and 3.2) were applied for calculation of LJ potential parameters between unlike species.

$$\sigma_{ij} = \frac{\sigma_{ii} + \sigma_{jj}}{2} \tag{3.1}$$

$$\varepsilon_{ij} = \sqrt{\varepsilon_{ii} \times \varepsilon_{jj}} \tag{3.2}$$

Electrostatic interactions were calculated by the Ewald summation technique [58]. Five million GCMC steps were run and data from the last 2.5 million steps were used for calculating the average adsorbed amounts for adsorption simulation of pure gases and mixtures not containing water. Adsorption simulations of mixtures containing water vapor as one of the components were carried out for eight million steps; again, data from the last four million steps were used for averaging. GCMC simulations provide the absolute amounts adsorbed in the simulation box, which were converted to excess adsorbed amounts for direct comparison to experimental isotherms. Excess number density in the adsorbed phase was computed by subtracting the bulk number density from the absolute number density obtained from simulation, as given in using equation 3.3

$$N_{ex-ad} = N_{sim} - V_b \times \rho_{cal} \tag{3.3}$$

where N_{ex-ad} is the excess adsorbed amount, N_{sim} is the absolute number of adsorbed molecules obtained from GCMC simulation, V_b is the solvent (helium) accessible pore volume in the simulation box, and ρ_{cal} is the bulk number density of the adsorbate in the gas phase. ρ_{cal} is obtained by carrying out constant NPT MC simulations on only the adsorbate species at the same temperature and pressure as that of the respective GCMC simulation. After constant NPT MC

equilibration of the adsorbate species in the bulk gas phase at constant temperature and pressure, the system attains the appropriate density, which is used as ρ_{cal} in equation 3.3.

For binary, ternary and quaternary mixtures, the appropriate molar ratio of the different components in the gas mixture was ensured by providing the corresponding chemical potential value of the component as input to the GCMC simulation. MC simulation of the bulk gas mixture was first carried out in the constant NPT ensemble where the molar content of the different species in the gas mixture was maintained by ensuring correct ratio of the number of molecules of each species in the simulation box. For example, to simulate an equimolar (50:50) binary mixture of 200 molecules in the simulation box, the number of molecules of each species was maintained at 100. After equilibration, chemical potentials for each species in the gas mixture were calculated using the Towhee software package. These chemical potential values, which correspond to the temperature, pressure and molar composition of the simulated bulk gas phase, were then used in the GCMC simulations for adsorption in the MCM-41 models.

3.3 Results and Discussion

3.3.1. Characterization of MCM-41 Models

The structural characteristics of the MCM-41 models were carried out by calculating the specific surface area, pore volume, skeletal density and surface hydroxyl group density. In order to compare the experimental BET surface area of MCM-41 with the corresponding surface area of the MCM-41 models, a spherical probe of diameter 3.64 Å (representative of nitrogen molecule) was rolled over the surface of the pores of the models. The surface area thus obtained compare favorably with the reported experimental values of BET surface area of MCM-41 in the range

1090–1150 m^2/g [87,88]. The slight discrepancy between the calculated accessible surface areas and the experimental surface areas could possibly be due to the fact that actual MCM-41 material shows a distribution of pore sizes whereas in the models we have considered a single pore size, at a value representative of the average pore size of real MCM-41 materials. Further, the exact roughness and atomic arrangement of MCM-41 pore surface is not known experimentally, and the models just attempt to capture the pore wall roughness to a reasonable accuracy. Nevertheless, all models show reasonably good agreement with experimental data, with the agreement being best for Model 1. Table 3.2 lists the various structural characteristics of the three MCM-41 models.

Table 3.2 Structural characteristics of the MCM-41 models.

Properties	Model 1	Model 2	Model 3	MCM-41 (Experimental)
Simulation box dimensions (Å)	42.8, 42.8, 64.2	42.96, 42.96, 64.44	40.60, 40.60, 36.60	
Simulation box angles (°)	90, 90, 90	90, 90, 90	90, 90, 120	
Specific surface area (m^2/g)	1225.71	1260.51	1386.36	1090–1150 (from [87,88])
Accessible pore volume (cm^3/g)	0.547	0.490	0.499	
Skeletal density (g/cm^3)	2.48	2.345	2.26	2.2 (from [65])
OH group density ($/nm^2$)	4.79	4.45	4.68	

Powder XRD patterns for all the three models were simulated using Materials Studio 7.0 [63] and are shown in Figure 3.3 along with an experimental XRD pattern for real MCM-41 sample (adapted from [79]). The location of the first low-angle XRD peak of the MCM-41 models,

indicating the (100) plane, matches well with that of the experimental XRD pattern; however, the experimental XRD peak is much broader due to the more amorphous nature of the actual material.

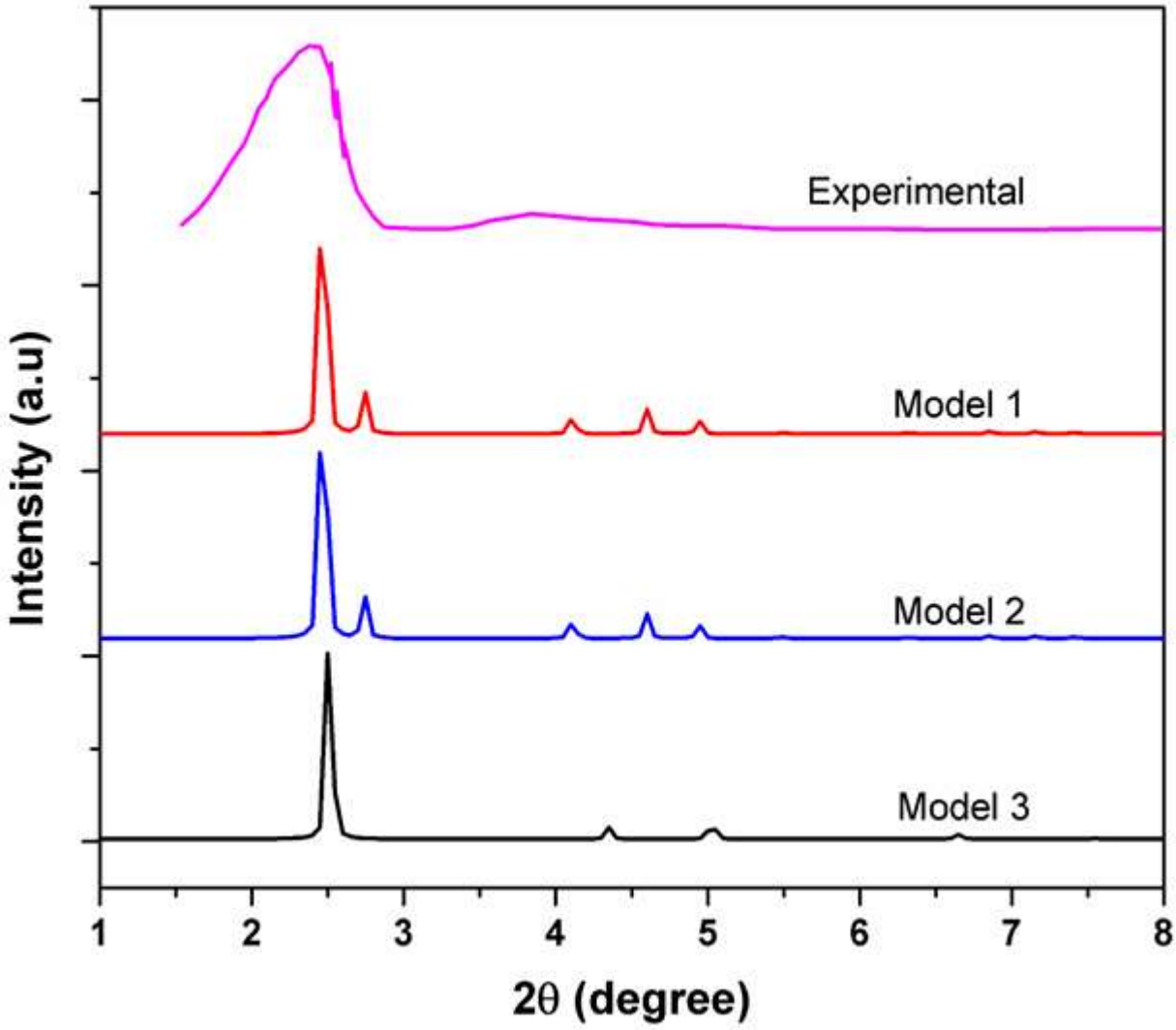

Figure 3.3 Powder XRD diffraction pattern of the three models compared with experiment (data from Loganathan et al. [79]).

Figure 3.4 (a) to (e) show plots of the RDFs for Si−O, O−H, O−O, Si−Si and H−H in the three models. RDF is a measure of the probability of finding atoms of a certain type in the neighborhood of a central atom (of same or different type). Thus, the sharp first peaks in the Si−O (Figure 3.4(a)) and O−H (Figure 3.4 (b)) RDFs indicate a very narrow distribution of the Si−O and O−H bond

lengths in the three MCM-41 models. The Si−O bond lengths in the models are in good agreement with the Si−O bond lengths observed in quartz and α-cristobalite [89]. The absence of any small peaks before the first prominent sharp peak also confirms that no strained bonds or significant structural overlaps are present. Figure 3.4(b) also indicates the possible presence of hydrogen bonding in 3 (and to some extent, in model 1), where a second broad peak is observed at ~2 Å. The first peaks in Figure 3.4 (c) and (d) correspond to the O−O and Si−Si distances of the O−Si−O and Si−O−Si linkages respectively in the model frameworks. These next-bonded-neighbor peaks are in general broader than the bonded-neighbor peaks shown in Figure 3.4 (a) and (b), due to the disordered nature of the MCM-41 wall. Peaks for model 1 are broader than the corresponding peaks for the other two models, which suggests that model 1 is more disordered. The hydrogen atoms present in the hydroxyl groups on the pore surface are well-separated and do not show any significant overlap, as is evident from Figure 3.4 (e) which shows that no other hydrogen atoms are present within 2 Å of a given hydrogen atom.

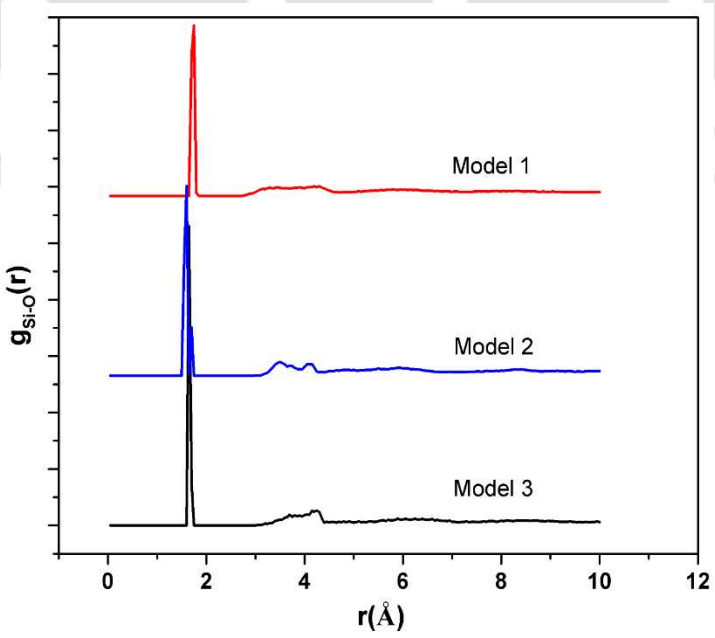

(a)

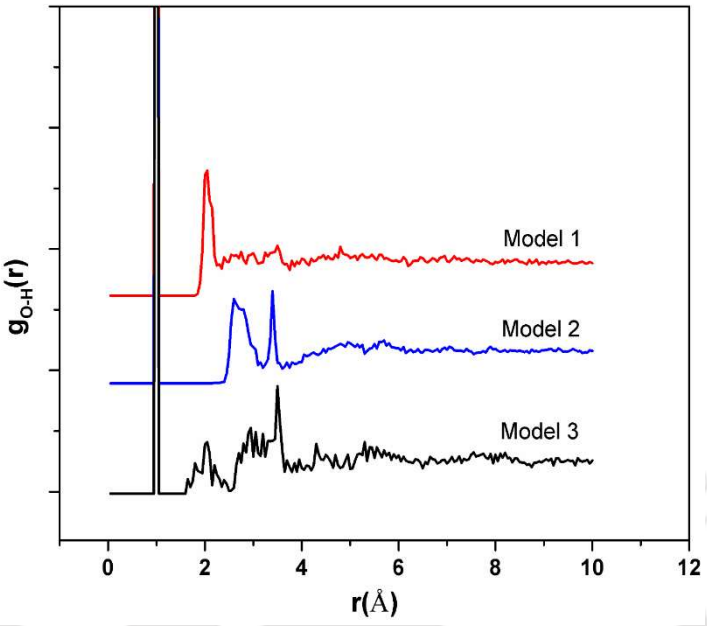

(b)

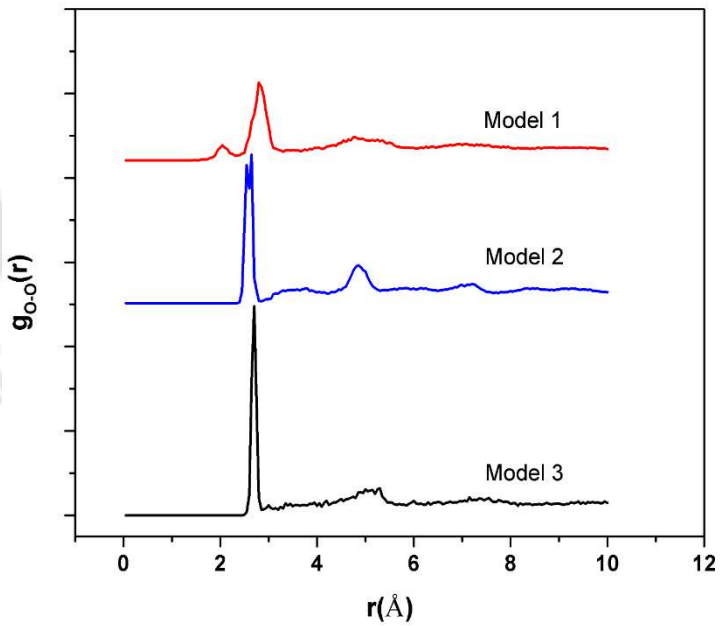

(c)

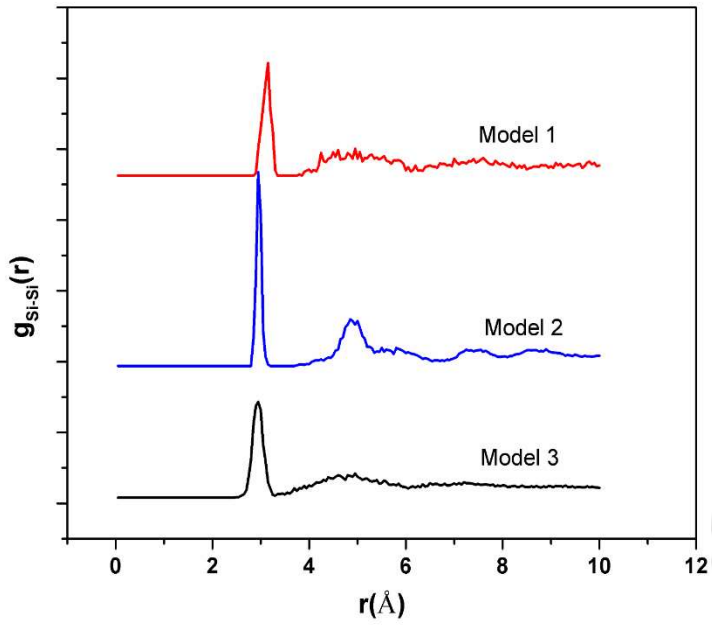

(d)

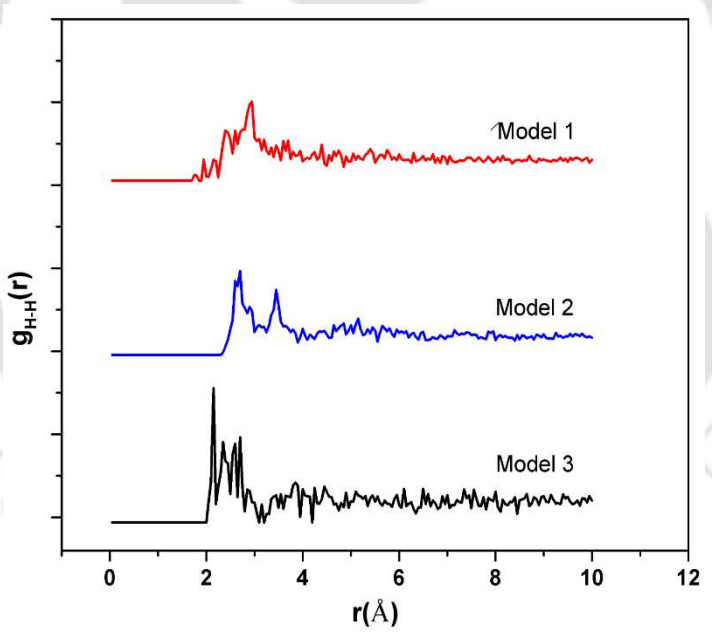

(e)

Figure 3.4 Radial distribution functions of the three models for the atomic pairs a) Si–O b) O–H c) O–O d) Si–Si and e) H–H. In (b), all three models show strong peaks at ~1 Å, and the peak of model 3 almost completely overlaps with the peaks of the other models.

3.3.2. Adsorption of Pure Gases

Adsorption of pure CO_2 on all three models was studied by GCMC simulation and the results were compared with the experimental results of Seaton et al. [65] at two different temperatures, namely 273.2 K and 303.2 K . At both the temperatures the simulated adsorption isotherm for model 1 was found to be in good agreement with the experimental results over the entire pressure range considered, as shown in the Figure 3.5a and b. CO_2 isotherms for model 3 also show reasonable agreement with experimental results for low to moderate pressures but deviate at high pressures. However, model 2 underpredicts the amount of CO_2 adsorbed over the entire pressure range.

The isosteric heats of adsorption, ΔH_{ads}^{st}, of CO_2 on the different models were calculated [62,90] using equation 2.32 as shown in section 2.2.4. Figure 3.6 shows the isosteric heats of adsorption of CO_2 on the three models and experimental data from He and Seaton [66]. The values for model 1 show good match with experiment over the entire loading range whereas the values for models 2 and 3 compare less favorably. Model 1 also shows a decreasing trend in ΔH_{ads}^{st} values with increasing loading, consistent with experimental results. The decrease in the number of available sites for adsorption unfavorably affects the adsorbent-adsorbate interactions leading to decrease in ΔH_{ads}^{st} values. Model 2 slightly underpredicts the isosteric heat values while model 3 overpredicts the values.

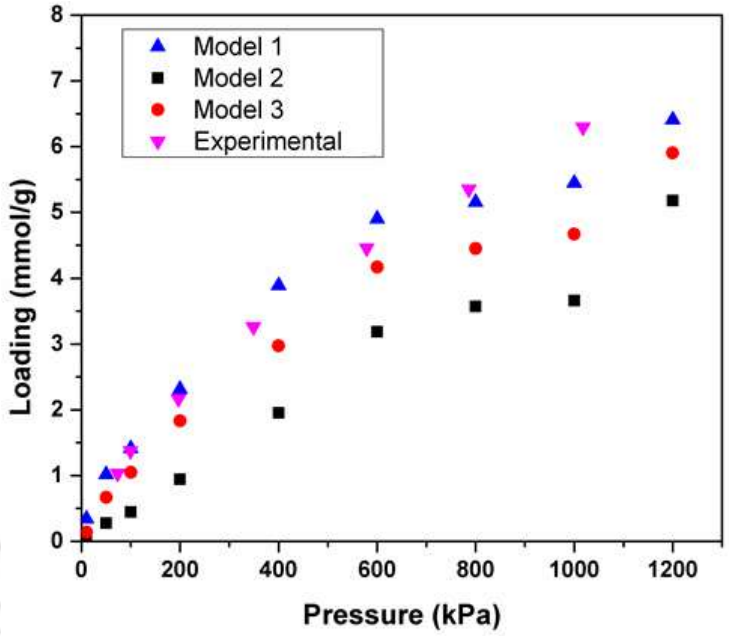

(a)

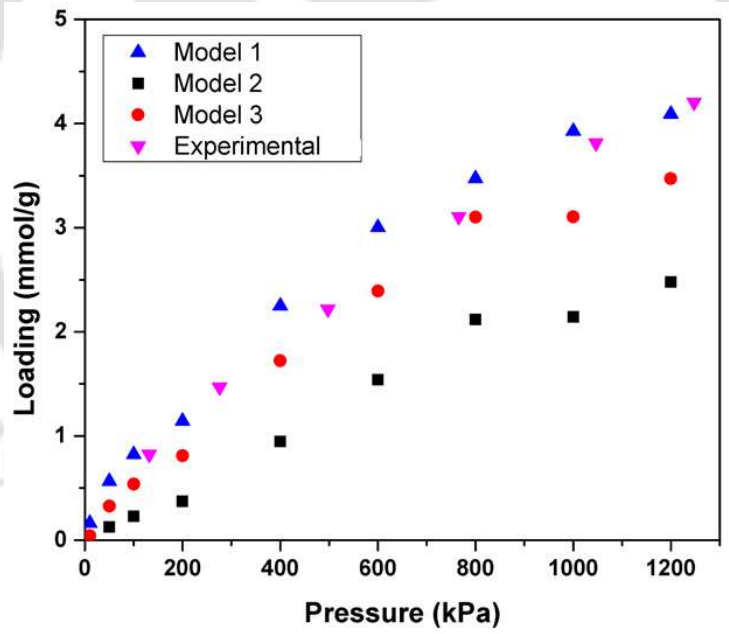

(b)

Figure 3.5 Pure CO_2 adsorption isotherm at a) 273.2 K and b) 303.2 K for the three models compared to experiment (experimental data from He and Seaton [65]).

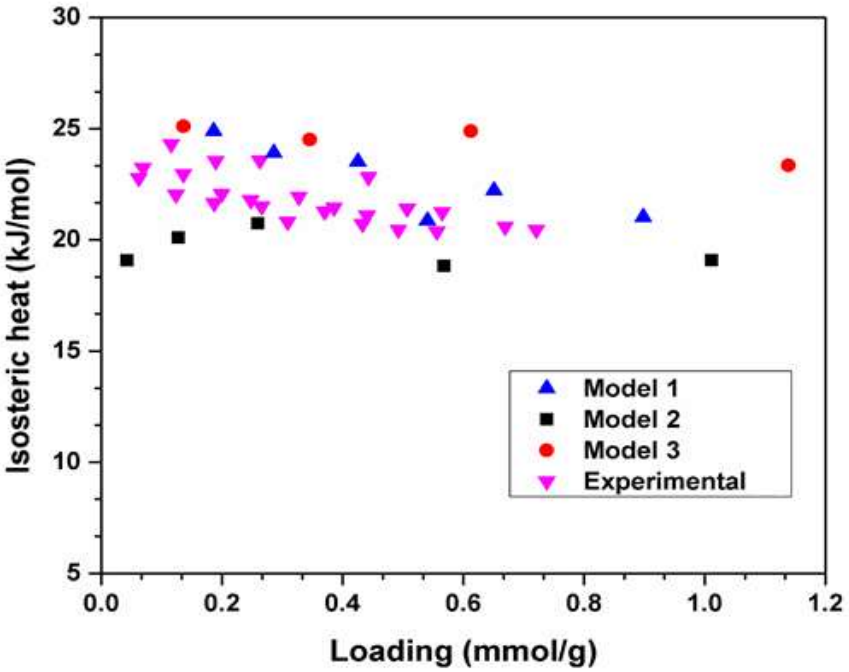

Figure 3.6 Isosteric heats of adsorption of CO_2 in the three MCM-41 models compared with experimental values (from He and Seaton [66]) at 298 K.

RDF was also calculated for adsorbate carbon atoms with respect to the adsorbent oxygen atoms ($C-O_{ads}$) and the carbon atom centers of other adsorbate molecules ($C-C$) to investigate the spatial arrangement of the CO_2 molecules inside the pore. The RDFs shown in Figure 3.7 for CO_2 adsorption in model 1 suggest that even at high loading CO_2 molecules do not show any preferential arrangement about the oxygen atoms of the framework. The RDF of CO_2 molecules around oxygen atoms has been calculated by averaging over all the oxygen atoms in the MCM-41 framework. RDF of CO_2 molecules may show some peak if only the oxygen atoms on the pore surface are considered; however, CO_2 will definitely not show any preferential arrangement with respect to the oxygen atoms located deep in the pore walls of the framework (away from the surface). Therefore, the average RDF of CO_2 considering all oxygen atoms in the framework also does not show any noticeable peaks. It may be noted from Table 3.1 that the value of the LJ well depth (ε) of silicon atoms is much higher than that of the framework oxygen atoms. Hence, the

framework silicon atoms are expected to have much stronger van der Waals interactions with the adsorbate gases than the framework oxygen atoms. Figure 3.7 also shows the C−C RDF for the adsorbed CO_2 molecules. The first peak position of this RDF suggests that the carbon centers of the nearest CO_2 molecules are separated by ~4 Å. Orientation profile for the CO_2 molecule inside the pores was obtained by calculating the angle between the CO_2 molecules and the radial direction (normal to the pore wall surface), as shown in the Figure 3.8. It is evident from the orientation profiles at three different pressures shown in the Figure 3.9 that a large fraction of CO_2 molecules are aligned perpendicular to the radial direction and hence, parallel to the pore surface of MCM-41.

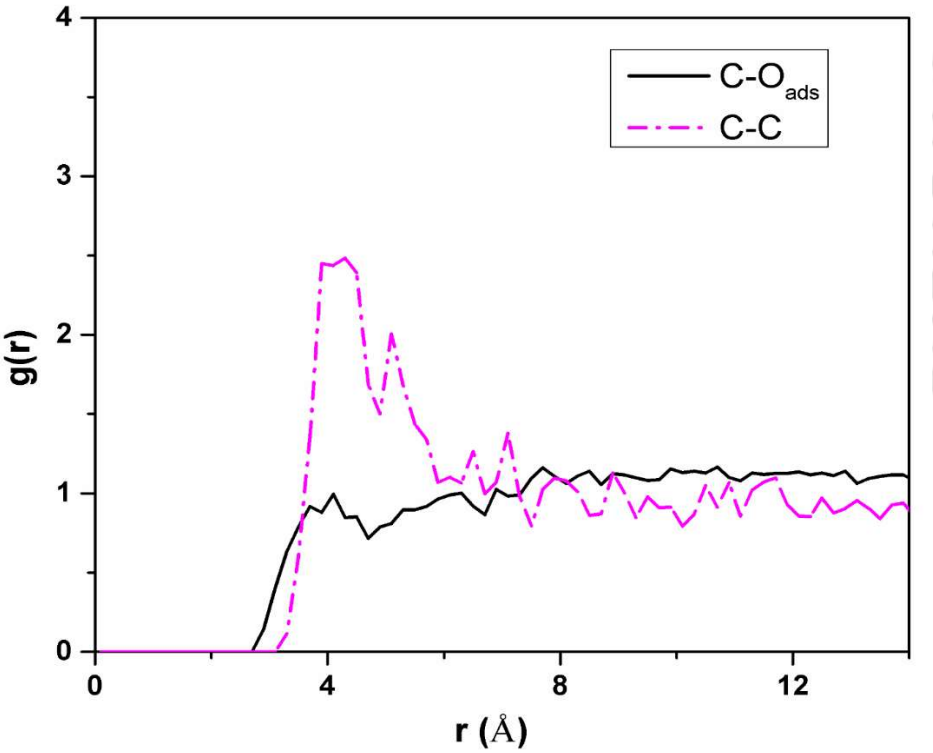

Figure 3.7 Adsorbate(C)-adsorbent(O) and adsorbate(C)-adsorbate(C) RDFs at 10 bar and 303.2 K for CO_2 adsorption in model 1.

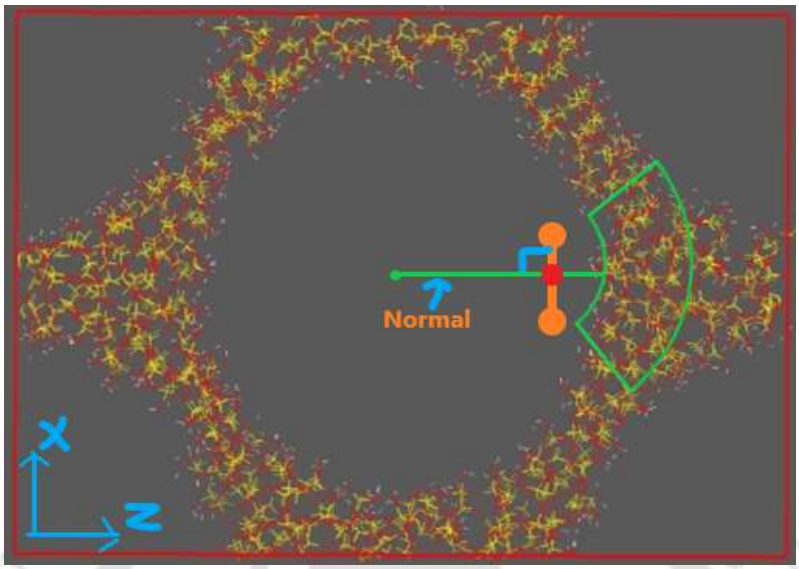

Figure 3.8 Schematic diagram for calculating orientation profile

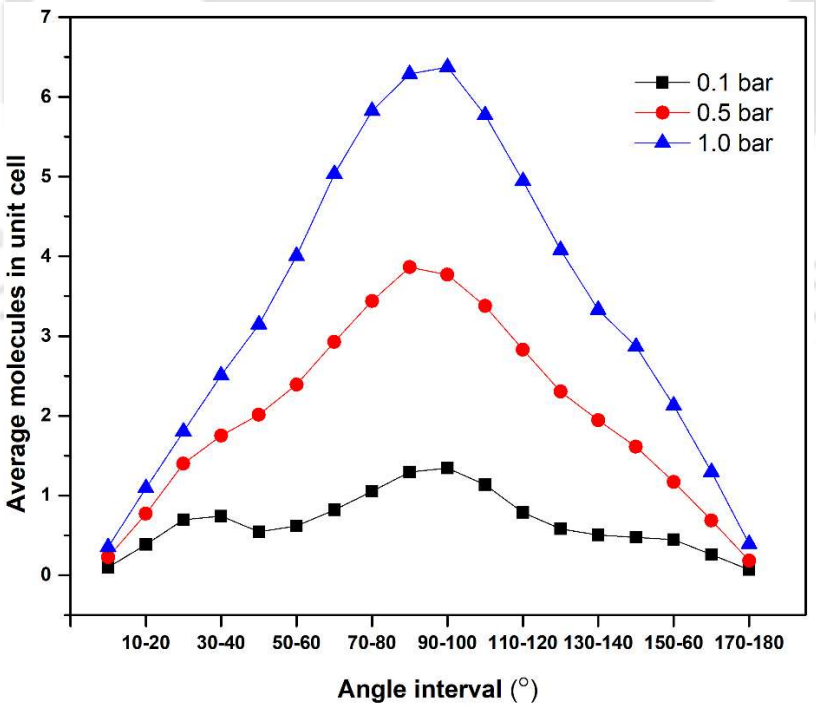

Figure 3.9 CO_2 orientation profile inside the pores of MCM-41 at three different pressures and a temperature of 298 K. Note: angle on the x-axis is between normal to the surface of pore and vector of CO_2 molecule as shown in Figure 3.8

3.3.3. Binary, Ternary and Quaternary Gaseous Mixture Adsorption

Binary mixture adsorption simulations were performed on models 1 and 3, which showed acceptable agreement with the pure CO_2 experimental adsorption data (see previous section), whereas model 2 was not considered further. Binary CO_2/N_2 gas mixtures were studied at two different molar compositions, namely 0.5:0.5 and 0.15:0.85 (CO_2:N_2). Figure 3.10a–c show the plots of binary gas adsorption isotherms on the two models at the two compositions. Due to its larger quadrupole moment and stronger van der Waals interactions, CO_2 interacts more favorably with the MCM-41 framework than N_2 resulting in higher loading of CO_2 at both bulk gas compositions. Even at flue gas composition (with 85% N_2), amount of CO_2 adsorbed was found to be higher than that of N_2 in both the models (Figure 3.10a and b). Figure 3.10c shows that the adsorption loadings of both CO_2 and N_2 are higher in model 1 than in model 3.

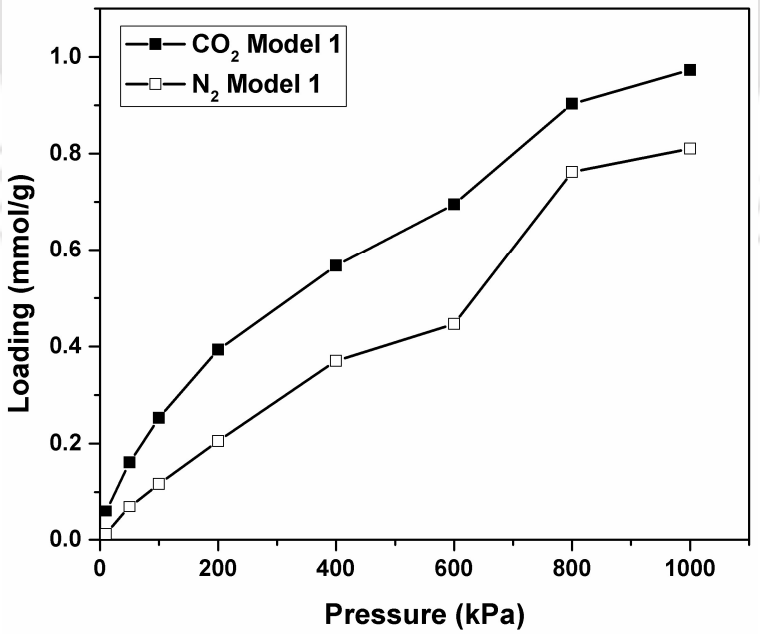

(a)

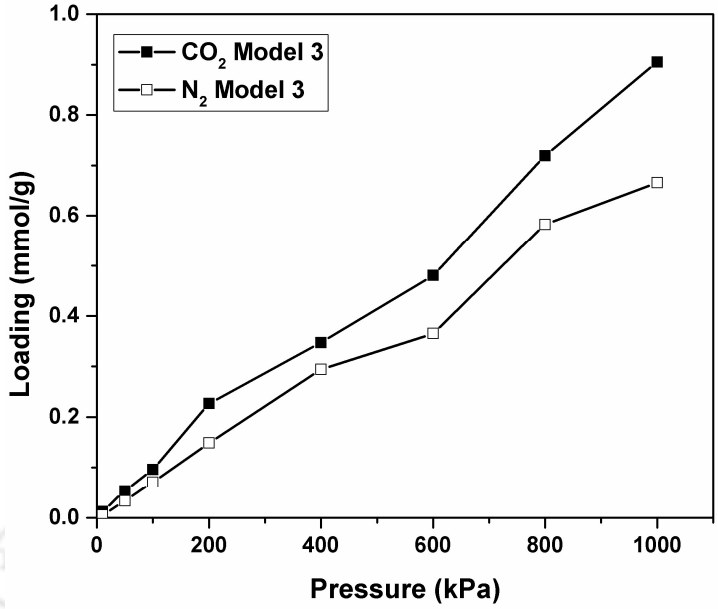

(b)

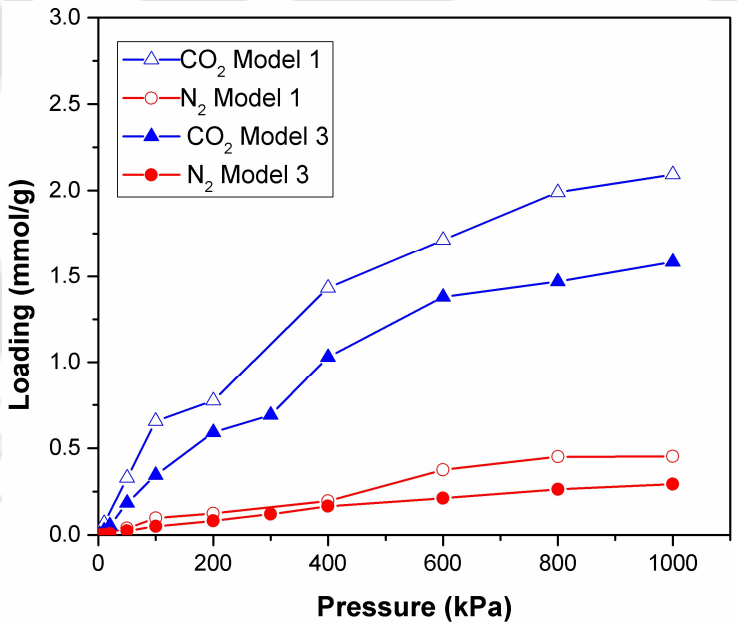

(c)

Figure 3.10 Adsorption isotherms for binary CO_2/N_2 mixture of composition 15:85 at 303.15 K in a) model 1 and b) model 3. (c) Adsorption isotherms for equimolar binary CO_2/N_2 mixture in models 1 and 3 at 303.15 K (lines are drawn only to guide the eye).

Selectivity of CO_2 over N_2 (S_{CO_2/N_2}) is calculated using equation (2.41), which is discussed in section 2.2.7. Selectivities of CO_2 over N_2 for adsorption of equimolar bulk gas mixture in model 1 at two different temperatures are shown in Figure 3.11. The selectivities at both the temperatures lie primarily in the range of 4–8, and show a general decreasing trend with increasing pressure, although the reduction is not very pronounced. Further, the selectivities show a decreasing trend with temperature in general, which is consistent with the fact that the factor primarily responsible for higher selectivity of CO_2 over N_2 (i.e., their relative strengths of interaction with MCM-41) becomes less dominant as the temperature (and hence the kinetic energy) is increased.

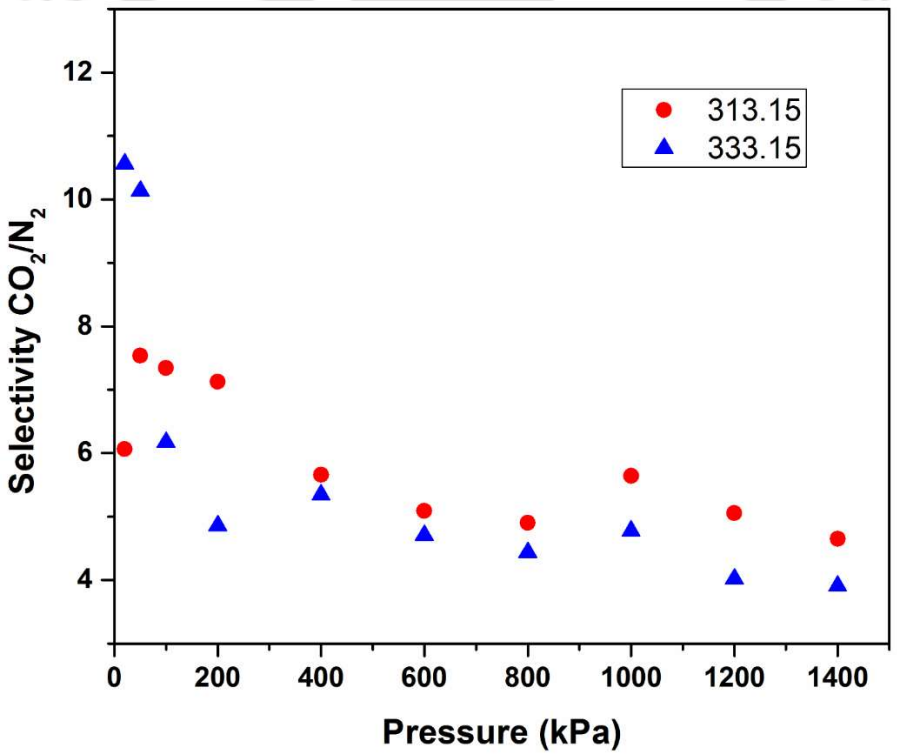

Figure 3.11 Selectivity of CO_2 over N_2 for adsorption of equimolar binary CO_2/N_2 mixture on model 1 of MCM-41 at two different temperatures (in K).

The observed CO_2/N_2 selectivity is comparable to values reported in literature for other unfunctionalized porous materials such as nanoporous carbon [91] and ordered mesoporous carbon [92]. Zhou et al. [91] reported CO_2/N_2 selectivity of ~4 at 298 K, 100 kPa for unfunctionalized

nanoporous carbon having a surface area of 3191.09 m^2/g using GCMC simulations whereas Yuan et al. [92] reported CO_2/N_2 selectivity of ~8 at 318 K, 100 kPa for synthesized ordered mesoporous carbon having a surface area of 2255 m^2/g. In comparison, the CO_2/N_2 selectivity of MCM-41 model 1 is ~7–8 at 100 kPa, 313 K (see Figure 3.11). The CO_2 loading reported by Zhou et al. [91] for the nanoporous carbon at 298 K and 1 bar is less than 1 mmol/g and at 10 bar is ~5 mmol/g. These values are comparable to those observed for Model 1 of MCM-41 in our study, i.e., ~0.8 mmol/g at 1 bar, 303.15 K and ~4 mmol/g at 10 bar, 303.15 K (see Figure 3.5). CO_2 loading reported by Yuan et al. [92] in ordered mesoporous carbon at 1 bar and 298 K is higher (~ 2 mmol/g). Microporous metal-organic frameworks such as Cu-BTC have been reported to exhibit somewhat higher CO_2/N_2 selectivity (~20 at 298 K and 100 kPa for Cu-BTC [93]). The CO_2 loading reported for Cu-BTC at 1 bar and 298 K is ~ 5 mmol/g [27] which is significantly higher than that in MCM-41.

Figure 3.12a and b show the distribution of the adsorbate molecules inside the pore of MCM-41 (model 1) at different pressures. To calculate the distribution, the pore was divided into concentric annular cylindrical bins of thickness 0.5 Å centered at the pore axis, and for each bin the number of adsorbate molecules whose center of mass was inside the bin was counted. The resulting number of adsorbate molecules in each bin was plotted against the radial distance of the bin from the center of the pore. As expected, the number densities of both the adsorbates show peaks close to the pore wall at both pressures. As CO_2 interacts more strongly with the pore wall, its peak intensity is significantly higher than that of N_2. Further, as the pressure is increased from 1 to 10 bar, the amount adsorbed increases significantly resulting in higher peaks for both the adsorbates at the higher pressure. Figure 3.12a shows that at 1 bar pressure, adsorption primarily takes place very

close to the pore wall (within a distance of ~5–6 Å from the pore wall). In contrast, at a higher pressure of 10 bar, the distribution is broader for both the adsorbates with an elongated tail that extends up to ~9 Å from the pore wall. The favorable adsorption sites on the pore wall are almost completely occupied, and onset of multilayer adsorption is observed.

Figure 3.13a–d show snapshots of binary CO_2-N_2 equimolar adsorption in model 1 over the pressure range of 0.5–12 bar. At 0.5 bar, the pore wall is mostly uncovered and adsorption of CO_2 is strongly preferred over N_2. As the pressure is increased, the wall coverage progressively increases; at 12 bar, almost the entire pore surface is covered and evidence of adsorption in a second layer can be seen (Figure 3.13d).

The ternary and quaternary mixture adsorption were carried out only for model 1 as this model showed the best agreement with experimental data for pure CO_2 adsorption . Presence of unburnt oxygen gas in the flue gas [94] was investigated at a CO_2:N_2:O_2 composition of 15:80:5. Adsorption and separation was studied at two different temperatures, namely 303.15 and 323.15 K. Partial charges were assigned to the O_2 molecule to account for the small quadrupole moment of O2 (see Table 3.1). Figure 3.14a and b show the adsorption isotherms of ternary mixture of CO_2/N_2/O_2 at two different temperatures. Comparison of Figure 3.14a with the binary CO_2/N_2 adsorption isotherm in Figure 3.10a shows that the presence of O_2 does not have any significant effect on adsorption capacity of CO_2. The size of O_2 molecules and their interactions with the adsorbent (MCM-41) are quite similar to those of N_2 molecules due to which the presence of O_2 in the ternary mixture does not significantly change the CO_2 loading from that of CO_2/N_2 binary mixture.

As water vapor is invariably present in flue gas, we studied the effect of water vapor on the adsorption and separation of CO_2/N_2 mixture. Adsorption simulations were carried out at two different temperatures (303.15 and 348.15 K) and an at two different mole fractions of water vapor (5% and 10%) in the ternary $CO_2/N_2/H_2O$ mixture. As water is more polar than the other two adsorbates, it is expected to interact more strongly with the surface hydroxyl groups on the pore walls of MCM-41. Figure 3.15 shows the adsorption isotherms of $CO_2/N_2/H_2O$ mixtures at the two different temperatures, namely 303.15 K and 348.15 K. In all the adsorption simulations of mixtures containing water vapor, the partial pressure of water vapor in the gas mixture was kept below its saturation pressure at the corresponding temperature. Adsorption simulations were conducted for two different compositions—one with low water vapor content (5 mol%) and the other with higher fraction of water vapor (10 mol%)—to explore the effect of water vapor content on CO_2 loading and CO_2/N_2 selectivity. It is evident from Figure 3.15a–d that the amount of water vapor adsorbed on MCM-41 in the pressure range studied is not significant. Although the polar water molecules are expected to interact strongly with the surface silanol groups of MCM-41, it appears that the surface density of silanol groups is not large enough to effect any significant adsorption of water at the low water vapor content in the gas phase and in the presence of other adsorbates, especially CO_2, which will compete for the adsorption sites. Further, a comparison of the low-pressure region of Figure 3.10a with Figure 3.15a shows that the presence of water vapor in the gas mixture does not have a substantial effect on the amount of CO_2 adsorbed as well as on CO_2/N_2 selectivity. Thus, CO_2/N_2 mixture adsorption behavior in MCM-41 is not significantly affected in the presence of up to 10 mol% water vapor in the gas mixture over a temperature range of 303.15–348.15 K (30°C to 75°C).

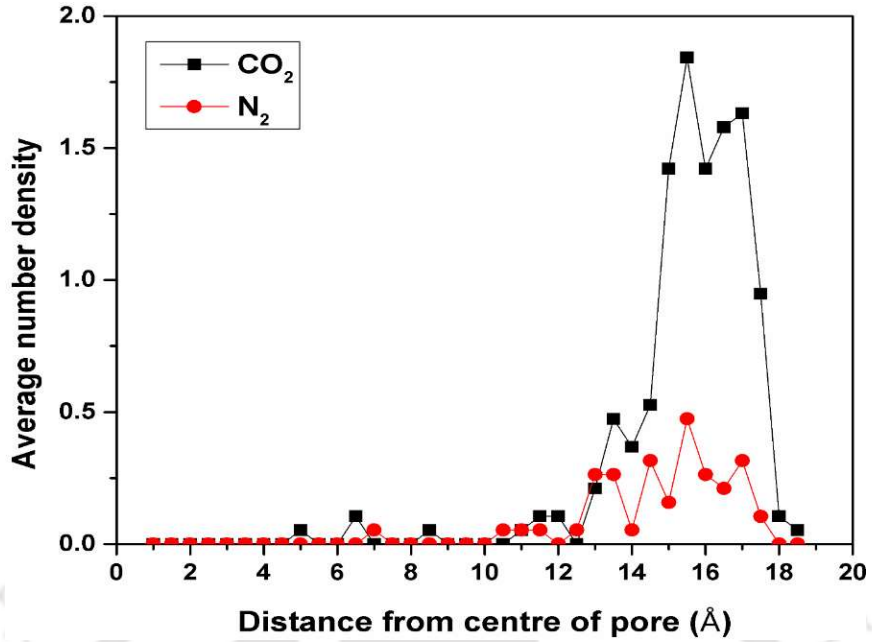

(a)

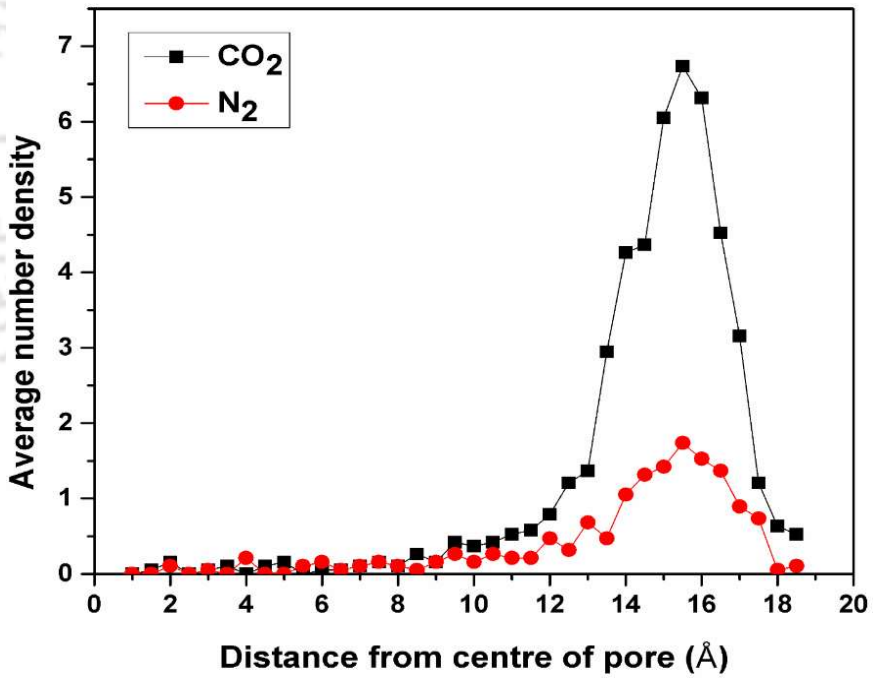

(b)

Figure 3.12 Number density of adsorbate molecules in the principal pore of model 1 of MCM-41 for adsorption of equimolar binary CO_2/N_2 mixture at (a) 1.0 bar, and (b) 10 bar at 303.15 K.

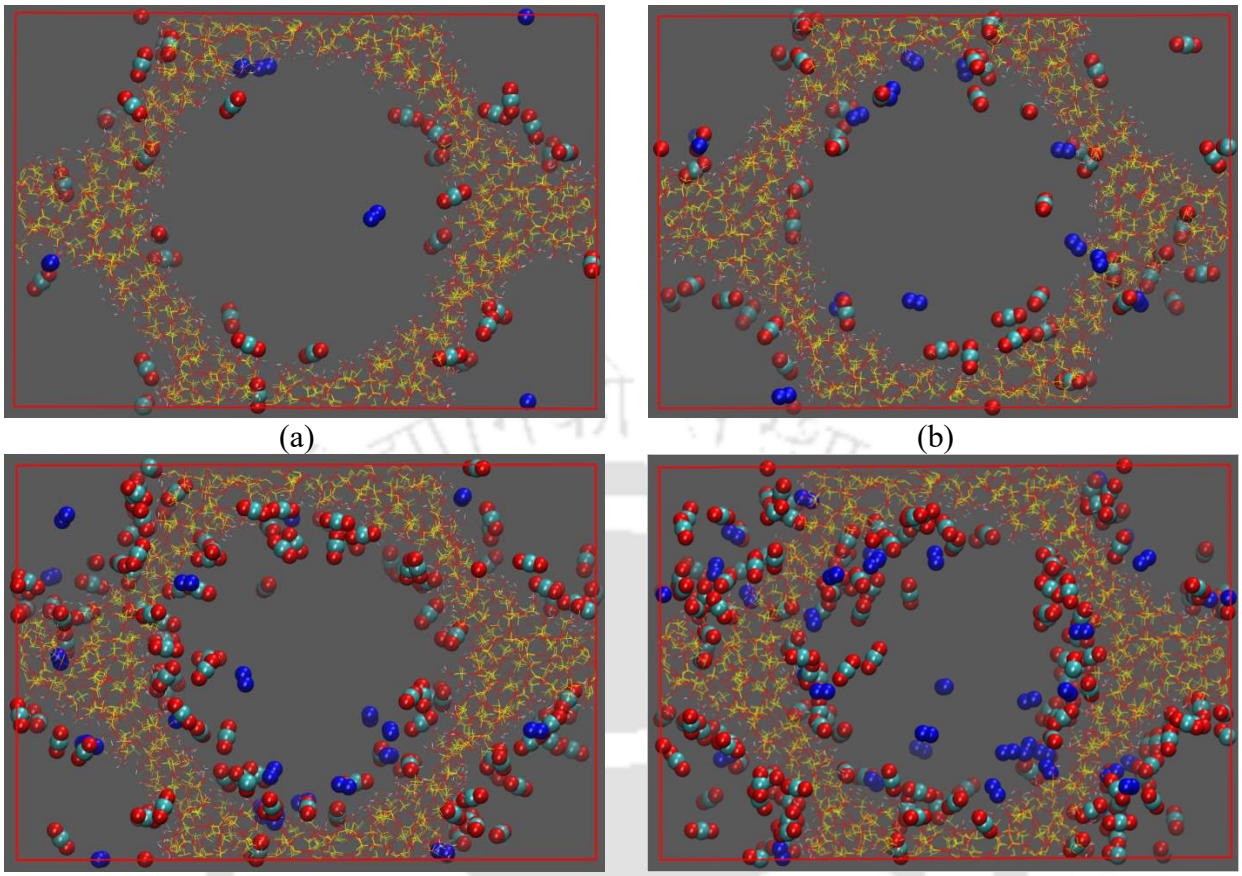

Figure 3.13 Snapshots of adsorbed CO_2 and N_2 molecules in model 1 of MCM-41 for adsorption of equimolar mixture at (a) 0.5 (b) 2.0 (c) 6.0 and (d) 12.0 bar at 303.15 K.

Flue gas may contain O_2 in addition to CO_2, N_2, and H_2O. Therefore, the adsorption of a quaternary mixture of CO_2, N_2, O_2 and H_2O was considered at a composition consistent with those observed in post-combustion carbon capture [95]. Adsorption of a quaternary mixture of CO_2, N_2, O_2 and H_2O in the proportion 15:75:5:5 (by mole) respectively was studied at two temperatures (303.15 K and 323.15 K). Adsorption isotherms at the two temperatures, shown in Figure 3.16a and b, reveal that the presence of O_2 and H_2O did not significantly affect the adsorption behavior of CO_2 and N_2. Further, the amount of H_2O adsorbed is slightly less than that of O_2 adsorbed (for identical gas-phase mole fractions) indicating the overall hydrophobic nature of MCM-41 pores. The

surface density of silanol groups on MCM-41 pore walls is not high enough to cause significant adsorption of water.

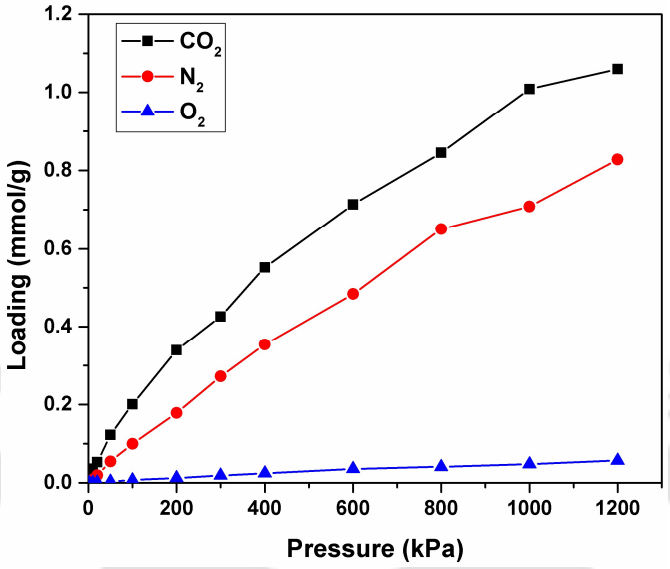

(a)

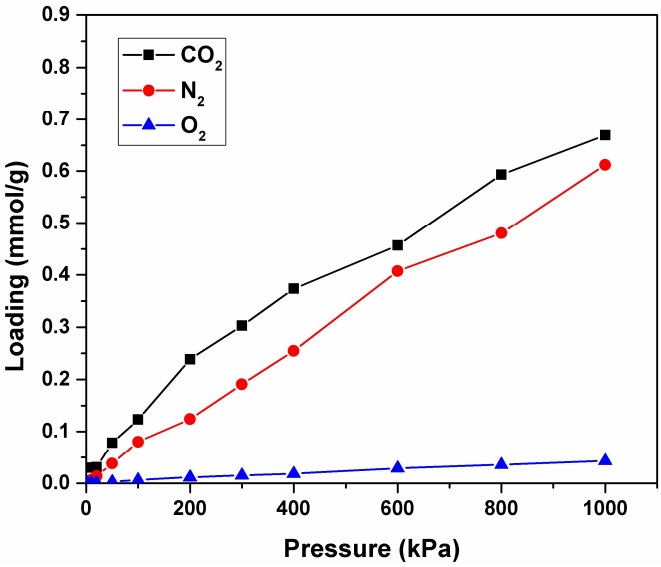

(b)

Figure 3.14 Adsorption isotherms of CO_2, N_2 and O_2 for ternary mixture adsorption of composition 15:80:5 (CO_2:N_2:O_2) in model 1 of MCM-41 at a) 303.15 K and b) 323.15 K (lines are drawn only to guide the eye).

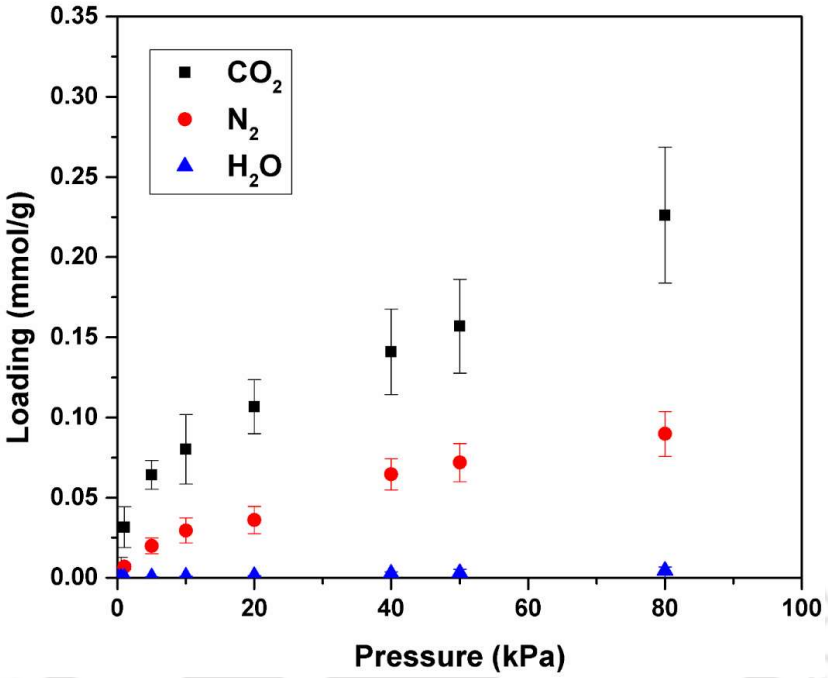

(a)

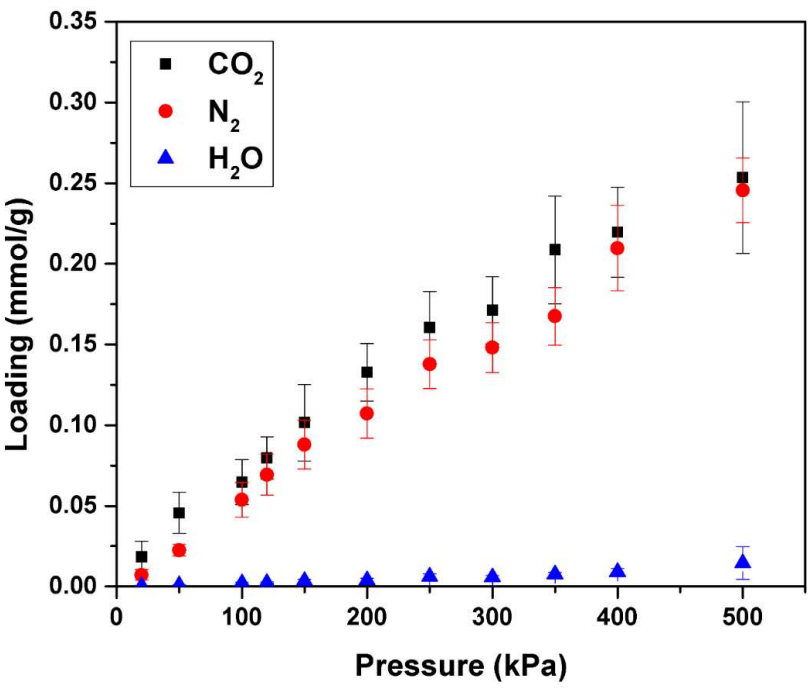

(b)

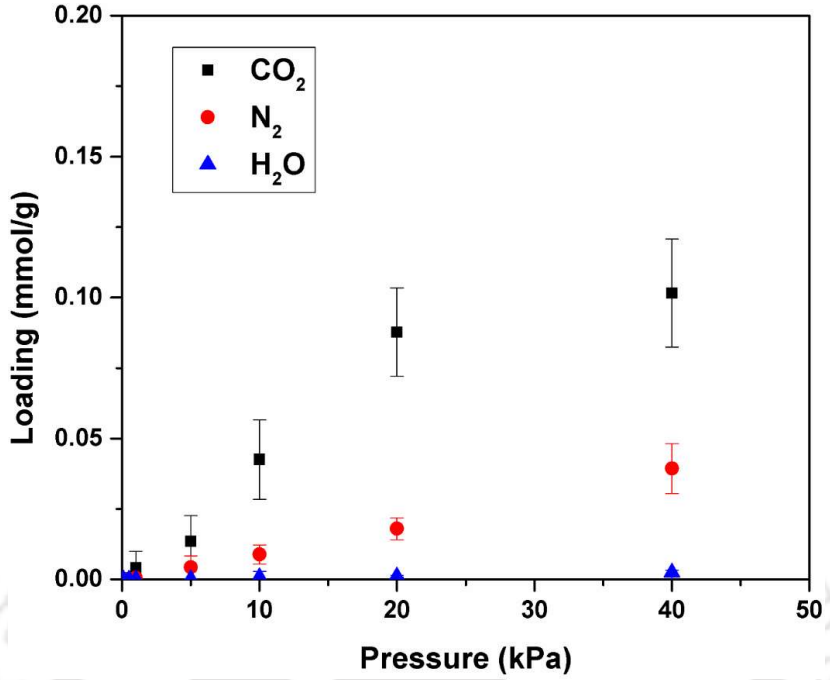

(c)

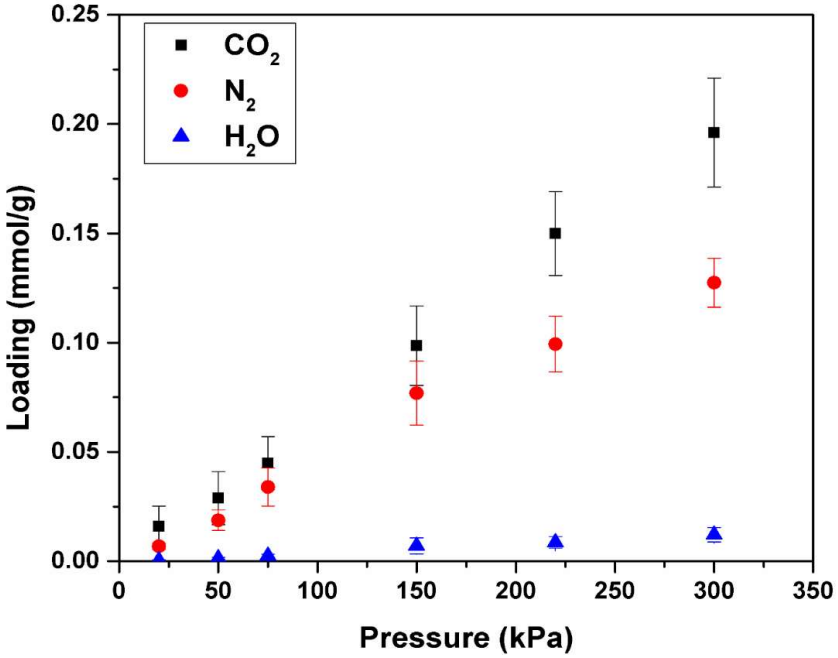

(d)

Figure 3.15 Adsorption isotherms of CO_2, N_2 and H_2O for ternary mixture adsorption of composition 15:80:5 (CO_2:N_2: H_2O) at (a) 303.15 K, (b) 348.15 K, and for composition 15:75:10 (CO_2:N_2:H_2O) at (c) 303.15 K, (d) 348.15 K in model 1 of MCM-41.

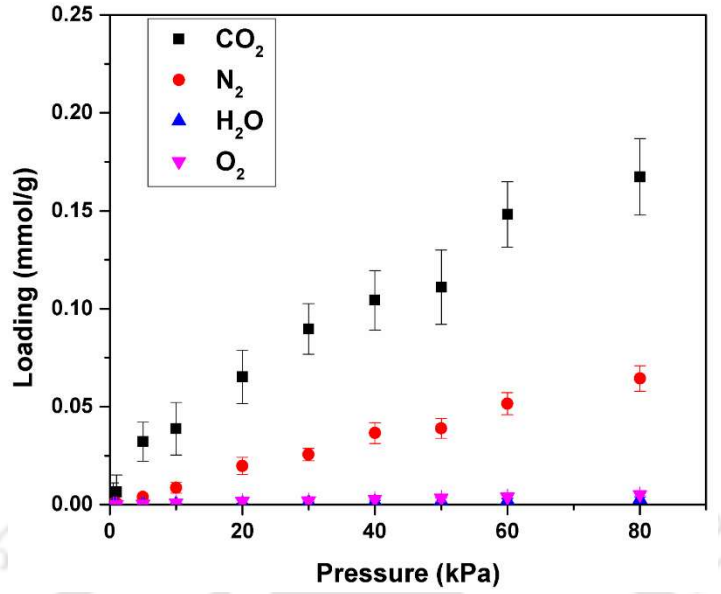

(a)

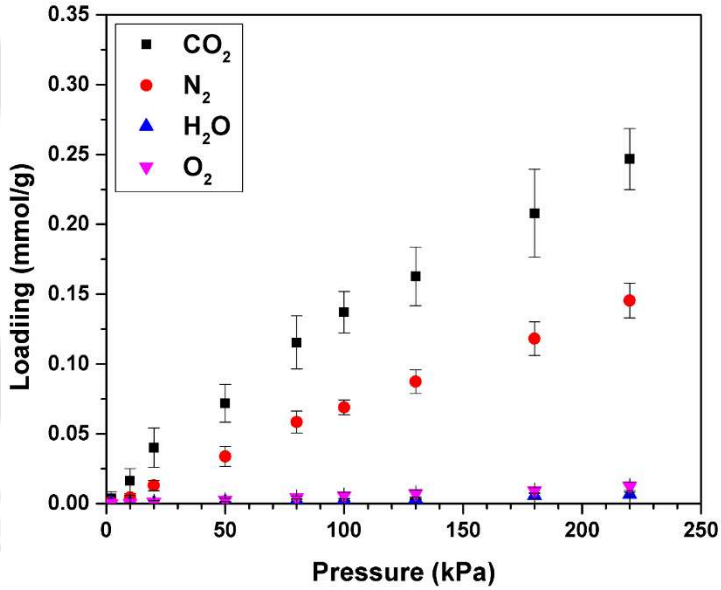

(b)

Figure 3.16 Adsorption isotherms of CO_2, N_2, O_2 and H_2O for quaternary mixture adsorption of composition 15:75:5:5 (CO_2:N_2:O_2:H_2O) at (a) 303.15 K, (b) 323.15 K in model 1 of MCM-41.

3.4 Conclusions

The present work compares realistic molecular models MCM-41 for studying adsorption of multicomponent gas mixtures representative of flue gas, and separation of CO_2 from such mixtures. The MCM-41 models were characterized by calculating the XRD pattern, RDF and surface area, and validated by comparing the results obtained with those reported for real MCM-41 samples. The pure CO_2 adsorption results predicted by model 1, prepared from a block of amorphous silica matrix with Si:O ratio of 1:2, were found to be in better agreement with experimental results than those predicted by the other models. The adsorption of binary mixtures of CO_2 and N_2, ternary mixtures of CO_2, N_2 and H_2O and CO_2, N_2 and O_2, and quaternary mixture of CO_2, N_2, O_2 and H_2O was studied at different temperatures on MCM-41 model 1. Adsorption study of binary mixture of CO_2 and N_2 shows that CO_2 is preferentially adsorbed over N_2 at all the temperatures considered owing to the stronger dispersion interactions and larger quadrupole moment of CO_2. Presence of small amounts of O_2 in the CO_2/N_2 mixture, whose size and interactions with MCM-41 are similar to N_2, does not affect the CO_2/N_2 selectivity. Further, ternary mixture simulations of CO_2/N_2/water vapor mixtures establish that up to 10 mol% of water vapor in the gas mixture does not have a significant effect on CO_2 adsorption and CO_2/N_2 separation over a temperature range of 30–75°C. Finally, adsorption studies of quaternary mixtures of $CO_2/N_2/O_2$/water vapor on MCM-41 do not reveal any significant effect of the simultaneous presence of O_2 and H_2O on the CO_2/N_2 adsorption behavior. Despite the presence of surface silanol groups on the pore walls, MCM-41 does not show any clear preference for the adsorption of the polar water molecules over O_2 (or N_2) molecules.

CHAPTER 4

Effect of Pore Size and Wall Microporosity on CO_2 Adsorption and Separation on Mesoporous Silica

4.1 Introduction

SBA-15 considered to be a potential material for adsorption of light hydrocarbon, volatile organic compounds because of its large pore diameter in the range of 7-10 nm [96–99]. Several, catalytic activity were supported by the SBA-15 type of material because of its high surface area and presence of large number of hydroxyl group. Triblock copolymer poly(ethylene glycol)-block-poly(propyleneglycol)-block-poly(ethylene glycol) (EO20PO70EO20; average molecular weight, 5800) was used as a surfactant, which was dispersed in acidic aqueous solution of hydrogen chloride (HCl) [50]. Tetra ethyl orthosilicate was used as a silica source, which was added to the solution under constant stirring for some hours followed by thermal treatment at 100 degree Celsius. The resulting solution was therefore calcined in order to remove the surfactant and other volatile material to obtain the pure SBA-15 material [47,50].

Martin et al. [100] confirmed that SBA-15 contains hexagonal array of large mesopores in addition to significant volume of micropores. Presence of micropores in the SBA-15 was justified by BET analysis and BJH pore distribution analysis, Which can be tuned upon tuning the synthesis temperature. SBA-15 synthesized at higher temperature than 120 degree Celsius contains almost no micropores. Pore size distribution was seen to be broader when the synthesis temperature is higher than compared to SBA-15 materials prepared at low temperature [100]. Texture, geometry, wall thickness and microporosity of SBA-15 mesoporous material remained unexplored till the year 2000. Peter et al. [96] in 2001 explained the various theoretical and experimental approach like Nonlocal Density Functional Theory (NLDFT) Method, geometrical consideration and X-ray diffraction to insight into the microporosity, wall thickness, microchannel volume of SBA-15 material. SBA-15 posses a regular cylindrical channels in hexagonal arrangement containing

mesopore. Intrawall pores contributes about 30% of the total porosity unless the sample is specially treated at higher temperature. The structural parameter was obtained by nitrogen adsorption isotherm, which was in a good agreement with the geometrical considerations and X-ray diffraction [96]. Adsorptive separation of light hydrocarbon such as CH_4, C_2H_6, C_2H_4, C_2H_2, C_3H_8 and C_3H_6 on SBA-15 was studied by Newalkar et al. [98] in order to explore and understand the potential application [99]. Adsorption of volatile organic compounds (VOCs) such as benzene, n-heptane, n-hexane, c-hexane, 3-methylpentane, 1-hexene and toluene on the as-synthesized SBA-15 were also studied to explore the applicability in separation industries [100–102]. Because of having large mesopores in SBA-15, these materials are modified upon amine functionalization in order to selectively capture the guest molecule. Apart from the above mentioned application, modified SBA-15 have been utilized for CO_2 capture and separation. Wang et al. [103] followed two different protocol to create porosity in the mesoporous silica (SBA-41) to achieve higher silanol surface density. Surface silanol group was found to increased, when ethanol extraction process was employed than normal calcination process. Therefore, hydroxyl group density was increased from 3.4 OH/nm^2 to 8.5 OH/nm^2. This increased silanol surface density is attributed to higher CO_2 loading and selectivity of CO_2 was found to be increased from 46 to 131 [103]. It was noticed that, there is ample scope to investigate the microporosity of SBA-15 at an atomic level to understand the mechanism of CO_2 capture and diffusion inside the narrow pores.

Therefore, in this chapter, we discussed the role of micropores for the selective capture of CO_2 from CH_4 and N_2 mixture at atomic level. Pure gas isotherm from GCMC was calculated and compared with the literature reported experimental data. Binary mixture adsorption of CO_2, N_2 and CH_4 were studied to evaluate the selectivity of CO_2 over N_2 and CH_4.

4.2 Models and Simulation Details

4.2.1. Mesoporous Silica Models:

In this chapter, the effect of wall microporosity on adsorption capacity and separation of CO_2 inside the mesoporous silica SBA-15 has been studied to understand the role of interconnected micropores at atomic level. Four different models of mesoporous silica have been considered, spanning a range of micropore-to-mesopore volume ratios. First of all, a unit cubic amorphous silica slab of dimension 21.395 Å (same as that taken to generate model 1 in chapter 3) is replicated 7, 5 and 2 times in x, y and z directions respectively to generate a large amorphous silica block from which the SBA-15 models can be carved. A cylindrical mesopore of diameter 74.88 Å was carved from the centre of the replicated slab while quarter pores of the same diameter were cut at the four corners of the slab. The pore diameter selected to model the SBA-15 material is representative of the values reported in literature for experimental SBA-15 samples [96], which depict a range of pore diameters between 5–30 nm [96],. The model generated contains only mesopores and is representative of a pore-expanded MCM-41 material [79], without wall microporosity. This model is referred to as SBA-15-np hereafter (where suffix 'np' is short for no-pore, signifying the absence of micropores in mesopore walls). To incorporate varying degrees of wall microporosity, multiple parallel, cylindrical micropores of diameter 10 Å each were carved across the mesopore walls along the y-direction. Attempt was made to ensure that any two adjacent micropores were separated by at least 10 Å along the x-direction. Three models were generated following this method: SBA-15-2p, SBA-15-4p and SBA-15-8p, having two, four and eight micropores respectively running across the pore walls in the y-direction. After carving out the pores from the slab, dangling bonds were saturated in the following manner: silicon atoms having

more than two dangling bonds were replaced by hydrogen atoms, silicon atoms having one or two dangling bonds were connected to the appropriate number of hydroxyl groups to satisfy the valence requirement, and oxygen atoms having one dangling bond were connected to single hydrogen atoms. After the complete saturation of the dangling bonds, the models possess strained bonds and angles at the pore surface due to the addition and deletion of atoms. Thus, models were subjected to geometry optimization using the Forcite module available in Materials Studio 7.0 software [63]. The front (x-y plane) and top (x-z plane) views of SBA-15-np are shown in Figure 4.1(a) and Figure 4.1(b) respectively whereas the top views (x-z plane) of SBA-15-2p, SBA-15-4p and SBA-15-8p are shown in Figure 4.1(c), (d) and (e) respectively.

4.2.2. Force Field:

In this work, the non-bonded van der Waals interactions were modeled using the 12-6 Lennard-Jones (LJ) potential for all the adsorbates. N_2 was modeled with two LJ sites at the atoms (N–N bond length of 1.1 Å) and three partial point charges, one each on the two nitrogen atoms and the third at the center of mass. LJ parameters and partial charges for N_2 molecule were taken from transferrable potentials for phase equilibria (TraPPE) force field [84]. CO_2 was modeled as a rigid linear molecule with three LJ sites and partial charges on the respective atoms. The C=O bond length (of 1.16 Å), the LJ parameters and the partial charges on the CO_2 molecule were taken from the EPM2 model [104]. A united atom approach was used to model CH_4 using the TraPPE united atom (TraPPE-UA) force field, proposed by Martin and Siepmann [105]. The detailed force field parameters for the adsorbate gases as well as the adsorbent (SBA-15) have been taken from literature and are summarized in Table 4.1.

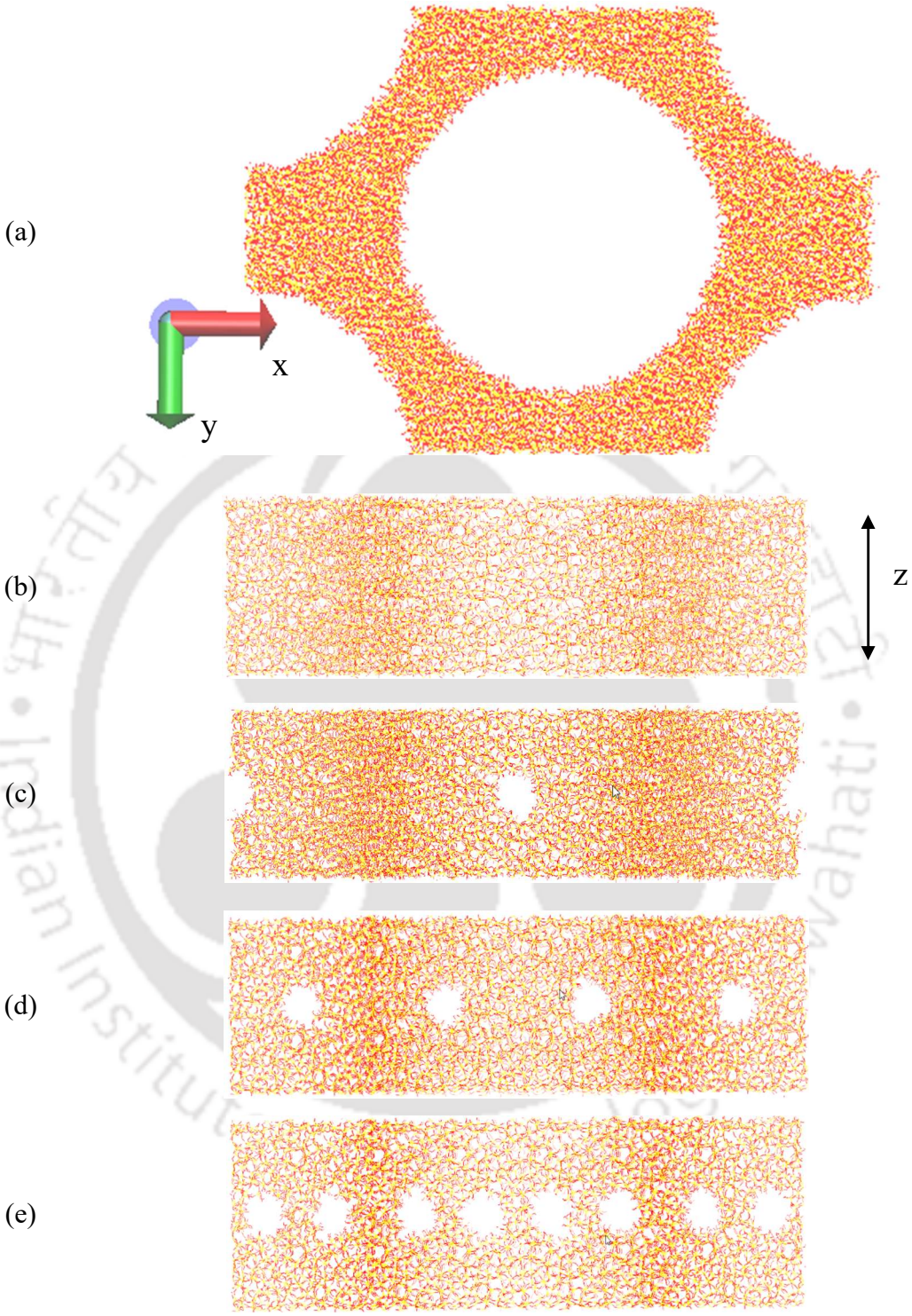

Figure 4.1 Mesoporous silica models: (a) Front view, and top views of (b) SBA-15-np, (c) SBA-15-2p, (d) SBA-15-4p and (e) SBA-15-8p.

Table 4.1 LJ potential parameters, charges and bond lengths in adsorbent and adsorbate molecules

Molecule	Site	$\sigma(\text{Å})$	$\varepsilon(K)$	$q(e)$	Bond length (Å)
SBA-15 [72]	Si	3.804	155.858	0.1222	
	O	3.033	48.115	-0.0615	
	H	2.846	0.050	0.0318	
CO_2 [104]	C	2.757	28.129	0.6512	1.152 (C=O)
	O	3.033	80.507	-0.3256	
N_2 [84]	N	3.310	36.000	-0.4820	1.10 (N≡N)
	N(COM)†	0.000	0.000	0.9640	
CH_4 [105]	CH_4	3.730	148.00	0.0000	

†COM stands for center of mass

Simulation Details: Framework of the SBA-15 models was maintained rigid and frozen during the GCMC simulations neglecting any stretching, bending, torsion and inversion interactions within the framework. Four different types of GCMC moves [53] viz. insertion, deletion, translation and rotation were employed for pure gas adsorption (except for CH_4 where no rotation moves were used). Insertion and deletion moves were assigned equal probability of 0.3 each, and rotation and translation were given equal probability of 0.2 each. In the case of mixture of adsorbate species, particle swap moves (or identity exchange moves) [56,57] were performed in addition to the other four types of move to achieve faster equilibrium. Non-bonded interactions were computed as the sum of LJ potential and Coulombic interactions. A cutoff of 12 Å was used the LJ potential along with tail correction. Lorentz-Berthelot mixing rules were applied for calculation of LJ potential parameters between unlike species. Electrostatic interactions were calculated by the Ewald summation technique [58]. Two million GCMC steps were run and data

from the last one million steps were used for calculating the average adsorbed amounts for adsorption simulation of pure gases and mixtures. GCMC simulations provide the absolute amounts adsorbed in the simulation box, which were converted to excess adsorbed amounts for direct comparison to experimental isotherms.

4.3 Results and Discussion

The structural properties and other details of the four mesoporous silica models are listed in Table 4.2. The mesopore and micropore diameters listed correspond to the size of the pores originally carved out of the amorphous silica block. After saturation of dangling bonds, these values may decrease by 1–2 Å. As the pore wall thickness is not uniform throughout, the listed pore wall thickness corresponds to a particular location, measured perpendicular to the x-z plane along the centre of the simulation box. The micropore and mesopore volumes listed in Table 4.2 have been calculated purely from geometric considerations; the actual volume accessible to a particular probe molecule will be different and depend on the pore wall roughness and probe size. Based on the geometrical pore volumes, the ratio of the micropore and mesopore volumes in the different models ranges from 0 to 5.5% (SBA-15-np to SBA-15-8p). The accessible surface areas, calculated using the Poreblazer 3.0.2 software [106], show an increasing trend with increase in the degree of microporosity, as expected.

The adsorption isotherms of pure CO_2 for different mesoporous silica models considered are compared in Figure 4.2. Compared to the pure CO_2 isotherms for MCM-41 reported in chapter 3 (see Figure 3.5), the CO_2 uptake (per unit mass) in the large-pore SBA-15 models is much lower. This can be attributed to the smaller surface area (per unit mass) of these models compared to the

models of MCM-41 in chapter 3. At low pressures (up to 1 bar), the model without any micropores (i.e., SBA-15-np, corresponding to pore-expanded MCM-41) shows somewhat lower uptake than the model with eight micropores, i.e., SBA-15-8p. However, at higher pressures, the adsorption in SBA-15-np is seen to be the highest. At low pressures, the micropores are expected to be preferred due to the stronger interactions in the confined environment. However, as the pressure is increased and the micropores start filling up, the available mesopore surface area becomes the dominant factor, which is highest for SBA-15-np. Further, as the number of micropores increases, the CO_2 uptake initially goes down (at pressures above 1 bar) and then increases. Thus, as we go from two to four and finally eight micropores, amount of CO_2 adsorbed decreases first and then increases. Thus, as the micropore volume in increased, at first the extra adsorption in the micropores is not able to compensate for the loss in mesopore surface area (at the mouths of the micropore). However, when higher microporosity is present (as in the case of SBA-15-8p), the contribution from micropore adsorption nearly balances the lower adsorption in the mesopores. It is expected that models with even higher microporosity may lead to higher adsorption than the SBA-15-np model.

Snapshots of CO_2 adsorption in the four models at 298.15 K and 1 bar, shown in Figure 4.3 and 4.4, provide a visual confirmation of the discussion above. In SBA-15-np, in the absence of wall microporosity, adsorption primarily takes place on the mesopore surface. However, as the wall microporosity is increased, adsorption of CO_2 increasingly takes place more in the micropores and less on the mesopore surface. This is clearly evident by comparing SBA-15-np and SBA-15-8p (Figure 4.3(a) and Figure 4.3(d) respectively). The adsorption in SBA-15-8p mostly takes place

inside the walls (in the micropores) while that in SBA-15-np takes place almost entirely on the mesopore surface at 1 bar.

Table 4.2 Structural properties of the different mesoporous silica models

Properties	SBA-15-np	SBA-15-2p	SBA-15-4p	SBA-15-8p	experiment
Mesopore diameter† (Å)	74.88	74.88	74.88	74.88	71 [47]
Micropore diameter† (Å)	—	10	10	10	
Number of micropores (along y-axis)	0	2	4	8	
Pore wall thickness† (at centre of box, along y-axis)	32.1	32.1	32.1	32.1	
Micropore volume† ($Å^3$)	0	5038.5	10077.1	20154.2	
Mesopore volume† ($Å^3$)	376705.0	376705.0	376705.0	376705.0	
No. of oxygen atoms	14328	14162	13875	13395	
No. of silicon atoms	6810	6699	6509	6181	
No. of hydrogen atoms	1452	1560	1736	2069	
Mass of framework (g/mol)	4,21,959	4,16,295	4,06,544	3,89,988	
Surface area* (m^2/g)	320	330	337	385	452.0 [48], 588.5 [47]

†denotes values from geometric calculations; *denotes values obtained from Poreblazer [106]

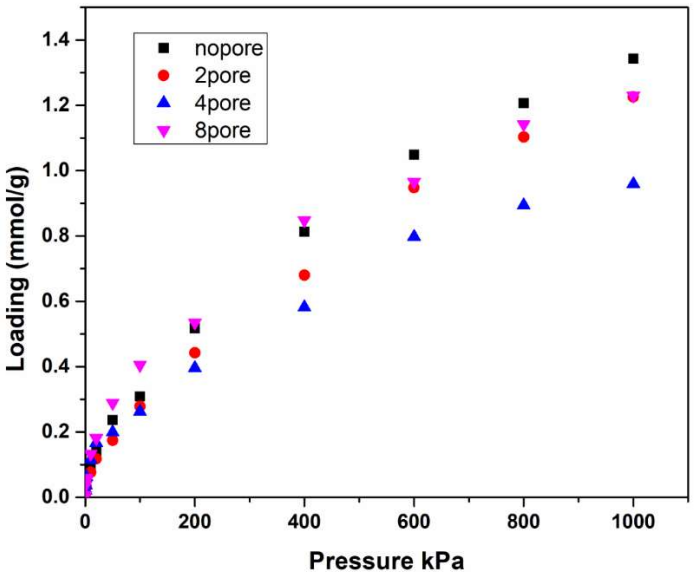

Figure 4.2 Adsorption isotherms of pure CO_2 in the different models at 298.15 K.

The effect of adsorption pressure on the adsorption locations of CO_2 molecules in the models can be visualized through the snapshots shown in Figure 4.5. Here, CO_2 adsorption in SBA-15-np and SBA-15-8p is shown at a low pressure (0.2 bar) and a high pressure (10 bar) value. At low pressures, Figure 4.5(b) shows that the adsorption in SBA-15-8p occurs primarily in the micropores and the number of CO_2 molecules adsorbed on the mesopore surface is smaller than that in SBA-15-np (Figure 4.5(a)). At high pressure (10 bar), the adsorption sites on the walls of the mesopores of SBA-15-np are completely occupied and multilayer adsorption can be seen to begin in Figure 4.5(c). The micropores of SBA-15-8p are almost completely filled at this high pressure and significant adsorption on the mesopore surface can also be observed. Thus, at low pressures, the micropores start filling first and as the pressure is increased, the mesopore surface begins to get saturated as well.

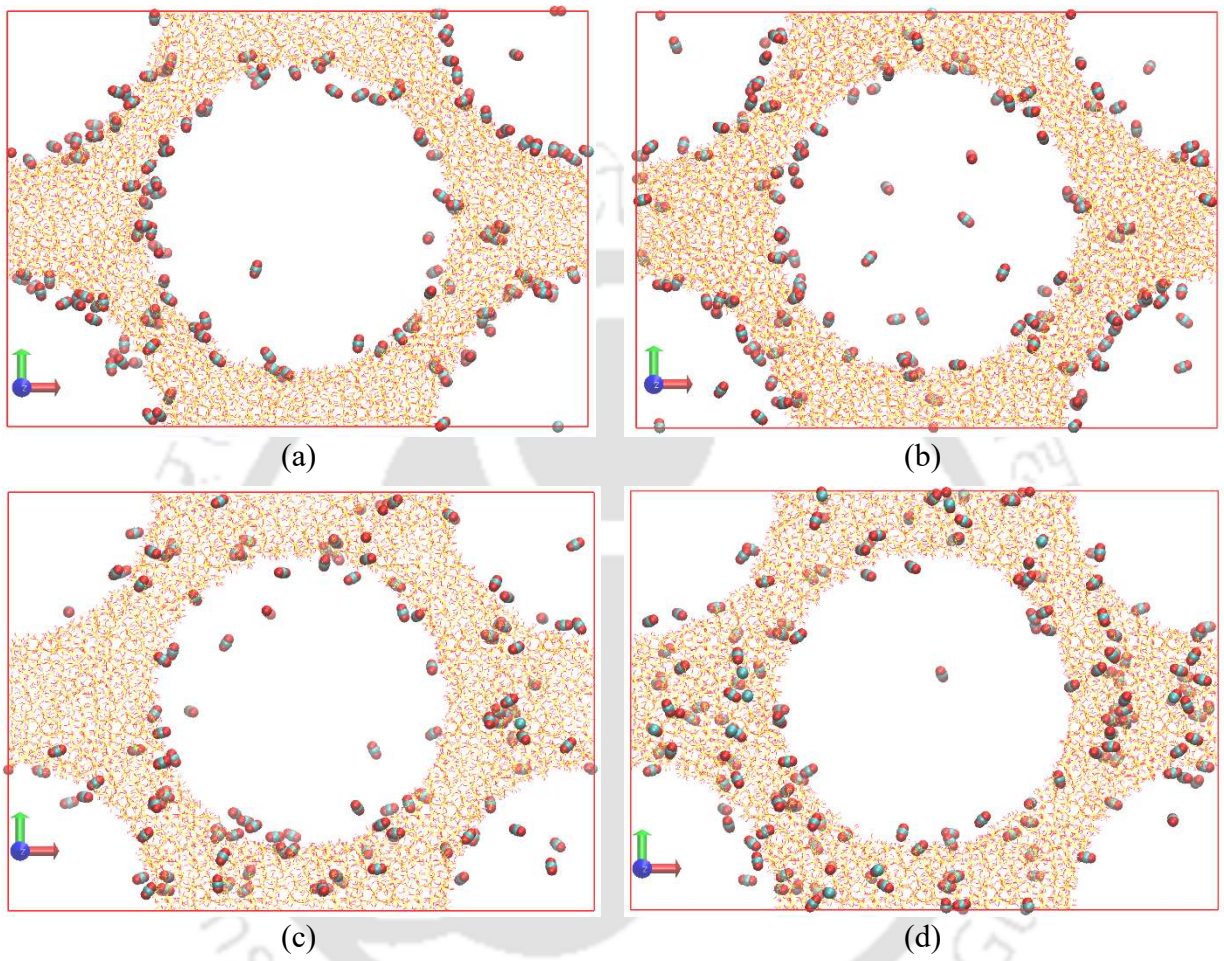

Figure 4.3 Snapshots (xy plane) of pure CO_2 adsorption at 298.15 K and 1 bar in (a) SBA-15-np (b) SBA-15-2p (c) SBA-15-4p, and (d) SBA-15-8p models. The locations of the micropores in (b), (c) and (d) correspond to those shown in Fig. 1(c), 1(d) and 1(e) respectively.

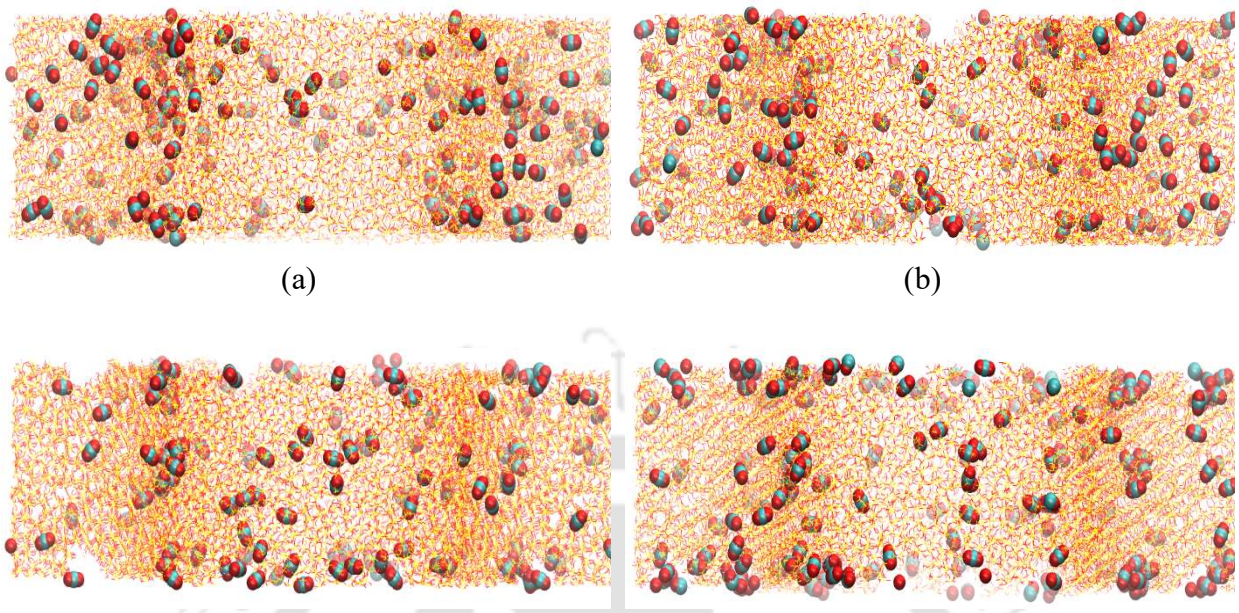

Figure 4.4 Snapshots (xz plane) of pure CO_2 adsorption at 298.15 K and 1 bar in (a) SBA-15-np (b) SBA-15-2p (c) SBA-15-4p, and (d) SBA-15-8p models.

Adsorption of pure N_2 and CH_4 was also carried out on the four mesoporous silica models. The interaction of N_2 with the silica framework is weaker than that of CO_2 as is evident from the lower uptakes of N_2 shown in Figure 4.6(a), compared to CO_2 (see Figure 4.2). The model with no wall microporosity (i.e., SBA-15-np) shows the highest uptakes and as in the case of CO_2 adsorption, increasing the wall microporosity leads initially to decrease in the amounts adsorbed (from SBA-15-2p to SBA-15-4p) followed by an increase (from SBA-15-4p to SBA-15-8p). For pure CH_4, the adsorbed amounts lie in between that of pure N_2 and pure CO_2, as shown in Figure 4.6(b). This can be attributed to the stronger van der Waals interactions that CH_4 molecules have with the adsorbent compared to N_2 but negligible electrostatic interactions (due to being non polar) in contrast to CO_2. The adsorption of CH_4 follows a trend SBA-15-np ≈ SBA-15-8p > SBA-15-2p > SBA-15-4p between 1 and 8 bar above which SBA-15-np > SBA-15-8p. Thus, for the case of CH_4

too, as the degree of wall microporosity is progressively increased, there is first a decrease in uptake followed by an increase.

Isosteric heat of adsorption of CO_2 in the four different models of SBA-15, obtained from the GCMC simulations, are shown in Figure 4.7. Although the data is somewhat scattered, it is evident that the 8-pore model (SBA-15-8p) shows the highest isosteric heats in general due to the presence of high wall microporosity.

Adsorption of binary mixtures of CO_2/CH_4 and CO_2/N_2 has also been studied on the different representative SBA-15 models using GCMC simulations. All the simulations have been carried out at 298.15 K and at a molar composition of 10:90 for CO_2/CH_4 and 15:85 for CO_2/N_2 where 10% and 15% are the amounts of CO_2 present in the respective mixtures. Figure 4.8 shows the adsorption isotherms of CH_4 and CO_2 for adsorption of CO_2/CH_4 mixture on the four models. At higher total pressures (above 5 bar), adsorption of CH_4 follows the trend SBA-15-np > SBA-15-8p ≈ SBA-15-2p > SBA-15-4p whereas that of CO_2 shows SBA-15-np ≈ SBA-15-8p > SBA-15-2p > SBA-15-4p. These trends are similar to those exhibited by the corresponding pure component adsorption isotherms. The adsorption isotherms of N_2 and CO_2 for the 15:85 CO_2/N_2 mixture are shown in Figure 4.9. Although the amount of N_2 in the bulk gas is almost 6 times that of N_2, the adsorbed amounts are comparable indicating good selectivity of the models for CO_2 over N_2.

The selectivities of CO_2 over CH_4 and N_2 in the different models are shown in Figure 4.10. The CO_2/CH_4 selectivities are in the range of 4–8 at low pressures (up to 1 bar). At the low pressure values, the SBA-15 models with microporosity clearly show higher selectivity for CO_2 as the strong confinement in the micropores is more favorable to CO_2 due to its stronger interactions with the framework and possible also due to its slightly smaller size. Even at higher pressures, all

models have selectivities above 2.5, with SBA-15-4p and SBA-15-8p showing higher values than the other two. The CO_2/N_2 selectivities (see Figure 4.10(b)) also show a similar behavior, with high values at low pressures which progressively decrease with increasing pressure. At 1 bar, the selectivities are in the range 7–10 and even at higher pressures, the selectivities are lie between 4 and 6. The higher selectivities at lower pressures, especially in models with wall microporosity, can again be attributed to the preferred adsorption of CO_2, particularly in the micropores. Thus, based on the different models studied, wall microporosity is seen to have an effect on CO_2 adsorption and separation, especially at low pressures.

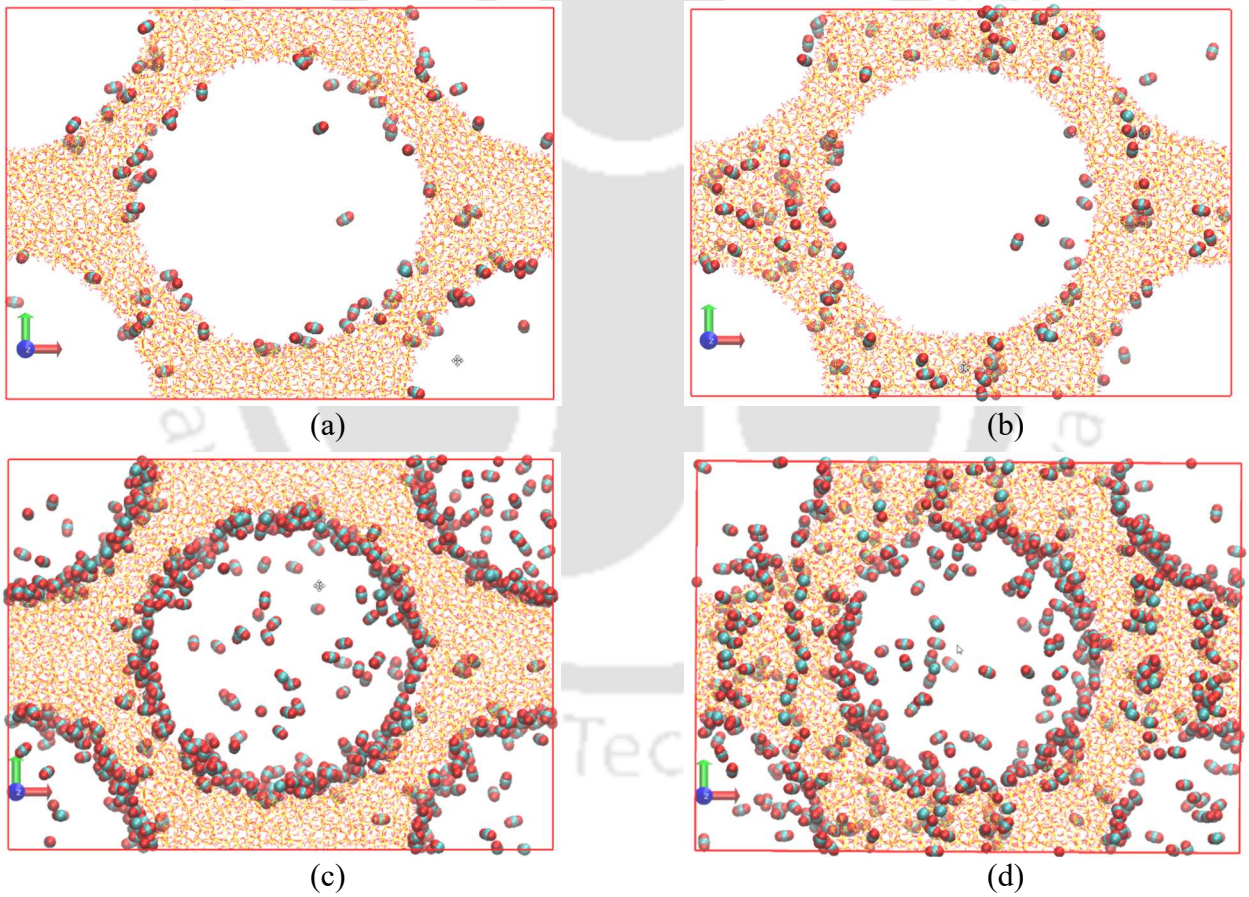

Figure 4.5 Snapshots of pure CO_2 adsorption at 298.15 K and 0.2 bar in (a) SBA-15-np (no micropores) (b) SBA-15-8p (8 micropores), and at 10 bar in (c) SBA-15-np, and (d) SBA-15-8p.

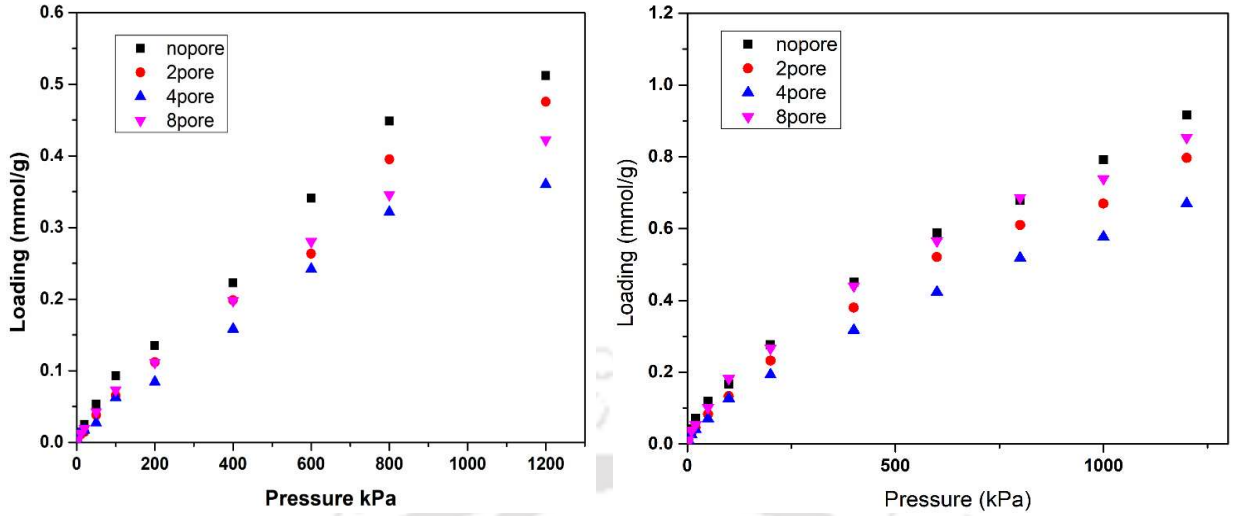

(a) (b)

Figure 4.6 Adsorption isotherms of (a) pure N_2 at 298.15 K, and (b) pure CH_4 at 303.15 K in the different models.

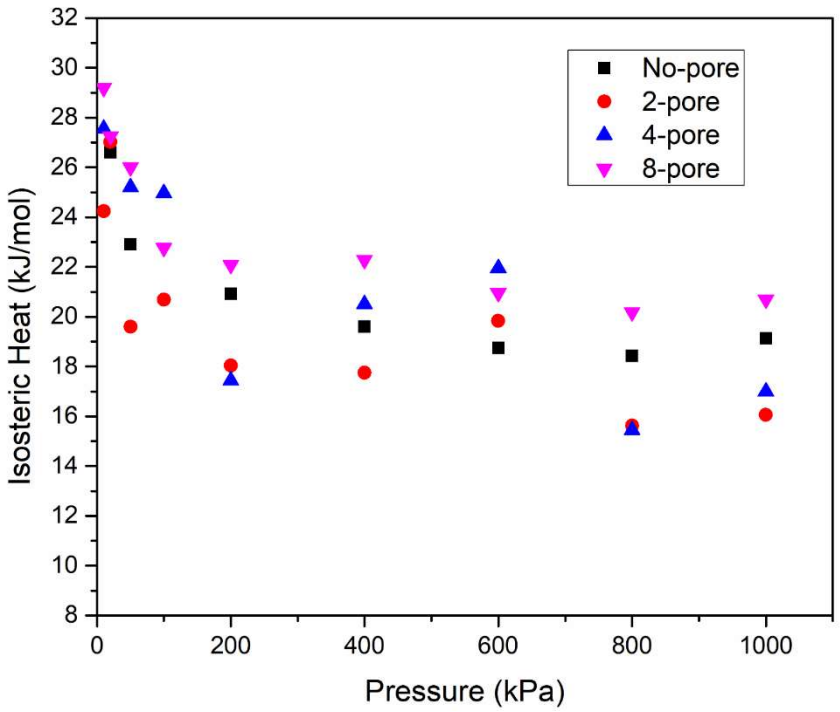

Figure 4.7 Isosteric heat of adsorption of CO_2 molecule in all the four different proposed model of SBA-15.

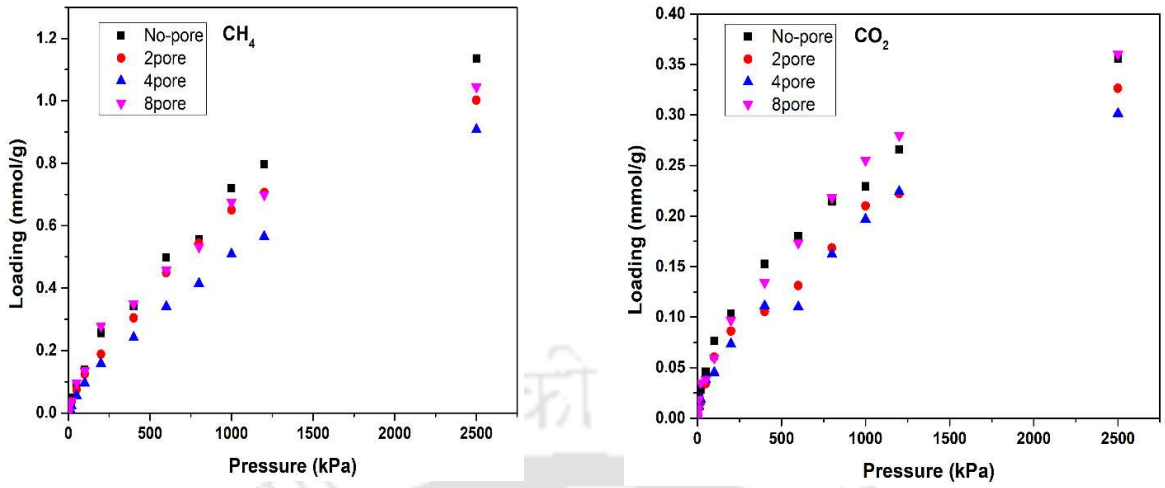

Figure 4.8 Adsorption isotherms of (a) CH_4 and (b) CO_2 for adsorption of CH_4/CO_2 mixture having composition 90:10 (CH_4:CO_2) by mole in the different models at 298.15 K.

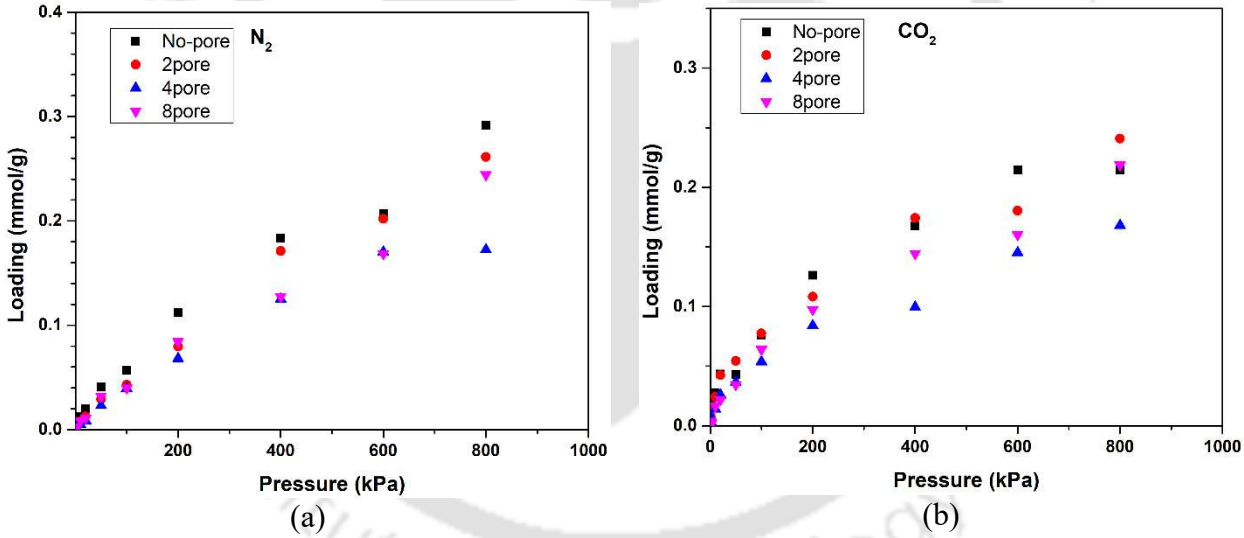

Figure 4.9 Adsorption isotherms of (a) N_2 and (b) CO_2 for adsorption of CO_2 and N_2 mixture having molar ratio 15:85 (CO_2:N_2) in the different models at 298.15 K.

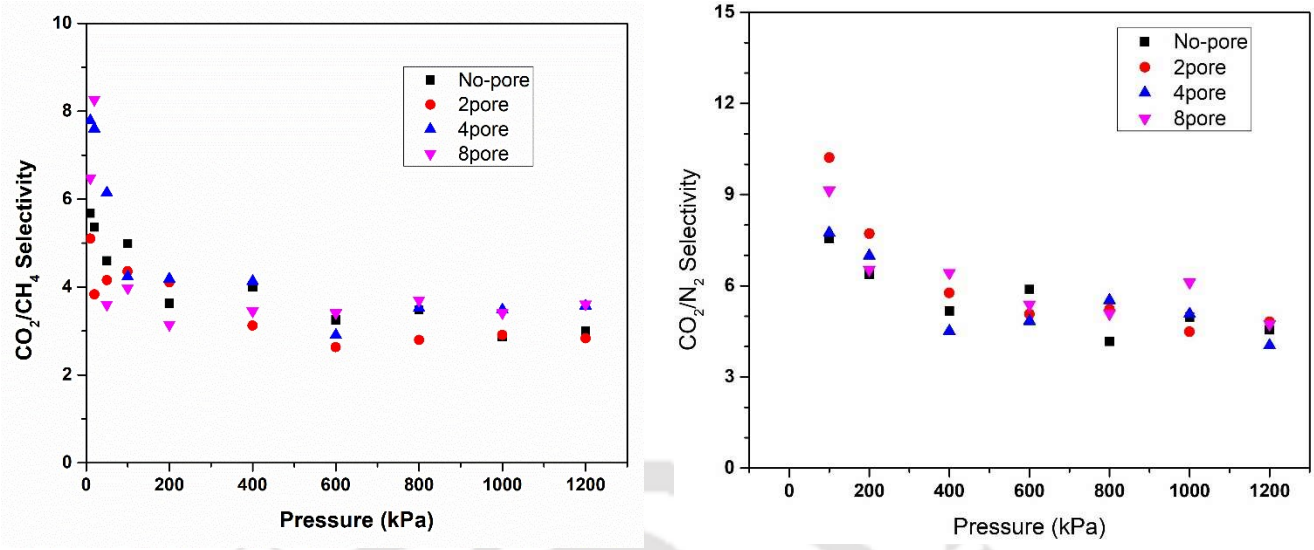

(a) (b)

Figure 4.10 (a) CO_2/CH_4 selectivities for adsorption of 10:90 binary mixture of CO_2 and CH_4 in the different models at 298.15 K, and (b) CO_2/N_2 selectivities for adsorption of 15:85 mixture of CO_2 and N_2 in the different models at 298.15 K.

4.4 Conclusions

The effect of wall microporosity in large-pore mesoporous silica materials, representing SBA-15 and pore-expanded MCM-41, on the adsorption and separation of CO_2 and its mixtures with CH_4 and N_2 was studied using GCMC simulations. The amount of CO_2 adsorbed was found to be lower in SBA-15-np (the model with no wall microporosity, representing pore-expanded MCM-41) than corresponding the MCM-41 model with smaller pores (studied in chapter 3) due to lower specific surface area. Further, with increase in wall microporosity, the uptake of CO_2 was observed to first decrease and then increase. At low pressures, the CO_2 uptake in the SBA-15-8p model (having the highest microporosity among the models studied) was the largest due to the CO_2 molecules preferentially adsorbing in the micropores at low pressures. However, at higher pressures, CO_2

adsorption in SBA-15-np was observed to be somewhat larger, possibly because of the micropores getting filled. Adsorption simulation of the binary mixtures CO_2/CH_4 and CO_2/N_2 revealed that the frameworks have good selectivity toward CO_2 over CH_4 and N_2, especially at low pressures, with CO_2/CH_4 and CO_2/N_2 selectivities in the range of 2.5–8 and 4–10 respectively. At low pressures, the selectivities in the models with wall microporosity is in general higher, probably due to the preferential adsorption of CO_2 in the micropores.

CHAPTER 5

Pore Modification of Mesoporous Silica by Ionic Liquid Impregnation for Enhanced CO_2 Separation

5.1 Introduction

In recent years, there has been considerable interest in porous materials modified through functionalization and physical impregnation for the efficient capture and separation of CO_2. Separation of CO_2 from gas mixtures is of interest in several operations, most important of which may be CO_2 capture from flue gas, as the release of large amounts of CO_2 into the atmosphere has been identified as contributing to global warming through greenhouse effect. Some of the industrially relevant gas separation operations involving CO_2 are: a) CO_2 capture from flue gas containing CO_2, N_2, CO, NOx, SO_2, O_2 etc., b) CO_2 separation from blast furnace gas containing CO_2, CO, C_xH_y, H_2S, N_2, O_2, and NO_x, c) production and separation of CO_2 from landfill gas containing CO_2 and CH_4, d) separation of CO_2/CH_4 for natural gas upgradation and high purity methane [11,12,92,107–109].

Many studies on metal-organic frameworks (MOFs), consisting of microporous channels and cages, have been conducted as they are considered to be promising materials for efficient gas storage and separation applications owing to their large surface areas and pore volumes as well as tunable pore size [110]. Functionalized MOFs are also being actively explored to enhance the separation and capture of different gases of interest [111–115]. However, covalently grafted long chain functional groups inside MOFs require large pore diameters and cages, which are difficult to synthesize because of their low thermal stability [116–118]. On the other hand, mesoporous materials are well suited for pore-modification through covalent functionalization or physical impregnation of larger groups/molecules because of their large pore diameter, pore volume and surface area [66,73,79,119–121].

MCM-41 belongs to a family of mesoporous silica materials and has been extensively studied for applications in drug delivery [119], separation and capture of gases [79], and catalysis [122]. Pore size of these materials can be tuned during their synthesis by using appropriate surfactant and increasing the pH level [79]. Regular hexagonal arrangement of one-dimensional cylindrical pores in MCM-41 makes this material suitable for understanding gas adsorption at the molecular level. Although numerous studies involving metal doping, drug loading, capturing small organic volatile compounds, and surface functionalization (e.g. for enhanced CO_2 selectivity towards other gases) have been conducted experimentally on MCM-41 [119,122–128], very few reports on incorporation of ionic liquids (IL) inside the mesopores of MCM-41 are available in literature [129–133]. In contrast, impregnation of IL molecules inside MOFs have been reported by several researchers and found to be effective in CO_2 capture and separation [134–136]. Computational exploration of ionic liquid-assisted IRMOF-1 at different IL loadings was carried out by Chen et al. [134] which revealed the composite adsorbent to be an efficient system for capturing CO_2 over N_2. Moreover, MOFs with IL molecules confined in their pores were found to be more promising in H_2S removal from natural gas (mainly CH_4) in the computational study by Li et al. [135]. Computational and experimental studies of CO_2 + IL systems have also been carried out in recent years. Clyde et al. [136] conducted experimental as well as computer simulation investigation of CO_2 vibrational frequencies in an IL environment.

IL molecules can be incorporated into the pores of mesoporous materials by either chemical grafting or physical impregnation. Vangeli et al. [129] prepared immobilized imidazolium-based ionic liquid inside the pores of MCM-41 and Vycor silica, and successfully grafted the cationic part of the IL in order to further investigate the physicochemical and thermodynamic properties of

the grafted material. In addition, they found the selectivity of CO_2 over CO to be higher for IL-grafted porous materials. Stefanopoulos et al. [130] conducted small-angle neutron scattering (SANS), contrast-matching SANS, and nitrogen adsorption on the IL [BMIM][PF6] confined inside the pores of MCM-41 and SBA-15. Nitrogen adsorption at 77K in both the IL-loaded materials was lowered significantly compared to the respective pure MCM-41 and SBA-15. Tripathi et al. [132] synthesized MCM-41 with the IL 1-ethyl-3-methyl imidazolium tetrafluoroborate [EMIM][BF4] confined in the mesopores, and studied the thermal, electrical and structural properties of synthesized material. They confirmed the interaction of oxygen atoms on pore wall of MCM-41 with the cationic part of IL from Fourier-transform infrared spectroscopy vibrational bands. Thus, it is evident that there is ample scope to investigate the capabilities of IL-loaded mesoporous materials such as MCM-41 for adsorption and separation of gases. Molecular simulation techniques can be employed to determine the extent of enhancement in CO_2 adsorption and separation, and computationally identify the optimum IL loadings in the mesopore, to screen the more promising combinations for subsequent experimental investigation.

In the present work, computational exploration of different loadings of the pyrrolidinium-based IL 1-methyl-1-butyl-pyrrolidinium bis(trifluoromethanesulfonyl)imide ($[C4PYR]^+[TF2N]^-$) confined in the pores of MCM-41 was carried out in order to study the capture and separation of CO_2 from N_2 and CH_4. Pure component adsorption study for CO_2, N_2 and CH_4 was carried out at three different temperatures on pristine and IL-loaded MCM-41. Three-dimensional spatial distribution maps and radial distribution functions (RDFs) of CO_2 were calculated to identify the locations preferred by CO_2 inside the adsorbent pores. Further, grand canonical Monte Carlo

(GCMC) simulations of CO_2/N_2 and CO_2/CH_4 binary mixtures were performed to establish the enhancement of CO_2 selectivities in IL-loaded MCM-41.

5.2 Model and Simulation Details

5.2.1. Structures of MCM-41 and Ionic Liquid

Molecular model of MCM-41 was constructed by carving cylindrical pores in an amorphous silica block, ensuring that the pore arrangement is hexagonal and keeping the pore diameter similar to that observed in realistic MCM-41 samples. The dangling bonds of silicon and oxygen atoms on the surface of the pores were saturated with hydroxyl groups and hydrogen atoms respectively. The constructed model was further subjected to geometry optimization using Forcite module of Materials Studio 7.0 software package [63]. The MCM-41 model thus obtained has unit cell dimensions of 42.8 Å × 42.8 Å × 64.2 Å and an average pore diameter of 32.8 Å, calculated from the average distance between the center of the pore and all the surface hydrogen atoms. The simulation box containing one central principal pore and four quarter-pores at the four corners of the box is shown in Figure 5.2(a). The accessible surface area, computed using nitrogen probe molecule of radius 1.82 Å, was found to be 951.30 m^2/g which is in a good agreement with the experimental values of BET surface area in the range 1090–1150 m^2/g for MCM-41 [87,88]. Geometry of IL pair of methyl-1-butyl-pyrrolidinium $[C4PYR]^+$ and bis(trifluoromethanesulfonyl)imide $[TF2N]^-$ was optimized using density functional theory (DFT) at B3LYP/6-311++G** level of theory using GAUSSIAN 09 software [137]. The structure of the cation and anion of the IL is shown in Figure 5.1.

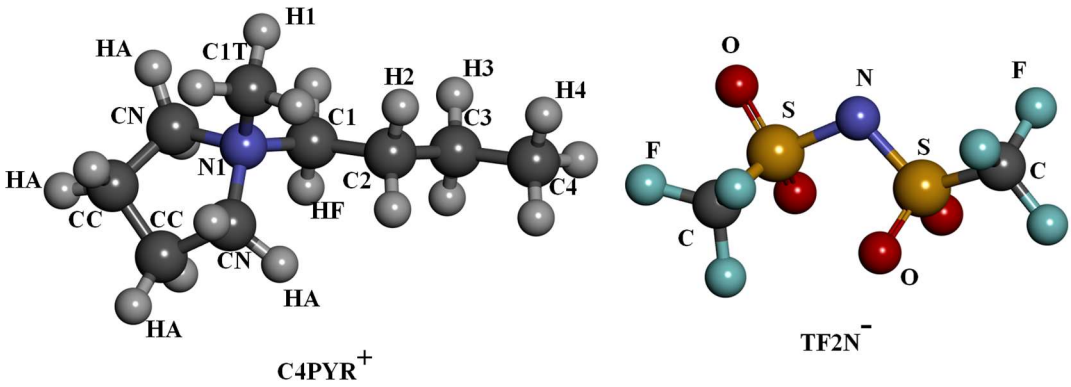

Figure 5.1 Molecular structures of the cation ($C4PYR^+$) and the anion ($TF2N^-$) of the IL.

Two separate IL-impregnated MCM-41 models having different loadings of the IL were then prepared by inserting 16 and 32 cation-anion pairs of the IL respectively into the central pore of the MCM-41 model using the Packmol software package [138]. An equal number of IL molecules was also inserted in the four quarter-pores of the MCM-41 models using Packmol so that the total number of IL molecules (cation-anion pairs) present in the simulation box in the two models is 32 and 64 respectively. The MCM-41/IL system was equilibrated by conducting molecular dynamics (MD) simulations in the NVT ensemble. The equilibrated IL-impregnated MCM-41 models, referred to as MCM-41-IL1 and MCM-41-IL2 henceforth and shown in Figure 5.2(b) and 2(c) respectively, were used for adsorption simulations using GCMC technique.

5.2.2. Force Fields

Adsorbates: In this work, the non-bonded van der Waals interactions were modeled using the 12-6 Lennard-Jones (LJ) potential for all the adsorbates. N_2 was modeled as having two LJ sites at the two nitrogen atoms with N–N bond length of 1.1 Å and three partial point charges, one each on the two nitrogen atoms and a third at the center of mass of the nitrogen molecule, in order to effectively capture the effect of quadrupole moment. LJ parameters and partial charges for N_2 molecule were taken from transferrable potentials for phase equilibria (TraPPE) force field [84]. Three LJ sites

were used to represent the rigid CO_2 linear molecule with partial charges on the respective atoms. The C=O bond length (of 1.16 Å), the LJ parameters and the partial charges on the CO_2 molecule were taken from the EPM2 model [104]. A united atom approach was used to model CH_4 where only one LJ site was considered. TraPPE united atom (TraPPE -UA) force field, proposed by Martin and Siepmann [105], was used to model the CH_4 molecule.

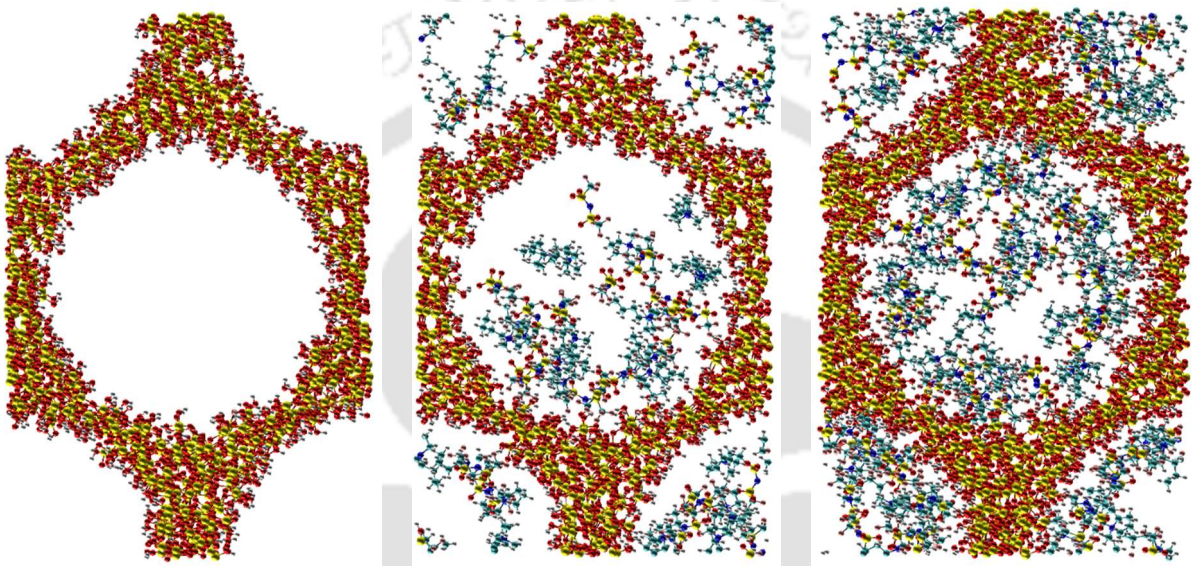

Figure 5.2 Molecular models of (a) pure MCM-41, (b) MCM-41-IL1, and (c) MCM-41-IL2.

Adsorbents: Several studies on ILs have used optimized potentials for liquid simulations (OPLS) force field [139–142] and satisfactorily reproduced experimentally determined properties of ILs. In the present work, we have used OPLS force field for the studied IL. To test the validity of the employed force field for ILs, density of the IL was simulated using the forcefield and compared with literature data. First, 250 cation-anion pairs of the ILs were packed in a cubic box of size $50\ \text{Å} \times 50\ \text{Å} \times 50\ \text{Å}$ and MD simulation was carried out in the NVT ensemble for 5ns followed by MD simulation in the NPT ensemble for 40 ns with a timestep of 1 fs. Configurations of the

simulation run were saved for the last 2000 frames and were used to obtain average of the system. The simulated density is found to compare well with the reported by Haskins et al. [143] over the range of temperatures, as shown in the Figure 5.3. Thus the forcefield selected for the IL is acceptable. MCM-41 was modeled as a rigid, frozen framework and force field parameters were taken from the work of Jing et al. [72]. During MD equilibration of the IL-loaded MCM-41 structures, the IL cations and anions were modeled as flexible ions moving inside the rigid, frozen MCM-41 framework. However, during GCMC simulations of gas adsorption in the MCM-41-IL structures, both the MCM-41 framework and the IL molecules were maintained rigid and fixed. Only non-bonded interactions were considered between the framework atoms, IL ions and the adsorbed gas molecules. To ensure that considering the IL molecules immobile during the GCMC simulations did not have a significant effect on the adsorption behavior, we calculated the accessible surface areas and pore volumes of five independent configurations of the IL-loaded MCM-41, taken from the last 10 ns of the MD equilibration, spaced 2 ns apart. The properties listed in Table 5.1 vary by less than 5% between the different MCM-41-IL1 configurations indicating that variation in arrangement of IL molecules in the mesopore does not have a significant effect on the accessible surface area and pore volume. As these properties are important characteristics of an adsorbent, it is expected that different MCM-41-IL1 configurations will show similar adsorption behavior. We also carried out pure CO_2 adsorption simulations on the five configurations of MCM-41-IL1 and MCM-41-IL2 systems, the results of which are shown in the Figure 5.4. The CO_2 adsorption isotherm for the different configurations are close to each other for both the MCM-41-IL1 and MCM-41-IL2, further suggesting that neglecting the mobility (and flexibity) of ILs does not have strong effect on the adsorption behavior. Thus, considering only a

single configuration of IL-loaded MCM-41 and assuming IL molecules to be immobile should not result in significant errors.

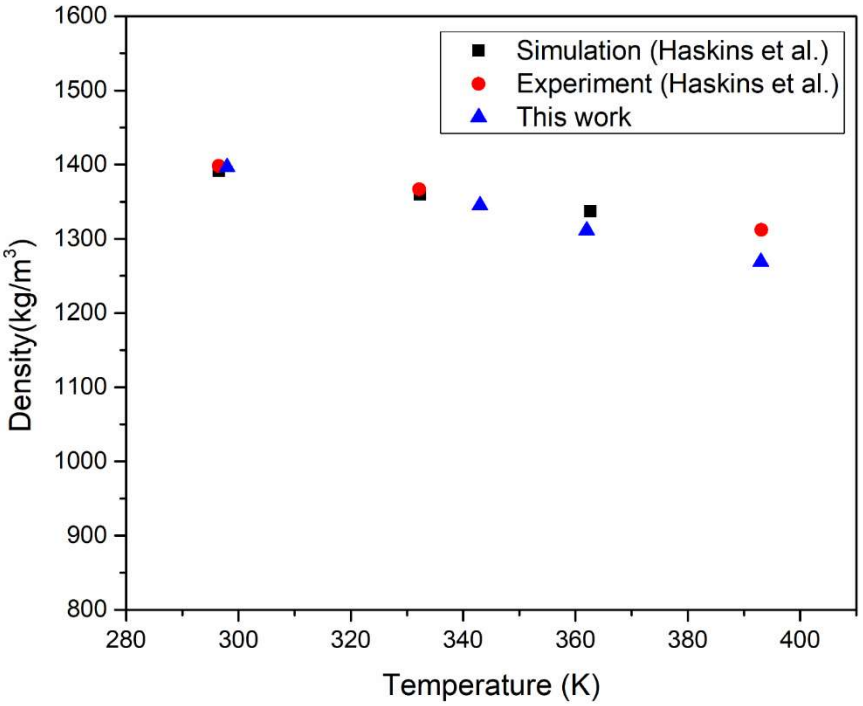

Figure 5.3 Density calculation of pure ILs at different temperatures, and comparison with the simulation and experimental data of Haskins et al. [143]

Table 5.1 Accessible surface areas and pore volume fractions of different configurations of MCM-41-IL1.

Adsorbent Configurations	Accessible pore volume fraction (probe radius 1.4 Å)	Accessible pore volume fraction (probe radius 1.82 Å)	Surface area in m^2/g (probe radius 1.4 Å)	Surface area in m^2/g (probe radius 1.82 Å)
Config1	0.2814	0.2199	1491.05	1216.83
Config2	0.2859	0.2237	1448.41	1199.93
Config3	0.2852	0.2254	1431.27	1170.53
Config4	0.2833	0.2201	1487.22	1222.58
Config5	0.2812	0.2178	1492.77	1217.57

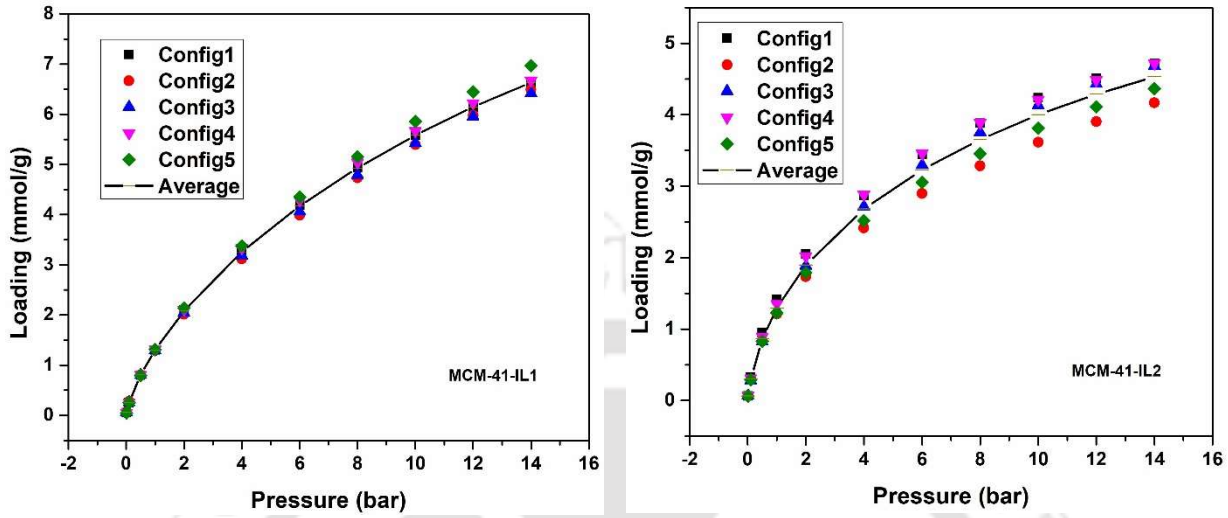

(a) (b)

Figure 5.4 CO_2 adsorption capacity in five different configurations of MCM-41-IL1 and MCM-41-IL2.

The detailed LJ parameters and partial charges for the adsorbate gases as well as the adsorbent material (MCM-41 and IL) are listed in Table 5.2.

5.2.3. Simulation Details

MD equilibration of the ionic liquid confined inside the pores of MCM-41 was carried out using the large-scale atomic/molecular massively parallel simulator (LAMMPS) software package [144] . MD simulation of CO_2 inside IL-impregnated MCM-41 was also carried out using LAMMPS to determine the spatial distribution of CO_2 and RDFs between different atom types. The SHAKE algorithm [145] was used to constrain the C=O bond length. The particle-particle particle-mesh (PPPM) solver implemented in LAMMPS was used to calculate the non-bonded Coulombic potential.

Table 5.2 LJ potential parameter and charges in adsorbent and adsorbate molecule

Molecule	Site	σ (Å)	ε (K)	q (e)	Bond length (Å)
MCM-41	Si	3.804	155.858	0.12242285	
	O	3.033	48.115	-0.0614741	
	H	2.846	0.05	0.0318	
IL $[C4PYR]^+$	C1	3.465	26.5682	-0.08	
	C2	3.465	26.5682	-0.288	
	C3	3.465	26.5682	-0.288	
	C4	3.465	26.5682	-0.432	
	CC	3.516	28.18	-0.28	
	CN	3.516	28.18	-0.096	
	C1T	3.465	26.5682	-0.24	
	H1	2.394	12.07536	0.16	
	H2	2.475	12.07536	0.144	
	H3	2.475	12.07536	0.144	
	H4	2.475	12.07536	0.144	
	HA	2.394	12.07536	0.16	
	HF	2.394	12.07536	0.16	
	N1	3.216	68.435	-0.208	
IL $[TF2N]^-$	C	3.465	26.5682	0.28	
	F	2.919	21.34837	-0.128	
	S	3.516	100.71619	0.816	
	O	2.929	84.599	-0.424	
	N	3.216	68.435	-0.528	
CO_2	C	2.757	28.129	0.6512	1.152
	O	3.033	80.507	-0.3256	(C=O)
N_2	N	3.310	36.0003	-0.4820	1.1
	N(COM)	0.000	0.000	0.9640	(N≡N)
CH_4	CH_4	3.730	148.00	0.0000	

A cutoff of 12.5 Å was used for both the LJ potential and the real part of the Coulombic interactions. The MCM-41/IL system was equilibrated for 40 ns using MD simulation in the constant NVT ensemble with a time step of 1 fs. The final configuration of the IL confined in MCM-41 obtained at the end of the MD equilibration was used to conduct the GCMC simulation of gas adsorption.

All the GCMC simulations were carried out using RASPA software package developed by Dubbeldam et al. [55]. This package has been extensively tested for a large number of systems and validated against experimental data [62,133,146]. Insertion, deletion, translation and rotation moves were employed in all GCMC simulations. In the case of mixture adsorption simulations, identity exchange trial moves were also used [56,57]. For pure gas adsorption, the four types of moves are assigned a probability of 0.25 each. For mixture adsorption, identity exchange move is assigned a probability of 0.05 by reducing the probabilities of translation and rotation moves equally and maintaining the probabilities of insertion and deletion moves unchanged at 0.25. During each MC cycle, one MC trial move (of any type) is attempted on all the N adsorbate molecules in the simulation box if the number of adsorbed molecules, $N \geq 20$. However, if $N < 20$, the number of trial moves attempted in each cycle is equal to 20. A total of 2.5×10^6 MC cycles were carried out for equilibration followed by another 2.5×10^6 MC cycles for production of adsorption data. The results obtained from the GCMC simulation are the absolute amounts adsorbed which were converted to excess adsorbed amounts using equation (2.36), which is provided in the section 2.2.5.

Dual-site Langmuir (DSL) model was used to fit the isotherm data for pure CO_2, CH_4 and N_2 isotherms. Adsorption isotherm modelling was done at three different temperatures for pure gases.

The equations describing the Langmuir and DSL models are provided in the section 2.2.3(a) and 2.2.3(b) respectively. The ideal adsorbed solution theory (IAST) proposed by the Myers and Prausnitz [64] was used to predict the mixture adsorption isotherms using the pure component adsorption data. Pure gas isotherm model parameters, obtained by fitting Langmuir or dual-site Langmuir models to simulation data, were provided as input to the IAST calculation to obtain mixture adsorption isotherm predictions. Governing equations related to IAST predictions are given in the section 2.2.6.

5.3 Results and Discussion

5.3.1. Adsorption of Pure Gases: CO_2, N_2 and CH_4

GCMC simulations were carried out to study the effect of impregnation of IL into the mesopores of MCM-41 on the adsorption of CO_2, N_2 and CH_4 as well as on the separation of CO_2 from gas mixtures. Figure 5.5 shows a comparison between the simulated adsorption isotherm of pure CO_2 in MCM-41 at 303.15 K with experimental data of dos Santos et al. [44]. The two isotherms compare well indicating that the models and interaction parameters employed are appropriate for simulating CO_2 adsorption on MCM-41. The surface areas and accessible pore volume fractions of the three MCM-41 models, calculated using the Materials Studio software with two different probe sizes, are listed in Table 5.3

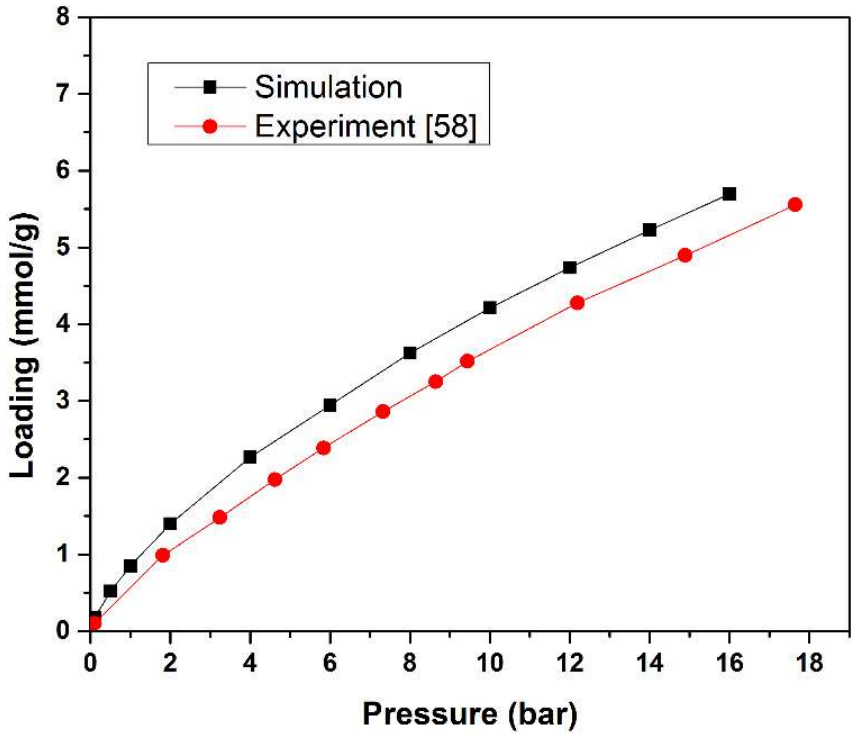

Figure 5.5 Comparison of simulated adsorption isotherm of pure CO_2 on MCM-41 with experimental data of dos Santos et al. [44] at 303.15 K.

Table 5.3 Accessible pore volume and surface area of different MCM-41 models considered in this work.

Adsorbent Name	Accessible pore volume fraction (probe radius 1.4 Å)	Accessible pore volume fraction (probe radius 1.82 Å)	Surface area in m^2/g (probe radius 1.4 Å)	Surface area in m^2/g (probe radius 1.82 Å)
MCM-41	0.4962	0.4576	1061.22	951.30
MCM-41-IL1	0.2812	0.2178	1492.77	1217.57
MCM-41-IL2	0.1446	0.0951	1050.70	724.14

The accessible pore volume fraction decreases significantly with increase in the amount of IL incorporated, as expected. However, the accessible surface area increases at the lower IL loading in MCM-41 and decreases as the loading is increased. The adsorption isotherms of pure CO_2, N_2,

and CH_4 in MCM-41, MCM-41-IL1 and MCM-41-IL2 along with respective dual-site Langmuir (DSL) model fits are shown in Figure 5.6.

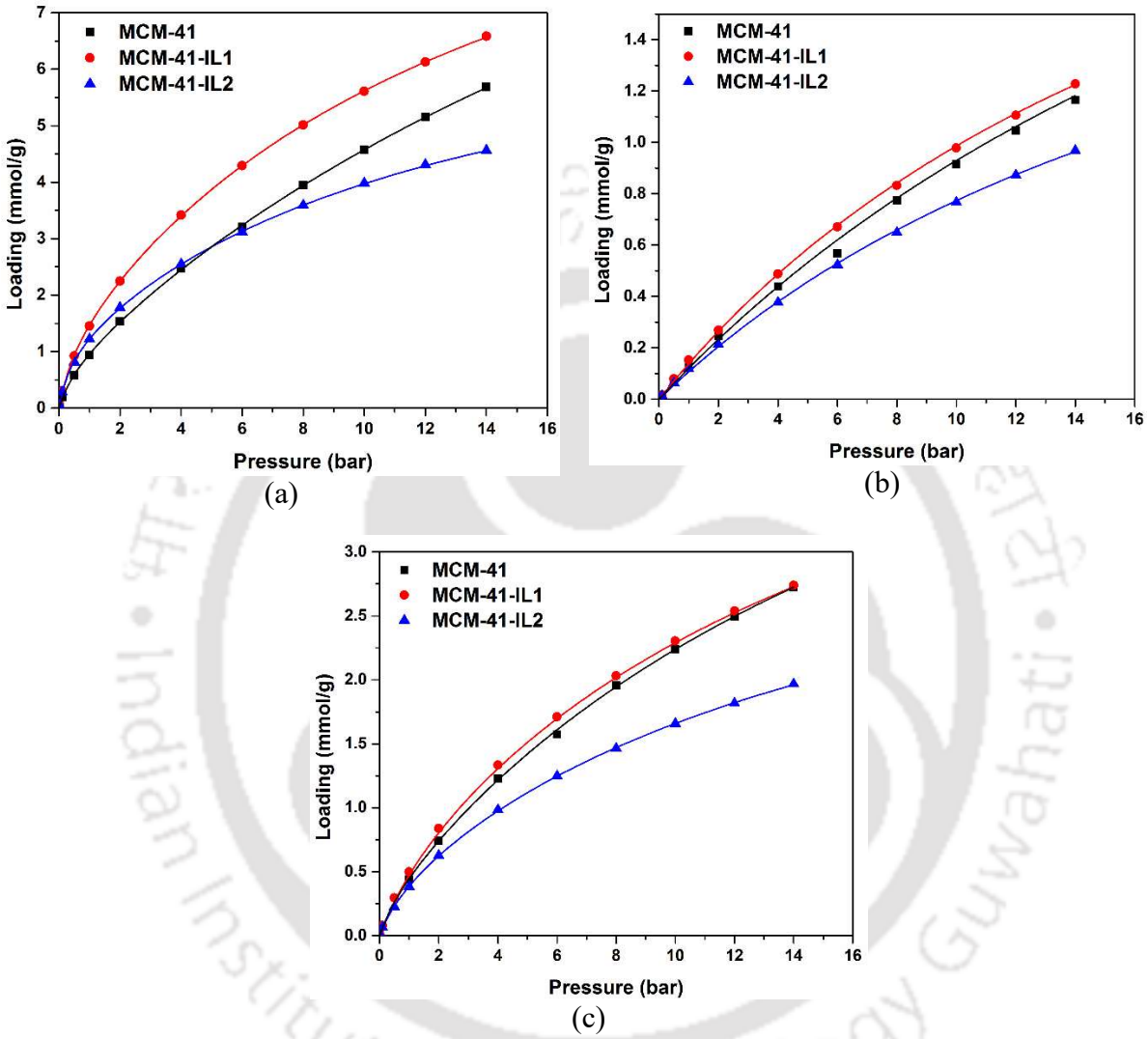

Figure 5.6 Adsorption isotherms of pure (a) CO_2 (b) N_2 and (c) CH_4 at 298.15 K in the pure MCM-41 and IL-loaded MCM-41 models. Lines represents dual-site Langmuir model fits for CO_2, N_2 and CH_4.

The saturation loading is lowest in MCM-41-IL2 for all three gases due to the lower accessible surface area and pore volume fraction. The accessible surface area includes the surface of MCM-41 pore walls as well as the surface around the IL molecules that is accessible to the adsorbent

molecules. In contrast, MCM-41-IL1 showed the highest loadings for all the three adsorbates, viz. CO_2, N_2 and CH_4, over the pressure range studied (0–14 bar) possibly due to the larger accessible surface area. Interestingly, CO_2 loading was significantly higher in MCM-41-IL1 than in the other two models whereas CH_4 and N_2 loadings were only slightly higher in MCM-41-IL1 than in pure MCM-41. This can be attributed to the stronger electrostatic interactions between the ionic liquid molecules and CO_2 due to its larger quadrupole moment. On the other hand, less polar N_2 and nonpolar CH_4 molecules do not interact as strongly with the ionic liquid molecules and hence, their loadings are only marginally higher in MCM-41-IL1 (and lower in MCM-41-IL2) than in pure MCM-41. A notable feature of Figure 5.6(a) is that up to pressures of ~5 bar, the amount of CO_2 adsorbed in MCM-41-IL2 is higher than that in pure MCM-41. Although the accessible surface area and void fraction of MCM-41-IL2 are lower than that of pure MCM-41, the strong CO_2-ionic liquid interactions are responsible for higher loading at low pressures. At higher pressures (> 5 bar), when the number of adsorbed CO_2 molecules becomes high, the smaller accessible surface area and pore volume of MCM-41-IL2 becomes the limiting factor and despite strong CO_2-ionic liquid interactions, the loading in MCM-41-IL2 drops below that in pure MCM-41. Figure 5.6 also shows the dual-site Langmuir model fits to the adsorption isotherms of pure CO_2, CH_4 and N_2 isotherms. The respective models are observed to fit the simulated adsorption data well. Adsorption simulations were also carried out at two other temperatures and model fitting was carried out on the adsorption isotherms at the three different temperatures. Adsorption isotherms and fitted parameters at all three temperatures in the three MCM-41 models are shown in Figure 5.7–Figure 5.9 and Table 5.4–Table 5.6.

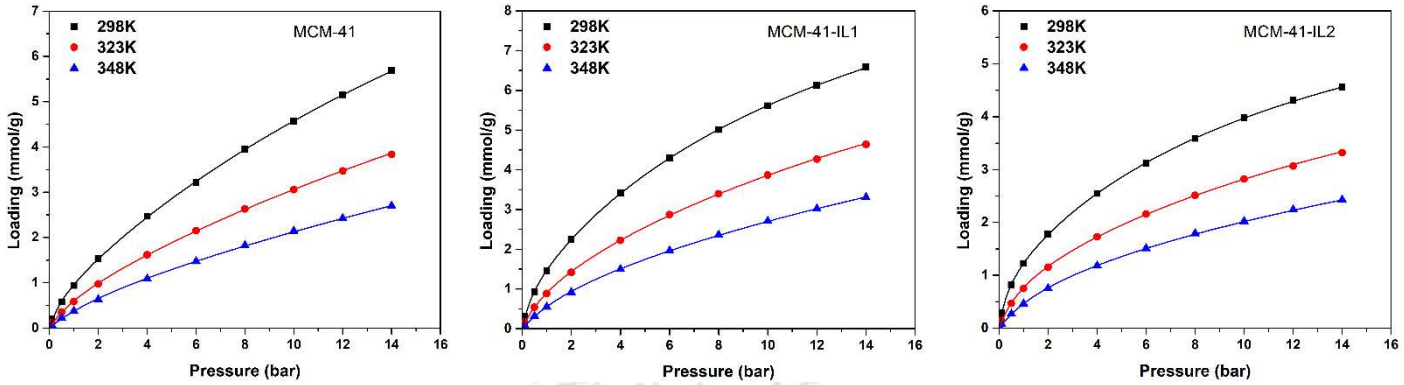

(a) (b) (c)

Figure 5.7 Simulated adsorption isotherms and corresponding DSL model fits for CO_2 adsorption at three temperatures on (a) pure MCM-41, (b) MCM-41-IL1, and (c) MCM-41-IL2.

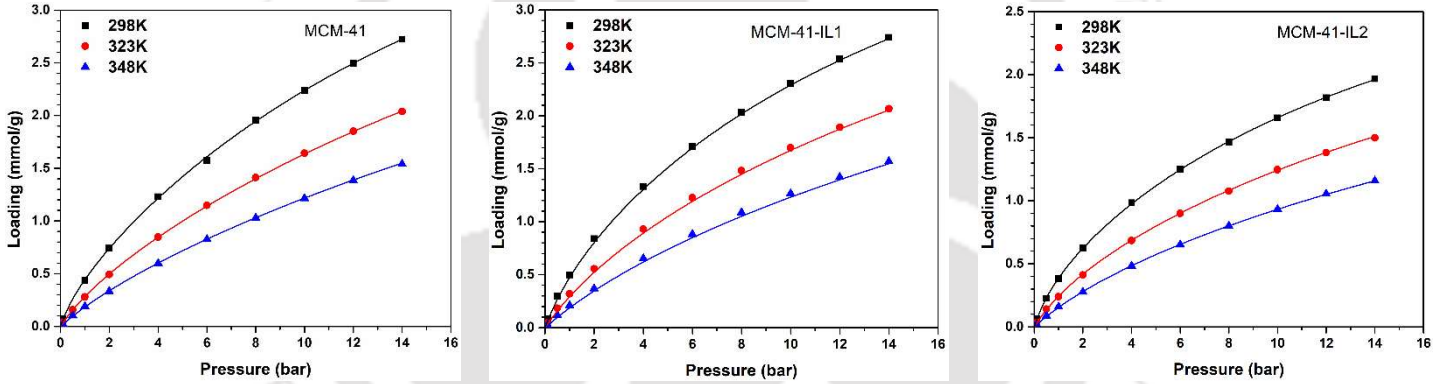

(a) (b) (c)

Figure 5.8 Simulated adsorption isotherms and corresponding DSL model fits for CH_4 adsorption at three temperatures on (a) pure MCM-41, (b) MCM-41-IL1, and (c) MCM-41-IL2.

The isosteric heats of adsorption were calculated for the gases from simulation, based on fluctuations in the grand canonical ensemble. Fig. 5.10 shows the isosteric heats of the adsorbate gases in the three adsorbents at 298.15 K and different pressures. Isosteric heats of the gases are higher in the IL-loaded MCM-41 models, with MCM-41-IL2 showing the largest values. Isosteric heat of adsorption initially decreases with increase in pressure as the favourable sites become occupied. At high pressures, when all the favorable sites are occupied, the isosteric heat remains

relatively constant. CO_2 shows the highest values of isosteric heat in all three models followed by CH_4 and N_2.

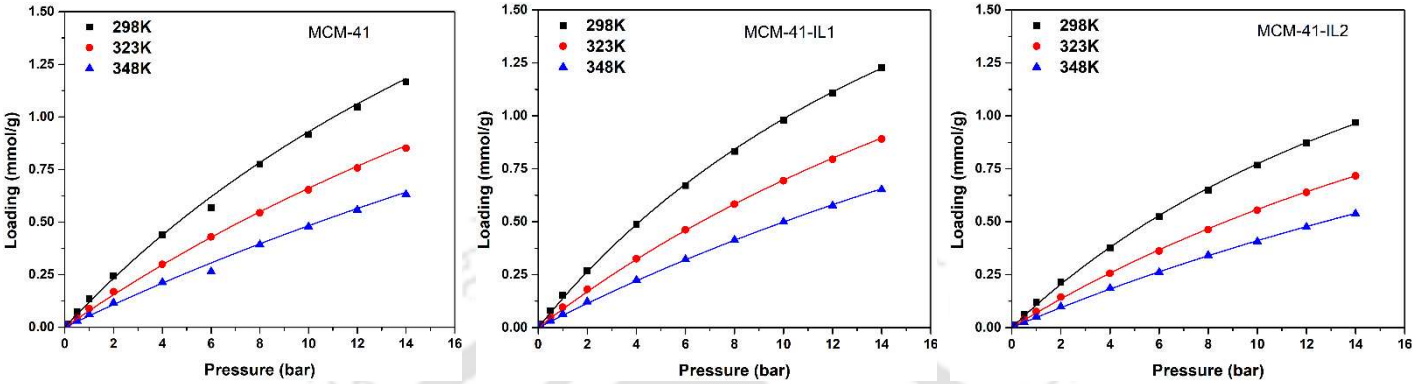

Figure 5.9 Simulated adsorption isotherms and corresponding Langmuir model fits for N_2 adsorption at three temperatures on (a) pure MCM-41, (b) MCM-41-IL1, and (c) MCM-41-IL2.

Table 5.4 Parameters of the DSL model for CO_2 adsorption on the three MCM-41 models

DSL Parameters	MCM-41	MCM-41-IL1	MCM-41-IL2
N_1^{max}(mmol g^{-1})	0.6143	11.1324	6.8505
N_2^{max}(mmol g^{-1})	15.6071	1.0066	0.9416
β_{10}(bar^{-1})	4.85E-05	9.56E-06	8.67E-06
β_{11}(bar^{-1})	3216.284	2661.03	2725.459
β_{20}(bar^{-1})	1.71E-05	4.36E-05	1.46E-05
β_{21}(bar^{-1})	2267.701	3261.36	3646.443
R^2	0.9999	0.9999	0.9999

Table 5.5 Parameters of the DSL model for CH_4 adsorption on the three MCM-41 models

Parameters	MCM-41	MCM-41-IL1	MCM-41-IL2
N_1^{max}(mmol g^{-1})	6.1734	5.1995	3.5612
N_2^{max}(mmol g^{-1})	0.259	0.4347	0.2912
β_{10}(bar^{-1})	9.88E-05	6.89E-05	9.13E-05
β_{11}(bar^{-1})	1842.658	2007.817	1953.496
β_{20}(bar^{-1})	4.20E-05	1.00E-04	4.23E-05
β_{21}(bar^{-1})	3141.719	2689.746	3102.813
R^2	0.9999	0.9999	0.9999

Table 5.6 Parameters of the DSL model for N_2 adsorption on the three MCM-41 models

Parameters	MCM-41	MCM-41-IL1	MCM-41-IL2
N_1^{max}(mmol g^{-1})	5.0075	3.4514	3.5027
N_2^{max}(mmol g^{-1})	0.0644	0.0493	0.054
β_{10}(bar^{-1})	0.0001	8.55E-05	0.0001
β_{11}(bar^{-1})	1569.543	1810.614	1642.633
β_{20}(bar^{-1})	2.19E-07	3.16E-05	5.08E-06
β_{21}(bar^{-1})	4651.182	3145.306	3640.18
R^2	0.9993	0.9999	0.9999

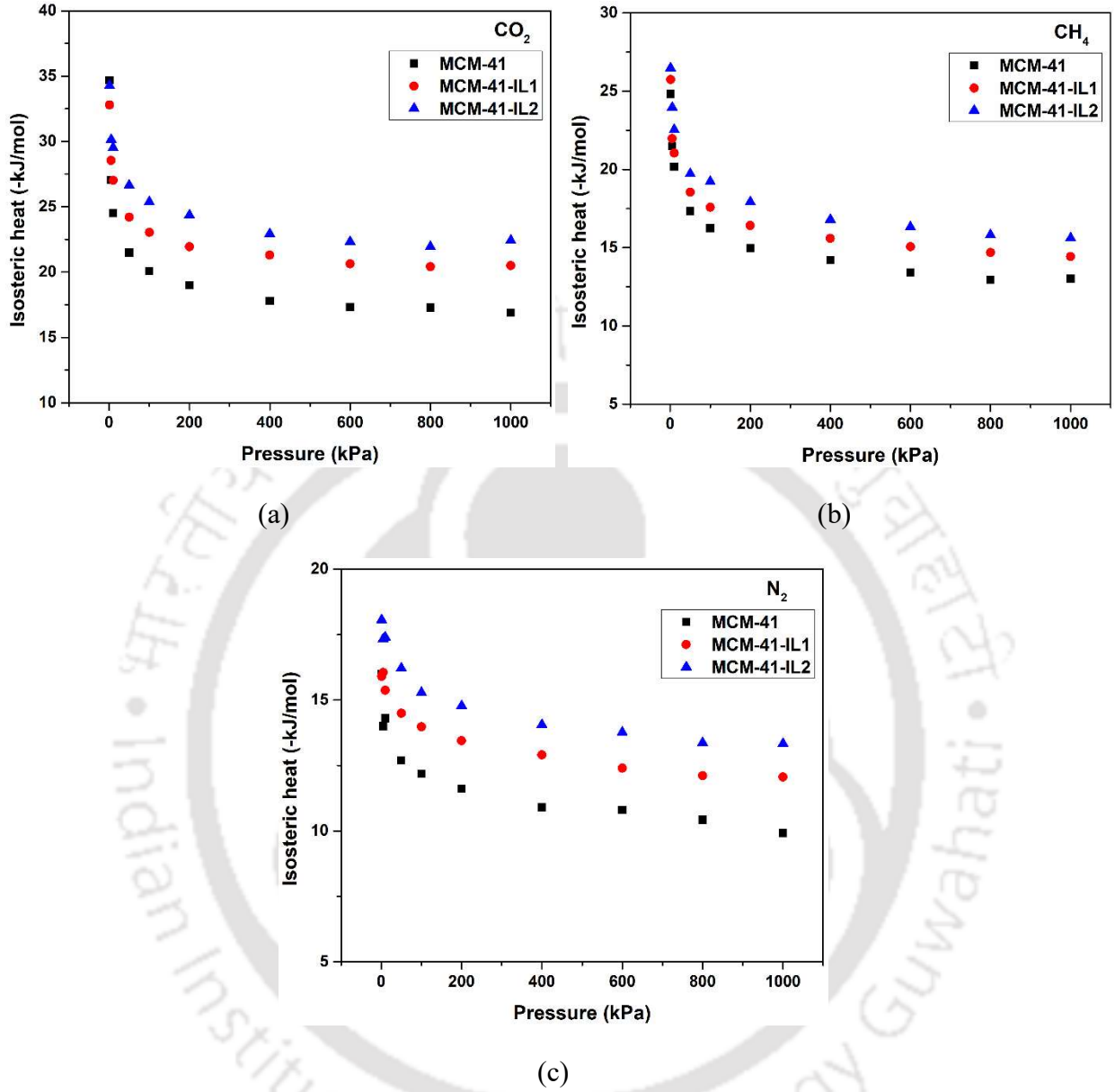

Figure 5.10 Isosteric heats of adsorption of pure (a) CO_2 (b) CH_4 and (c) N_2 at 298.15 K in the pure MCM-41 and IL-loaded MCM-41 models.

5.3.2. Distribution of CO_2 in the Frameworks

The distribution of CO_2 molecules inside pure and IL-loaded MCM-41 was further studied using 3D density distribution maps of CO_2 and RDFs, obtained from MD trajectories of CO_2 and IL molecules inside the MCM-41 pores. The number of CO_2 molecules considered was 32 and 64 in

the case of MCM-IL-1 and MCM-IL-2 respectively (half in the principal pore and the rest equally divided in the four quarter pores). Figure 5.11(a) and (b) show the 3D isosurface plots of the distribution of CO_2 molecules in MCM-41-IL1 and MCM-41-IL2, obtained by considering the location of the CO_2 molecules in the adsorbent framework over 1000 snapshots from the last 20 ns of the MD trajectory spaced 20 ps apart.

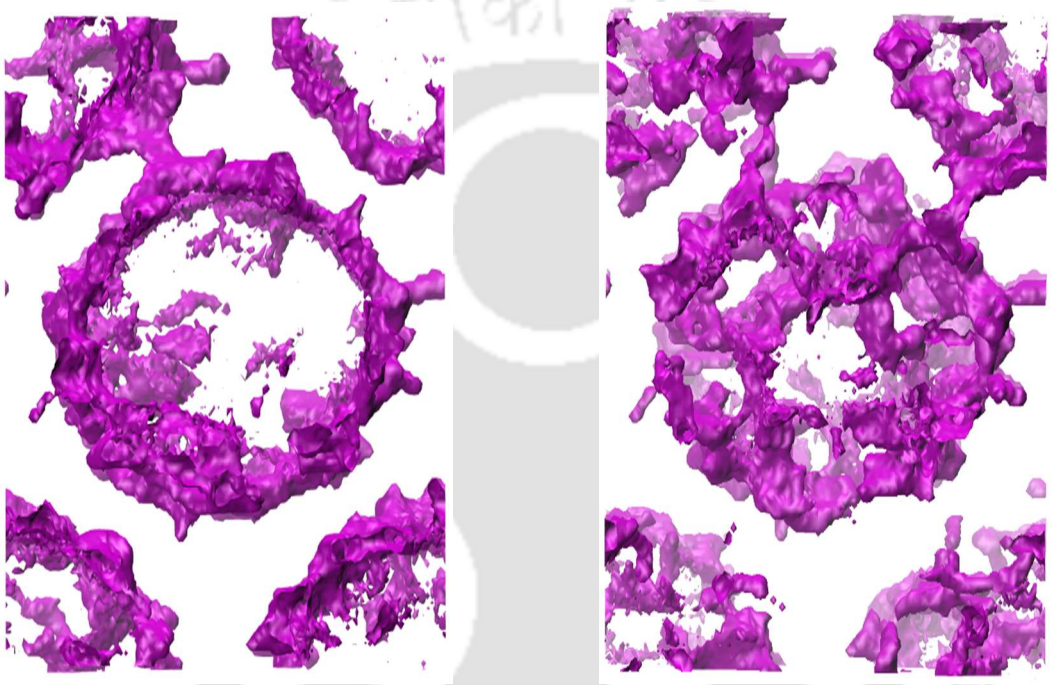

(a) (b)

Figure 5.11 3D spatial distribution maps of CO_2 in (a) MCM-41-IL1, and (b) MCM-41-IL2, obtained from MD simulations at 298.15 K. The framework atoms (MCM-41 and IL) have not been shown for clarity.

The plots reveal that in addition to the surface of the pore walls of MCM-41, CO_2 molecules also prefer sites around IL molecules away from the pore walls. The average distribution of CO_2 molecules away from the pore walls is considerably more pronounced in the case of MCM-41-IL2 (see Figure 5.11(b)) which contains larger loading of IL molecules within the MCM-41 mesopores.

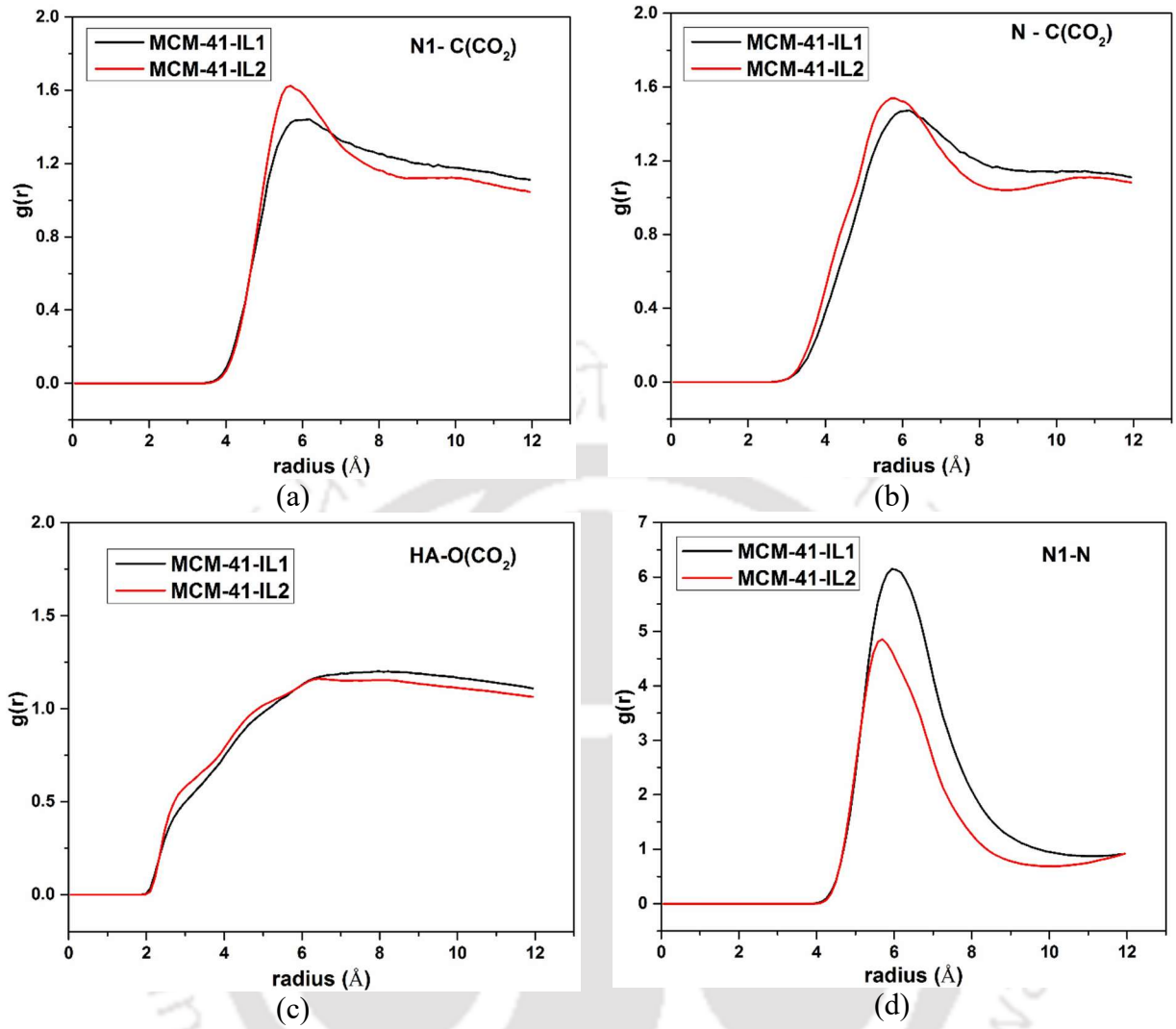

Figure 5.12 RDFs between (a) C4PYR cation and CO_2, (b) TF2N anion and CO_2, (c) Hydrogen atoms on pyrrolidinium ring of cation (marked as HA in Figure 5.1) and oxygen atoms of CO_2, and (d) the cation and the anion of the IL. In (a), (b) and (d), the reference atom for the cation is the nitrogen atom of the pyrrolidinium ring (marked as N1 in Figure 5.1), that for the anion is the central (and only) nitrogen atom (marked as N in Figure 5.1) and that for CO_2 is the carbon atom center of the CO_2 molecules.

The RDF of CO_2 molecules around the cations and anions of IL molecules provide more quantitative information about the spatial distribution of CO_2. Figure 5.12(a) and (b) show the RDFs of CO_2 molecules (their carbon centers to be precise) with respect to the nitrogen atoms of the cations and anions of the IL molecules respectively (marked as N1 and N in Figure 5.1). The RDFs show that there are almost no CO_2 molecules up to a distance of ~4 Å from the nitrogen

atom of the cation (N1 in Figure 5.1) and up to a distance of ~3.5 Å from the nitrogen atom of the anion (N in Figure 5.1), for both MCM-41-IL1 and MCM-41-IL2. The RDFs show a broad peak around ~6Å for both cationic and anionic nitrogen atoms, in both MCM-41-IL1 and MCM-41-IL2, indicating higher probability of finding CO_2 molecules at this distance around the IL ions. Thus, CO_2 prefers locations around both the cations and anions of IL molecules. The RDFs of the oxygen atoms of CO_2 molecules around the hydrogen atoms of the pyrrolidinium group of the cations (marked as HA in Figure 5.1) are plotted in Figure 5.12(c). The RDFs for both MCM-41-IL1 and MCM-41-IL2 do not show any discernible peaks indicating the absence of any hydrogen bonding. Figure 5.12(d) shows the RDFs of the nitrogen atom of anion (marked N in Figure 5.1) around the nitrogen atom of the pyrrolidinium group of cations (marked N1 in Figure 5.1). A strong peak can be seen around ~6 Å for both MCM-41-IL1 and MCM-41-IL2 confirming that the cations and anions of the IL are closely associated and paired with each other inside the MCM-41 pores during the course of the MD simulation.

5.3.3. Adsorption of Binary Mixtures of CO_2/N_2 and CO_2/CH_4

GCMC simulations were carried out to study the adsorption and separation of binary mixtures of CO_2/N_2 and CO_2/CH_4, both in the molar ratio 15:85, at 298.15 K. Figure 5.13 shows the mixture adsorption isotherms of N_2, CO_2 and CH_4 in the three adsorbent models.

The amount of N_2 adsorbed is similar for MCM-41 and MCM-41-IL1 models at pressures up to ~6 bar, as is evident from Figure 5.13(a). Even at higher pressures, the amount of N_2 adsorbed in MCM-41 is not significantly higher than that in MCM-41-IL1. However, in MCM-41-IL2, the amount of N_2 adsorbed is considerably lower than that in the other two models, over the entire pressure range shown. The adsorption isotherms of CH_4 in Figure 5.13(b) show similar trend with

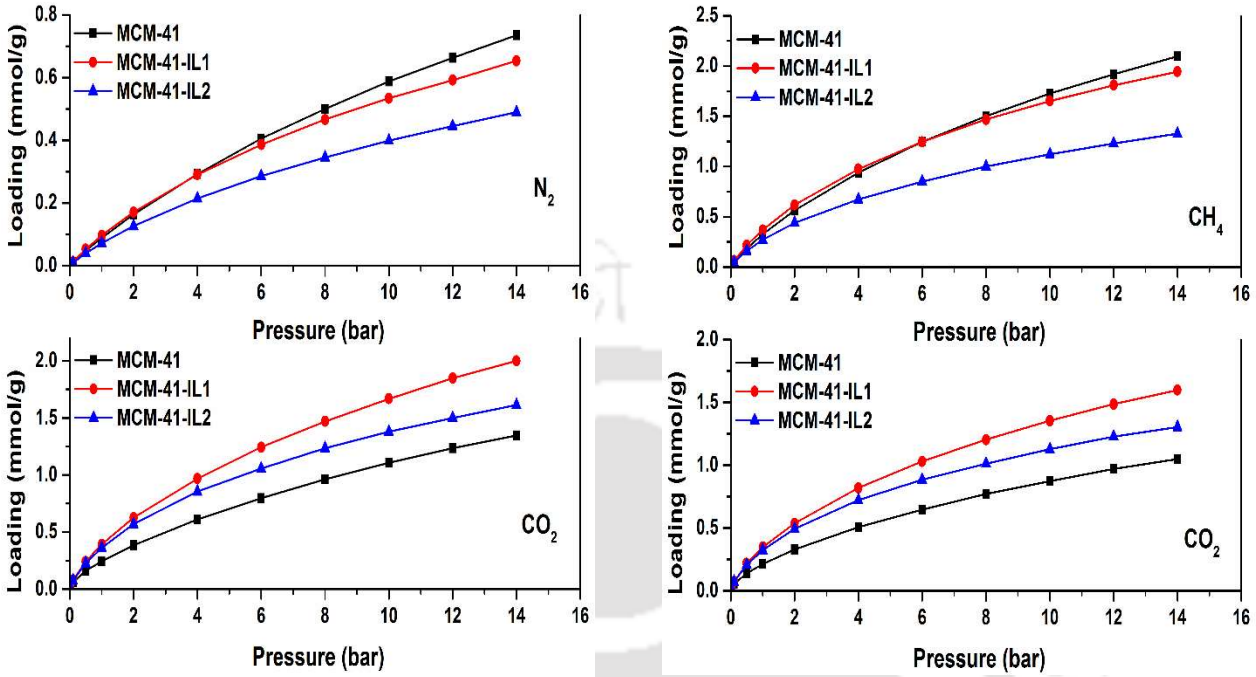

Figure 5.13 Simulated adsorption isotherms of (a) N_2 and CO_2 for 15:85 (by mole) binary CO_2/N_2 mixture, and (b) CH_4 and CO_2 for 15:85 (by mole) binary CO_2/CH_4 mixture. All isotherms are at 298.15K (lines have been shown only as guide to the eye).

the amounts adsorbed in MCM-41 and MCM-41-IL1 very similar over the entire pressure range and that in MCM-41-IL2 substantially lower than the other two models. Both N_2 and CH_4 are relatively nonpolar molecules, and hence do not show any noticeable preference for the charged ions of the IL over the surface atoms of MCM-41 pore wall. The major factor determining the adsorption behavior of these gases is thus primarily the available surface area and pore volume (important at high pressures) which are the lowest for MCM-41-IL2 leading to low adsorption. The adsorption behavior of CO_2 on the three models is however much different. In both mixtures, CO_2 adsorption is highest in MCM-41-IL1 followed by MCM-41-IL2 and pure MCM-41 in that order. The greater quadrupole moment of CO_2, compared to N_2 and CH_4, results in stronger

interactions with the IL ions leading to higher adsorption in both the IL-loaded MCM-41 models over the entire pressure range studied (0.1–14 bar), despite the larger accessible surface area of pure MCM-41 than MCM-41-IL2. This may appear to be somewhat in contrast with pure CO_2 adsorption behavior (see Figure 5.6(a)) where MCM-41 shows higher adsorption than MCM-41-IL2 above 5 bar due to the adsorption in MCM-41-IL2 approaching saturation. However, the amount of CO_2 in the binary mixtures is only 15%, so that even at a total pressure of 14 bar, the fugacity of CO_2 in the mixture would be significantly lower than that expected at saturation. CO_2 adsorption in the models clearly does not approach saturation at total pressures of up to 14 bar and therefore, the favorable interactions of CO_2 molecules with IL dominate over the higher accessible pore volume of pure MCM-41, leading to larger adsorption of CO_2 in MCM-41-IL2. In the case of MCM-41-IL1, the combined effect of strong CO_2-IL interactions and large accessible surface area leads to higher CO_2 adsorption than the other two models.

Figure 5.14 shows snapshots of CO_2/N_2 and CO_2/CH_4 binary mixture adsorption on the three models at 298.15 K and 12 bar. In pristine MCM-41, the adsorption of the CO_2 molecules is primarily on the pore walls whereas some N_2 and CH_4 molecules are present away from the pore walls as well. In IL-loaded MCM-41 models, CO_2 molecules are not only present near the pore wall surface but are also distributed away from the walls, in the pore interior, near the IL molecules. Although the mole fraction of CO_2 in the bulk gas mixture is only 0.15, the amount of CO_2 adsorbed is higher than N_2 and comparable to CH_4 (especially for the IL-loaded models), as can be seen from Figure 5.13 and visually verified from Figure 5.14.

The selectivities of CO_2 over N_2 and CH_4 as a function of pressure, obtained from GCMC simulations and IAST calculations, are shown in Figure 5.15. At 1 bar and 298.15 K, the CO_2/N_2

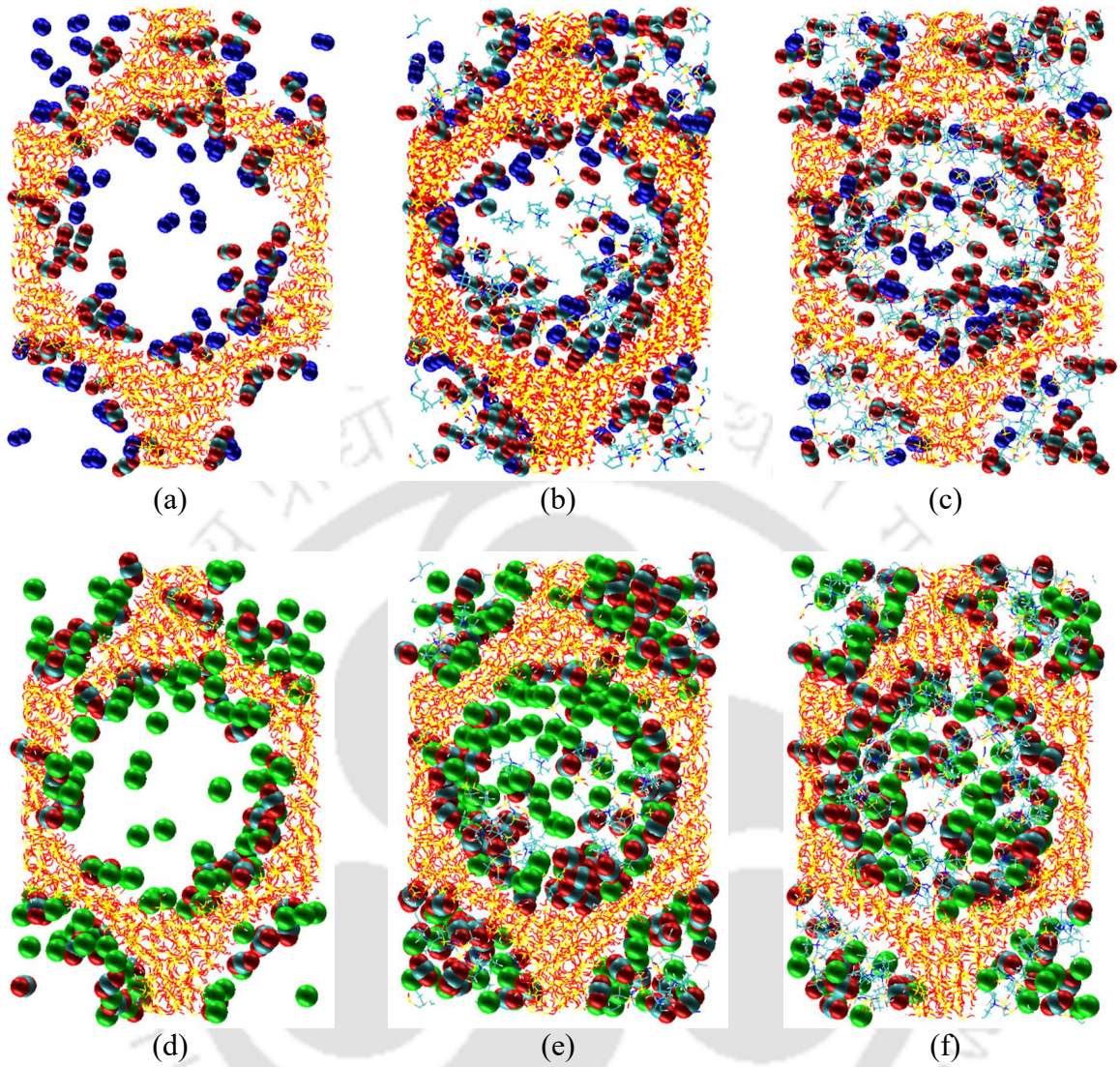

Figure 5.14 Snapshots of adsorption of CO_2/N_2 mixture (15:85 molar ratio) in (a) pure MCM-41, (b) MCM-41-IL1 and (c) MCM-41-IL2, and of CO_2/CH_4 mixture (15:85 molar ratio) in (d) pure MCM-41, (e) MCM-41-IL1 and (f) MCM-41-IL2 at 298.15 K and 12 bar. The adsorbent (MCM-41 and IL) is shown in wireframe representation whereas the atoms in the adsorbate gas molecules are represented as spheres. CO_2 is shown with carbon atoms in cyan and oxygen atoms in red; N_2 is shown with nitrogen atoms in blue; CH_4 is shown as single effective sphere in green.

selectivity in pristine MCM-41, obtained from GCMC simulations, is ~15 whereas selectivities in MCM-41-IL1 and MCM-41-IL2 are ~23 and ~28 respectively (see Figure 5.15(a)). The CO_2/N_2 selectivity values decrease with pressure and become relatively constant at higher pressures.

Above 5 bar, pristine MCM-41 shows a selectivity of ~10 whereas IL-loaded MCM-41 show selectivities in the range 17–20. Thus, the CO_2/N_2 selectivity is 50–100% higher in the presence of IL in the MCM-41 mesopores over the entire pressure range explored. The higher affinity of CO_2 toward the IL molecules than N_2 results in the significantly higher selectivities observed in MCM-41-IL1 and MCM-41-IL2. The IAST predictions of CO_2/N_2 selectivity in Figure 5.15(a) show similar trend to the GCMC results, although the numerical values are different, especially for adsorbents containing IL.

CO_2/CH_4 selectivities, shown in Figure 5.15(b), also follow the trend MCM-41-IL2 > MCM-41-IL1 > MCM-41, with the values being significantly higher in the IL-loaded models. The CO_2/CH_4 selectivities obtained from GCMC simulations in pristine MCM-41, MCM-41-IL1 and MCM-41-IL2 at 1 bar are ~3.7, ~5.4 and ~6.8 respectively, whereas at pressures above 5 bar, the selectivity values are ~3, ~4.6 and ~5.5–6 respectively. The IAST predictions display the same overall trend as GCMC results with MCM-41-IL2 showing highest selectivities. Moreover, above 2 bar pressure, the IAST results show good quantitative match with values obtained from GCMC simulations. MCM-41-IL2 is the most desirable of the three adsorbents in terms of the selectivity of CO_2 over CH_4 and N_2, over the entire pressure range studied (up to 14 bar).

5.4 Conclusions

We have studied the effect of impregnating the pores of mesoporous silica MCM-41 with the IL C4PYR-TF2N on the adsorption behavior of CO_2, N_2, CH_4 and the separation of binary mixtures CO_2/N_2 and CO_2/CH_4. Two models were generated by packing IL molecules in the mesopores of MCM-41 at different loadings (~21% and 42% by weight) and equilibrating the composite

structure using MD simulations. The accessible surface area of the models showed the trend MCM-41-IL1 > MCM-41 > MCM-41-IL2, whereas the void fraction was observed to follow MCM-41 > MCM-41-IL1 > MCM-41-IL2.

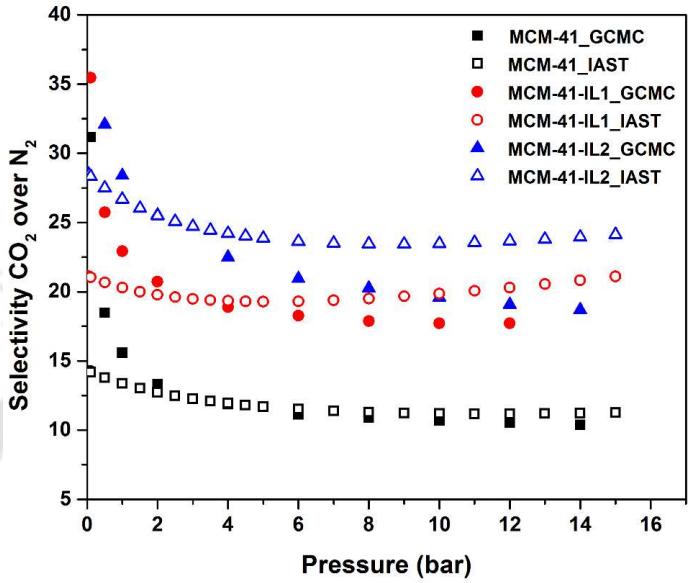

(a) CO_2/N_2

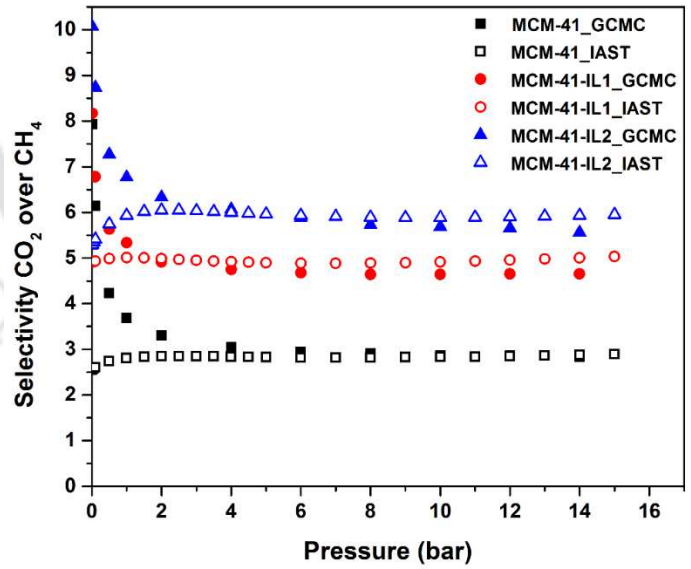

(b) CO_2/CH_4

Figure 5.15 Adsorptive selectivity of CO_2 over (a) N_2 and (b) CH_4 in the three adsorbent models, obtained from GCMC simulations and IAST calculations.

The adsorption of pure CO_2 in the model with 21% IL content, i.e. MCM-41-IL1, was observed to be significantly higher than that in pristine MCM-41. In the model with 42% IL content, i.e. MCM-41-IL2, pure CO_2 adsorption was slightly higher than that in pristine MCM-41 at pressures below 5 bar and lower above that. In the case of pure N_2 and CO_2 adsorption, although MCM-41-IL1 showed the highest adsorbed amounts, the enhancement with respect to pristine MCM-41 was small. The high adsorption loading of CO_2 in MCM-41-IL1 can be attributed to the larger accessible area and stronger interactions with the IL molecules. For the less polar N_2 and CH_4 (essentially nonpolar), the slight enhancement in loading in MCM-41-IL1 is primarily due to increased accessible area. In the case of MCM-41-IL2, favorable interaction between CO_2 and IL molecules results in higher CO_2 adsorption than pure MCM-41 at pressures below 5 bar. However, at higher pressures, the effect of interactions is offset by the lower accessible area and void fraction due to which saturation sets in leading to lower CO_2 adsorption than in pure MCM-41. The RDFs and spatial distribution maps of CO_2 show that in addition to the MCM-41 pore walls, CO_2 molecules are also distributed in the neighborhood of IL molecules. The simulation of binary CO_2/N_2 and CO_2/CH_4 mixtures revealed that the amount of CO_2 adsorbed is higher in IL-loaded MCM-41 models whereas the amounts of N_2 and CH_4 adsorbed were higher in the pristine MCM-41. Selectivity of CO_2 over N_2 and CO_2 over CH_4 was 50–100% higher in the IL-loaded MCM-41 models than in pure MCM-41. Although the amount of CO_2 adsorbed is higher in MCM-41-IL1, the selectivities are higher in MCM-41-IL2. Thus, modification of MCM-41 mesopores by impregnation of IL molecules can potentially improve the CO_2 separation behavior of mesoporous silica. The relative improvements in the amount of CO_2 adsorbed and CO_2 selectivity may be tuned by adjusting the loading of IL in the mesopores.

CHAPTER 6

CO_2 Adsorption and Separation on Zirconium-based MOFs

6.1 Introduction

Microporous metal organic frameworks (MOFs) are a relatively new class of porous materials that have received considerable attention in recent years as they show excellent potential for gas separation and storage. They possess several desirable properties such as high surface area, tunable pore size and available pore volume [147–150]. The ability to adsorb large amounts of gases at relatively low pressures makes the materials suitable for applications in gas storage. As the name suggests, MOFs consist of metal atoms or clusters coordinated by several organic linker groups, forming a three-dimensional ordered, porous network. Chemistry of inorganic clusters as well as organic linkers plays an important role in designing new MOFs suitable for applications of interest. Several new MOFs have been designed and synthesized for applications in gas separation and storage [151–156], drug delivery [157–161], biosensors for disease detection [162,163] , lithium ion battery [164] etc. Recently discovered zirconium-based MOFs, UiO-66/67/68 have received increased attention due to their remarkably high surface area, tunable pore size and most importantly, their structural stability at high temperatures [165,166]. Inorganic clusters/bricks forming UiO-series of MOFs, $Zr_6O_4(OH)_4(CO_2)_{12}$, have a coordination number of 12, the highest among the reported MOFs. 1,4-benzene-dicarboxylate (BDC), 4,4′ biphenyl-dicarboxylate (BPDC) and terphenyl dicarboxylate (TPDC) linkers are incorporated with the inorganic bricks to form UiO-66, UiO-67 and UiO-68 respectively [147,167].

Schaate et al.[168] were the first to synthesize and study zirconium-based single crystal MOFs by scanning electron microscopy, X-ray diffraction and argon sorption experiments. They also tuned the crystal size and particle size through addition of modulators and longer functionalized linkers during synthesis. Chavan et al. [147] studied the storage of hydrogen in zirconium-based UiO-66

and UiO-67 MOFs, and found the storage capacity to be high but below those of MIL-101, IRMOF-20 and MOF-177. Katz et al [169] reported a tailored method to synthesize a number of UiO-66 and UiO-67 derivatives with remarkable porosity and surface area. Bristow et al. [170] have developed a transferable forcefield for MOF-5, IRMOF-10, IRMOF-14, UiO-66, UiO-67, and HKUST-1 considering the framework to be flexible. Adsorption of xylene isomers on UiO-66 MOFs was studied by Granato et al. [171] using grand canonical Monte Carlo (GCMC) simulation. Ligand functionalization has been employed to appropriately tune the adsorption characteristics of UiO MOFs. Wang et al. [172] tuned the selective adsorption of CO_2 over CH_4 and N_2 through ligand functionalization during the UiO-67 synthesis process. Ko et al. [173] investigated the water uptake capacity of amine-functionalized UiO-67 at relatively very low pressures. Øien-Ødegaard et al. [174] synthesized UiO-67-Me and UiO-67-BN MOFs having higher stability to water and increased volumetric adsorption capacity for methane than UiO-67. Several studies have also investigated the separation of mixtures containing small gas molecules such as CO_2, CH_4, N_2 by MOFs. Karra et al. [175] focused on the separation of the polar CO from mixtures containing 95%, 50% and 5% CH_4 (a non-polar molecule) using Cu-BTC metal-organic framework. A molecular simulation investigation on Cu-BTC framework was carried out by Guteirrez-Sevillano et al. [146] using GCMC and molecular dynamics simulations to study the adsorption and diffusion of CO_2 and CH_4 mixtures. Zhang et al. [176] studied the separation of CO_2 from several gases (such as N_2, H_2, CH_4) through computational screening of MOFs having rht topology. They predicted the adsorption isotherms, selectivity, breakthrough curves and radial distribution functions (RDFs) for different atom sites inside the frameworks of Cu- TDPAT, PCN-61, -66, -68, NOTT-112, NU-111 and NU-110.

In the present work, molecular simulation has been used to investigate two different Zr-based MOFs, namely UiO-66 and UiO-67, in detail for adsorption and separation of several gases such as CO_2, CH_4, N_2, CO and their mixtures. Selectivity of CO_2 in binary gas mixtures such as CO_2/CH_4 and CO_2/N_2 has been studied over a wide range of pressures and temperatures using the GCMC technique. CO_2 selectivities were also computed using the ideal adsorbed solution theory (IAST) and compared with the GCMC results to better understand the real behavior of gas molecules inside the framework environment. Effect of pressure and temperature variation over a wide range on gas selectivity has been studied to better predict the operating conditions for application in gas separation. The adsorption of CO_2 has been investigated in detail by analyzing the RDFs of the adsorbed CO_2 molecules around different types of framework atoms (metal atom, oxygen, benzene group of organic linker) to determine the adsorbate distribution in the neighborhood of different atoms. Density profile of CO_2 around different framework species in the zirconium-based MOFs has also been examined to locate the availability of favorable sites. Thus, this work provides a comprehensive, comparative investigation of adsorption of CO_2, CH_4, CO and N_2, and separation of their binary mixtures in two Zr-based MOFs, UiO-66 and UiO-67.

6.2 Models and Methodology

6.2.1. MOF Structure

Optimized geometries for both the frameworks, UiO-66 and UiO-67, were taken from the work of Yang et al. [177]. Both UiO-66 and UiO-67 have a cubic unit cell having sides of length 20.978 Å and 27.094 Å respectively. Unit cell of UiO-66 was replicated two times in each direction (x, y and z) to construct the simulation box so that a cutoff radius of 12.5 Å for non-bonded interactions could be implemented. For UiO-67, a single unit cell was directly used as the simulation box. As

shown in Figure 6.1, both MOFs contain cages of two different sizes; UiO-67 contains larger cages due to the larger organic linkers present.

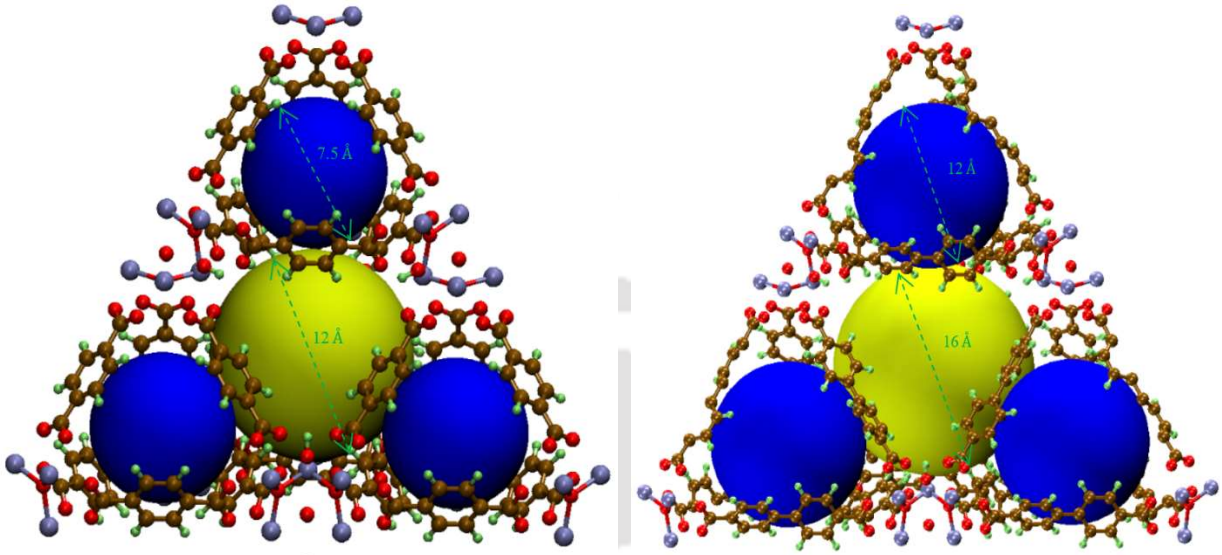

(a) (b)

Figure 6.1 Two different cages in (a) UiO-66 and (b) UiO-67.

6.2.2. Force field

In this work, the frameworks of the studied MOFs were assumed rigid and hence, bonded interactions (bond stretching, angle bending and dihedral interactions) were not considered for the framework atoms. The van der Waals and electrostatic adsorbate-adsorbate and adsorbate-adsorbent interactions were calculated as the sum of the Lennard-Jones (LJ) and Coulomb potentials given in equation (2.15) of section 2.1.2.

Coulomb interactions were calculated using the Ewald summation technique [58]. Non-bonded parameters for the MOFs were taken from the DREIDING force field [80] except zirconium for which LJ parameters were taken from the Universal force field (UFF) [178]. All the LJ-parameters for the framework atoms were scaled by a factor of 0.97 to obtain good agreement of simulation

data with experimental CO_2 loading in the low-pressure region (see Figure 6.4). CO_2 was modeled as a rigid linear molecule with three sites, one at each atom, and having a C–O bond length of 1.16 Å. LJ parameters and the corresponding partial charges at each site were taken from the elementary physical model (EPM2) developed by Harris and Yung [104]. Transferrable potentials for phase equilibria (TraPPE) [84] force field was used to model N_2 as a rigid molecule with three sites for non-bonded interactions and an N–N bond length of 1.1 Å. The sites are located at the two N atoms and the center of mass (COM) of the molecule, with partial charges assigned to each individual site. The COM of N_2 molecule was treated as a pseudo site for the calculation of electrostatic interactions only and was excluded in the calculation of LJ potential during simulation. We have used a three-site model for CO which was developed and validated by Martín-Calvo et al.[179] for CO adsorption on MOFs. CO was treated as a rigid molecule having a C–O bond length of 1.128 Å with the third site located at a distance of 0.6443 Å from the C atom (the other two sites are located at the respective C and O atoms). Similar to N_2, partial charges were assigned on all the three sites of the CO model whereas only two sites at C and O were considered for van der Waals interactions. TraPPE-United Atom (TraPPE-UA) force field by Martin and Siepmann [105] was used to model CH_4 as a single LJ interaction site. All the information regarding force field parameters for framework atoms as well as guest (adsorbate) molecules is shown in Table 6.1, Table 6.2 and Table 6.3.

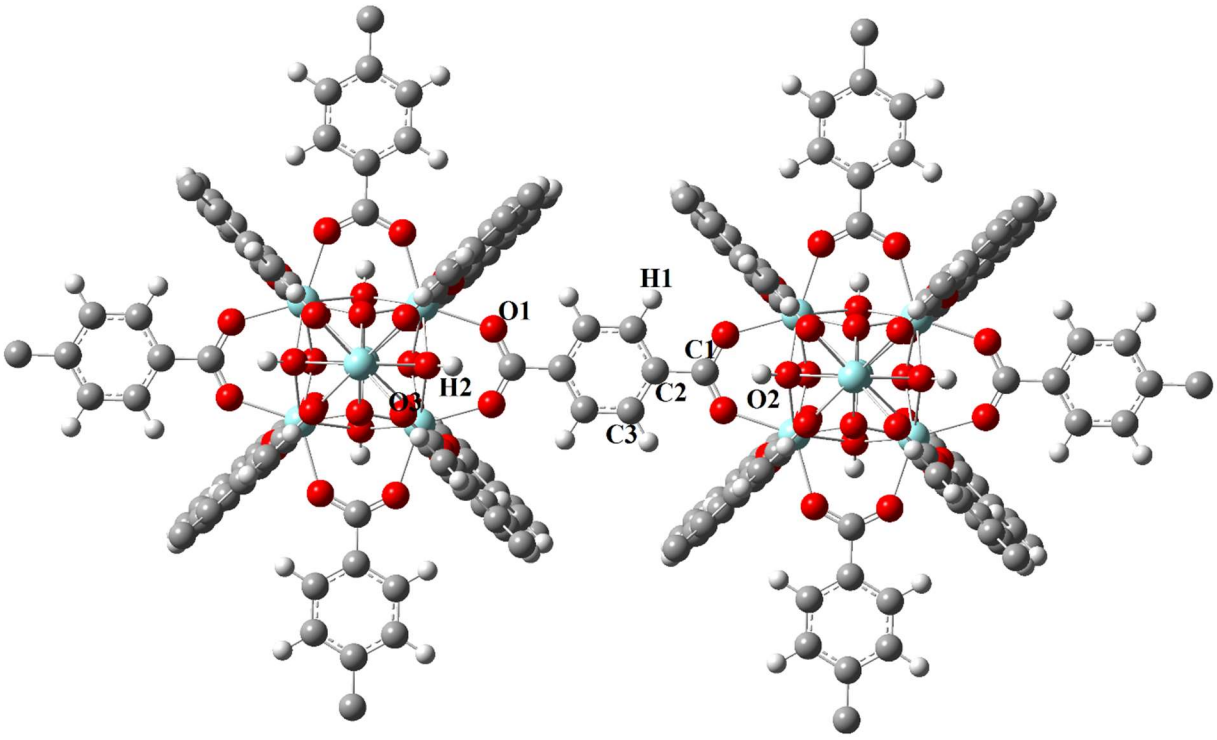

Figure 6.2 UiO-66 cluster and the respective atom types used (H atoms omitted on terminal methyl groups for clarity)

Table 6.1 Partial charges of different atom types in UiO-66, obtained after slight adjustment in the values of charges from CHELPG scheme

Type of atom	Zr	O1	O2	O3	H1	H2	C1	C2	C3
Partial charge	2.008	-0.582	-1.179	-0.741	0.127	0.495	0.625	-0.002	-0.121

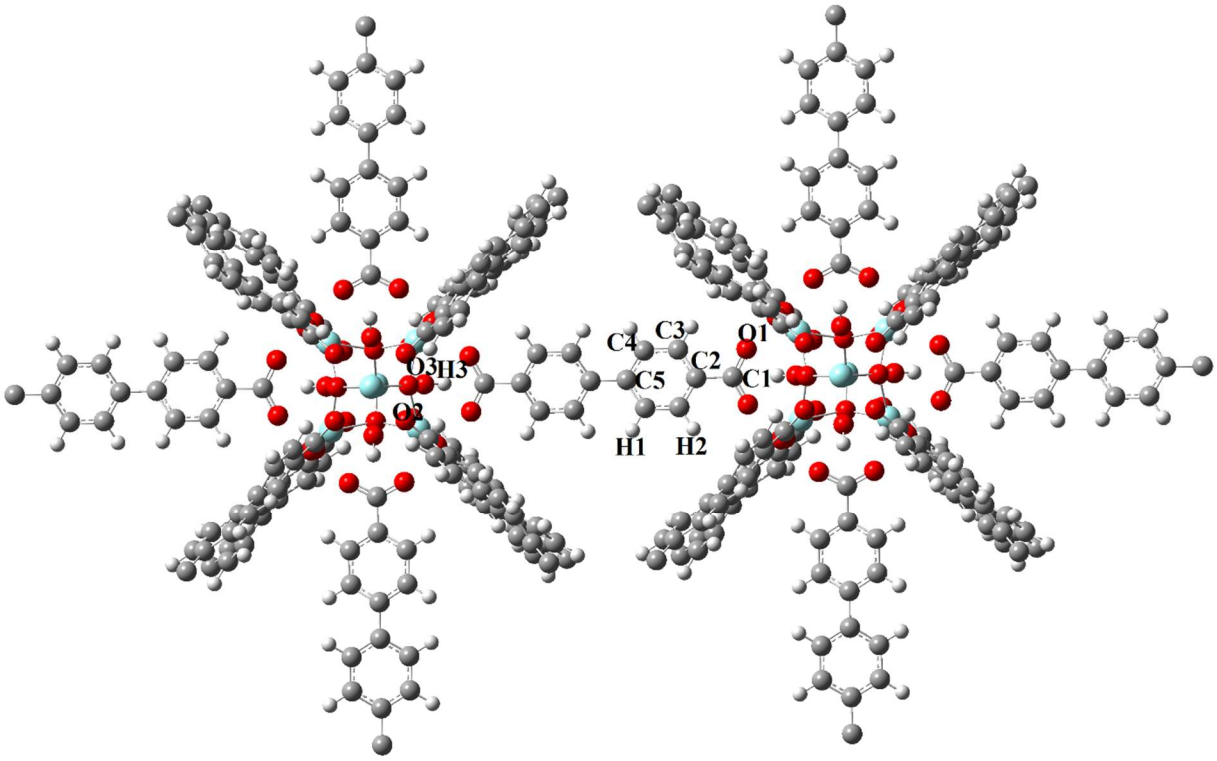

Figure 6.3 UiO-67 cluster and the respective atom types used (H atoms omitted on terminal methyl groups for clarity)

Table 6.2 Partial charges of different atom types in UiO-67, obtained after slight adjustment in the values of charges from CHELPG scheme

Type of atom	Zr	O1	O2	O3	H1	H2	H3	C1	C2	C3	C4	C5
Partial charge	1.876	-0.61	-0.723	-0.99	0.119	0.135	0.45	0.678	-0.011	-0.134	-0.138	0.072

Table 6.3 LJ potential parameter, charges and bond lengths in adsorbent and adsorbate molecules

Molecule	Site	$\sigma(\text{Å})$	$\varepsilon(K)$	$q(e)$	Bond length (Å)
UiO-66 & 67	Zr	2.6996749	33.680437		
	O	2.9421555	46.713357		
	H	2.7610274	7.4194621		
	C	3.3688003	46.420514		
CO_2	C	3.473	47.813	0.6040	1.152 (C-O)
	O	3.033	48.115	-0.3020	
N_2	N	3.310	36.000	-0.4820	1.1 (N-N)
	N(COM)	0.000	0.000	0.9640	
CH_4	CH_4	3.730	148.00	0.0000	
CO	C	3.636	16.141	−0.2424	
	O	2.979	98.014	−0.2744	1.128 (C-O)
	site			0.5168	0.6443 (C-site)

The Lorentz-Berthelot mixing rule was used to obtain the LJ parameters $\boldsymbol{\sigma_{ij}}$ and $\boldsymbol{\varepsilon_{ij}}$ for interaction between unlike species. Partial charges assigned on the guest molecules were taken from the corresponding force fields while those for the host (adsorbent) atoms were directly taken from the work of Yang et al. [177], obtained using density functional theory (DFT) calculations. Unrestricted B3LYP functional with 6-31G* basis set was applied to all atoms except the Zr metal atom for which LANL2DZ basis set was used. Dangling bonds from the cleaved portion of the MOF clusters were saturated with $–CH_3$ (methyl) groups. The MOF clusters for DFT calculations are shown in Figure 6.2 (for UiO-66) and Figure 6.3 (for UiO-67). The CHELPG charges thus obtained were modified slightly in order to maintain charge neutrality of the system so that the Ewald sum technique could be applied to calculate the electrostatic interactions. The different

framework atom types considered and the respective partial charges are listed in Table 6.1 (for UiO-66) and Table 6.2 (for UiO-67).

6.2.3. Grand Canonical Monte Carlo (GCMC) Simulations

GCMC simulations were used to compute the adsorption isotherms, where the chemical potential, volume and temperature of the system were maintained constant. Peng-Robinson equation of state was used to describe the non-ideal behavior of the gas molecules at high pressures. One million Monte Carlo cycles were carried out for system equilibration followed by another one million cycles for production run. Each cycle consists of N Monte Carlo steps where N represents the number of adsorbed gas molecules in the system. However, at low pressures where $N < 20$, 20 steps are considered in each cycle. For pure species, each step consisted of either a rotation, translation, insertion or a deletion move, carried out with equal probability. In the case of gas mixtures, apart from the aforementioned four types of moves, identity exchange moves [56,57] were also carried out with a probability of 5%. GCMC simulations give the absolute amount adsorbed whereas experimental results obtained from gravimetric analysis give excess amount adsorbed. Therefore, to compare with experimental results, all adsorption loading data obtained from GCMC simulations were converted to corresponding excess quantities using equation (2.36) of section 2.2.5. Heat of adsorption was calculated by energy/particle fluctuation at constant chemical potential in the grand canonical (constant μVT) ensemble using equation (2.32) provided in the section 2.2.4. All the adsorption simulations were carried out using the RASPA software package [55].

6.2.4. Isotherm Fitting and Ideal Adsorbed Solution Theory Calculations

Various mathematical models for describing adsorption behavior exist (such as the Langmuir model, Toth model etc.) that have been applied to fit the adsorption isotherms of gases on a variety of adsorbents [60,180]. In this work, a dual-site Langmuir (DSL) model was used to fit the simulated adsorption isotherms of the pure gases over UiO-66. The DSL model assumes the existence of two different energetically favorable adsorption sites and is expressed mathematically according to equation (2.29, 2.30 and 2.31) discussed in section 2.2.3(a). For UiO-67, the Langmuir model (single-site) given by equation (2.27) of section 2.2.3(b) was used to fit the isotherms of the pure gases.

Ideal adsorbed solution theory (IAST) by Myers and Prausnitz [64] permits the theoretical prediction of multi-component adsorption isotherms and selectivities from adsorption equilibrium data of pure species. The adsorbed gas mixture is treated as an ideal solution and no energetic heterogeneity of adsorption sites is assumed to be present. The parameters of the Langmuir/DSL model are determined by fitting the model to the pure species adsorption data (obtained from GCMC simulations). The resulting model equation is used to evaluate the integral to find the adsorbed phase mole fractions at any given temperature, pressure and bulk gas composition. Detailed description for calculating IAST have provided in the section 2.2.6.

6.3 Results and discussion:

6.3.1. Pure Gas Adsorption:

GCMC simulations were carried out to investigate the potential of UiO-66 and UiO-67 for gas storage and separation. In particular, the adsorption of pure CO_2, CH_4, CO, N_2 and the mixtures CO_2/N_2 and CO_2/CH_4 was studied in detail. Surface area of the adsorbents, calculated using

Materials Studio 7.0 software package [63], by rolling a spherical probe of diameter 3.6 Å on the surface, was found to be 1096.65 m^2/g for UiO-66 and 2982.19 m^2/g for UiO-67. The calculated surface areas are in good agreement with reported experimental values of 1067 m^2/g [35] and 2500 m^2/g [181] for UiO-66 and UiO-67 respectively. The simulated CO_2 isotherms for adsorption on UiO-66 and UiO-67 compare well with experimental values, as shown in Figure 6.4 where a comparison with the experimental isotherms of Zhang et al. [182] (for UiO-66) and Wang et al. [172] (for UiO-67) is shown.

The adsorption of pure CO_2, CH_4, CO and N_2 on UiO-66 was simulated at four different temperatures (in the range 273–348 K); the corresponding adsorption isotherms are shown in Figure 6.5. Adsorption of all the gases decreases with increasing temperature, as expected. The DSL model was used to fit the adsorption isotherms for all the gases at the four temperatures. Very good match is obtained between the simulation data and the respective Langmuir fits, shown as solid curves in Figure 6.5(a)–(d). The fitted parameters of the dual-site Langmuir model are listed in Table 6.4 and have been used for calculating adsorption isotherms of binary gas mixtures using IAST.

At all the temperatures considered and over the entire pressure range (up to 20 bar), CO_2 adsorption is the highest among the four gases followed by CH_4, CO and N_2. Adsorption of CO_2 is especially more pronounced at low pressures ($\leq$ 1 bar) compared to the other gases. The simulated adsorption isotherms for adsorption of CO_2, CH_4, CO and N_2 on UiO-67 are shown in Figure 6.5(a)–(d).

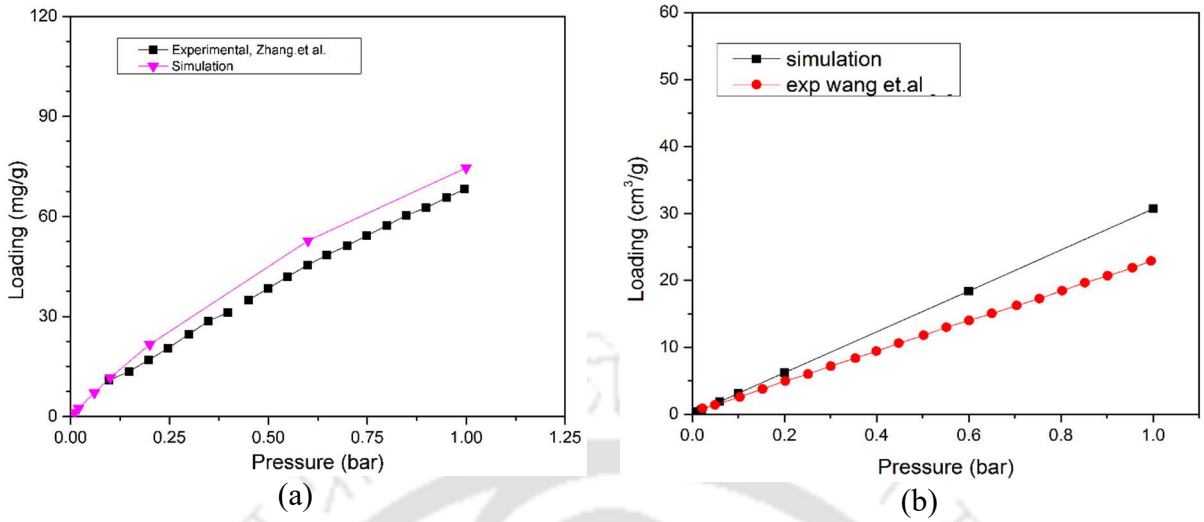

Figure 6.4 Comparison of simulated CO_2 adsorption isotherm on (a) UiO-66 and (b) UiO-67 (experiment Zhang et al. [182] and Wang et al. [172])

The simulated isotherms were fitted with the Langmuir model (single site) for all gases at the four temperatures. The Langmuir fits are shown as solid curves in Figure 6.6(a)–(d) and the corresponding Langmuir model parameters are tabulated in Table 6.4. The adsorption amounts of different gases on UiO-67 over the entire pressure and temperature range considered follows the trend $CO_2 > CH_4 > CO > N_2$, similar to that observed for UiO-66. The higher adsorption of CO_2 can be attributed to substantial contributions from both dispersion and electrostatic interactions with the MOF framework. In contrast, CH_4 is non-polar and hence does not have explicit Coulombic interactions whereas dispersion interactions for CO are weaker. CO_2 uptake capacity

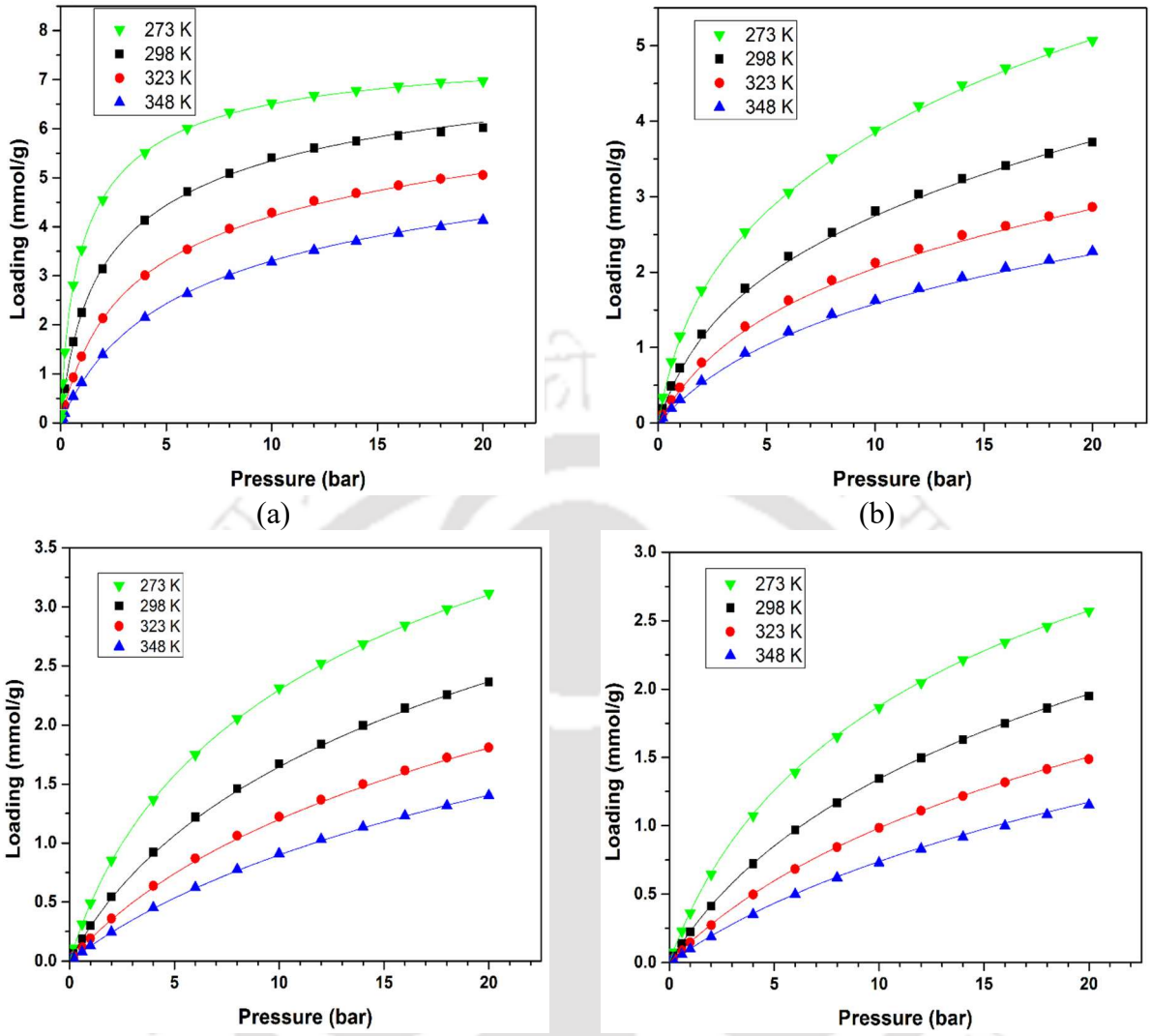

Figure 6.5 Simulated adsorption isotherm for pure (a) CO_2, (b) CH_4, (c) CO and (d) N_2 in UiO-66 at four different temperatures (lines represent dual site Langmuir isotherm fitted for all the isotherms).

at low pressures is high for UiO-66 (see Figure 6.5(a)) because of narrow window size and smaller cage diameter, compared to UiO-67. However, at higher pressures the amount of gas adsorbed is significantly larger for UiO-67 due to the larger surface area of UiO-67. The enhancement in adsorption loading (over that for UiO-66) is particularly pronounced for CO_2 where ~250% increase is observed at 298 K and 20 bar (see Figure 6.5(a) and Figure 6.6(a)). The other three

gases show a corresponding increase of ~150% at the same temperature and pressure. Isosteric heats of adsorption of the pure gases in UiO-66 and UiO-67 at 298.15 K are shown in Figure 6.7. For all gases, higher values of isosteric heats were observed for adsorption in UiO-66, because of smaller cages and narrow window size. Further, in both MOFs, the isosteric heat followed the order CO_2>CH_4>CO>N_2 reflecting the relative strengths of interactions of the different gases with the MOF framework. CO_2 shows a higher isosteric heat of adsorption than the other gases in both MOFs due to the stronger dispersion and electrostatic interactions with the host framework.

We have investigated the adsorption of CO_2 in UiO-66 and UiO-67 in detail by identifying the location of adsorbed gas molecules in the MOF framework relative to the positions of the metal atoms and linker groups. Density contour maps and isosurface plots of the framework with adsorbed gas molecules have been generated to provide qualitative information about adsorption sites and preferred adsorbate locations. RDF of the adsorbed CO_2 molecules with respect to metal and linker atoms of the framework have been calculated to obtain a more quantitative description of the distribution of adsorbate molecules around the different adsorption sites of the framework. All the RDFs have been calculated using equation (2.19) provided in the section 2.1.3.

Density contour plots and isosurface plots for pure CO_2 adsorbed on UiO-66 and UiO-67 are shown in Figure 6.8 and Figure 6.9 respectively. The density contour plots show the adsorbate number density on a planar surface, obtained by taking a slice of the simulation box at a particular location. The 3D isosurface plots give a visual three-dimensional representation of the different locations in the simulation box where the adsorbate molecules are present. Figure 6.8(a) and (b) show the density contour plots of CO_2 in UiO-66 on planes perpendicular to the x-axis, cutting at one-third

and half of the simulation box length in the x-direction; similar density plots for CO_2 adsorption on UiO-67 are shown in Figure 6.8(c) and (d).

Table 6.4 Fitted parameters for pure components adsorption in UiO-66 and UiO-67

Model Parameters	CO_2 Coefficient (Std. Error)	CH_4 Coefficient (Std. Error)	CO Coefficient (Std. Error)	N_2 Coefficient (Std. Error)
UiO-66 (Dual-Site Langmuir Model)				
N_1^{max}(mmol g^{-1})	3.5511 (0.10)	7.00 (0.184)	3.93 (0.08)	3.432 (0.09)
N_2^{max}(mmol g^{-1})	4.0542 (0.11)	2.227 (0.064)	1.3906 (0.124)	1.1474 (0.141)
β_{10}(bar^{-1})	3.66E-07 (8.9E-8)	3.09E-06 (4.0E-07)	1.78E-05 (2.6E-06)	2.42E-05 (4.07E-06)
β_{11}(bar^{-1})	3702.65 (65.80)	2570.987 (29.39)	2153.866 (27.71)	2053.651 (29.78)
β_{20}(bar^{-1})	6.45E-05 (8.87E-6)	0.0004 (4.92E-05)	0.0005 (8.0E-05)	6.00E-4 (1.0E-04)
β_{21}(bar^{-1})	2848.364 (38.67)	2004.579 (30.51)	1730.76 (35.26)	1641.122 (40.80)
UiO-67 (Langmuir Model)				
N_1^{max}(mmol g^{-1})	28.68 (0.60)	17.33 (0.14)	12.42 (0.23)	10.24 (0.188)
β_{10}(bar^{-1})	1.1E-5 (9.6E-7)	8.08E-5 (1.5E-6)	1.09E-4 (3.59E-6)	1.373E-4 (3.07E-6)
β_{11}(bar^{-1})	2544.3 (33.15)	1753.1 (7.38)	1527.4 (12.34)	1443.3 (9.06)

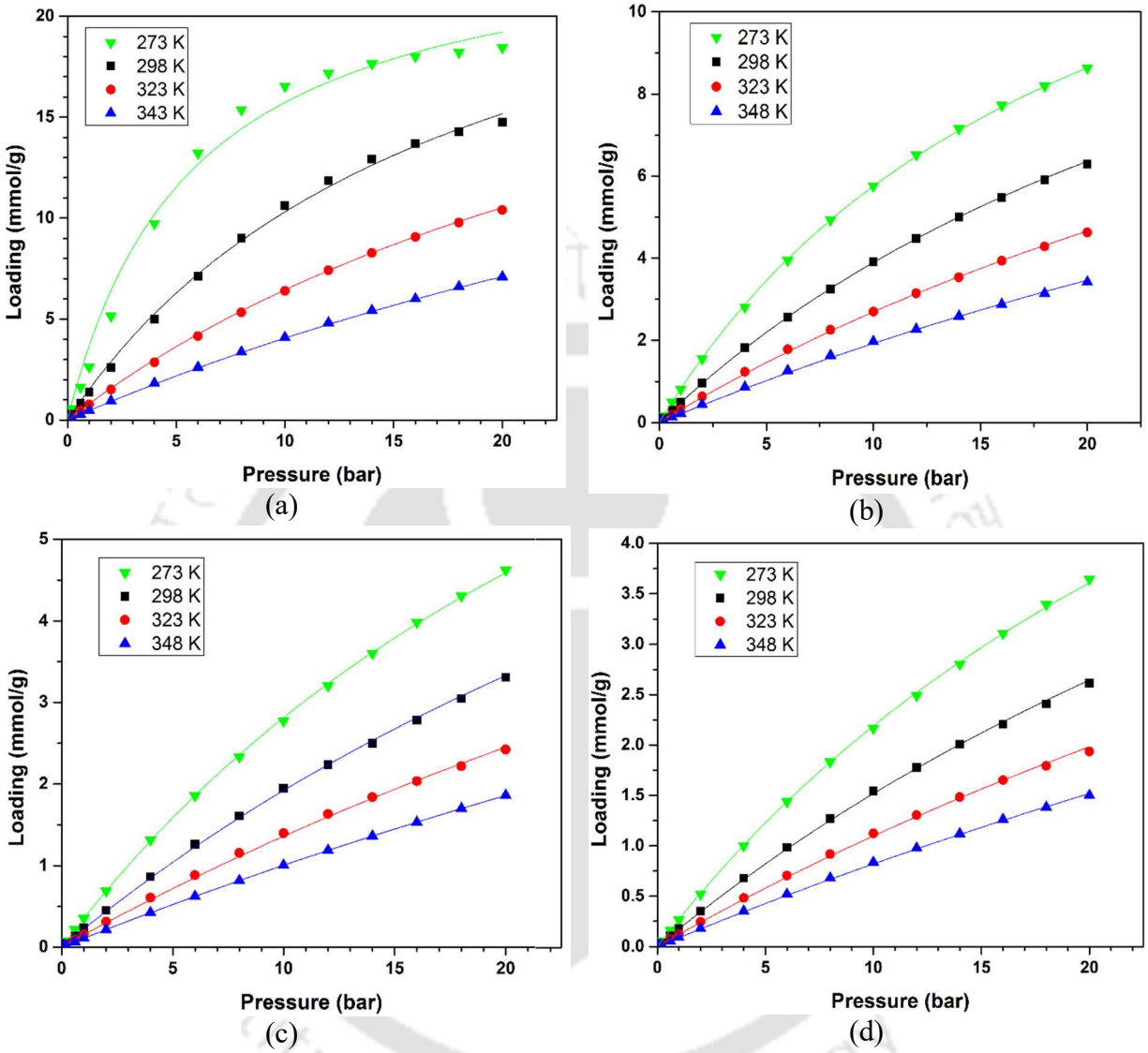

Figure 6.6 Simulated adsorption isotherm for pure (a) CO_2, (b) CH_4, (c) CO and (d) N_2 in UIO-67 at four different temperatures (lines represent Langmuir model fitted for all the isotherms).

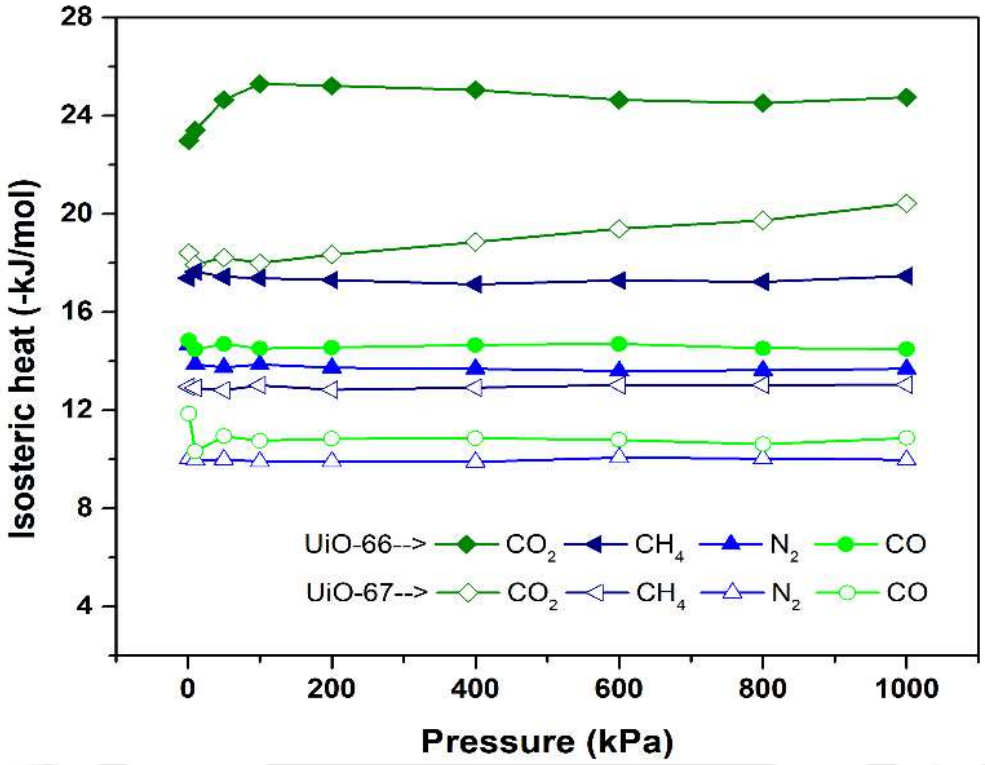

Figure 6.7 Isosteric heats of adsorption of pure gases in UiO-66 (filled symbols) and UiO-67 (open symbols).

The 3D isosurface plots of the guest CO_2 molecules in the MOFs at two different pressures are shown in Figure 6.9. The density contour and isosurface plots have been constructed by considering the location of the adsorbate CO_2 molecules in the MOF framework over 100 snapshots at a particular temperature and pressure. These plots reveal that the CO_2 molecules preferentially adsorb near the organic linkers of the MOF framework. Further, for both UiO-66 and UiO-67, more adsorption takes place in the smaller, outer cages of the frameworks than the larger, central cage. In fact, at low pressures (~10 kPa), CO_2 adsorption almost entirely takes place near the organic linkers in the outer cages (see Figure 6.9(a) and (c)).

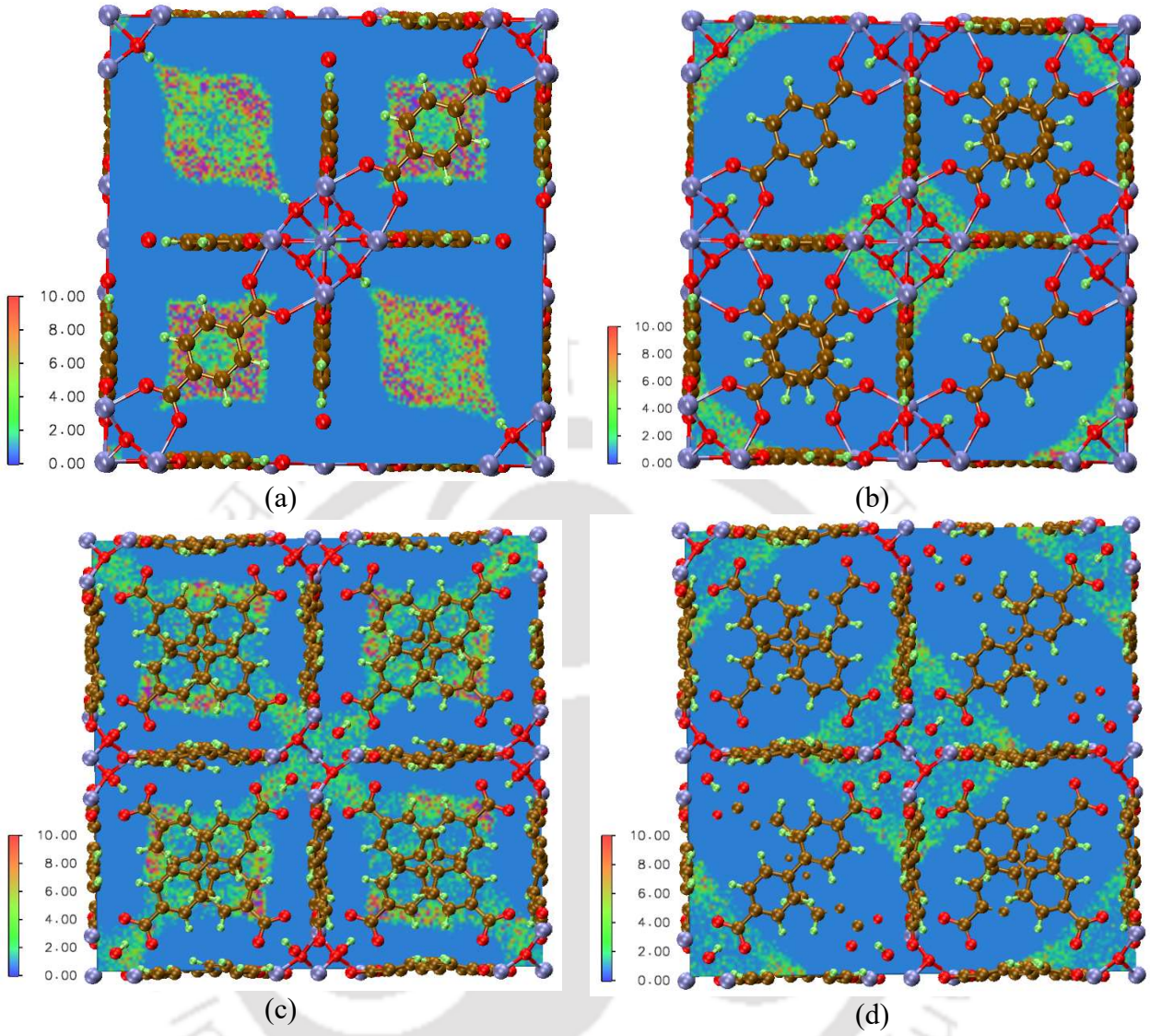

Figure 6.8 Density contour plots of CO_2 molecules in UiO-66 at 1 bar and 298 K onto (a) a plane perpendicular to the x-axis and cutting at 0.34*L_x, and (b) a perpendicular plane cutting the x-axis at 0.50*L_x, where L_x is the dimension of the unit cell in the x-direction. (c) and (d) represent the density contour plots of CO_2 in UiO-67 on planes cutting the x-axis at 0.34*L_x and 0.50*L_x, respectively at the same conditions.

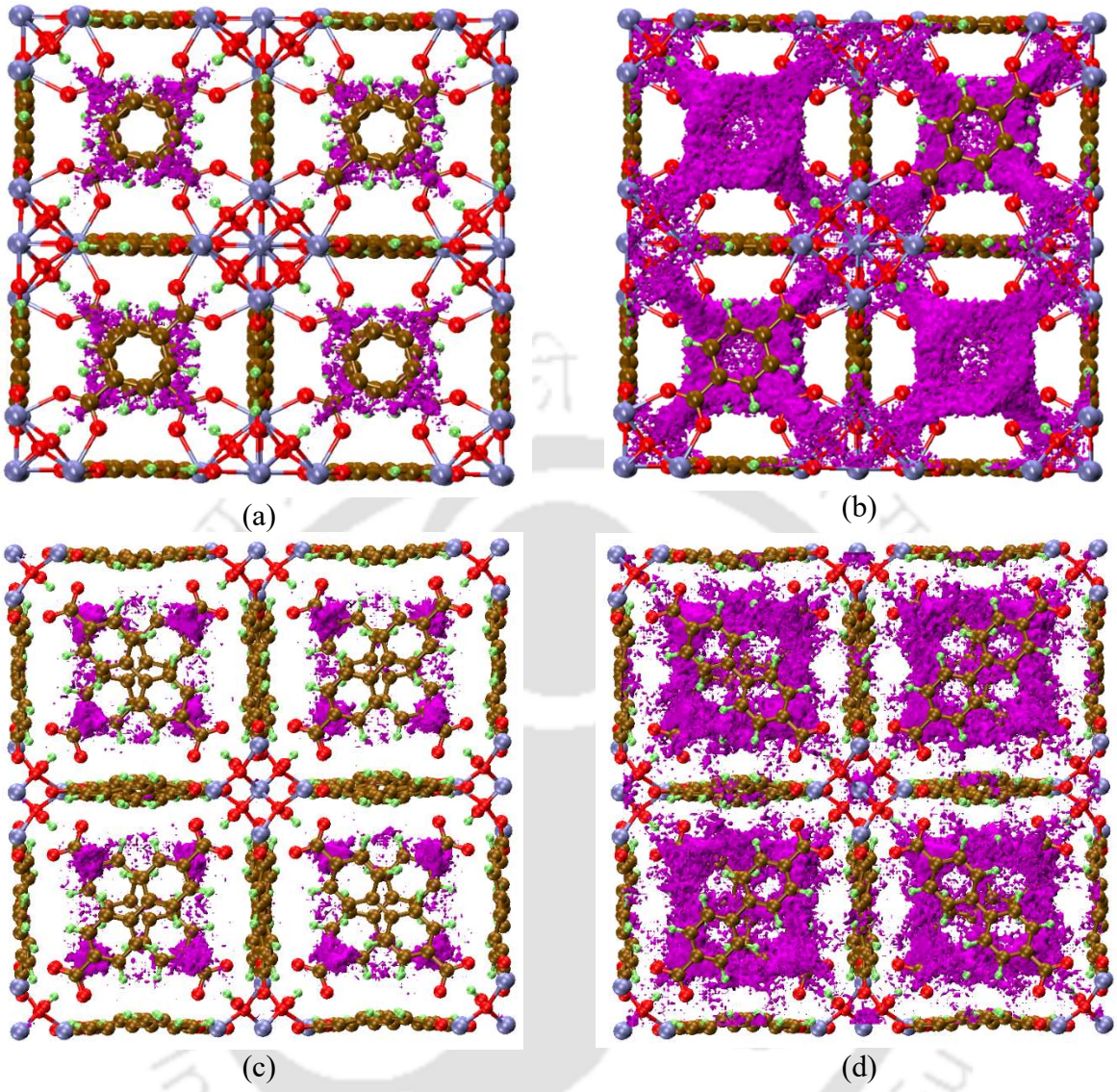

Figure 6.9 3D isosurface plots for CO_2 guest molecules inside UiO-66 framework at (a) 10 kPa and (b) 100 kPa, and inside UiO-67framework at (c) 10 kPa and (d) 100 kPa. All plots are for adsorption at 298 K.

RDFs were calculated for pairs of host-guest atoms as well as host-host atoms at a temperature of 298 K and pressure of 1 bar, as shown in Figure 6.10 (for UiO-66) and 9 (for UiO-67). The host-guest RDFs for CO_2 in UiO-66 are plotted in Figure 6.10(a), where the distribution of CO_2 molecules around the C and O atoms of the organic linker and the metal (Zr) atom of the framework is shown. The RDFs reveal that CO_2 molecules preferentially adsorb near the carbon atoms of the

organic linkers (i.e., the benzene rings), as evident from the peak at ~4–4.5 Å. In contrast, the Zr-CO_2 RDF does not show the presence of any CO_2 molecules up to a distance of 6 Å from the Zr sites whereas the O-CO_2 RDF only shows substantial peaks at distances greater than 7 Å. The guest-guest (i.e., CO_2-CO_2) RDFs for CO_2 molecules adsorbed in UiO-66 show a strong peak at ~4–4.5 Å (see Figure 6.10(b)), which corresponds to the average C-C separation between neighboring adsorbed CO_2 molecules. The host-guest RDFs for UiO-67 in Figure 6.11(a) show the CO_2 molecules to be preferentially distributed closer to the C atoms of the organic linkers than the Zr atom sites. The first peak of the C-CO_2 RDF is located at ~4–4.5 Å, similar to that observed for UiO-66 (see Figure 6.10 (a)), whereas that of the Zr-CO_2 RDF is located at ~6.5 Å. In Figure 6.11(b), the CO_2-CO_2 RDFs of the CO_2 molecules adsorbed in UiO-67 show a strong first-neighbor peak at ~4–4.5 Å. Due to the larger cages of UiO-67, a weak second-neighbor peak at ~7–8 Å is also visible.

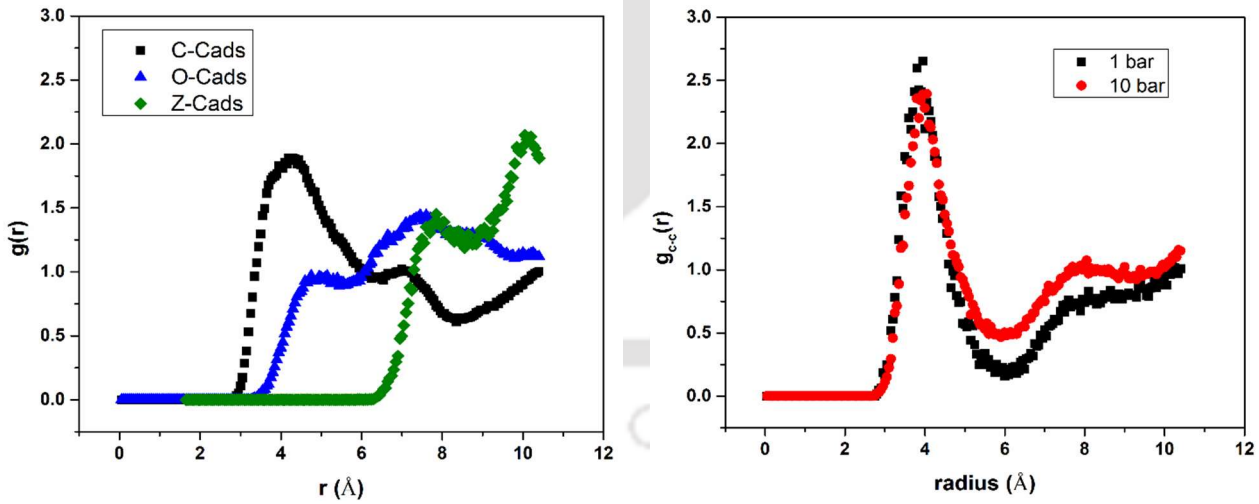

(a) (b)

Figure 6.10 Radial distribution function for (a) host-guest species (guest: CO_2 center of mass 'Cads', host: UiO-66 framework atoms, i.e., C, O, Zr), and (b) guest-guest species.

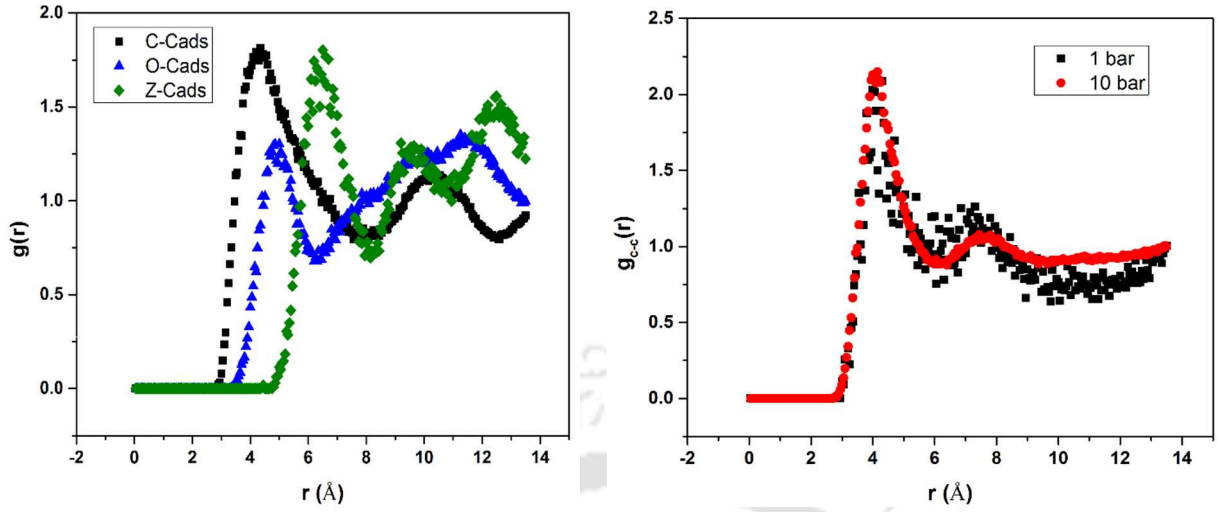

(a) (b)

Figure 6.11 Radial distribution function calculated for (a) host-guest species (guest: CO_2 center of mass 'Cads', host: UiO-67 framework atoms, i.e., C, O, Zr), and (b) guest-guest species.

6.3.2. Binary Mixture Adsorption

GCMC simulations were carried out to study the adsorption behavior of CO_2/CH_4 and CO_2/N_2 binary mixtures in UiO-66 and UiO-67 at two molar compositions for both gas mixtures (equimolar and 15:85), at three different temperatures viz. 273.15 K, 298.15 K and 323.15 K. The adsorption isotherms obtained from GCMC simulations of equimolar mixtures at two temperatures (298.15 K and 323.15 K) are shown in Figure 6.12 (for CO_2/CH_4) and Figure 6.13 (for CO_2/N_2). For both mixtures, the amount of CO_2 adsorbed in both UiO-66 and UiO-67 is higher than the other component over the entire pressure range and at both temperatures (298.15 K and 323.15 K). At low to moderate pressures, the amount of CO_2 adsorbed in UiO-66 is higher than that in UiO-67 for all the cases considered due to the smaller cages and channels in UiO-66, resulting in stronger host-guest interactions. However, at high pressures the CO_2 isotherms in UiO-66 and UiO-67 show a crossover, as the amount of CO_2 adsorbed becomes higher in UiO-67 due to the larger surface area available, whereas CO_2 adsorption in UiO-66 approaches saturation. Similar

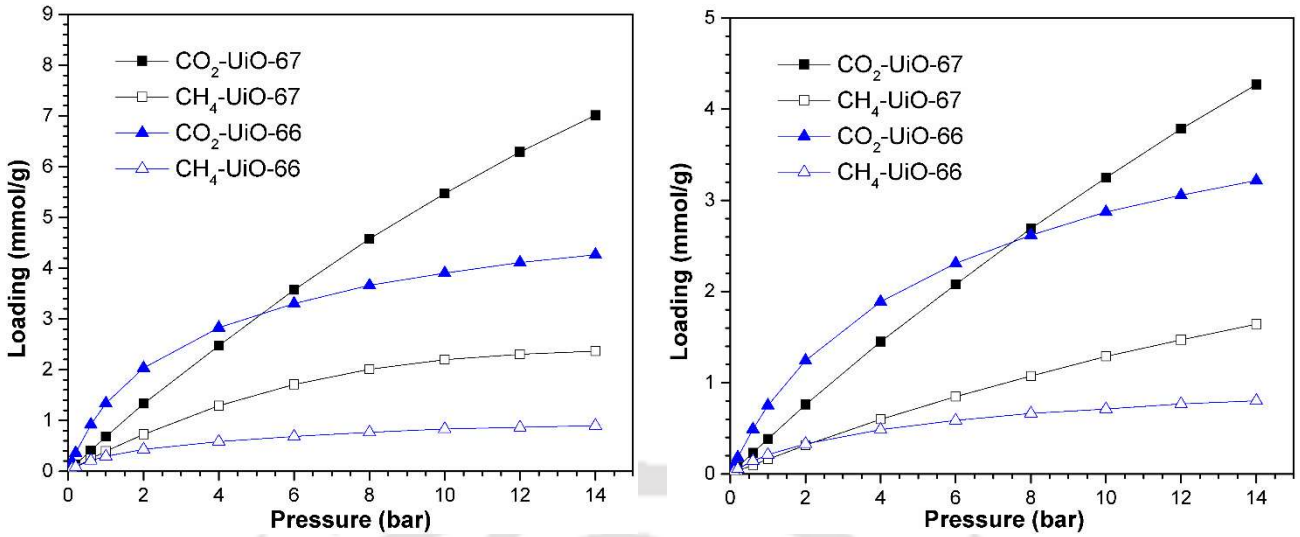

Figure 6.12 Simulated adsorption isotherms of equimolar CO_2-CH_4 binary mixture in UiO-66 and UiO-67 at (a) 298.15 K and (b) 323.15K (lines are drawn as a guide to the eye).

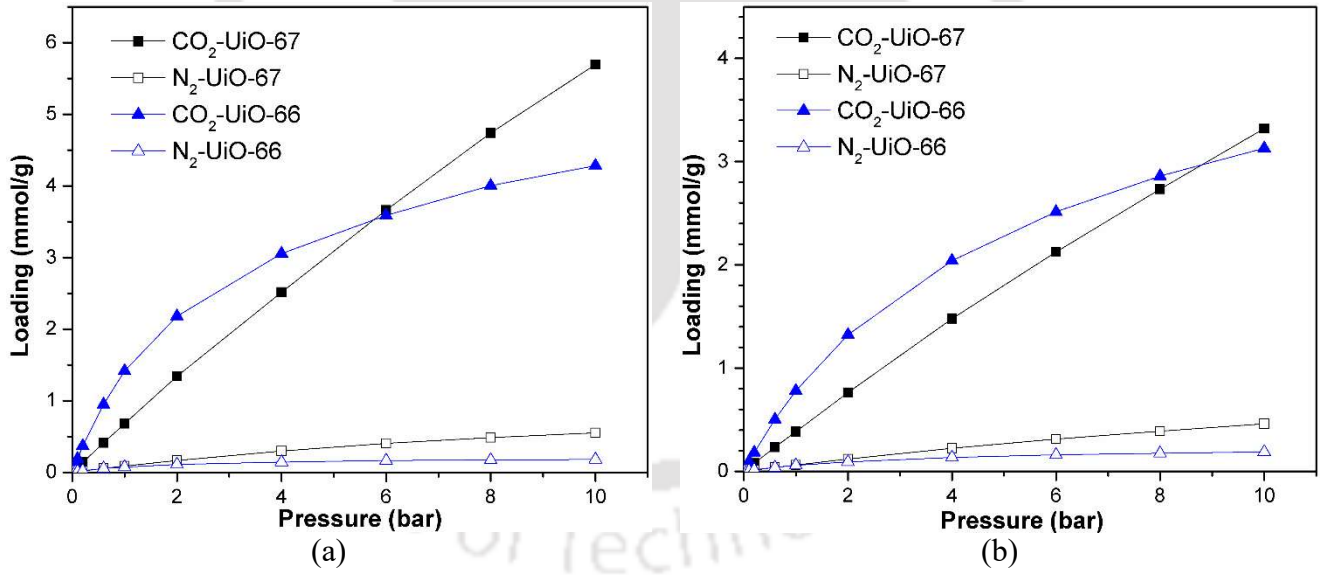

Figure 6.13 Simulated adsorption isotherms of equimolar CO_2-N_2 binary mixture in UiO-66 and UiO-67 at (a) 298.15 K and (b) 323.15K (lines are drawn as a guide to the eye).

crossover is also observed in the isotherms of CH_4 and N_2, albeit at lower pressures than for CO_2. Adsorption simulations of 15:85 CO_2/CH_4 and CO_2/N_2 gas mixtures were also carried out and the corresponding isotherms are shown in Figure 6.14 and Figure 6.15 respectively.

Binary selectivities of CO_2 over CH_4 and N_2 were calculated using equation (2.41), as discussed in section 2.2.7. Selectivites obtained from both GCMC simulations and IAST calculations at different temperatures are shown in Figure 6.16 (for CO_2/CH_4) and Figure 6.17 (for CO_2/N_2) for mixtures having 15:85 molar ratio (15% CO_2 and 85% other component in bulk gas phase). From Figure 6.16(a) it is evident that selectivity of CO_2 over CH_4 in the UiO-66 framework increases with pressure at low to moderate pressures. However, at high pressures, as the adsorption approaches saturation, the selectivities tend to become constant. The CO_2/CH_4 selectivities in UiO-67, shown in Figure 6.16(b), are lower than those in UiO-66 and show relatively less variation over the pressure range explored.

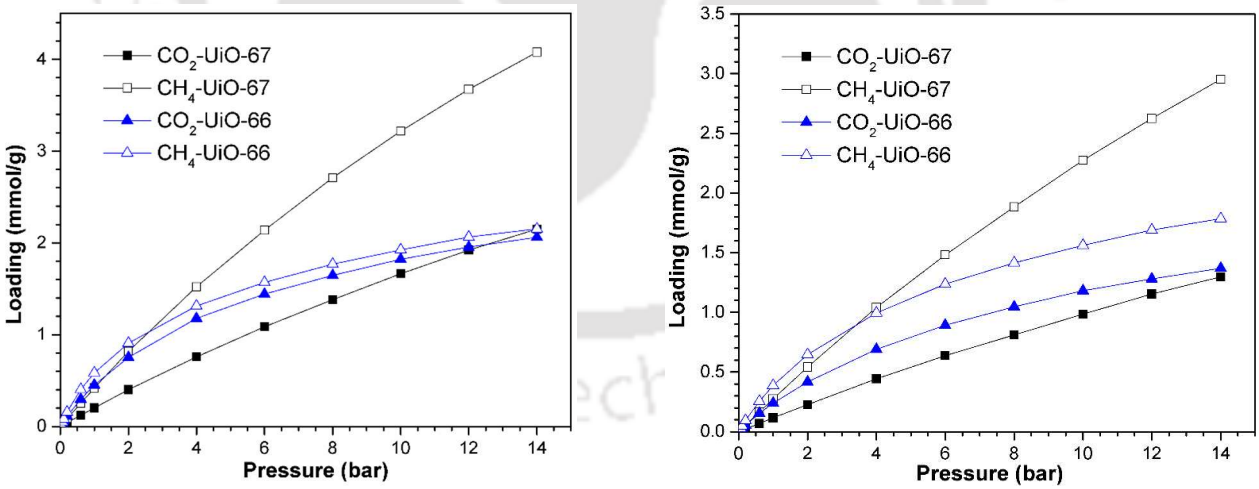

Figure 6.14 Simulated adsorption isotherms of CO_2-CH_4 binary mixture at 15:85 molar ratio in UiO-66 and UiO-67 at (a) 298.15 K and (b) 323.15 K (lines are drawn as a guide to the eye).

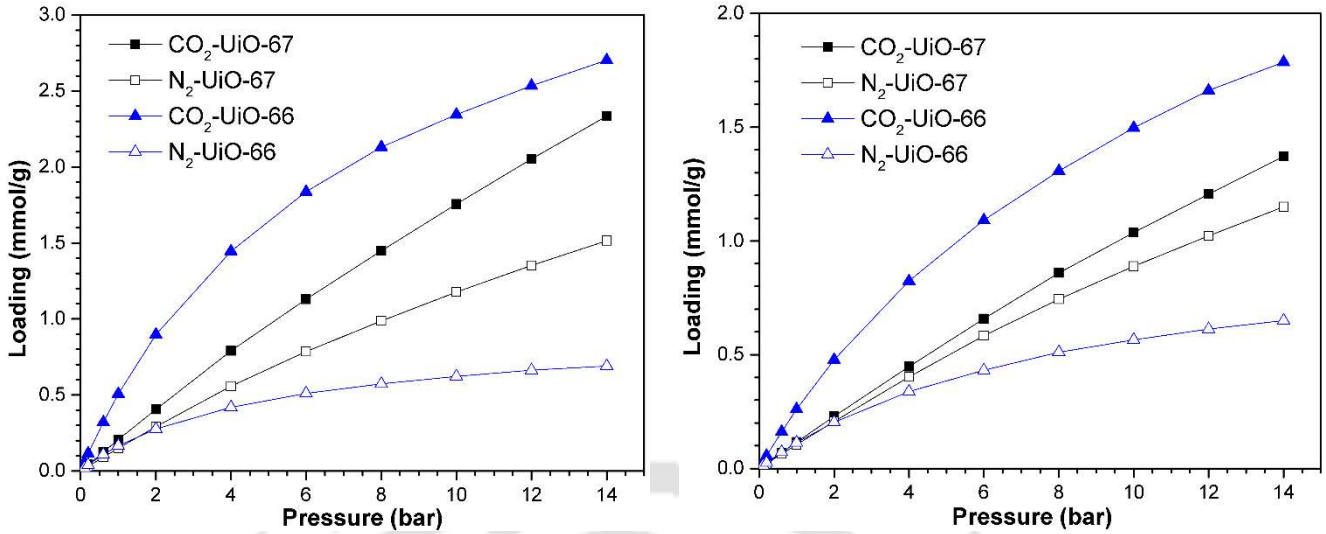

Figure 6.15 Simulated adsorption isotherms of CO_2-N_2 binary mixture at 15:85 molar ratio in UiO-66 and UiO-67 at (a) 298.15 K and (b) 323.15 K (lines are drawn as a guide to the eye).

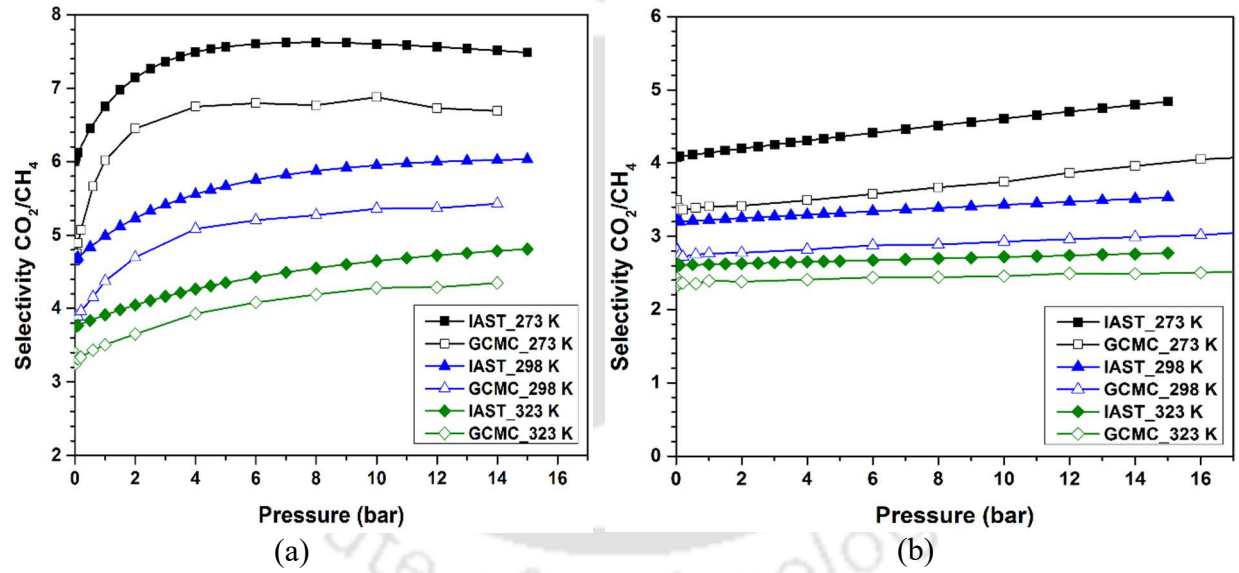

Figure 6.16 Selectivity of CO_2 over CH_4 in CO_2/CH_4 mixtures at 15:85 molar ratio in (a) UiO-66 and (b) UiO-67 (lines are drawn as a guide to the eye).

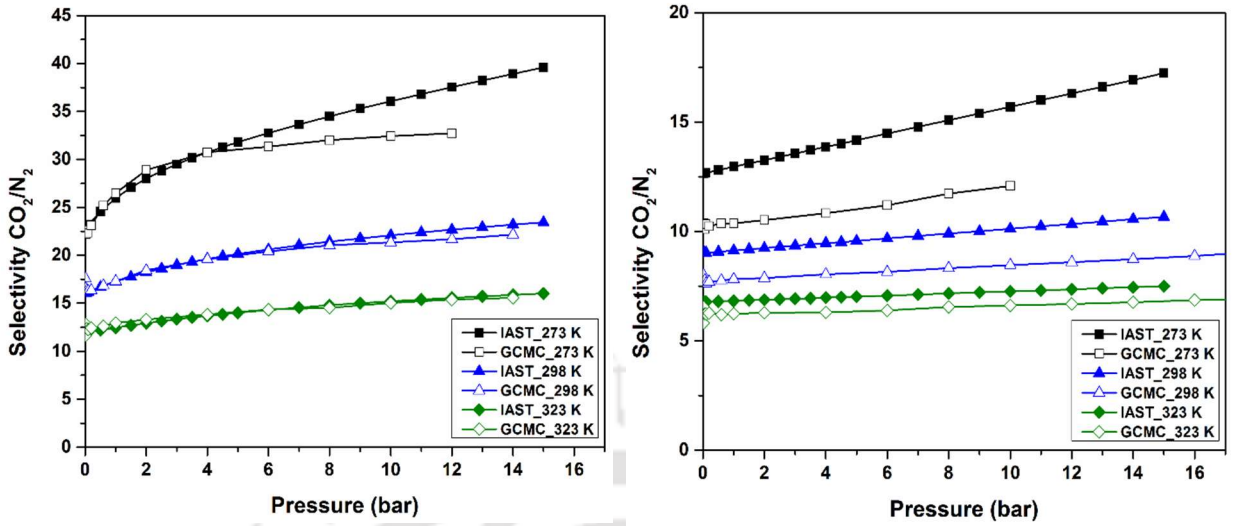

Figure 6.17 Selectivity of CO_2 over N_2 in CO_2/N_2 mixtures at 15:85 molar ratio in (a) UiO-66 and (b) UiO-67 (lines are drawn as a guide to the eye).

Figure 6.17(a) and (b) show that the selectivity of CO_2 over N_2 in UiO-66 is much higher (twice or more) than that in UiO-67 at all the temperatures studied. The smaller cages in UiO-66 provide more confinement and hence stronger interactions (for CO_2 compared to N_2) resulting in higher CO_2/N_2 selectivities than in UiO-67. The binary selectivities for both mixtures in both adsorbents decrease with increasing temperature as the effect of the gas-framework interactions becomes less pronounced with increasing temperature. The selectivities obtained from GCMC simulations and IAST calculations for both CO_2/CH_4 and CO_2/N2 mixtures show similar trends, and in general are in good agreement. The selectivities for equimolar CO_2/CH_4 and CO_2/N_2 mixtures were also calculated (not shown here) and were found to be similar to those for the 15:85 mixtures.

6.4 Conclusions

The simulated adsorption isotherms of pure CO_2 on UiO-66 and UiO-67, using LJ interaction parameters for the framework from DREIDING and Universal force fields with slight

modification, showed good agreement with experimental data. Simulation of pure gas adsorption of CO_2, CH_4, CO and N_2 in UiO-66 and UiO-67 showed that the amount of gas adsorbed follows the order $CO_2 > CH_4 > CO > N_2$ in both the MOFs at all the temperatures and pressures studied. At low pressures, amount of gas adsorbed is higher in UiO-66 due to smaller cages and channels leading to stronger interactions. Consequently, the isosteric heats of adsorption were also higher in UiO-66 and followed the order $CO_2 > CH_4 > CO > N_2$. However, at higher pressures, storage capacity of UiO-67 was observed to be higher due to the larger cages and higher surface area. The density contour plots and RDFs reveal that CO_2 molecules preferentially adsorb near the carbon atoms of the organic linkers. Further, for both UiO-66 and UiO-67, more adsorption takes place in the smaller, outer cages of the frameworks than the larger, central cage. Adsorption simulations of binary mixtures show that both MOFs are more selective towards CO_2 over CH_4 and N_2, with the CO_2 selectivity almost twice as high in UiO-66 than in UiO-67 because of the narrow window size and smaller cages in UiO-66. The binary selectivities decrease with increasing temperature as the effect of the differing strengths of interactions of the adsorbate gases with the framework weakens at higher temperatures. Selectivities calculated using IAST show similar trends and are in reasonably good agreement with those obtained from GCMC simulations.

CHAPTER 7

Effect of Functional Groups on CO_2 Loading and Selectivity in Functionalized Cu-BTC MOFs

7.1 Introduction

Industrial effluent gases like CO_2, CO, H_2S are considered to be very hazardous for the environment and matter of concern for the current research field. Metal organic frameworks (MOFs) are considered to be promising material for the application in separation of the hazardous gases from the industrial effluents. In addition, Methane from the natural gas where purity of methane gas is highly desirable, MOFs are also considered to be potentially applicable material for separation and purification of methane gas present in the mixture with traces of CO_2, N_2 and C_2H_6 gas [107,146,175,183,184]. Since traces of heavier gases like ethane, propane as well as lighter gases like CO_2, N_2 seriously reduces the combustion efficiency of natural gas, which mainly contains 95% of CH4 gas [110,185]. While, CO_2 selectivity towards N_2 are considered to be most important factor in flue gas separation and selective separation of CO_2 is desirable for reducing the risk of global warming [186]. Since MOFs have been considered to be promising material for the separation and storage of lighter alkanes as well as other effluent gases. Several other applications like loading of targeted drug in drug delivery system [158,159], acts as a biosensors [162,187], as an electrode in Li-ion battery [164], adsorption of Volatile Organic Compounds (VOC) [189,190] etc. were also explored and allows to investigate the MOFs at its atomistic level. Chui et al. [191] were first to synthesize the HKUST-1, a highly porous material with coordination formula [Cu3(TMA)2(H2O)3]*n* (where TMA is benzene 1,3,5- tricarboxylate) with 80% yield value of three dimensional channels comprising a pore diameter of 1 nanometer (nm) and a 40 % porosity in the solid was found. Majano et al. [192] studied the effect upon changing the synthesis protocol like molar composition of DMF/EtOH/H_2O to dimensionality of HKUST-1. Lin et al. [193] prepared and characterized the HKUST-1 for the application of hydrogen storage. Karra et

al. [194] studied CO_2, CO and N_2 adsorption on Cu-BTC, IRMOF-1, IRMOF-3 and Zn2[bdc]2-[dabco] from experimental and computer simulation approach. They evaluated the selectivity of CO_2 over N_2 and seen to be highest for Cu-BTC MOF in a wide range of pressure. Although the synthesis protocol of Cu-BTC is very familiar to the research world of MOFs [194,195], several researchers are contributing their valuable time in functionalizing and decorating these MOFs by different functional groups in order to increase its physical and chemical properties like thermal stability, tunable pore size, increased hydrophobic nature [196]. Like many MOFs, ligands can be functionalized covalentally with other functional groups like –COOH, -X, $-NH_2$, $-CH_3$, -Pyridines etc. Functionalized MOFs can be targeted and utilized in various aspects and applications like in CO_2 selective capture, hydrogen storage and in upgradation of natural gas. Various literatures have been found to explore the potential of Cu-BTC MOF on anchoring the ligands with different functional groups and via different procedure for synthesis [111,197]. Maity et al. [198] synthesized nitro ($–NO_2$) functionalized Cu(II)-MOFs in order to enhance the CO_2 selectivity and reported a higher selectivity towards CH_4, N_2 and H_2 but did not measured the binary mixture isotherms. They found the selectivity using the pure component adsorption isotherm by utilizing the slope ratio of the pure component adsorption isotherms and thus obtained selectivity were not compared with the unfunctionalized Cu(II)-MOFs. Large pore MIL-53 was functionalized using $(CH_3)_2–$, $(OH)_2–$, $NH_2–$ and COOH– groups to investigate the CO_2 adsorption capacity from Grand Canonical Monte Carlo (GCMC) simulations and Density Functional Theory (DFT) calculations by Torrisi et al. [197]. In the current scenario, Functionalized MOFs are gaining much attention for achieving the target and can be used in different applications.

In this work, three different functionalized Cu-BTC MOFs namely Iodo, Dimethyl and Methyl were elucidated for selectivity of CO_2 over CH_4 and N_2 and compared the results with pure Cu-BTC named as Plane. First, adsorption isotherm obtained from GCMC was compared with the previously reported experimental and simulation work of the different researchers in pure Cu-BTC. Pure component adsorption isotherms of CO_2, CH_4 and N_2 were found using GCMC technique at three different temperature. Binary mixture of CO_2/CH_4 and CO_2/N_2 at two different molar composition viz 15/85 and 50/50 were obtained using GCMC. Selectivity of CO_2 over CH_4 and N_2 were found using the results obtained from the binary mixture GCMC simulation. Radial Distribution Function (RDF) plots and isosurface density plots were discussed to gain the understanding of the favorable adsorption sites in these functionalized MOFs.

7.2 Functionalized Cu-BTC Models and Computational Details

7.2.1. Functionalized Cu-BTC Models

Molecular model for pure CuBTC was obtained from experimental XRD crystallographic data with water molecules removed from the models [199]. Cu-BTC has two different pore location, (a) 5 Å with a window size of 3.5 Å (b) a square shaped void (9 Å × 9 Å) [194]. All the three functionalized Cu-BTC viz. Iodo, Dimethyl, and Methyl were built by replacing a particular hydrogen atom of same topology present at the benzene tricarboxylate (BTC) linker as shown in the Figure 7.1.

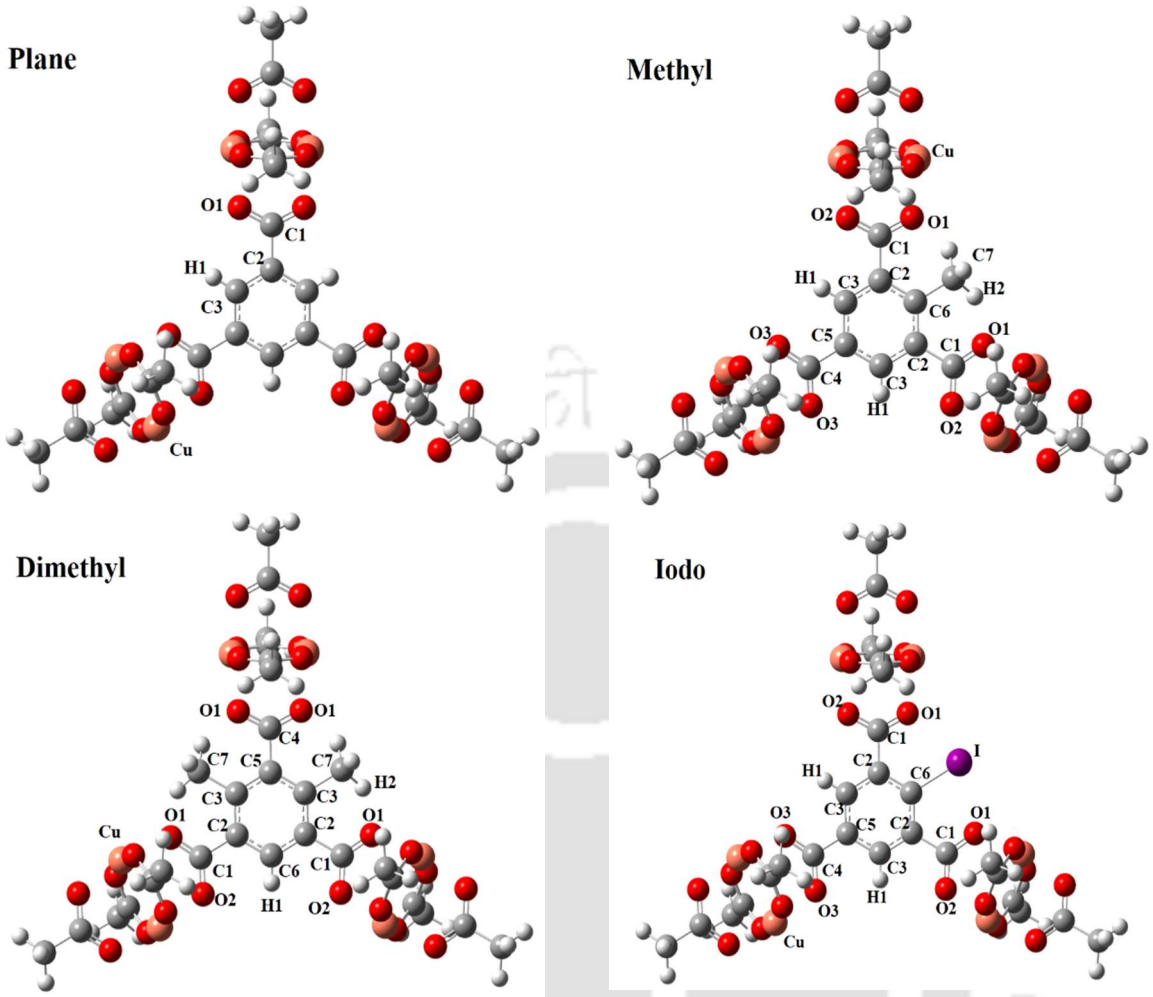

Figure 7.1 Cluster models used to calculate charges on different atom types in the Cu-BTC framework (both pure and functionalized).

Framework were considered as a rigid molecule during the GCMC simulation. Van der Waals interactions were computed using Lennard-Jones (LJ) 12-6 potential while long range interactions were computed using electrostatic potential between adsorbate-framework and adsorbate-adsorbate. In order to calculate the electrostatic interaction, Ewald summation technique was employed to reduce the computational time. Molecular models have a unit cell dimension of $26.343 \times 26.343 \times 26.343$ Å^3 and a cutoff of 12.5 Å was used to calculate the LJ potential, which is less than half of the simulation cell dimension. LJ potential parameters were taken from the DREIDING force field [80] except Cu atoms of the framework while parameters for the metal

atom Cu were taken from universal force field (UFF) [178]. Partial charges assigned on the frameworks were evaluated prior to simulation run using Density Functional Theory (DFT) calculation implemented in GAUSSIAN software [137]. Cluster models for all the four frameworks were subjected to DFT calculation using CHELPG method. Unrestricted B3LYP functional with 6-31G* basis set was applied to all atom except Cu metal atom. Los Almos National laboratory basis set known as LANL2DZ basis set was developed by Hay and Wadt for quantum calculation and widely used to study compounds and cluster model containing heavy elements. Cu metal atom present in the cluster was assigned effective core potential (ECP) basis set LANL2DZ. Cleaved part of the developed cluster from these MOFs were saturated with –CH3 (methyl) group. Cluster used in the calculation and resulting calculated partial charges are shown in the Figure 7.2 and Table 7.1.

In this work three different adsorbate molecule were modelled to study the adsorption in functionalized MOFs. LJ parameter and partial charges for CO_2 guest molecule was taken from the work of Potoff and Siepmann [84]. CO_2 was modelled as a linear molecule with three LJ sites having partial charges on each site with a bond length of 1.16 Å between C-O sites. Partial charges were used to compute the contribution of quadrupole moment present in the CO_2 molecule. Tranferrable potential for phase equilibria (TraPPE) forcefield was seen to be promising in accurate description of vapor-liquid equilibria curve, and hence N_2 molecule was modelled according to the TraPPE forcefield developed by Potoff and Siepmann [84]. N_2 molecule was modelled as a linear rigid molecule having three site with a bond length of 1.1 Å between the two extreme sites. Thus two extreme sites were treated as LJ site while third site located between the

(a) CuBTC

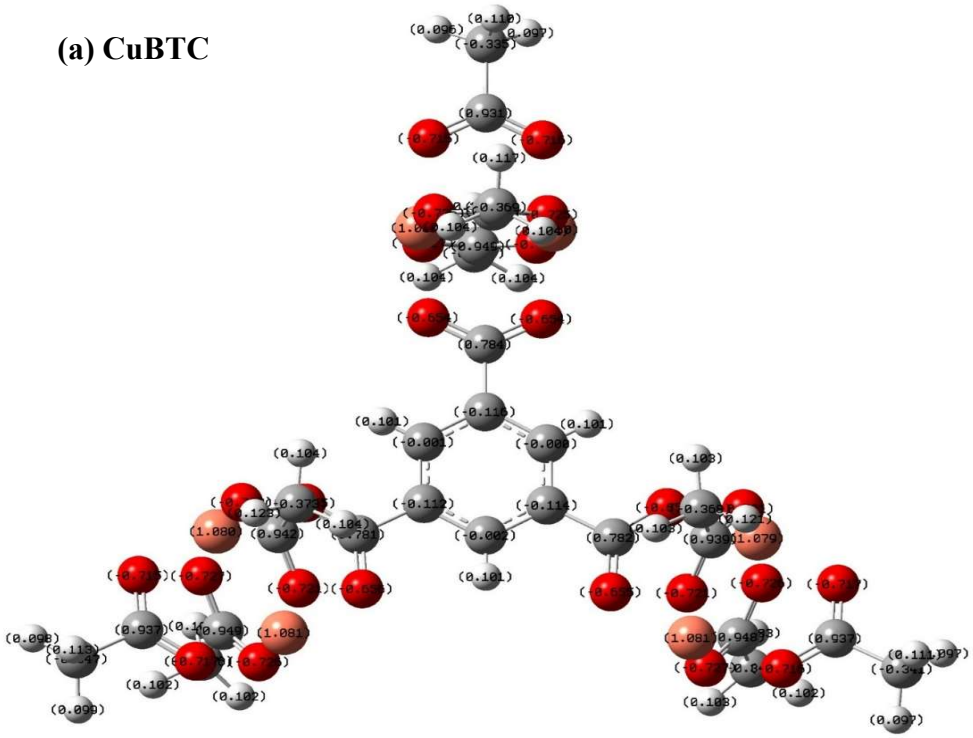

(b) Methyl

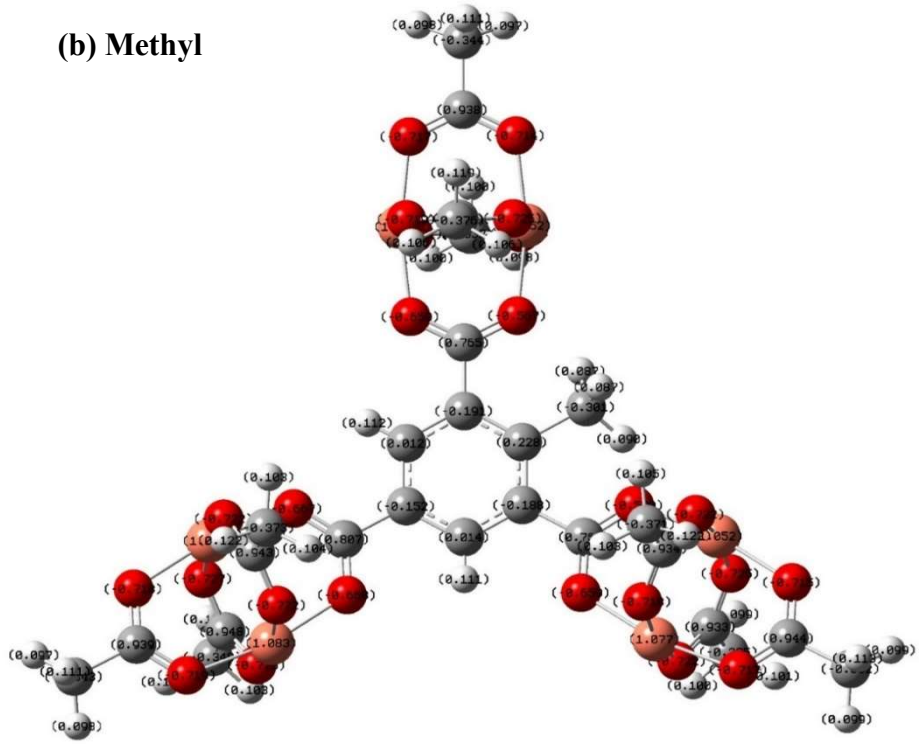

(c) Dimethyl

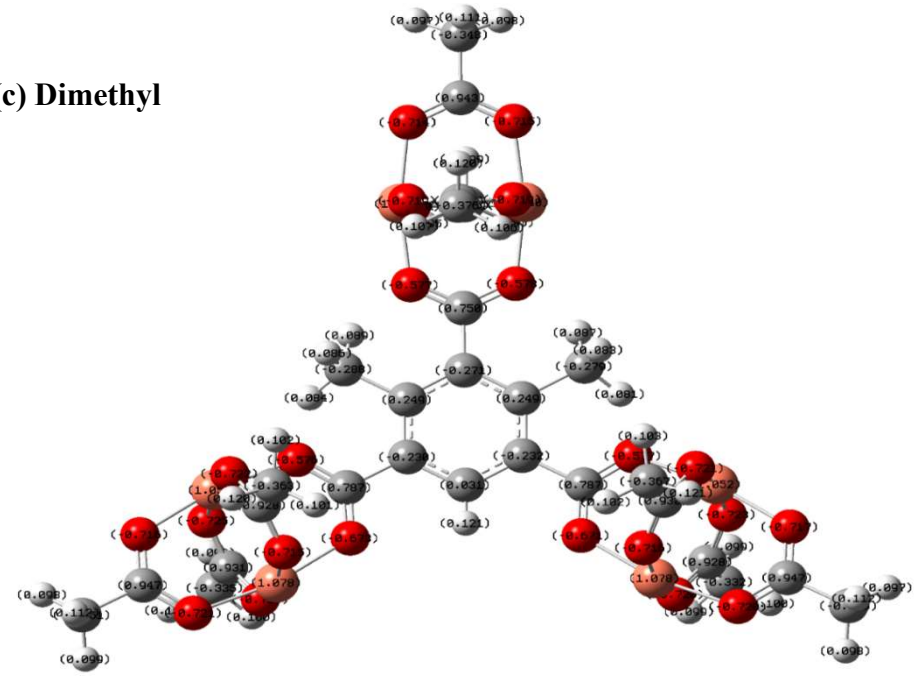

(d) Iodo

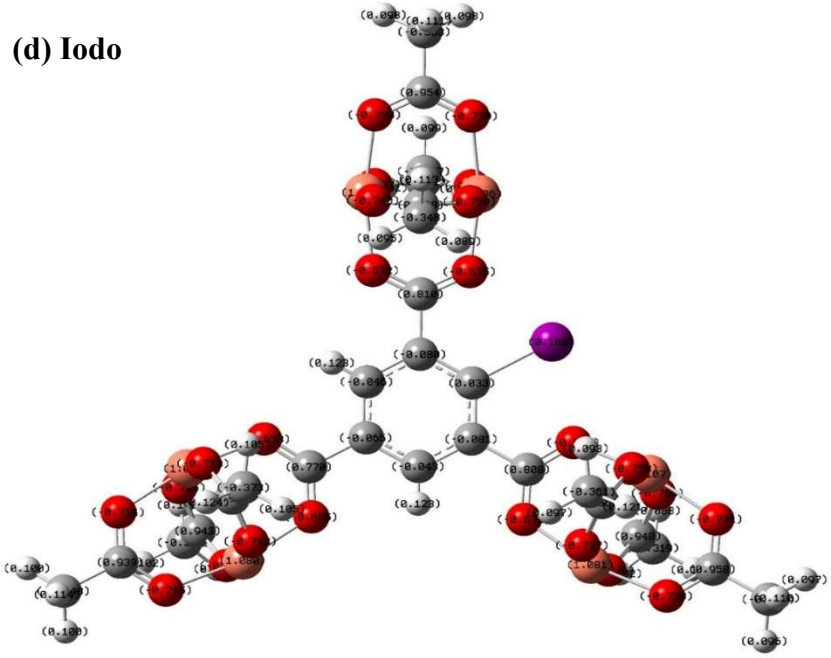

Figure 7.2 Clusters optimized using DFT calculations: (a) pure Cu-BTC, (b) methyl-functionalized Cu-BTC, (c) dimethyl-functionalized Cu-BTC, and (d) iodo-functionalized Cu-BTC

Table 7.1 Partial charges used in the GCMC simulation for the frameworks

Types of atom	Plane CuBTC	Methyl-CuBTC	Dimethyl-CuBTC	Iodo-CuBTC
C1	0.782767	0.757668	0.777615	0.794258
C2	-0.11393	-0.19034	-0.23382	-0.08162
C3	-0.0015	0.012909	0.246031	-0.04693
C4		0.801361	0.741056	0.755036
C5		-0.15308	-0.27431	-0.06631
C6		0.226407	0.03063	0.032359
C7		-0.30313	-0.28696	
O1	-0.65461	-0.57253	-0.58405	-0.68763
O2		-0.66367	-0.68021	-0.68559
O3		-0.67223		-0.6662
H1	0.10106	0.110721	0.119557	0.12061
H2		0.087385	0.083986	
Cu	1.081645	1.067488	1.046697	1.085486
I				0.156891

two extreme sites (centre of mass COM of N_2 molecule) was treated as pseudo site to account for any polarity developed in the molecule. In this work, Transferrable potential for phase equilibria for united atom (TraPPE-UA) proposed by Martin and Siepmann [105] was used to model CH_4 molecule. Methane molecule was modelled as a single LJ site only. Forcefield parameters for host (adsorbent) as well as guest (adsorbate) molecule were shown in the Table 7.2.

Table 7.2 Force field parameters for adsorbent and adsorbate molecules

Molecule	Site	σ(Å)	$\varepsilon(K)$	$q(e)$	Bond length (Å)
Functionalized Cu-BTC	Cu	3.113691	2.516083		
	C	3.472990	47.855898		
	O	3.033153	48.157828		
	H	2.8464214	7.648892		
	I	4.009044	170.59042		
CO_2	C	2.80	27.0	0.70	C=O
	O	3.05	79.0	-0.35	1.16
N_2	N	3.310	36.0003	-0.4820	N≡N
	N(COM)	0.000	0.000	0.9640	1.1
CH_4	CH_4	3.730	148.00	0.0000	

7.2.2. Computational Details

Pure as well as binary mixture adsorption were studied using GCMC simulation technique. Non bonded LJ interactions were computed using a spherical cutoff of 12.5 Å including long range correction in order to ensure any further effective potential beyond the cutoff value. Electrostatic interactions were handled using Ewald summation technique with a cutoff value of 12 Å for the contribution from real part. GCMC simulations were carried out using the open source package (RASPA) developed by the research group of Dubbeldam et al. [55]. Previously, the package was validated and compared with several experimental results in order to explore the applicability of programme [62,146]. To imitate the real behavior of gases, Peng-Robinson equation of state was used to convert the pressure into fugacity. Four different types of trial moves were implemented for single component GCMC adsorption with an equal probability of 25 % for each type of trial moves (Insertion, Deletion, Rotation and Translation). Identity exchange moves [56,57] was attempted for the case of multicomponent GCMC simulation with a probability of 5 % in order to

achieve a faster equilibrium. A total of 2×10^6 cycle for equilibrium and 2×10^6 cycle for sampling the average molecule were used throughout the GCMC simulation. Each cycle consisted of 20 steps when N (number of adsorbate molecules in the simulation box) was less than 20 while for N>20, number of steps in each cycle was equal to N. Final GCMC simulation run always provides the total adsorbate molecule (absolute amount) in the simulation box and needed to be converted into the excess amount in order to evaluate the number of adsorbate molecule in the adsorbed phase using the equation (2.36) discussed in section 2.2.5. Selectivity was calculated for binary mixture over one another using the obtained GCMC results of binary mixture according to the equation (2.41) given in section 2.2.7.

7.3 Results and Discussion

The force field parameters and calculated CHELPG charges employed in the adsorption simulations were first validated by comparing the adsorption isotherm of pure CO_2 on unmodified Cu-BTC to experimental and simulation data available in literature. For this purpose, adsorption isotherm of pure CO_2 on Cu-BTC, calculated using GCMC simulation over a pressure range of 0–25 bar and at a temperature of 295 K, was compared with the experimental results of Chowdhury et al. [61] and simulation results of Hu et al. [114], as shown in the Figure 7.3. The isotherm from our GCMC simulations shows excellent agreement with both the experimental and the simulation data from literature.

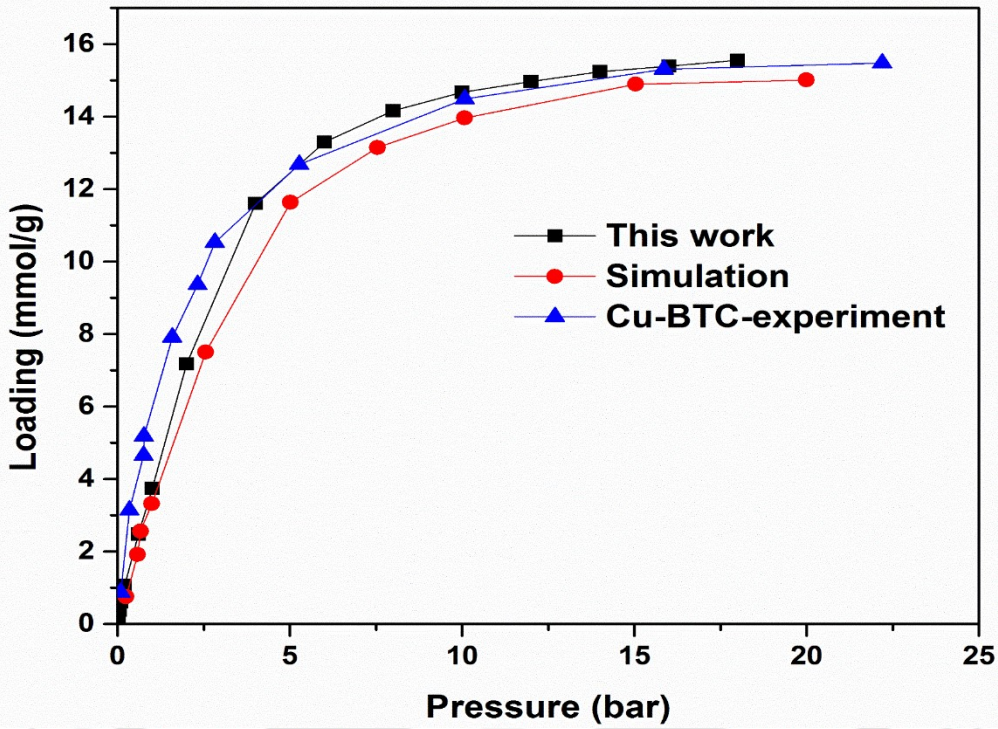

Figure 7.3 Comparison of the simulated adsorption isotherm of pure CO_2 on Cu-BTC at 295.0 K from the present work with the experimental results of Chowdhury et al. [61] and simulation results of Hu et al. [114].

7.3.1. Pure CO_2 Adsorption

We studied the adsorption of pure CO_2, N_2 and CH_4 at 298.15 K on the four MOF models (unmodified Cu-BTC and three functionalized Cu-BTC) to evaluate the effect of the functional groups on the adsorption behavior of the different gases. The adsorption isotherms for pure CO_2 in the low-pressure and high-pressure regions are shown in Figure 7.4(a) and Figure 7.4(b) respectively.

It may be noted that the adsorbed amounts are shown as molecules of CO_2/unit cell (uc). Due to the additional mass of the functional groups, the adsorption loadings expressed in milimole per gram, will display a different trend. At high pressures (Figure 7.4(b)), the CO_2 adsorption approaches saturation with saturation loadings following the order Cu-BTC > Cu-BTC-Met ≈

Cu-BTC-Iodo > Cu-BTC-DiMet. The high-pressure loading was the largest in unmodified Cu-BTC because of the larger accessible surface area and void volume for adsorption. Iodo- and methyl-functionalized Cu-BTC, both having similar topology and size of functional group, exhibit almost equal saturation loading. In the case of Cu-BTC functionalized with two methyl groups attached at different locations on the linker, a lower saturation loading is observed because of lower void fraction (see Table 7.3) and hence, smaller accessible volume. In the lower pressure range of 0.2–1.4 bar shown in Figure 7.4(a), iodo-functionalized Cu-BTC exhibits higher loading of CO_2. Thus, at ambient conditions, i.e., 298.15 K and 1 bar, iodo-functionalized Cu-BTC shows the highest adsorption loading of CO_2. In Figure 7.4(b), a crossover can be observed above 2 pressure, and the CO_2 loading in unmodified Cu-BTC becomes the highest.

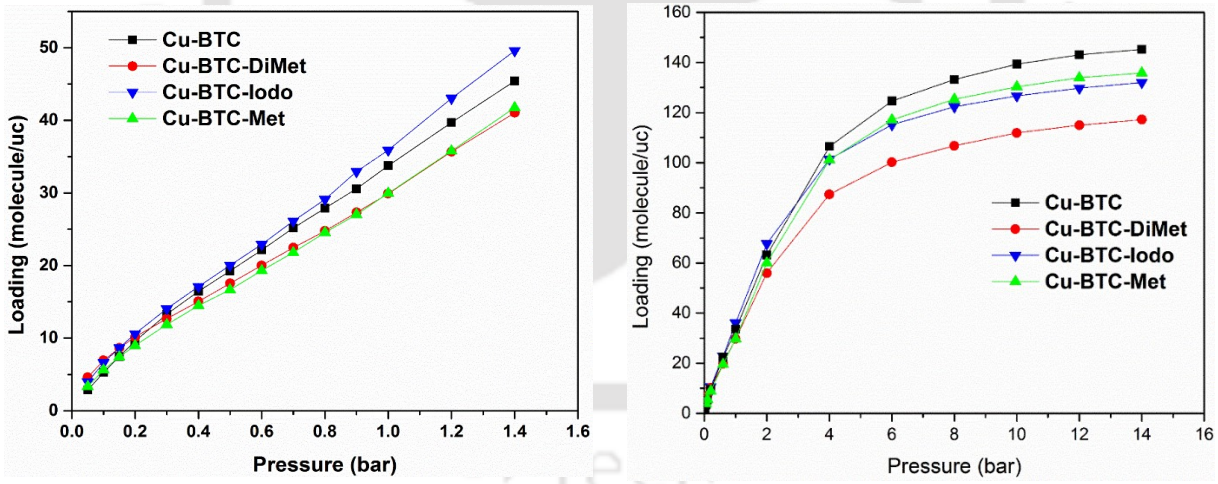

Figure 7.4 Adsorption isotherms of pure CO_2 in unmodified and functionalized Cu-BTC at 298.15 K: (a) in the low pressure regime, and (b) at higher pressures (lines are shown only as guide to the eye).

Table 7.3 Void fraction and surface area of the pure and functionalized Cu-BTC models

	Cu-BTC pure	Cu-BTC-iodo	Cu-BTC-methyl	Cu-BTC-dimethyl
*Surface area (m^2/g)	2178.3	1343.0	1881.8	1741.4
Void fraction	0.6905	0.6396	0.6521	0.6052
*Experimental Surface area	1628 m^2/g			

To investigate the adsorption behavior of CO_2 in more detail, spatial distribution of adsorbed CO_2 molecules was visualized and RDFs were calculated. The 3D spatial distribution maps of CO_2 adsorbed in unmodified and functionalized Cu-BTC at 298.15 K and 1 bar are shown in Figure 7.5. Such maps provide a useful visual representation of locations preferred by the adsorbing molecules in the framework, and are informative for locating the accessible pores and channels inside the framework and the sites visited by the adsorbing guest molecules over the course of the simulation. In unmodified Cu-BTC, there are two different-sized pockets, the smaller one around 5 Å, which is expected to fill at lower pressures, and the larger one $9\ Å \times 9\ Å$ in size, which is expected to fill at higher pressures. In Figure 7.5(a), the adsorbed CO_2 molecules at 1 bar can be observed to prefer the four smaller cages at the corners and the narrow windows connecting these smaller cages to the larger cage. However, no significant adsorption is seen in the large central cage. The distribution maps for iodo- and methyl-functionalized Cu-BTC (see Figure 7.5 (b) and 4(c) respectively) are similar because both the functional groups have similar size and are grafted at the same location on the organic linker. For both frameworks, adsorption in seen to take place in the smaller cages and windows as well as in the larger cages. Due to the presence of functional groups, the effective size of the cages gets reduced resulting in filling at lower pressures than in unmodified Cu-BTC. The two methyl groups present at two different locations on the same linker

in dimethyl-functionalized Cu-BTC block the windows connecting the smaller and larger cages due to steric hindrance. Figure 7.5(d) shows the distinctive locations visited by CO_2 molecules inside the framework of dimethyl-functionalized Cu-BTC. Although the smaller and larger cages on the framework are frequently visited, very few CO_2 molecules can be seen visiting the narrow channels between the smaller and larger cages. Owing to the presence of two functional groups per linker, the effective size of the cages is reduced leading to substantial adsorption even in the larger cages.

The RDFs between the adsorbate molecules and the atoms in the adsorbent framework can provide quantitative description of the average distribution of the adsorbate molecules around specific sites of the adsorbent. Therefore, RDFs between the CO_2 molecules and Cu-BTC framework sites were calculated, as shown in Figure 7.6(a) and (b). The RDFs of CO_2 around the different functional groups, shown in Figure 7.6(a), show multiple peaks. For dimethyl-functionalized Cu-BTC, two broad peaks at ~5 Å and ~10 Å indicate the presence of two layers of CO_2 molecules at these respective distances from the methyl groups. For methyl-functionalized Cu-BTC, in addition to two broad peaks at ~5 Å and ~10 Å, the RDF shows a hump at ~4 Å suggesting the presence of some CO_2 molecules at this distance as well. Iodo-functionalized Cu-BTC shows a weak, sharp peak at ~4 Å followed by broader peaks at 5.5 Å and 10 Å. Thus, although some molecules of CO_2 may be present at a distance of ~4 Å from the iodine atoms, most of the CO_2 molecules are located beyond 5 Å. Figure 7.6(b) shows the RDFs between the CO_2 molecules and the oxygen atoms of the organic linker. RDFs of the unmodified and the functionalized Cu-BTCs exhibit a broad peak

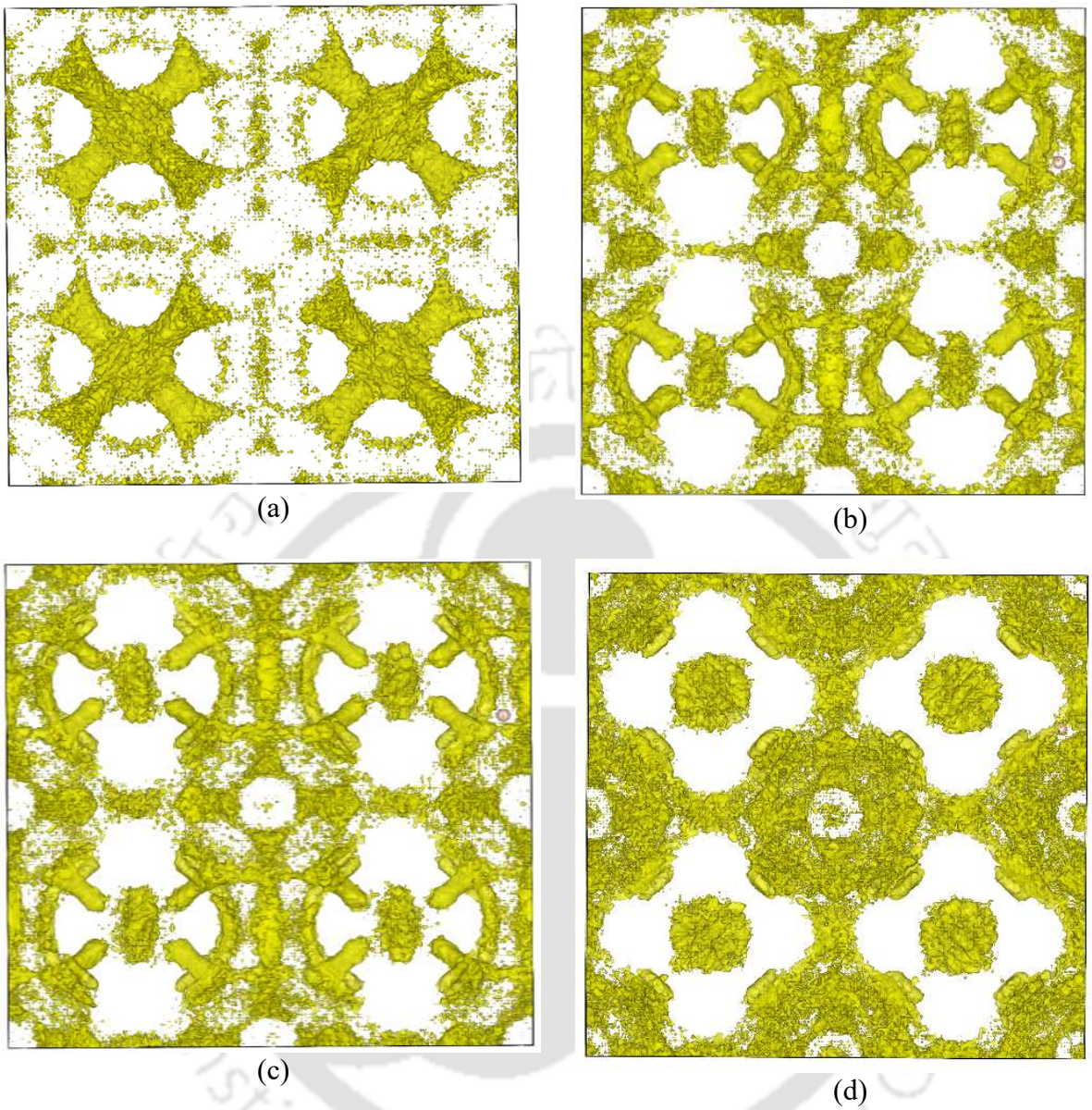

Figure 7.5 Spatial distribution of CO_2 adsorbed 1 bar and 298.15 K in (a) unmodified Cu-BTC and in Cu-BTC functionalized with (b) iodo, (c) single methyl and (d) two methyl (dimethyl) functional groups. The framework atoms of Cu-BTC have not been shown for clarity.

at ~5–5.5 Å. However, if we focus on the region between 3 and 4 Å, the different RDFs show different behavior. Due to the strong steric hindrance by the two methyl groups on the linker, the amount of CO_2 adsorbed around the oxygen atom of the linker at 3–4 Å is negligible. The RDFs for methyl- and iodo-functionalized Cu-BTC show somewhat greater amount of CO_2 around 3–4

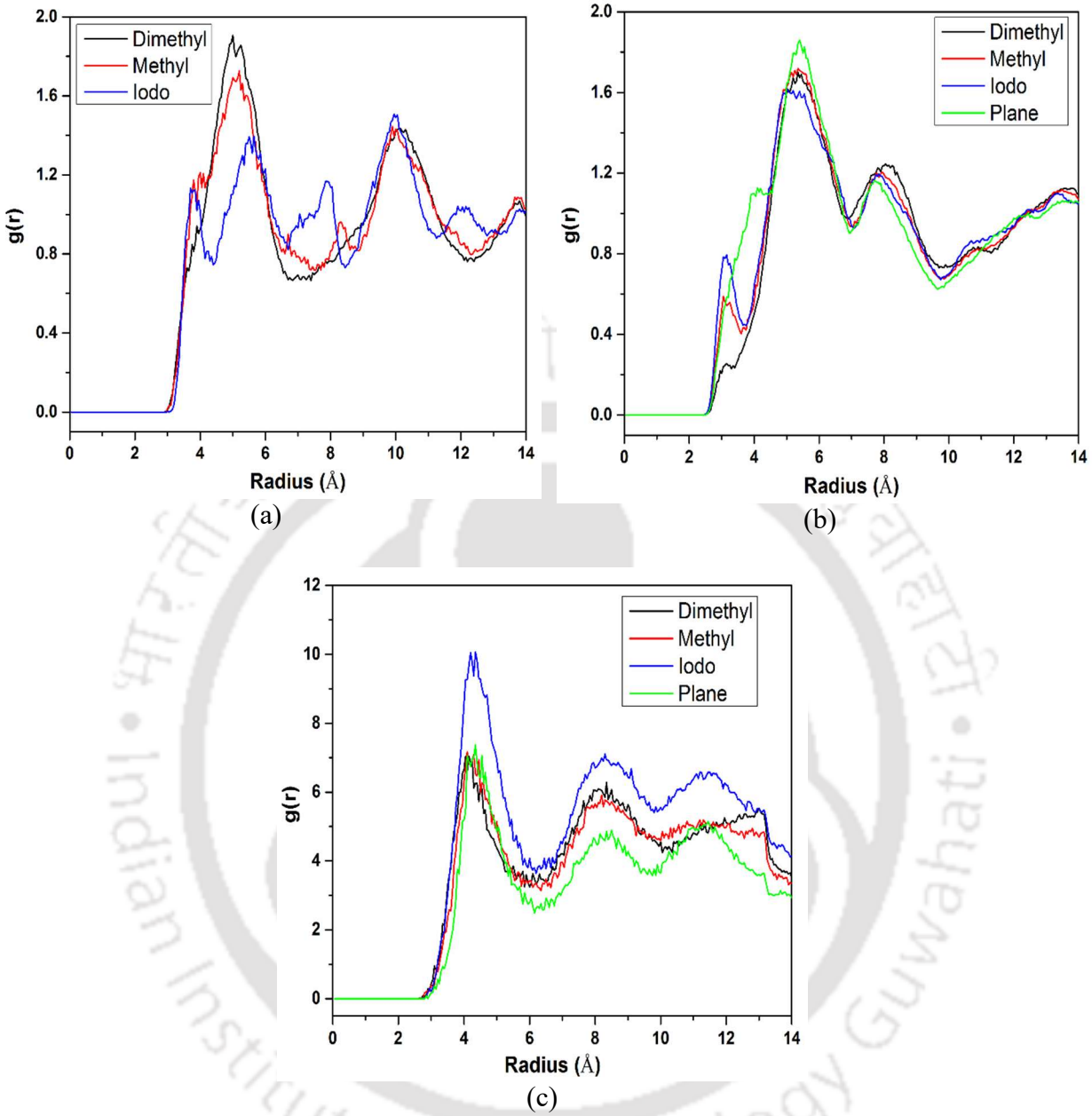

Figure 7.6 RDF plots between (a) functional groups and CO_2, (b) O-CO_2, (c) CO_2-CO_2 for adsorption of pure CO_2 on unmodified and functionalized Cu-BTC at 298.15 K and 1 bar.

Å of the linker oxygen atoms, due to lesser steric hindrance, whereas unmodified Cu-BTC shows the largest probability of finding CO_2 molecules around 3–4 Å of the linker oxygen atoms due to the absence of functional groups in the vicinity of the oxygen atoms. The CO_2-CO_2 RDFs in Figure 7.6(c) show the first-neighbor peaks at around 4 Å followed by next neighbor peaks at ~ 8 Å.

7.3.2. Pure CH_4 and N_2 Adsorption

The higher adsorption of CO_2 in iodo-functionalized Cu-BTC at ambient conditions motivated us to further investigate the adsorption of other gases such as N_2 and CH_4 as well as the effect of functional groups on CO_2 selectivity towards these gases. Pure CH_4 adsorption isotherms in unmodified and functionalized Cu-BTC are shown in Figure 7.7.

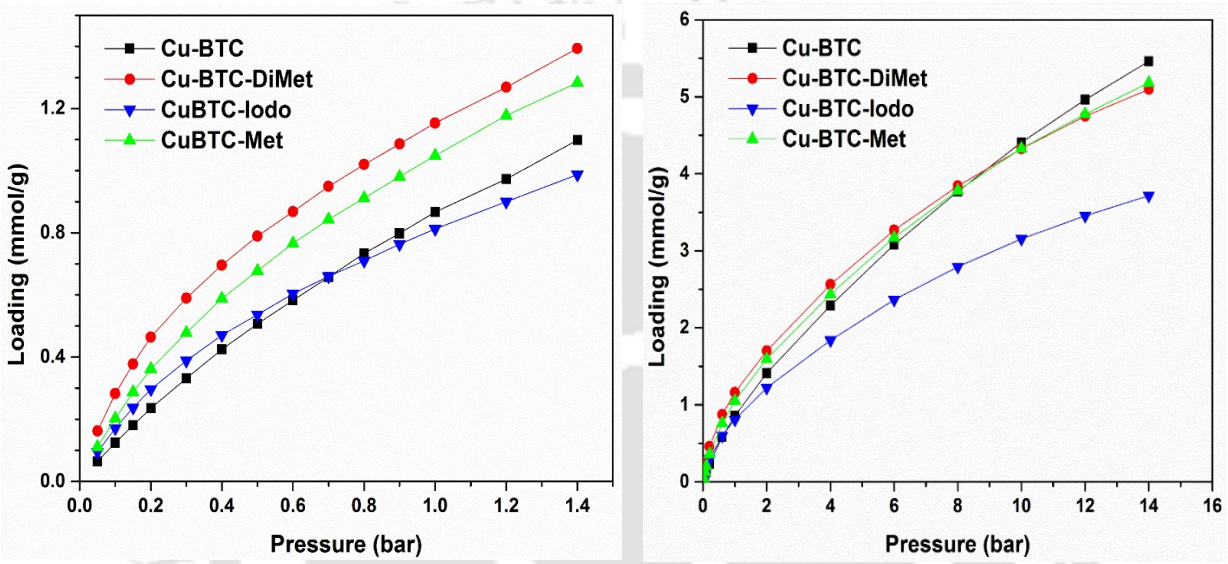

Figure 7.7 Adsorption isotherms of pure CH_4 in unmodified and functionalized Cu-BTC at 298.15 K: (a) in the low pressure regime, and (b) at higher pressures (lines are shown only as guide to the eye).

At low pressures (Figure 7.7(a)), the amount adsorbed is higher in methyl- and dimethyl-functionalized Cu-BTC whereas iodo-functionalized and unmodified Cu-BTC show similar loading. However, at higher pressures, the amount of CH_4 adsorbed in unmodified Cu-BTC becomes comparable to and even exceeds that in methyl- and dimethyl-functionalized Cu-BTC. CH_4 adsorption in iodo-functionalized Cu-BTC is significantly lower than that in the other frameworks at high pressures, as shown in Figure 7.7(b). There is a crossover at ~0.7 bar in Figure 7.7(a) after which CH_4 adsorption in unmodified Cu-BTC goes above iodo-functionalized Cu-

BTC, and another crossover at ~9 bar in Figure 7.7(b) after which CH_4 adsorption in unmodified Cu-BTC becomes the highest. Such crossover generally implies the interplay of competing effects. At very low pressures, the interactions or affinity of adsorbates with the adsorbent framework dominate and hence, unmodified Cu-BTC shows the lowest adsorption amounts. As the pressure is increased, the number of available sites for adsorption (i.e., surface area) becomes important and at high enough pressures, the available pore volume becomes a limiting factor. Unmodified Cu-BTC has the largest surface area and pore volume (see Table 7.3) and thus, shows highest adsorbed amounts at high pressures. Adsorption of N_2 shows a similar qualitative trend to that observed for CH_4 adsorption although the amount adsorbed is less than half. Further, the pressures at which adsorption in unmodified Cu-BTC crosses that in Cu-BTC-Iodo (see Figure 7.8(a)) and those in Cu-BTC-Met and Cu-BTC-DiMet (see Figure 7.8(b)) are higher (~1.2 bar and >14 bar respectively).

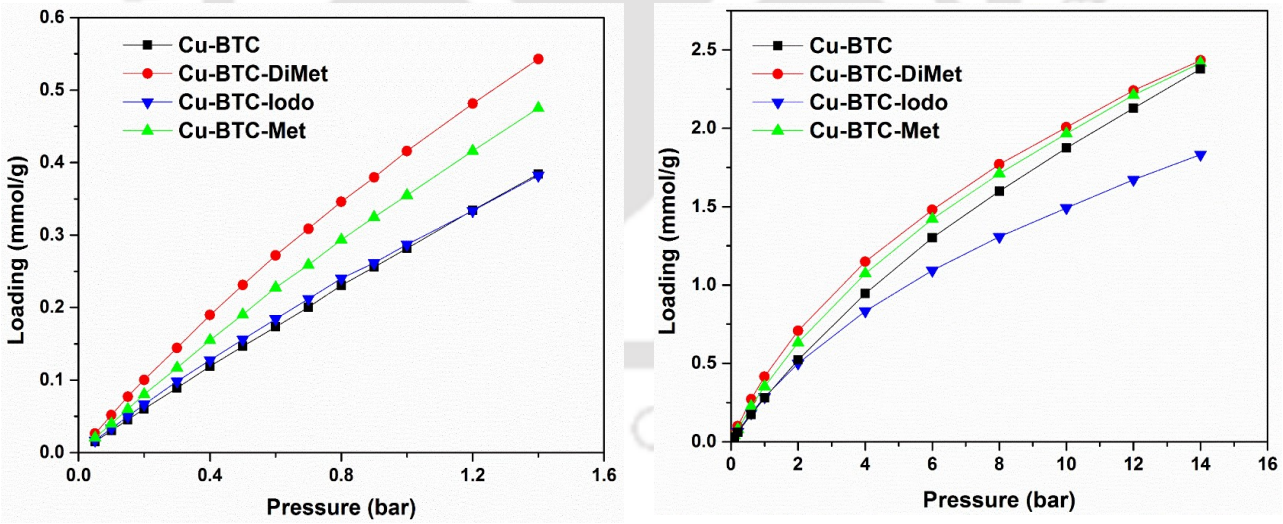

(a) (b)

Figure 7.8 Adsorption isotherms of pure N_2 in unmodified and functionalized Cu-BTC at 298.15 K: (a) at low pressures, and (b) at higher pressures (lines are guide to the eye).

Again, the more favorable interactions in the presence of functional groups leads to higher adsorption at very low pressures. However, as pressure increases, the effects of higher surface area and larger accessible pore volume (as saturation sets in) become dominant.

Isosteric heats of adsorption were also calculated for the gases in pure and functionalized Cu-BTC. At low pressures the isosteric heats decreases with increase in loading (see Figure 7.9) possible because of favorable adsorption sites occupied. In the case of CO_2, shown in Figure 7.9 (a), isosteric heat increases at higher pressures due to favorable adsorbate-adsorbate lateral interactions. Isosteric heat of adsorption for CO_2 was seen to be highest in the Cu-BTC-Iodo model in the moderate pressure range of 1–5 bar as shown in the Figure 7.9 (a). For CH_4, the isosteric heat of adsorption quite similar for all the models as shown in the Figure 7.9 (b). Figure 7.9 (c) shows that below 5 bar the isosteric heat of adsorption of N_2 is highest for Cu-BTC-DiMet followed by Cu-BTC-Iodo>Cu-BTC-Met>Cu-BTC. The isosteric heats of CO_2 are observed to be highest followed by CH_4 and N_2, in all the models studied.

7.3.3. Binary Mixture Adsorption

CO_2 separation from CO_2/N_2 and CO_2/CH_4 binary gas mixtures, both having a molar ratio of 0.15:0.85, was studied using GCMC simulation. The simulated adsorption isotherms for both the mixtures in all the functionalized Cu-BTC frameworks are shown in Figure 7.10 over the pressure range of 0–14 bar at 298.15 K. For CO_2/CH_4 mixture, at pressures above 2 bar, the amount of CH_4 adsorbed can be seen to follow the trend Cu-BTC > Cu-BTC-Met ≈ Cu-BTC-DiMet > Cu-BTC-Iodo whereas CO_2 loading follows Cu-BTC > Cu-BTC-Met > Cu-BTC-DiMet ≈ Cu-BTC-Iodo. The higher loading in unmodified Cu-BTC at higher pressures is primarily due to the larger

available surface area and pore volume, which become the limiting factors as saturation is approached. Cu-BTC-Iodo has the lowest surface area and hence shows the lowest adsorption. The

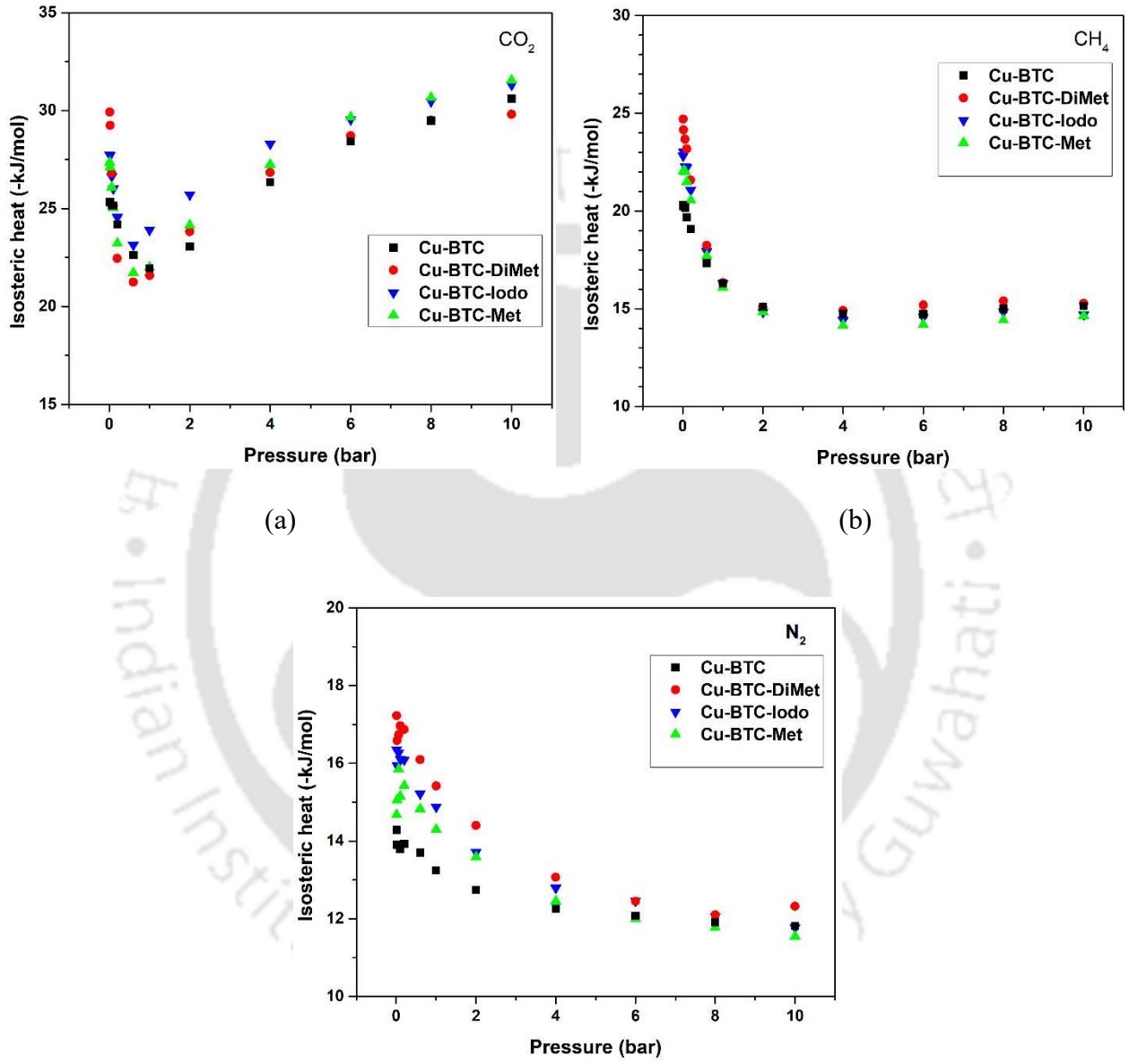

Figure 7.9 Isosteric heat of adsorption of (a) CO_2 (b) CH_4 and (c) N_2 in pristine and functionalized Cu-BTC models.

adsorption behavior of CO_2/N_2 mixture, shown in Figure 7.10(b), shows a similar trend to that of the CO_2/CH_4 mixture. Thus, at pressures above 2 bar, unmodified Cu-BTC shows the highest loadings and Cu-BTC-Iodo shows the lowest loadings (for both CO_2 and N_2). On the other hand, at low pressures in the range 0–1.0 bar, CO_2 uptake in CO_2/N_2 mixture is highest for dimethyl-functionalized Cu-BTC. This is because at low pressures, when many adsorption sites are available, the stronger interactions between the adsorbate molecules and adsorbent framework, due to the presence of the methyl groups in the framework, dictate the adsorption behavior. As the pressure is raised, the surface area and pore volume become the limiting factors and hence, adsorption in Cu-BTC-DiMet drops much below that in unmodified Cu-BTC.

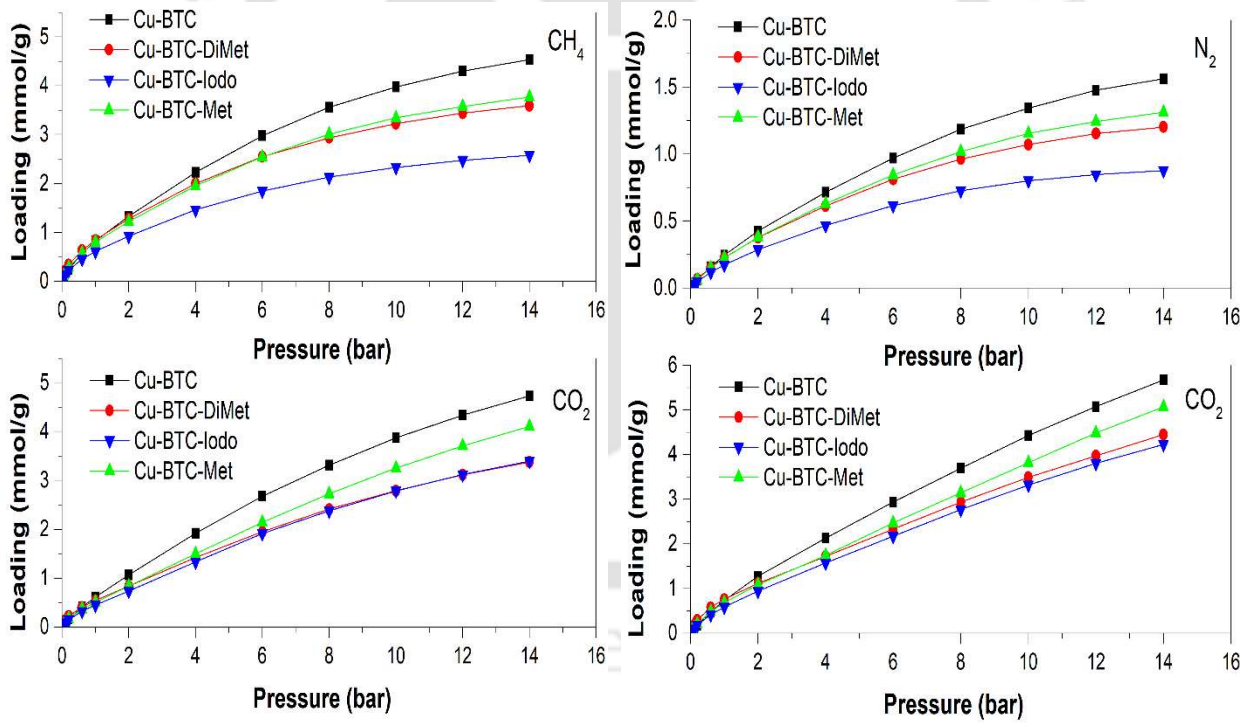

Figure 7.10 Adsorption isotherms of binary mixtures of (a) CO_2/CH_4 in molar ratio 15:85, and (b) CO_2/N_2 in molar ratio 15:85 at 298.15 K on unmodified and functionalized Cu-BTC (lines are shown only as guide to the eye).

Although the adsorption loading in Cu-BTC-Iodo is the lowest among all the models investigated, interestingly, the CO_2/N_2 and CO_2/CH_4 selectivities at 298.15 K and pressures above 2 bar are the highest in the iodo-functionalized frameworks, as shown in Figure 7.11. For CO_2/CH_4 mixtures, where separation is of interest at high pressures (> 5 bar), unmodified Cu-BTC and Cu-BTC-Met show similar selectivities whereas Cu-BTC-DiMet is the least selective. In CO_2/N_2 separations are typically carried out at atmospheric pressures where Cu-BTC-DiMet and Cu-BTC-Iodo show high selectivities (~20) and unmodified Cu-BTC shows the lowest selectivity. Thus, although iodo-functionalization of Cu-BTC results in low adsorption loadings, it shows the highest selectivities over most of the pressure range explored, with selectivity enhancements as high as 30–35% in comparison to unmodified Cu-BTC.

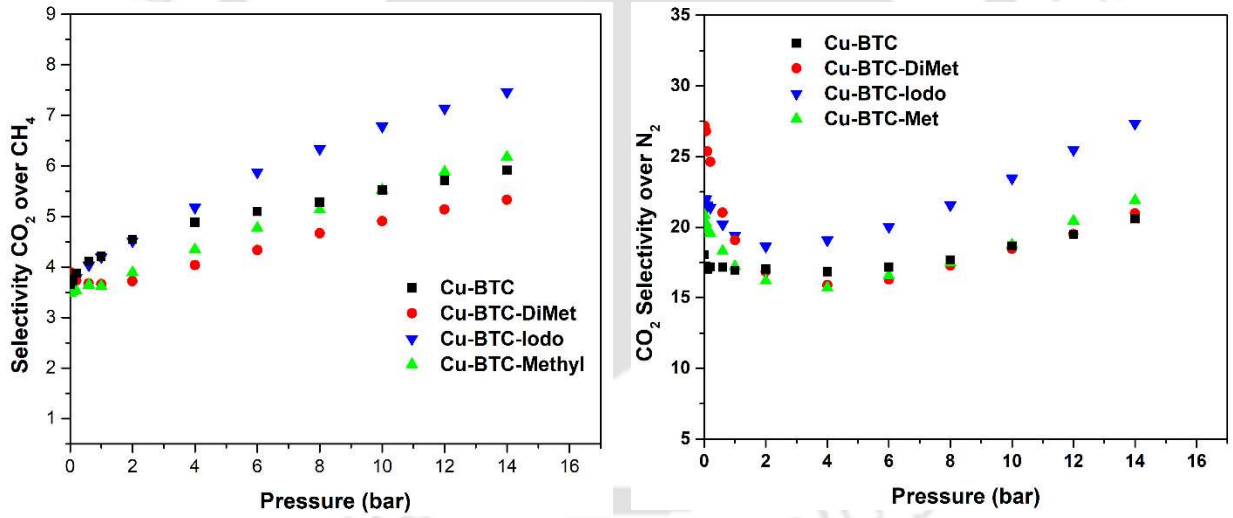

(a) (b)

Figure 7.11 Selectivity of (a) CO_2 over CH_4, and (b) CO_2 over N_2, for adsorption of 15:85 (by mole) binary gas mixtures on unmodified and functionalized Cu-BTC at 298.15 K.

7.4 Conclusions

Modification of the pores of MOFs through grafting can result in change in pore structure and interaction environment, which can be useful in enhancing the selective adsorption of certain molecules based on the physical size and interactions of the adsorbate. Here, we have modified the Cu-BTC framework by grafting iodo, single methyl and two methyl groups respectively on the linker to evaluate the effect of functionalization on gas adsorption and CO_2 separation. Uptake of pure CH_4 was seen to be significantly higher for the dimethyl functionalized Cu-BTC, which was seen to be promising for CH_4 storage. At higher pressure, CO_2 selectivity over CH_4 and N_2 was seen to be highest for the case of iodo functionalized Cu-BTC. Dimethyl functionalized Cu-BTC was found to be a promising adsorbent where higher selectivity of CO_2 over N_2 is required at ambient temperature and pressure condition. Moreover, volatile organic materials can also be exclusively adsorbed in the different pore texture of the functionalized Cu-BTC, which may be a different perspective of research scope. Current research suggests the synthesis of functionalized Cu-BTC by anchoring the dimethyl group at two different topologies, which may lead to a pronounced change in the pore texture and chemical environment for beneficial utilization of their physical and chemical properties.

CHAPTER 8

Conclusions and Future Directions

8.1 Conclusions

This chapter contains a summary of the conclusions drawn from the different adsorption studies on mesoporous silica and microporous metal-organic frameworks, and suggestions on the scope for future work. Grand canonical Monte Carlo (GCMC) simulations have been used to study the adsorption of multicomponent gas mixtures and separation of CO_2 from such mixtures using pure and modified mesoporous silica adsorbents. Atomistic models of realistic MCM-41 were developed and characterized by calculating the surface area and simulated X-ray diffraction pattern, which compared favorably with experimental data reported in literature. The excellent agreement between CO_2 adsorption amounts obtained from GCMC simulations and experimental results (from literature) further validated the developed models. CO_2 is preferentially adsorbed over N_2 in binary mixture simulations owing to the stronger dispersion interactions and larger quadrupole moment of CO_2, with selectivities of CO_2 over N_2 in the range 4–10. The presence of other species in the gas mixture such as O_2 and water vapor did not significantly affect the CO_2/N_2 selectivity at the studied temperatures, pressures and compositions. Despite the presence of surface silanol groups on the pore walls, MCM-41 does not preferentially adsorb the polar water molecules over O_2 (or N_2) molecules. To study the effect of mesopore size and wall microporosity on the adsorption and separation of CO_2, models representative of the mesoporous silica SBA-15 were developed by considering an MCM-41 model with large mesopores and carving micropores across the walls of the mesopore. With increase in wall microporosity, the uptake of CO_2 was observed to first decrease and then increase. At low pressures, the CO_2 uptake in the SBA-15 model having the highest microporosity among the models studied was the largest due to the CO_2 molecules preferentially adsorbing in the micropores at low pressures. However, at higher pressures, CO_2

adsorption in model with no microporosity was somewhat larger, possibly because of the micropores getting filled. Adsorption simulation of the binary mixtures CO_2/CH_4 and CO_2/N_2 revealed that the frameworks are selective toward CO_2 over CH_4 and N_2. At low pressures, the selectivities in the models with wall microporosity is in general higher, probably due to the preferential adsorption of CO_2 in the micropores. Although the amount of CO_2 adsorbed (per unit adsorbent mass) is lower in the SBA-15 models than in the MCM-41 models of chapter 3 (due to the lower surface areas), the CO_2/N_2 selectivity is comparable in the two mesoporous silica materials.

The developed and validated MCM-41 model was modified by impregnation of pyrrolidinium-based ionic liquid (IL) 1-methyl-1-butyl-pyrrolidinium bis(trifluoromethanesulfonyl)imide $[C4PYR^+)][TF2N^-]$ inside the MCM-41 pores. Two different loadings of ILs (21 wt% and 42 wt%) were incorporated in the pores of MCM-41 to study the effect on adsorption and separation of CO_2. The adsorption of pure CO_2 in the model with 21% IL content was observed to be significantly higher than that in pristine MCM-41. The high adsorption loading of CO_2 can be attributed to the larger accessible area and stronger interactions with the IL molecules. In the model with 42% IL, favorable interaction between CO_2 and IL molecules results in higher CO_2 adsorption than pure MCM-41 at pressures below 5 bar. However, at higher pressures, the effect of interactions is offset by the lower accessible area and void fraction due to higher IL loading resulting in lower CO_2 adsorption than in pure MCM-41. Selectivity of CO_2 over N_2 and CH_4 was 50–100% higher in the IL-loaded MCM-41 models than in pure MCM-41. Thus, physical incorporation of IL molecules in MCM-41 mesopores potentially improve the CO_2 separation

behavior of mesoporous silica. The enhancement in CO_2 uptake and selectivity may be tuned by adjusting the loading of IL in the mesopores.

Microporous metal-organic frameworks (MOFs) have also been explored as candidates for CO_2 capture in this work. The effect of variation in cage and channel sizes on CO_2 adsorption and separation has been studied in topologically similar zirconium-based MOFs of the UiO series, namely UiO-66 and UiO-67, having high thermal stability and good tolerance to moisture. Gas uptake was higher in UiO-66 at low pressures due to smaller cages and channels leading to stronger interactions. However, at higher pressures, gas storage capacity of UiO-67 was higher due to the larger cages and higher surface area. The density contour plots and RDFs reveal that CO_2 molecules preferentially adsorb near the carbon atoms of the organic linkers. Further, for both MOFs, more adsorption takes place in the smaller, outer cages of the frameworks than the larger, central cage. Both UiO-66 and UiO-67 were more selective towards CO_2 than CH_4 and N_2, with the CO_2 selectivity almost twice as high in UiO-66 than in UiO-67 because of the narrow window size and smaller cages. In addition to variation in pore size and surface area, adsorption behavior can also be influenced by changing the interaction environment within the pores by grafting functional groups on the linker. The effect of linker functionalization on CO_2 separation was explored by considering three functionalized Cu-BTC MOFs (having iodo, single methyl and two methyl functional groups per linker) and comparing with unmodified Cu-BTC. CH_4 uptake was found to be highest for the dimethyl functionalized Cu-BTC. CO_2 selectivity over CH_4 and N_2 was the highest for iodo-functionalized Cu-BTC at high pressures. At ambient pressure and temperature, selectivity of CO_2 over N_2 was found to be highest for dimethyl functionalized Cu-BTC.

The studies on CO_2 adsorption and separation on different mesoporous and microporous adsorbents in this work show that the uptake and selectivity of CO_2 is a function of pore size, nature of pore wall and interaction environment within the pore. The different analysis tools also revealed the preferred location of CO_2 molecules within the pores. The suitable modification of the pore environment through the two strategies explored in this work, namely physical impregnation and covalent grafting, can result in significant enhancement in the preferential adsorption of CO_2 in the adsorbent frameworks. The type and loading of the modifying agent present inside the pores also affect the adsorption behavior significantly and hence, their control can be used to further tune the adsorptive separation of CO_2 from gas mixtures.

8.2 Future Directions

Based on the outcome of the studies carried out in this thesis, the following areas appear promising and may be explored in the future:

- Density Functional Theory (DFT) and Quantum Chemical Investigations: Binding energy between adsorbates and adsorbent can be determined using periodic DFT calculations to get more accurate estimates for screening best adsorbents for CO_2 capture. Further, in systems where amine is present (e.g. grafted or physically incorporated in the mesopores), studying adsorption using classical simulation methods is not convenient due to the formation of chemical bonds between the amine groups and CO_2 molecules. For such systems, DFT calculations may be employed for studying the adsorbate-adsorbent interactions in more detail. Accurate representation of MOFs by classical force fields is difficult to achieve. Thus,

gas interactions with MOFs can also be explored using DFT and quantum chemical calculations.

- Pore-Modification by Ionic Liquids and Deep Eutectic Solvents (DES): The studies reported in chapter 5 show that ionic liquids can have greater affinity for CO_2 than N_2 or CH_4. Thus, pore modification of mesoporous silica using other solvents such as DES and other classes of ionic liquids such as imidazolium, pyridinium etc. can be investigated for studying and developing a model potential candidates for CO_2 capture. Thus, the future scope of this work can be the study of the confinement of DES and other families of ILs in MCM-41, as well as in large pore silica materials such as SBA-15, and the subsequent effect on CO_2 separation.
- Adsorption of Volatile Organic Compounds (VOCs): Computer simulations can be used to study the adsorption of VOCs on functionalized MOFs to explore their potential for treatment of VOC mixtures. In particular, computational screening of appropriate functional groups most effective for removal of certain VOCs can be performed. Classical simulation techniques such as GCMC can be used in conjunction with quantum techniques such as DFT for better accuracy.

REFERENCES

[1] A. Garg, P.R. Shukla, B. Kankal, D. Mahapatra, CO_2 emission in India: trends and management at sectoral, sub-regional and plant levels, Carbon Manag. 8 (2017) 111–123. doi:10.1080/17583004.2017.1306406.

[2] A. Chakrabarti, R.K. Arora, India's Energy Security: Critical Considerations, Glob. Bus. Rev. 17 (2016) 1480–1496. doi:10.1177/0972150916660443.

[3] Petroleum Planning and Analysis Cell, http://ppac.org.in/.

[4] D.M. D'Alessandro, B. Smit, J.R. Long, Carbon Dioxide Capture: Prospects for New Materials, Angew. Chemie Int. Ed. 49 (2010) 6058–6082. doi:10.1002/anie.201000431.

[5] J.F. Brennecke, B.E. Gurkan, Ionic Liquids for CO_2 Capture and Emission Reduction, J. Phys. Chem. Lett. 1 (2010) 3459–3464. doi:10.1021/jz1014828.

[6] F. Karadas, M. Atilhan, S. Aparicio, Review on the Use of Ionic Liquids (ILs) as Alternative Fluids for CO_2 Capture and Natural Gas Sweetening, Energy & Fuels. 24 (2010) 5817–5828. doi:10.1021/ef1011337.

[7] V.M. A. Rojey, C. Jaffret, Cornot-Grandolphe, B.Durand, Jullian . S, Natural Gas Production Processing Transport, Editions Technip, Paris, 1994.

[8] M. Hedayat, M. Soltanieh, S.A. Mousavi, Simultaneous separation of H 2 S and CO_2 from natural gas by hollow fiber membrane contactor using mixture of alkanolamines, J. Memb. Sci. 377 (2011) 191–197. doi:10.1016/j.memsci.2011.04.051.

[9] S. Sridhar, B. Smitha, T.M. Aminabhavi, Separation of Carbon Dioxide from Natural Gas

Mixtures through Polymeric Membranes—A Review, Sep. Purif. Rev. 36 (2007) 113–174. doi:10.1080/15422110601165967.

[10] M.B. Shiflett, A.M.S. Niehaus, A. Yokozeki, Separation of CO_2 and H_2S Using Room-Temperature Ionic Liquid [bmim][MeSO 4], J. Chem. Eng. Data. 55 (2010) 4785–4793. doi:10.1021/je1004005.

[11] C. Zhang, Z. Sun, S. Chen, B. Wang, Enriching blast furnace gas by removing carbon dioxide, J. Environ. Sci. 25 (2013) S196–S200. doi:10.1016/S1001-0742(14)60655-0.

[12] T. Islamoglu, T. Kim, Z. Kahveci, O.M. El-Kadri, H.M. El-Kaderi, Systematic Postsynthetic Modification of Nanoporous Organic Frameworks for Enhanced CO_2 Capture from Flue Gas and Landfill Gas, J. Phys. Chem. C. 120 (2016) 2592–2599. doi:10.1021/acs.jpcc.5b12247.

[13] M. Ramdin, T.W. de Loos, T.J.H. Vlugt, State-of-the-Art of CO_2 Capture with Ionic Liquids, Ind. Eng. Chem. Res. 51 (2012) 8149–8177. doi:10.1021/ie3003705.

[14] A. Dąbrowski, Adsorption - From theory to practice, Adv. Colloid Interface Sci. 93 (2001) 135–224. doi:10.1016/S0001-8686(00)00082-8

[15] E.O. Pedram, A.L. Hines, Pure vapor adsorption of water on Mobil Sorbead R silica gel, J. Chem. Eng. Data. 28 (1983) 11–14. doi:10.1021/je00031a004.

[16] A.H. Berger, A.S. Bhown, Comparing Physisorption and Chemisorption Solid Sorbents for use Separating CO_2 from Flue Gas using Temperature Swing Adsorption, Energy Procedia. 4 (2011) 562–567. doi:10.1016/j.egypro.2011.01.089.

[17] A. Das, P.D. Southon, M. Zhao, C.J. Kepert, A.T. Harris, D.M. D'Alessandro, Carbon dioxide adsorption by physisorption and chemisorption interactions in piperazine-grafted Ni2(dobdc) (dobdc = 1,4-dioxido-2,5-benzenedicarboxylate), Dalt. Trans. 41 (2012) 11739. doi:10.1039/c2dt31112g.

[18] V. Bolis, C. Busco, P. Ugliengo, Thermodynamic Study of Water Adsorption in High-Silica Zeolites, J. Phys. Chem. B. 110 (2006) 14849–14859. doi:10.1021/jp061078q.

[19] E.O. Wiig, A.J. Juhola, The Adsorption of Water Vapor on Activated Charcoal, J. Am. Chem. Soc. 71 (1949) 561–568. doi:10.1021/ja01170a051.

[20] O.K. Farha, I. Eryazici, N.C. Jeong, B.G. Hauser, C.E. Wilmer, A.A. Sarjeant, R.Q. Snurr, S.T. Nguyen, A.Ö. Yazaydın, J.T. Hupp, Metal–Organic Framework Materials with Ultrahigh Surface Areas: Is the Sky the Limit?, J. Am. Chem. Soc. 134 (2012) 15016–15021. doi:10.1021/ja3055639.

[21] H. Furukawa, N. Ko, Y.B. Go, N. Aratani, S.B. Choi, E. Choi, A.O. Yazaydin, R.Q. Snurr, M. O'Keeffe, J. Kim, O.M. Yaghi, Ultrahigh Porosity in Metal-Organic Frameworks, Science (80). 329 (2010) 424–428. doi:10.1126/science.1192160.

[22] J. Li, J. Sculley, H. Zhou, Metal–Organic Frameworks for Separations, Chem. Rev. 112 (2012) 869–932. doi:10.1021/cr200190s.

[23] J. Shen, G. Liu, K. Huang, W. Jin, K. Lee, N. Xu, Membranes with Fast and Selective Gas-Transport Channels of Laminar Graphene Oxide for Efficient CO_2 Capture, Angew. Chemie Int. Ed. (2014) n/a-n/a. doi:10.1002/anie.201409563.

[24] D. V Kosynkin, A.L. Higginbotham, A. Sinitskii, J.R. Lomeda, A. Dimiev, B.K. Price, J.M. Tour, Longitudinal unzipping of carbon nanotubes to form graphene nanoribbons, Nature. 458 (2009) 872–876. doi:10.1038/nature07872.

[25] Z. Bao, L. Yu, Q. Ren, X. Lu, S. Deng, Adsorption of CO_2 and CH_4 on a magnesium-based metal organic framework, J. Colloid Interface Sci. 353 (2011) 549–556. doi:10.1016/j.jcis.2010.09.065.

[26] A.O. Yazaydın, R.Q. Snurr, T.-H. Park, K. Koh, J. Liu, M.D. LeVan, A.I. Benin, P. Jakubczak, M. Lanuza, D.B. Galloway, J.J. Low, R.R. Willis, Screening of Metal−Organic Frameworks for Carbon Dioxide Capture from Flue Gas Using a Combined Experimental and Modeling Approach, J. Am. Chem. Soc. 131 (2009) 18198–18199. doi:10.1021/ja9057234.

[27] A.O. Yazaydın, A.I. Benin, S.A. Faheem, P. Jakubczak, J.J. Low, R.R. Willis, R.Q. Snurr, Enhanced CO_2 Adsorption in Metal-Organic Frameworks via Occupation of Open-Metal Sites by Coordinated Water Molecules, Chem. Mater. 21 (2009) 1425–1430. doi:10.1021/cm900049x.

[28] T.M. McDonald, D.M. D'Alessandro, R. Krishna, J.R. Long, Enhanced carbon dioxide capture upon incorporation of N,N′-dimethylethylenediamine in the metal–organic framework CuBTTri, Chem. Sci. 2 (2011) 2022. doi:10.1039/c1sc00354b.

[29] R. Banerjee, H. Furukawa, D. Britt, C. Knobler, M. O'Keeffe, O.M. Yaghi, Control of Pore Size and Functionality in Isoreticular Zeolitic Imidazolate Frameworks and their Carbon Dioxide Selective Capture Properties, J. Am. Chem. Soc. 131 (2009) 3875–3877.

doi:10.1021/ja809459e.

[30] W. Morris, B. Leung, H. Furukawa, O.K. Yaghi, N. He, H. Hayashi, Y. Houndonougbo, M. Asta, B.B. Laird, O.M. Yaghi, A Combined Experimental−Computational Investigation of Carbon Dioxide Capture in a Series of Isoreticular Zeolitic Imidazolate Frameworks, J. Am. Chem. Soc. 132 (2010) 11006–11008. doi:10.1021/ja104035j.

[31] Z. Zhao, Z. Li, Y.S. Lin, Adsorption and Diffusion of Carbon Dioxide on Metal−Organic Framework (MOF-5), Ind. Eng. Chem. Res. 48 (2009) 10015–10020. doi:10.1021/ie900665f.

[32] P.L. Llewellyn, S. Bourrelly, C. Serre, Y. Filinchuk, G. Férey, How Hydration Drastically Improves Adsorption Selectivity for CO_2 over CH_4 in the Flexible Chromium Terephthalate MIL-53, Angew. Chemie Int. Ed. 45 (2006) 7751–7754. doi:10.1002/anie.200602278.

[33] A.R. Millward, O.M. Yaghi, Metal−Organic Frameworks with Exceptionally High Capacity for Storage of Carbon Dioxide at Room Temperature, J. Am. Chem. Soc. 127 (2005) 17998–17999. doi:10.1021/ja0570032.

[34] P. Pachfule, R. Das, P. Poddar, R. Banerjee, Structural, Magnetic, and Gas Adsorption Study of a Two-Dimensional Tetrazole-Pyrimidine Based Metal−Organic Framework, Cryst. Growth Des. 10 (2010) 2475–2478. doi:10.1021/cg1003726.

[35] Z. Hu, A. Nalaparaju, Y. Peng, J. Jiang, D. Zhao, Modulated Hydrothermal Synthesis of UiO-66(Hf)-Type Metal–Organic Frameworks for Optimal Carbon Dioxide Separation, Inorg. Chem. 55 (2016) 1134–1141. doi:10.1021/acs.inorgchem.5b02312.

[36] R. Lin, A. Ladshaw, Y. Nan, J. Liu, S. Yiacoumi, C. Tsouris, D.W. DePaoli, L.L. Tavlarides, Isotherms for Water Adsorption on Molecular Sieve 3A: Influence of Cation Composition, Ind. Eng. Chem. Res. 54 (2015) 10442–10448. doi:10.1021/acs.iecr.5b01411.

[37] T.B. Reed, D.W. Breck, Crystalline Zeolites. II. Crystal Structure of Synthetic Zeolite, Type A, J. Am. Chem. Soc. 78 (1956) 5972–5977. doi:10.1021/ja01604a002.

[38] T. Willhammar, J. Sun, W. Wan, P. Oleynikov, D. Zhang, X. Zou, M. Moliner, J. Gonzalez, C. Martínez, F. Rey, A. Corma, Structure and catalytic properties of the most complex intergrown zeolite ITQ-39 determined by electron crystallography, Nat. Chem. 4 (2012) 188–194. doi:10.1038/nchem.1253.

[39] T. Yanagisawa, T. Shimizu, K. Kuroda, C. Kato, The Preparation of Alkyltriinethylaininonium–Kaneinite Complexes and Their Conversion to Microporous Materials, Bull. Chem. Soc. Jpn. 63 (1990) 988–992. doi:10.1246/bcsj.63.988.

[40] C.T. Kresge, M.E. Leonowicz, W.J. Roth, J.C. Vartuli, J.S. Beck, Ordered mesoporous molecular sieves synthesized by a liquid-crystal template mechanism, Nature. 359 (1992) 710–712. doi:10.1038/359710a0.

[41] C.T. Kresge, W.J. Roth, The discovery of mesoporous molecular sieves from the twenty year perspective, Chem. Soc. Rev. 42 (2013) 3663. doi:10.1039/c3cs60016e.

[42] E.B. Rinker, S.S. Ashour, O.C. Sandall, Absorption of Carbon Dioxide into Aqueous Blends of Diethanolamine and Methyldiethanolamine, Ind. Eng. Chem. Res. 39 (2000) 4346–4356. doi:10.1021/ie990850r.

[43] R.J. Littel, G.F. Versteeg, W.P.M. Van Swaaij, Kinetics of CO_2 with primary and secondary amines in aqueous solutions—I. Zwitterion deprotonation kinetics for DEA and DIPA in aqueous blends of alkanolamines, Chem. Eng. Sci. 47 (1992) 2027–2035. doi:10.1016/0009-2509(92)80319-8.

[44] T.C. dos Santos, S. Bourrelly, P.L. Llewellyn, J.W. de M. Carneiro, C. Machado Ronconi, Adsorption of CO_2 on amine-functionalised MCM-41: experimental and theoretical studies, Phys. Chem. Chem. Phys. 17 (2015) 11095–11102. doi:10.1039/C5CP00581G.

[45] W. Klinthong, K. Chao, C. Tan, CO_2 Capture by As-Synthesized Amine-Functionalized MCM-41 Prepared through Direct Synthesis under Basic Condition, Ind. Eng. Chem. Res. 52 (2013) 9834–9842. doi:10.1021/ie400865n.

[46] H.Y. Huang, R.T. Yang, D. Chinn, C.L. Munson, Amine-Grafted MCM-48 and Silica Xerogel as Superior Sorbents for Acidic Gas Removal from Natural Gas, Ind. Eng. Chem. Res. 42 (2003) 2427–2433. doi:10.1021/ie020440u.

[47] H. Chen, Z. Liang, X. Yang, Z. Zhang, Z. Zhang, Experimental Investigation of CO_2 Capture Capacity: Exploring Mesoporous Silica SBA-15 Material Impregnated with Monoethanolamine and Diethanolamine, Energy & Fuels. 30 (2016) 9554–9562. doi:10.1021/acs.energyfuels.6b01298.

[48] L. Wei, Z. Gao, Y. Jing, Y. Wang, Adsorption of CO_2 from Simulated Flue Gas on Pentaethylenehexamine-Loaded Mesoporous Silica Support Adsorbent, Ind. Eng. Chem. Res. 52 (2013) 14965–14974. doi:10.1021/ie402162x.

[49] R. Kishor, A.K. Ghoshal, Amine-Modified Mesoporous Silica for CO_2 Adsorption: The Role of Structural Parameters, Ind. Eng. Chem. Res. 56 (2017) 6078–6087. doi:10.1021/acs.iecr.7b00890.

[50] V. Zeleňák, M. Badaničová, D. Halamová, J. Čejka, A. Zukal, N. Murafa, G. Goerigk, Amine-modified ordered mesoporous silica: Effect of pore size on carbon dioxide capture, Chem. Eng. J. 144 (2008) 336–342. doi:10.1016/j.cej.2008.07.025.

[51] A. Demessence, D.M. D'Alessandro, M.L. Foo, J.R. Long, Strong CO_2 Binding in a Water-Stable, Triazolate-Bridged Metal−Organic Framework Functionalized with Ethylenediamine, J. Am. Chem. Soc. 131 (2009) 8784–8786. doi:10.1021/ja903411w.

[52] W. Klinthong, K.J. Chao, C.S. Tan, CO2 capture by as-synthesized amine-functionalized MCM-41 prepared through direct synthesis under basic condition, Ind. Eng. Chem. Res. 52 (2013) 9834–9842. doi:10.1021/ie400865n.

[53] D. Frenkel, B. Smit, Understanding Molecular Simulation From Algorithms to Applications, (1996). San Diego

[54] M. MG, Monte Carlo for complex chemical systems (MCCCS) towhee, version 6.2.12., (2010).

[55] D. Dubbeldam, S. Calero, D.E. Ellis, R.Q. Snurr, RASPA: molecular simulation software for adsorption and diffusion in flexible nanoporous materials, Mol. Simul. 42 (2016) 81–101. doi:10.1080/08927022.2015.1010082.

[56] S.A. Somers, A. V. McCormick, H.T. Davis, Superselectivity and solvation forces of a two

component fluid adsorbed in slit micropores, J. Chem. Phys. 99 (1993) 9890–9898. doi:10.1063/1.465473.

[57] R.F. Cracknell, D. Nicholson, N. Quirke, A grand canonical Monte Carlo study of Lennard-Jones mixtures in slit shaped pores, Mol. Phys. 80 (1993) 885–897. doi:10.1080/00268979300102741.

[58] B.A. Wells, A.L. Chaffee, Ewald Summation for Molecular Simulations, J. Chem. Theory Comput. 11 (2015) 3684–3695. doi:10.1021/acs.jctc.5b00093.

[59] T.J. Barton, L.M. Bull, W.G. Klemperer, D.A. Loy, B. McEnaney, M. Misono, P.A. Monson, G. Pez, G.W. Scherer, J.C. Vartuli, O.M. Yaghi, Tailored Porous Materials, Chem. Mater. 11 (1999) 2633–2656. doi:10.1021/cm9805929.

[60] P. Mishra, S. Mekala, F. Dreisbach, B. Mandal, S. Gumma, Adsorption of CO_2 , CO , CH_4 and N_2 on a zinc based metal organic framework, Sep. Purif. Technol. 94 (2012) 124–130. doi:10.1016/j.seppur.2011.09.041.

[61] P. Chowdhury, S. Mekala, F. Dreisbach, S. Gumma, Microporous and Mesoporous Materials Adsorption of CO , CO_2 and CH_4 on Cu-BTC and MIL-101 metal organic frameworks : Effect of open metal sites and adsorbate polarity, Microporous Mesoporous Mater. 152 (2012) 246–252. doi:10.1016/j.micromeso.2011.11.022.

[62] A. Poursaeidesfahani, A. Torres-Knoop, M. Rigutto, N. Nair, D. Dubbeldam, T.J.H. Vlugt, Computation of the Heat and Entropy of Adsorption in Proximity of Inflection Points, J. Phys. Chem. C. 120 (2016) 1727–1738. doi:10.1021/acs.jpcc.5b11606.

[63] Accelrys Inc., Materials Studio, 7.0, San Diego: Accelrys Inc., 2013.

[64] A.L. Myers, J.M. Prausnitz, Thermodynamics of mixed-gas adsorption, AIChE J. 11 (1965) 121–127. doi:10.1002/aic.690110125.

[65] Y. He, N.A. Seaton, Experimental and Computer Simulation Studies of the Adsorption of Ethane, Carbon Dioxide, and Their Binary Mixtures in MCM-41, Langmuir. 19 (2003) 10132–10138. doi:10.1021/la035047n.

[66] He, N.A. Seaton, Heats of Adsorption and Adsorption Heterogeneity for Methane, Ethane, and Carbon Dioxide in MCM-41, Langmuir. 22 (2006) 1150–1155. doi:10.1021/la052237k.

[67] Z. Luan, C. Cheng, W. Zhou, J. Klinowski, Mesopore Molecular Sieve MCM-41 Containing Framework Aluminum, J. Phys. Chem. 99 (1995) 1018–1024. doi:10.1021/j100003a026.

[68] P.B. Amama, S. Lim, D. Ciuparu, Y. Yang, L. Pfefferle, G.L. Haller, Synthesis, Characterization, and Stability of Fe−MCM-41 for Production of Carbon Nanotubes by Acetylene Pyrolysis, J. Phys. Chem. B. 109 (2005) 2645–2656. doi:10.1021/jp047158g.

[69] J. Yun, T. Düren, F.J. Keil, N.A. Seaton, Adsorption of Methane, Ethane, and Their Binary Mixtures on MCM-41: Experimental Evaluation of Methods for the Prediction of Adsorption Equilibrium, Langmuir. 18 (2002) 2693–2701. doi:10.1021/la0155855.

[70] S. Zhuo, Y. Huang, J. Hu, H. Liu, Y. Hu, J. Jiang, Computer Simulation for Adsorption of CO_2, N_2 and Flue Gas in a Mimetic MCM-41, J. Phys. Chem. C. 112 (2008) 11295–11300. doi:10.1021/jp803428n.

[71] S. Builes, L.F. Vega, Understanding CO_2 Capture in Amine-Functionalized MCM-41 by Molecular Simulation, J. Phys. Chem. C. 116 (2012) 3017–3024. doi:10.1021/jp210494f.

[72] Y. Jing, L. Wei, Y. Wang, Y. Yu, Molecular simulation of MCM-41 : Structural properties and adsorption of CO_2 , N_2 and flue gas, Chem. Eng. J. 220 (2013) 264–275. doi:10.1016/j.cej.2012.12.078.

[73] A. Pajzderska, M.A. Gonzalez, J. Mielcarek, J. Wąsicki, Water Behavior in MCM-41 As a Function of Pore Filling and Temperature Studied by NMR and Molecular Dynamics Simulations, J. Phys. Chem. C. 118 (2014) 23701–23710. doi:10.1021/jp505490c.

[74] L.N. Ho, Y. Schuurman, D. Farrusseng, B. Coasne, Solubility of Gases in Water Confined in Nanoporous Materials: ZSM-5, MCM-41, and MIL-100, J. Phys. Chem. C. 119 (2015) 21547–21554. doi:10.1021/acs.jpcc.5b06660.

[75] J.A. Mason, T.M. McDonald, T. Bae, J.E. Bachman, K. Sumida, J.J. Dutton, S.S. Kaye, J.R. Long, Application of a High-Throughput Analyzer in Evaluating Solid Adsorbents for Post-Combustion Carbon Capture via Multicomponent Adsorption of CO_2 , N_2 , and H_2O, J. Am. Chem. Soc. 137 (2015) 4787–4803. doi:10.1021/jacs.5b00838.

[76] F. Tielens, C. Gervais, J.F. Lambert, F. Mauri, D. Costa, Ab Initio Study of the Hydroxylated Surface of Amorphous Silica: A Representative Model, Chem. Mater. 20 (2008) 3336–3344. doi:10.1021/cm8001173.

[77] R.T. Downs, D.C. Palmer, The pressure behavior of alpha cristobalite, 79 (1994) 9–14.

[78] P. Ugliengo, M. Sodupe, F. Musso, I.J. Bush, R. Orlando, R. Dovesi, Realistic Models of

Hydroxylated Amorphous Silica Surfaces and MCM-41 Mesoporous Material Simulated by Large-scale Periodic B3LYP Calculations, Adv. Mater. 20 (2008) 4579–4583. doi:10.1002/adma.200801489.

[79] S. Loganathan, M. Tikmani, A.K. Ghoshal, Novel Pore-Expanded MCM-41 for CO_2 Capture: Synthesis and Characterization, Langmuir. 29 (2013) 3491–3499. doi:10.1021/la400109j.

[80] S.L. Mayo, B.D. Olafson, W.A. Goddard, DREIDING: a generic force field for molecular simulations, J. Phys. Chem. 94 (1990) 8897–8909. doi:10.1021/j100389a010.

[81] A.K. Rappe, W.A. Goddard, Charge equilibration for molecular dynamics simulations, J. Phys. Chem. 95 (1991) 3358–3363. doi:10.1021/j100161a070.

[82] M.L Conolly, Analytical Molecular Surface Calculation, (1983). doi:0021-8898/83/050548-12.

[83] D. Dubbeldam, A. Torres-knoop, K.S. Walton, D. Dubbeldam, A. Torres-knoop, K.S.W. On, On the inner workings of Monte Carlo codes, Mol. Simul. 39 (2017) 1253–1292. doi:10.1080/08927022.2013.819102.

[84] J.J. Potoff, J.I. Siepmann, Vapor–liquid equilibria of mixtures containing alkanes, carbon dioxide, and nitrogen, AIChE J. 47 (2001) 1676–1682. doi:10.1002/aic.690470719.

[85] L. Zhang, J.I. Siepmann, Direct calculation of Henry's law constants from Gibbs ensemble Monte Carlo simulations: nitrogen, oxygen, carbon dioxide and methane in ethanol, Theor. Chem. Acc. 115 (2006) 391–397. doi:10.1007/s00214-005-0073-1.

[86] H.J.C. Berendsen, J.R. Grigera, T.P. Straatsma, The missing term in effective pair potentials, J. Phys. Chem. 91 (1987) 6269–6271. doi:10.1021/j100308a038.

[87] K.A. Northcott, K. Miyakawa, S. Oshima, Y. Komatsu, J.M. Perera, G.W. Stevens, The adsorption of divalent metal cations on mesoporous silicate MCM-41, Chem. Eng. J. 157 (2010) 25–28. doi:10.1016/j.cej.2009.10.038.

[88] S. Oshima, J.M. Perera, K.A. Northcott, H. Kokusen, G.W. Stevens, Y. Komatsu, Adsorption Behavior of Cadmium(II) and Lead(II) on Mesoporous Silicate MCM-41, Sep. Sci. Technol. 41 (2006) 1635–1643. doi:10.1080/01496390600674786.

[89] Y. Xu, W.Y. Ching, Electronic and optical properties of all polymorphic forms of silicon dioxide, Phys. Rev. B. 44 (1991) 11048–11059. doi:10.1103/PhysRevB.44.11048.

[90] T.J.H. Vlugt, E. García-Pérez, D. Dubbeldam, S. Ban, S. Calero, Computing the Heat of Adsorption using Molecular Simulations: The Effect of Strong Coulombic Interactions, J. Chem. Theory Comput. 4 (2008) 1107–1118. doi:10.1021/ct700342k.

[91] S. Zhou, C. Guo, Z. Wu, M. Wang, Z. Wang, S. Wei, S. Li, X. Lu, Applied Surface Science Edge-functionalized nanoporous carbons for high adsorption capacity and selectivity of CO_2 over N_2, Appl. Surf. Sci. 410 (2017) 259–266. doi:10.1016/j.apsusc.2017.03.136.

[92] B. Yuan, X. Wu, Y. Chen, J. Huang, H. Luo, S. Deng, Adsorption of CO_2 , CH_4 , and N_2 on Ordered Mesoporous Carbon: Approach for Greenhouse Gases Capture and Biogas Upgrading, Environ. Sci. Technol. 47 (2013) 5474–5480. doi:10.1021/es4000643.

[93] Q. Yang, C. Xue, C. Zhong, J. Chen, Molecular simulation of separation of CO_2 from flue

gases in CU-BTC metal-organic framework, AIChE J. 53 (2007) 2832–2840. doi:10.1002/aic.11298.

[94] H. Wang, Y. Duan, Y. Li, Y. Xue, M. Liu, Investigation of mercury emission and its speciation from an oxy-fuel circulating fluidized bed combustor with recycled warm flue gas, Chem. Eng. J. 300 (2016) 230–235. doi:10.1016/j.cej.2016.04.131.

[95] E. Di Biase, L. Sarkisov, Molecular simulation of multi-component adsorption processes related to carbon capture in a high surface area , disordered activated carbon, Carbon N. Y. 94 (2015) 27–40. doi:10.1016/j.carbon.2015.06.056.

[96] P.I. Ravikovitch, A. V Neimark, Characterization of Micro- and Mesoporosity in SBA-15 Materials from Adsorption Data by the NLDFT Method, J. Phys. Chem. B. 105 (2001) 6817–6823. doi:10.1021/jp010621u.

[97] N. Hiyoshi, K. Yogo, T. Yashima, Adsorption characteristics of carbon dioxide on organically functionalized SBA-15, Microporous Mesoporous Mater. 84 (2005) 357–365. doi:10.1016/j.micromeso.2005.06.010.

[98] B.L. Newalkar, N. V Choudary, P. Kumar, S. Komarneni, T.S.G. Bhat, Exploring the Potential of Mesoporous Silica, SBA-15, as an Adsorbent for Light Hydrocarbon Separation, Chem. Mater. 14 (2002) 304–309. doi:10.1021/cm0106466.

[99] B.L. Newalkar, N. V Choudary, U.T. Turaga, R.P. Vijayalakshmi, P. Kumar, S. Komarneni, T.S.G. Bhat, Potential Adsorbent for Light Hydrocarbon Separation: Role of SBA-15 Framework Porosity, Chem. Mater. 15 (2003) 1474–1479. doi:10.1021/cm020889d.

[100] M. Hartmann, A. Vinu, Mechanical Stability and Porosity Analysis of Large-Pore SBA-15 Mesoporous Molecular Sieves by Mercury Porosimetry and Organics Adsorption, Langmuir. 18 (2002) 8010–8016. doi:10.1021/la025782j.

[101] E. Van Bavel, V. Meynen, P. Cool, K. Lebeau, E.F. Vansant, Adsorption of Hydrocarbons on Mesoporous SBA-15 and PHTS Materials, Langmuir. 21 (2005) 2447–2453. doi:10.1021/la0474417.

[102] H. Vinh-Thang, Q. Huang, M. Eić, D. Trong-On, S. Kaliaguine, Adsorption of C 7 Hydrocarbons on Biporous SBA-15 Mesoporous Silica, Langmuir. 21 (2005) 5094–5101. doi:10.1021/la050135o.

[103] L. Wang, R.T. Yang, Increasing selective CO2 adsorption on amine-grafted SBA-15 by increasing silanol density, J. Phys. Chem. C. 115 (2011) 21264–21272. doi:10.1021/jp206976d.

[104] J.G. Harris, K.H. Yungt, Carbon Dioxide â€TM s Liquid-Vapor Coexistence Curve and Critical Properties As Predicted by a Simple Molecular Model, (1995) 12021–12024.

[105] M.G. Martin, J.I. Siepmann, Transferable Potentials for Phase Equilibria. 1. United-Atom Description of n-Alkanes, J. Phys. Chem. B. 5647 (1998) 2569–2577. doi:10.1021/jp972543+.

[106] L. Sarkisov, A. Harrison, Computational structure characterisation tools in application to ordered and disordered porous materials, Mol. Simul. 37 (2011) 1248–1257. doi:10.1080/08927022.2011.592832.

[107] J.-R. Li, R.J. Kuppler, H.-C. Zhou, Selective gas adsorption and separation in metal–organic frameworks, Chem. Soc. Rev. 38 (2009) 1477. doi:10.1039/b802426j.

[108] J. Liu, J. Tian, P.K. Thallapally, B.P. McGrail, Selective CO_2 Capture from Flue Gas Using Metal–Organic Frameworks—A Fixed Bed Study, J. Phys. Chem. C. 116 (2012) 9575–9581. doi:10.1021/jp300961j.

[109] K. Yu, K. Kiesling, J.R. Schmidt, Trace Flue Gas Contaminants Poison Coordinatively Unsaturated Metal–Organic Frameworks: Implications for CO_2 Adsorption and Separation, J. Phys. Chem. C. 116 (2012) 20480–20488. doi:10.1021/jp307894e.

[110] J. Yu, L. Xie, J. Li, Y. Ma, J.M. Seminario, P.B. Balbuena, CO_2 Capture and Separations Using MOFs: Computational and Experimental Studies, Chem. Rev. 117 (2017) 9674–9754. doi:10.1021/acs.chemrev.6b00626.

[111] Z. Liu, Y. Wu, B. Liu, S.C. Oh, W. Fan, Y. Qian, H. Xi, Tuning the adsorption and separation properties of noble gases and N_2 in CuBTC by ligand functionalization, RSC Adv. 6 (2016) 91093–91101. doi:10.1039/C6RA08778G.

[112] B. Arstad, H. Fjellvåg, K.O. Kongshaug, O. Swang, R. Blom, Amine functionalised metal organic frameworks (MOFs) as adsorbents for carbon dioxide, Adsorption. 14 (2008) 755–762. doi:10.1007/s10450-008-9137-6.

[113] Y. Lin, C. Kong, L. Chen, Amine-functionalized metal–organic frameworks: structure, synthesis and applications, RSC Adv. 6 (2016) 32598–32614. doi:10.1039/C6RA01536K.

[114] J. Hu, J. Liu, Y. Liu, X. Yang, Improving Carbon Dioxide Storage Capacity of Metal

Organic Frameworks by Lithium Alkoxide Functionalization: A Molecular Simulation Study, J. Phys. Chem. C. 120 (2016) 10311–10319. doi:10.1021/acs.jpcc.6b01119.

[115] H.R. Abid, J. Shang, H. Ang, S. Wang, Amino-functionalized Zr-MOF nanoparticles for adsorption of CO_2 and CH_4, Int. J. Smart Nano Mater. 4 (2013) 72–82. doi:10.1080/19475411.2012.688773.

[116] T.A. Makal, X. Wang, H. Zhou, Tuning the Moisture and Thermal Stability of Metal–Organic Frameworks through Incorporation of Pendant Hydrophobic Groups, Cryst. Growth Des. 13 (2013) 4760–4768. doi:10.1021/cg4009224.

[117] A.J. Howarth, Y. Liu, P. Li, Z. Li, T.C. Wang, J.T. Hupp, O.K. Farha, Chemical, thermal and mechanical stabilities of metal–organic frameworks, Nat. Rev. Mater. 1 (2016) 15018. doi:10.1038/natrevmats.2015.18.

[118] D.-M. Chen, J. Tian, M. Chen, C. Liu, M. Du, Moisture-Stable Zn(II) Metal–Organic Framework as a Multifunctional Platform for Highly Efficient CO_2 Capture and Nitro Pollutant Vapor Detection, ACS Appl. Mater. Interfaces. 8 (2016) 18043–18050. doi:10.1021/acsami.6b04611.

[119] M. Vallet-Regi, A. Rámila, R.P. del Real, J. Pérez-Pariente, A New Property of MCM-41: Drug Delivery System, Chem. Mater. 13 (2001) 308–311. doi:10.1021/cm0011559.

[120] S.-H. Wu, C.-Y. Mou, H.-P. Lin, Synthesis of mesoporous silica nanoparticles, Chem. Soc. Rev. 42 (2013) 3862. doi:10.1039/c3cs35405a.

[121] T. Heikkilä, J. Salonen, J. Tuura, M.S. Hamdy, G. Mul, N. Kumar, T. Salmi, D.Y. Murzin,

L. Laitinen, A.M. Kaukonen, J. Hirvonen, V.P. Lehto, Mesoporous silica material TUD-1 as a drug delivery system, Int. J. Pharm. 331 (2007) 133–138. doi:10.1016/j.ijpharm.2006.09.019.

[122] J. Mondal, M. Nandi, A. Modak, A. Bhaumik, Functionalized mesoporous materials as efficient organocatalysts for the syntheses of xanthenes, J. Mol. Catal. A Chem. 363–364 (2012) 254–264. doi:10.1016/j.molcata.2012.06.017.

[123] M. Vallet-Regí, F. Balas, D. Arcos, Mesoporous Materials for Drug Delivery, Angew. Chemie Int. Ed. 46 (2007) 7548–7558. doi:10.1002/anie.200604488.

[124] S. Wang, Microporous and Mesoporous Materials Ordered mesoporous materials for drug delivery, Microporous Mesoporous Mater. 117 (2009) 1–9. doi:10.1016/j.micromeso.2008.07.002.

[125] J. Jiao, J. Cao, Y. Xia, L. Zhao, Improvement of adsorbent materials for CO_2 capture by amine functionalized mesoporous silica with worm-hole framework structure, Chem. Eng. J. 306 (2016) 9–16. doi:10.1016/j.cej.2016.07.041.

[126] G. Wang, A.N. Otuonye, E.A. Blair, K. Denton, Z. Tao, T.A. Ã, Journal of Solid State Chemistry Functionalized mesoporous materials for adsorption and release of different drug molecules : A comparative study, J. Solid State Chem. 182 (2009) 1649–1660. doi:10.1016/j.jssc.2009.03.034.

[127] S.I. Karpov, F. Roessner, V.F. Selemenev, Studies on functionalized mesoporous materials - Part I: Characterization of silylized mesoporous material of type MCM-41, J. Porous

Mater. 21 (2014) 449–457. doi:10.1007/s10934-014-9791-x.

[128] H.A. Santos, J. Salonen, L.M. Bimbo, V. Lehto, L. Peltonen, J. Hirvonen, Mesoporous materials as controlled drug delivery formulations, J. Drug Deliv. Sci. Technol. 21 (2011) 139–155. doi:10.1016/S1773-2247(11)50016-4.

[129] O.C. Vangeli, G.E. Romanos, K.G. Beltsios, D. Fokas, E.P. Kouvelos, K.L. Stefanopoulos, N.K. Kanellopoulos, Grafting of Imidazolium Based Ionic Liquid on the Pore Surface of Nanoporous Materials—Study of Physicochemical and Thermodynamic Properties, J. Phys. Chem. B. 114 (2010) 6480–6491. doi:10.1021/jp912205y.

[130] K.L. Stefanopoulos, G.E. Romanos, O.C. Vangeli, K. Mergia, N.K. Kanellopoulos, A. Koutsioubas, D. Lairez, Investigation of Confined Ionic Liquid in Nanostructured Materials by a Combination of SANS, Contrast-Matching SANS, and Nitrogen Adsorption, Langmuir. 27 (2011) 7980–7985. doi:10.1021/la201261r.

[131] H. Sanaeishoar, M. Sabbaghan, F. Mohave, Microporous and Mesoporous Materials Synthesis and characterization of micro-mesoporous MCM-41 using various ionic liquids as co-templates, Microporous Mesoporous Mater. 217 (2015) 219–224. doi:10.1016/j.micromeso.2015.06.027.

[132] A.K. Tripathi, Y.L. Verma, R.K. Singh, Thermal, electrical and structural studies on ionic liquid confined in ordered mesoporous MCM-41, J. Mater. Chem. A. 3 (2015) 23809–23820. doi:10.1039/C5TA05090A.

[133] J. Cheng, Y. Li, L. Hu, J. Zhou, K. Cen, CO_2 Adsorption Performance of Ionic Liquid [P

66614][2-Op] Loaded onto Molecular Sieve MCM-41 Compared to Pure Ionic Liquid in Biohythane/Pure CO_2 Atmospheres, Energy & Fuels. 30 (2016) 3251–3256. doi:10.1021/acs.energyfuels.5b02857.

[134] Y. Chen, Z. Hu, K.M. Gupta, J. Jiang, Ionic Liquid/Metal–Organic Framework Composite for CO_2 Capture: A Computational Investigation, J. Phys. Chem. C. 115 (2011) 21736–21742. doi:10.1021/jp208361p.

[135] Z. Li, Y. Xiao, W. Xue, Q. Yang, C. Zhong, Ionic Liquid/Metal–Organic Framework Composites for H 2 S Removal from Natural Gas: A Computational Exploration, J. Phys. Chem. C. 119 (2015) 3674–3683. doi:10.1021/acs.jpcc.5b00019.

[136] C.A. Daly, E.J. Berquist, T. Brinzer, S. Garrett-Roe, D.S. Lambrecht, S.A. Corcelli, Modeling Carbon Dioxide Vibrational Frequencies in Ionic Liquids: II. Spectroscopic Map, J. Phys. Chem. B. 120 (2016) 12633–12642. doi:10.1021/acs.jpcb.6b09509.

[137] Gaussian 09, Revision B.01, M. J. Frisch, G. W. Trucks, H. B. Schlegel, G. E. Scuseria, M. A. Robb, J. R. Cheeseman, G. Scalmani, V. Barone, G. A. Petersson, H. Nakatsuji, et al. Gaussian, Inc.,Wallingford CT, 2010.

[138] et al. Martínez L, Andrade R, Birgin EG, PACKMOL: a package for building initial configurations for molecular dynamics simulations., J. Comput. Chem. 30 (2009) 2157–2164.

[139] W.L. Jorgensen, D.S. Maxwell, J. Tirado-Rives, Development and Testing of the OPLS All-Atom Force Field on Conformational Energetics and Properties of Organic Liquids, J.

Am. Chem. Soc. 118 (1996) 11225–11236. doi:10.1021/ja9621760.

[140] N.A. McDonald, W.L. Jorgensen, Development of an All-Atom Force Field for Heterocycles. Properties of Liquid Pyrrole, Furan, Diazoles, and Oxazoles, J. Phys. Chem. B. 102 (1998) 8049–8059. doi:10.1021/jp981200o.

[141] W.L. Jorgensen, N.A. McDonald, Development of an all-atom force field for heterocycles. Properties of liquid pyridine and diazenes, J. Mol. Struct. THEOCHEM. 424 (1998) 145–155. doi:10.1016/S0166-1280(97)00237-6.

[142] R.C. Rizzo, W.L. Jorgensen, OPLS All-Atom Model for Amines: Resolution of the Amine Hydration Problem, J. Am. Chem. Soc. 121 (1999) 4827–4836. doi:10.1021/ja984106u.

[143] J.B. Haskins, W.R. Bennett, J.J. Wu, D.M. Hernández, O. Borodin, J.D. Monk, C.W. Bauschlicher, J.W. Lawson, Computational and Experimental Investigation of Li-Doped Ionic Liquid Electrolytes: [pyr14][TFSI], [pyr13][FSI], and [EMIM][BF 4], J. Phys. Chem. B. 118 (2014) 11295–11309. doi:10.1021/jp5061705.

[144] S. Plimpton, Fast Parallel Algorithms for Short-Range Molecular Dynamics, J. Comput. Phys. 117 (1995) 1–19.

[145] U.L. De Bruxelles, Numerical integration of the Cartesian Equations of Motion of a System with Constraints: Molecular Dynamics of n-Alkanes, 341 (1977).

[146] J.J. Gutiérrez-Sevillano, A. Caro-Pérez, D. Dubbeldam, S. Calero, Molecular simulation investigation into the performance of Cu–BTC metal–organic frameworks for carbon dioxide–methane separations, Phys. Chem. Chem. Phys. 13 (2011) 20453.

doi:10.1039/c1cp21761e.

[147] S. Chavan, J.G. Vitillo, D. Gianolio, O. Zavorotynska, B. Civalleri, S. Jakobsen, M.H. Nilsen, L. Valenzano, C. Lamberti, K.P. Lillerud, S. Bordiga, H 2 storage in isostructural UiO-67 and UiO-66 MOFs, Phys. Chem. Chem. Phys. 14 (2012) 1614–1626. doi:10.1039/C1CP23434J.

[148] D.N. Dybtsev, M.P. Yutkin, V.P. Fedin, Copper (II) camphorates with tunable pore size in metal organic frameworks, Russ. Chem. Bull. 58 (2009) 2246–2249. doi:1066?5285/09/5811?2246.

[149] H. Furukawa, K.E. Cordova, M. O'Keeffe, O.M. Yaghi, The Chemistry and Applications of Metal-Organic Frameworks, Science (80-.). 341 (2013) 1230444–1230444. doi:10.1126/science.1230444.

[150] Q. Zhai, X. Bu, X. Zhao, D. Li, P. Feng, Pore Space Partition in Metal–Organic Frameworks, Acc. Chem. Res. 50 (2017) 407–417. doi:10.1021/acs.accounts.6b00526.

[151] B.A. Wells, A.L. Chaffee, Modeling gas separation in metal-organic frameworks, Adsorption. 17 (2011) 255–264. doi:10.1007/s10450-010-9305-3.

[152] Z. Zhao, X. Ma, A. Kasik, Z. Li, Y.S. Lin, Gas Separation Properties of Metal Organic Framework (MOF-5) Membranes, Ind. Eng. Chem. Res. 52 (2013) 1102–1108. doi:10.1021/ie202777q.

[153] B. Li, H. Wen, W. Zhou, B. Chen, Porous Metal–Organic Frameworks for Gas Storage and Separation: What, How, and Why?, J. Phys. Chem. Lett. 5 (2014) 3468–3479.

doi:10.1021/jz501586e.

[154] B. Li, H. Wang, B. Chen, Microporous Metal-Organic Frameworks for Gas Separation, Chem. - An Asian J. 9 (2014) 1474–1498. doi:10.1002/asia.201400031.

[155] T. Rodenas, I. Luz, G. Prieto, B. Seoane, H. Miro, A. Corma, F. Kapteijn, F.X. Llabrés i Xamena, J. Gascon, Metal–organic framework nanosheets in polymer composite materials for gas separation, Nat. Mater. 14 (2015) 48–55. doi:10.1038/nmat4113.

[156] Y. Wang, D. Zhao, Beyond Equilibrium: Metal–Organic Frameworks for Molecular Sieving and Kinetic Gas Separation, Cryst. Growth Des. 17 (2017) 2291–2308. doi:10.1021/acs.cgd.7b00287.

[157] P. Horcajada, T. Chalati, C. Serre, B. Gillet, C. Sebrie, T. Baati, J.F. Eubank, D. Heurtaux, P. Clayette, C. Kreuz, J. Chang, Y.K. Hwang, V. Marsaud, P. Bories, L. Cynober, S. Gil, G. Férey, P. Couvreur, R. Gref, delivery and imaging, Nat. Mater. 9 (2009) 172–178. doi:10.1038/nmat2608.

[158] M.O. Rodrigues, M. V. de Paula, K.A. Wanderley, I.B. Vasconcelos, S. Alves, T.A. Soares, Metal organic frameworks for drug delivery and environmental remediation: A molecular docking approach, Int. J. Quantum Chem. 112 (2012) 3346–3355. doi:10.1002/qua.24211.

[159] X. Wang, Z. Dong, H. Cheng, S. Wan, W. Chen, M. Zou, J. Huo, H. Deng, X. Zhang, A multifunctional metal–organic framework based tumor targeting drug delivery system for cancer therapy, Nanoscale. 7 (2015) 16061–16070. doi:10.1039/C5NR04045K.

[160] D. Fairen-jimenez, Amorphous metal–organic frameworks for drug delivery,

Chem. Commun. 51 (2015) 13878–13881. doi:10.1039/C5CC05237H.

[161] S. Rojas, F.J. Carmona, C.R. Maldonado, P. Horcajada, T. Hidalgo, C. Serre, J.A.R. Navarro, E. Barea, Nanoscaled Zinc Pyrazolate Metal–Organic Frameworks as Drug-Delivery Systems, Inorg. Chem. 55 (2016) 2650–2663. doi:10.1021/acs.inorgchem.6b00045.

[162] X. Wu, J. Ma, H. Li, D. Chen, W. Gu, G. Yang, P. Cheng, Metal–organic framework biosensor with high stability and selectivity in a bio-mimic environment, Chem. Commun. 51 (2015) 9161–9164. doi:10.1039/C5CC02113H.

[163] J. He, H. Yang, Y. Zhang, J. Yu, L. Miao, Y. Song, L. Wang, Smart Nanocomposites of Cu-Hemin Metal-Organic Frameworks for Electrochemical Glucose Biosensing, Nat. Publ. Gr. (2016) 1–9. doi:10.1038/srep36637.

[164] X.-M. Lin, J. Niu, J. Lin, L. Wei, L. Hu, G. Zhang, Y. Cai, Lithium-Ion-Battery Anode Materials with Improved Capacity from a Metal–Organic Framework, Inorg. Chem. 55 (2016) 8244–8247. doi:10.1021/acs.inorgchem.6b01123.

[165] S.B. Kalidindi, S. Nayak, M.E. Briggs, S. Jansat, A.P. Katsoulidis, G.J. Miller, J.E. Warren, D. Antypov, F. Corà, B. Slater, M.R. Prestly, C. Martí-Gastaldo, M.J. Rosseinsky, Chemical and Structural Stability of Zirconium-based Metal-Organic Frameworks with Large Three-Dimensional Pores by Linker Engineering, Angew. Chemie Int. Ed. 54 (2015) 221–226. doi:10.1002/anie.201406501.

[166] H. Wu, T. Yildirim, W. Zhou, Exceptional Mechanical Stability of Highly Porous

Zirconium Metal–Organic Framework UiO-66 and Its Important Implications, J. Phys. Chem. Lett. 4 (2013) 925–930. doi:10.1021/jz4002345.

[167] J.H. Cavka, S. Jakobsen, U. Olsbye, N. Guillou, C. Lamberti, S. Bordiga, K.P. Lillerud, A New Zirconium Inorganic Building Brick Forming Metal Organic Frameworks with Exceptional Stability, J. Am. Chem. Soc. 130 (2008) 13850–13851. doi:10.1021/ja8057953.

[168] A. Schaate, P. Roy, A. Godt, J. Lippke, F. Waltz, M. Wiebcke, P. Behrens, Modulated Synthesis of Zr-Based Metal-Organic Frameworks: From Nano to Single Crystals, Chem. - A Eur. J. 17 (2011) 6643–6651. doi:10.1002/chem.201003211.

[169] M.J. Katz, Z.J. Brown, Y.J. Colón, P.W. Siu, K.A. Scheidt, R.Q. Snurr, J.T. Hupp, O.K. Farha, A facile synthesis of UiO-66, UiO-67 and their derivatives, Chem. Commun. 49 (2013) 9449. doi:10.1039/c3cc46105j.

[170] J.K. Bristow, D. Tiana, A. Walsh, Transferable Force Field for Metal–Organic Frameworks from First-Principles: BTW-FF, J. Chem. Theory Comput. 10 (2014) 4644–4652. doi:10.1021/ct500515h.

[171] M.A. Granato, V.D. Martins, A.F.P. Ferreira, A.E. Rodrigues, Microporous and Mesoporous Materials Adsorption of xylene isomers in MOF UiO-66 by molecular simulation, MICROPOROUS MESOPOROUS Mater. 190 (2014) 165–170. doi:10.1016/j.micromeso.2014.02.014.

[172] B. Wang, H. Huang, X. Lv, Y. Xie, M. Li, J. Li, Tuning CO_2 Selective Adsorption over N_2

and CH_4 in UiO-67 Analogues through Ligand Functionalization, Inorg. Chem. 53 (2014) 9254–9259. doi:10.1021/ic5013473.

[173] N. Ko, J. Hong, S. Sung, K.E. Cordova, H.J. Park, J.K. Yang, J. Kim, A significant enhancement of water vapour uptake at low pressure by amine-functionalization of UiO-67, Dalt. Trans. 44 (2015) 2047–2051. doi:10.1039/C4DT02582B.

[174] S. Øien-Ødegaard, B. Bouchevreau, K. Hylland, L. Wu, R. Blom, C. Grande, U. Olsbye, M. Tilset, K.P. Lillerud, UiO-67-type Metal–Organic Frameworks with Enhanced Water Stability and Methane Adsorption Capacity, Inorg. Chem. 55 (2016) 1986–1991. doi:10.1021/acs.inorgchem.5b02257.

[175] J.R. Karra, K.S. Walton, Effect of Open Metal Sites on Adsorption of Polar and Nonpolar Molecules in Metal−Organic Framework Cu-BTC, Langmuir. 24 (2008) 8620–8626. doi:10.1021/la800803w.

[176] K. Zhang, A. Nalaparaju, J. Jiang, CO_2 capture in rht metal–organic frameworks: multiscale modeling from molecular simulation to breakthrough prediction, J. Mater. Chem. A. 3 (2015) 16327–16336. doi:10.1039/C5TA01866H.

[177] Q. Yang, V. Guillerm, F. Ragon, A.D. Wiersum, P.L. Llewellyn, C. Zhong, T. Devic, C. Serre, G. Maurin, CH_4 storage and CO_2 capture in highly porous zirconium oxide based metal–organic frameworks, Chem. Commun. 48 (2012) 9831. doi:10.1039/c2cc34714h.

[178] A.K. Rappe, C.J. Casewit, K.S. Colwell, W.A. Goddard, W.M. Skiff, UFF, a full periodic table force field for molecular mechanics and molecular dynamics simulations, J. Am.

Chem. Soc. 114 (1992) 10024–10035. doi:10.1021/ja00051a040.

[179] A. Martín-Calvo, F.D. Lahoz-Martín, S. Calero, Understanding Carbon Monoxide Capture Using Metal–Organic Frameworks, J. Phys. Chem. C. 116 (2012) 6655–6663. doi:10.1021/jp211563e.

[180] P. Mishra, S. Edubilli, B. Mandal, S. Gumma, Adsorption of CO_2, CO, CH_4 and N_2 on DABCO based metal organic frameworks, Microporous Mesoporous Mater. 169 (2013) 75–80. doi:10.1016/j.micromeso.2012.10.025.

[181] G. Nickerl, M. Leistner, S. Helten, V. Bon, I. Senkovska, S. Kaskel, Integration of accessible secondary metal sites into MOFs for H_2S removal, Inorg. Chem. Front. 1 (2014) 325–330. doi:10.1039/C3QI00093A.

[182] W. Zhang, H. Huang, C. Zhong, D. Liu, Cooperative effect of temperature and linker functionality on CO_2 capture from industrial gas mixtures in metal–organic frameworks: a combined experimental and molecular simulation study, Phys. Chem. Chem. Phys. 14 (2012) 2317. doi:10.1039/c2cp23839j.

[183] A. Martín-Calvo, E. García-Pérez, J. Manuel Castillo, S. Calero, Molecular simulations for adsorption and separation of natural gas in IRMOF-1 and Cu-BTC metal-organic frameworks, Phys. Chem. Chem. Phys. 10 (2008) 7085. doi:10.1039/b807470d.

[184] L. Hamon, E. Jolimaître, G.D. Pirngruber, CO_2 and CH_4 Separation by Adsorption Using Cu-BTC Metal−Organic Framework, Ind. Eng. Chem. Res. 49 (2010) 7497–7503. doi:10.1021/ie902008g.

[185] M. Rubeš, A.D. Wiersum, P.L. Llewellyn, L. Grajciar, O. Bludský, P. Nachtigall, Adsorption of Propane and Propylene on CuBTC Metal–Organic Framework: Combined Theoretical and Experimental Investigation, J. Phys. Chem. C. 117 (2013) 11159–11167. doi:10.1021/jp401600v.

[186] Z. Liang, M. Marshall, A.L. Chaffee, CO_2 Adsorption-Based Separation by Metal Organic Framework (Cu-BTC) versus Zeolite (13X), Energy & Fuels. 23 (2009) 2785–2789. doi:10.1021/ef800938e.

[187] S.E. Miller, M.H. Teplensky, P.Z. Moghadam, D. Fairen-Jimenez, Metal-organic frameworks as biosensors for luminescence-based detection and imaging, Interface Focus. 6 (2016) 20160027. doi:10.1098/rsfs.2016.0027.

[188] F. Ke, Y. Wu, H. Deng, Journal of Solid State Chemistry Metal-organic frameworks for lithium ion batteries and supercapacitors, J. Solid State Chem. 223 (2015) 109–121. doi:10.1016/j.jssc.2014.07.008.

[189] Y. Wu, H. Chen, J. Xiao, D. Liu, Z. Liu, Y. Qian, H. Xi, Adsorptive Separation of Methanol–Acetone on Isostructural Series of Metal–Organic Frameworks M-BTC (M = Ti, Fe, Cu, Co, Ru, Mo): A Computational Study of Adsorption Mechanisms and Metal-Substitution Impacts, ACS Appl. Mater. Interfaces. 7 (2015) 26930–26940. doi:10.1021/acsami.5b07665.

[190] S.A. Prabhudesai, V.K. Sharma, S. Mitra, R. Mukhopadhyay, Transport of acetylene adsorbed in CuBTC metal organic framework, Eur. Phys. J. B. 86 (2013) 145. doi:10.1140/epjb/e2013-30977-6.

[191] S.S. Chui, A Chemically Functionalizable Nanoporous Material [Cu3(TMA)2(H2O)3]n, Science (80-.). 283 (1999) 1148–1150. doi:10.1126/science.283.5405.1148.

[192] G. Majano, J. Pe, Room Temperature Synthesis and Size Control of HKUST-1, Helv. Chim. Acta. 95 (2012) 2278–2286.

[193] K. Lin, A.K. Adhikari, C. Ku, C. Chiang, H. Kuo, Synthesis and characterization of porous HKUST-1 metal organic frameworks for hydrogen storage, Int. J. Hydrogen Energy. 37 (2012) 13865–13871. doi:10.1016/j.ijhydene.2012.04.105.

[194] J.R. Karra, K.S. Walton, Molecular Simulations and Experimental Studies of CO_2 , CO, and N_2 Adsorption in Metal−Organic Frameworks, J. Phys. Chem. C. 114 (2010) 15735–15740. doi:10.1021/jp105519h.

[195] S.S. Chui, A Chemically Functionalizable Nanoporous Material [Cu3(TMA)2(H2O)3]n, Science (80). 283 (1999) 1148–1150. doi:10.1126/science.283.5405.1148.

[196] C. Xin, X. Jiao, Y. Yin, H. Zhan, H. Li, L. Li, N. Zhao, F. Xiao, W. Wei, Enhanced CO_2 Adsorption Capacity and Hydrothermal Stability of HKUST-1 via Introduction of Siliceous Mesocellular Foams (MCFs), Ind. Eng. Chem. Res. 55 (2016) 7950–7957. doi:10.1021/acs.iecr.5b04022.

[197] A. Torrisi, R.G. Bell, C. Mellot-draznieks, Microporous and Mesoporous Materials Predicting the impact of functionalized ligands on CO_2 adsorption in MOFs : A combined DFT and Grand Canonical Monte Carlo study, Microporous Mesoporous Mater. 168 (2013) 225–238. doi:10.1016/j.micromeso.2012.10.002.

[198] D.K. Maity, A. Halder, B. Bhattacharya, A. Das, D. Ghoshal, Selective CO_2 Adsorption by Nitro Functionalized Metal Organic Frameworks, Cryst. Growth Des. 16 (2016) 1162–1167. doi:10.1021/acs.cgd.5b01686.

[199] D. Mustafa, E. Breynaert, S.R. Bajpe, J.A. Martens, C.E.A. Kirschhock, Stability improvement of $Cu_3(BTC)_2$ metal–organic frameworks under steaming conditions by encapsulation of a Keggin polyoxometalate, Chem. Commun. 47 (2011) 8037. doi:10.1039/c1cc12341f.

APPENDIX

A.1 Sample Towhee input file ('towhee_input') for grand canonical Monte Carlo simulation of CO_2+N_2 mixture adsorption on mesoporous silica.

```
inputformat
'Towhee'
random_number_generator
'RANLUX'
random_luxlevel
3
random_seed
1302552
random_allow_restart
T
ensemble
'uvt'
temperature
303.15d0
nmolty
3
nmolectyp
1 800 600
chempot
0 -5502.28d0 -4785.432d0
numboxes
1
stepstyle
'moves'
nstep
2000000
printfreq
200000
blocksize
40000
moviefreq
200000
backupfreq
200000
runoutput
'blocks'
pdb_output_freq
400000
trmaxdispfreq
200000
volmaxdispfreq
200000
potentialstyle
'internal'
```

```
ffnumber
1
ff_filename
/home/kishant/forcefields/towhee_ff_new2
classical_potential
'Lennard-Jones'
classical_mixrule
'Explicit'
lshift
.false.
ltailc
.true.
rmin
0.95d0
rcut
12.0d0
rcutin
12.0d0
electrostatic_form
'coulomb'
coulombstyle
'ewald_fixed_kmax'
kalp
5.6
kmax
5
dielect
1.0
linit
T
initboxtype
'dimensions'
initstyle
'coords' 'full cbmc' 'full cbmc'
initlattice
'none' 'center' 'center'
initmol
1 0 0
inix iniy iniz
1    1    1
hmatrix
42.8d0 0.0d0 0.0d0
0.0d0   42.8d0  0.0d0
0.0d0 0.0d0  64.2d0
pmuvtcbswap
0.6d0
          pmuvtcbmt
          0.0d0 0.5d0 1.00d0
pm1boxcbswap
0.65d0
          pm1cbswmt
```

```
          0.0d0 0.5d0 1.0d0
pmtracm
0.825d0
          pmtcmt
          0.0d0 0.5d0 1.0d0
          rmtrac
          0.5d0
          tatrac
          0.5d0
pmrotate
1.0d0
          pmromt
          0.0d0 0.5d0 1.0d0
          rmrot
          0.05d0
          tarot
          0.5d0
...
...
...
#Mesoporous Silica (adsorbent connectivity information)
input_style
'basic connectivity map'
nunit
3841
nmaxcbmc
3841
lpdbnames
F
forcefield
'new2'
charge_assignment
'manual'
unit  ntype qqatom
1     'Si'  0.122422882d0
vibration
0
improper torsion
0
unit  ntype qqatom
2     'Si'  0.122422882d0
vibration
0
improper torsion
0
unit  ntype qqatom
3     'Si'  0.122422882d0
vibration
0
improper torsion
0
```

```
...
...
...
#adsorbate connectivity information
#carbon_dioxide
input_style
'basic connectivity map'
nunit
3
nmaxcbmc
3
lpdbnames
F
forcefield
'new2'
charge_assignment
'manual'
unit ntype qqatom
1    'C'   0.60400d0
vibration
2
2 3
improper torsion
0
unit ntype qqatom
2    'Osp2'   -0.30200d0
vibration
1
1
improper torsion
0
unit ntype qqatom
3    'Osp2'   -0.30200d0
vibration
1
1
improper torsion
0
#nitrogen
input_style
'basic connectivity map'
nunit
3
nmaxcbmc
3
lpdbnames
F
forcefield
'new2'
charge_assignment
'manual'
```

```
unit ntype qqatom
1    'N_n2'   -0.482d0
vibration
1
3
improper torsion
0
unit ntype qqatom
2    'N_n2'   -0.482d0
vibration
1
3
improper torsion
0
unit ntype qqatom
3    'COM_n2'   0.964d0
vibration
2
1 2
improper torsion
0
```

A.2 Code for constructing Towhee force field file

```
#include<iostream>
#include<fstream>
#include<string>
#include<ctype.h>
#include<math.h>
#include<iomanip>

/***** GO DOWN AND CHANGE ffname *****/

using namespace std;
int main()
{
fstream input1 ;
fstream input2 ;
fstream input3 ;
fstream input4 ;
ofstream output2;
input1.open("lj_param.txt");
input2.open("bonds.txt");
input3.open("angles.txt");
input4.open("dihedrals.txt");
output2.open("towhee_ff_ionic");
```

```
/*** DEFINE TOTAL NUMBER OF ATOMS ****/
int TNOA=24;

/** ATOM TYPES IN EACH MOLECULES *****/
//READ FROM INPUT FILE
string atmtype[25];

/** ELEMENT NAMES OF EACH ATOM *****/
//READ FROM INPUT FILE
string elem[25];

/** BOND PATTERN OF EACH ATOM *****/
//READ FROM INPUT FILE
string bond[25];

/*** MASS OF EACH ATOM TYPES ****/
//READ FROM INPUT FILE
double mas[25];

/*** LJ POTENTIAL FOR EACH ATOM TYPES ****/
//READ FROM INPUT FILE
double lj_sig[25];
double lj_eps[25];

/*** SET POTENTIAL OF RIGID MOLECULE TO ZERO OTHERWISE ONE ****/
//READ FROM INPUT FILE
double pot[25];
int i,j,k;
double lj_epsilon,lj_sigma;

for(i=0;i<TNOA;i++)
{
// make a text_file_with name it as "lj_param.txt" and place the value in the
order shown below
input1>>atmtype[i]>>elem[i]>>mas[i]>>lj_sig[i]>>lj_eps[i]>>pot[i]>>bond[i];
}

output2<<"towhee_ff Version"<<endl;
output2<<15<<endl;
output2<<"Number of Nonbonded Types"<<endl;
output2<<TNOA<<endl;
output2<<"Potential Type"<<endl;
output2<<"Lennard-Jones"<<endl;
output2<<"Classical Mixrule"<<endl;
output2<<"Explicit"<<endl;

      for(j=0;j<TNOA;j++)
      {
               output2<<"Atom Type Number"<<"\n";
           output2<<j+1<<"\n";
       for(k=0;k<TNOA;k++)
```

```
        {
              if(k>=j)
              {
                    output2<<"Nonbond Coefficients"<<"\n";
                    if(pot[j]==0 && pot[k]==0)
                    {
                          output2<<"0.0000000000E+00"<<"\n";
                        output2<<"0.0000000000E+00"<<"\n";
                          output2<<"0.0000000000E+00"<<"\n";
                          output2<<"0.0000000000E+00"<<"\n";
                   }
                    else
                    {
                     lj_sigma=(lj_sig[j]+lj_sig[k])/2.0;
               lj_epsilon=sqrt(lj_eps[j]*lj_eps[k]);
                  output2<<lj_sigma<<"00000E+00"<<"\n";
                        output2<<lj_epsilon<<"00000E+00"<<"\n";
                          output2<<"0.0000000000E+00"<<"\n";
                          output2<<"0.0000000000E+00"<<"\n";
                    }
              }
        }
output2<<"Mass"<<"\n";
    output2<<mas[j]<<"00000E+00"<<"\n";
      output2<<"Element"<<"\n";
      output2<<elem[j]<<"\n";
      output2<<"Bond Pattern"<<"\n";
output2<<bond[j]<<"\n";
output2<<"Base Charge"<<"\n";
output2<<"0.0000000000E+00"<<"\n";
output2<<"Polarizability"<<"\n";
output2<<"0.1000000000E+01"<<"\n";
output2<<"Force Field Name"<<"\n";
output2<<"ffname"<<"\n";
output2<<"Atom Names"<<"\n";
output2<<atmtype[j]<<setw(10)<<"\n";
output2<<atmtype[j]<<setw(10)<<"\n";
output2<<atmtype[j]<<setw(10)<<"\n";
output2<<atmtype[j]<<setw(10)<<"\n";
      }

/*** DEFINE BONDING INFORMATION  ***/
int TNB=20; // total number of bonds
string atomb1[25];
string atomb2[25];
double bondcoeff[25];
// READING BONDING INFORMATION
for(i=0;i<TNB;i++)

// make a text_file_with name it as “bonds.txt” and place the value in the
order shown below
```

```
 input2>>atomb1[i]>>atomb2[i]>>bondcoeff[i];

output2<<"Number of Bonded Terms"<<endl;
output2<<TNB<<endl;

for(i=0;i<TNB;i++)
{
// mention bond style above of code
      output2<<"Bond Type Number"<<endl;
      output2<<i+1<<endl;
      output2<<"Bond Style"<<endl;
      output2<<1<<endl;
      output2<<"Bond Coefficients"<<endl;
      output2<<bondcoeff[i]<<"0000E+00"<<endl;
      output2<<"Vibration Order"<<endl;
      output2<<"wild"<<endl;
      output2<<"Force Field Name"<<endl;
      output2<<"ffname"<<endl;
      output2<<"Number of Atoms with Same Parameters"<<endl;
      output2<<1<<endl;
      output2<<"Atom Names"<<endl;
      output2<<atomb1[i]<<setw(11)<<atomb2[i]<<setw(10)<<endl;
}
      /*** DEFINE ANGLE INFORMATION ****/
      int TNAng=36; // total number of bonds
string atoma1[40];
string atoma2[40];
string atoma3[40];
double angcoeff[40];
double angle[40];
// READING ANGLE INFORMATION
for(i=0;i<TNAng;i++)
// make a text_file_with name it as "angles.txt" and place the value in the
order shown below
 input3>>atoma1[i]>>atoma2[i]>>atoma3[i]>>angcoeff[i]>>angle[i];

output2<<"Number of Angle Terms"<<endl;
output2<<TNAng<<endl;
for(i=0;i<TNAng;i++)
{
// mention ANGLE style and forcefield name above of code
      output2<<"Angle Type Number"<<endl;
      output2<<i+1<<endl;
      output2<<"Angle Style"<<endl;
      output2<<1<<endl;
      output2<<"Angle Coefficients"<<endl;
      output2<<angle[i]<<"0000E+00"<<endl;
      output2<<angcoeff[i]<<"0000E+00"<<endl;
      output2<<"Angle Order"<<endl;
      output2<<"wild"<<endl;
      output2<<"Force Field Name"<<endl;
```

```
      output2<<"ffname"<<endl;
      output2<<"Number of Atoms with Same Parameters"<<endl;
      output2<<1<<endl;
      output2<<"Atom Names"<<endl;
      output2<<atoma1[i]<<setw(11)<<atoma2[i]<<setw(11)<<atoma3[i]<<setw(10)<
<endl;
}

/*** DEFINE DIHEDRAL INFORMATION ****/
      int TNDehl=33; // total number of bonds
string atomd1[40];
string atomd2[40];
string atomd3[40];
string atomd4[40];
double dihed_coeff[40];
double dihedral_n[40];
double dihedral_thetha[40]; // thetha value should be provided in radian
// READING ANGLE INFORMATION
for(i=0;i<TNDehl;i++)
// make a text_file_with name it as "dihedral.txt" and place the value in the
order shown below

input4>>atomd1[i]>>atomd2[i]>>atomd3[i]>>atomd4[i]>>dihed_coeff[i]>>dihedral_
n[i]>>dihedral_thetha[i];

output2<<"Number of Torsion Terms"<<endl;
output2<<TNDehl<<endl;
for(i=0;i<TNDehl;i++)
{
// mention ANGLE style and forcefield name above of code
      output2<<"Torsion Type Number"<<endl;
      output2<<i+1<<endl;
      output2<<"Torsion Style"<<endl;
      output2<<3<<endl;
      output2<<"One-Four Nonbond Logical"<<endl;
      output2<<"T"<<endl;
      output2<<"One-Four Coulombic Scaling"<<endl;
      output2<<"0.5000000000E+00"<<endl;
      output2<<"Number of Torsion Loops"<<endl;
      output2<<"1"<<endl;
      output2<<"Torsion Coefficients"<<endl;
      output2<<dihed_coeff[i]<<"0000E+00"<<endl;
      output2<<dihedral_n[i]<<"0000E+00"<<endl;
      output2<<dihedral_thetha[i]<<"0000E+00"<<endl;
      output2<<"Torsion Order"<<endl;
      output2<<"wild"<<endl;
      output2<<"Force Field Name"<<endl;
      output2<<"ffname"<<endl;
      output2<<"Number of Atoms with Same Parameters"<<endl;
      output2<<1<<endl;
      output2<<"Atom Names"<<endl;
```

```
      output2<<atomd1[i]<<setw(11)<<atomd2[i]<<setw(11)<<atomd3[i]<<setw(11)<
<atomd4[i]<<endl;

}

output2<<"Number of Improper Terms"<<endl;
output2<<"0"<<endl;
output2<<"Number of Angle-Angle Terms"<<endl;
output2<<"0"<<endl;
output2<<"Number of One-Five Types "<<endl;
output2<<"0"<<endl;
output2<<"Number of Bond Increments"<<endl;
output2<<"0"<<endl;

input4.close();
input3.close();
input2.close();
input1.close();
output2.close();

return 0;
}
```

A.3 Code for Calculating Radial Distribution function

```
#include<iostream>
#include<fstream>
#include<math.h>
#include<string.h>
#include<stdlib.h>
#include<ctime>
#include<iomanip>
float sgn(double);
using namespace std;
int const nof=2000;    // number of frames to be read
int const mnm=696;   //number of maximum molecules inserted "keep this value
eqal to frameworkatoms"
//double g[nof][5000]={ };                /******** INITIALIZE ALL THE g(r)
VALUES WITH ZERO *******/
//double
x[nof+1][mnm],y[nof+1][mnm],z[nof+1][mnm],serial[nof+1][mnm],charge[nof+1][mn
m],mass[nof+1][mnm],skip[mnm],serial1[mnm];
//char TOA2[nof+1][mnm];
double g[2000][5000]={ };              /******** INITIALIZE ALL THE g(r)
VALUES WITH ZERO *******/
double x[2001][696], y[2001][696], z[2001][696], serial[2001][696],
charge[2001][696], mass[2001][696], skip[696], serial1[696];
char TOA2[2001][696];
```

```
int main()
{
fstream input_adsorbate;
input_adsorbate.open("movie1.pdb");
fstream input_frame;
input_frame.open("uio-67.pdb");
ofstream rdfout;
rdfout.open("rdf_out.dat");

time_t t=time(0);
struct tm * now = localtime( & t );
rdfout<<"REMARK   "<<"RDF by kishant, File created on "<<   (now->tm_year +
1900) << '-' <<(now->tm_mon + 1) << '-' <<(now->tm_mday)<<endl;

/**** Define box dimensions ****/
double Lx=27.94;
double Ly=27.94;
double Lz=27.94;
double bin_size=0.05;
double xa=90.00;
double ya=90.00;
double za=90.00;
const double v=Lx*Ly*Lz;
double s,tt,u,r;
int l,k;
//l=tot_r/bin_size;


double sum[5000]={ };
double PI=3.14159;
double gsum[5000],gavg[5000];
int nosa[nof],noca[nof];  //"nosa" number of sitting atom "noca" number of
counting atom

char TOA3[20],TOA4[20];
double del_x,del_y,del_z;

string str;
string TOA1;
int i,j;
int nofwa=696;  //Number of framework atoms "nofwa"

int noas[nof];


//ATOM      1  N   MOL             5.057  21.018  17.653  1.00  0.00      N
for(i=0;i<2;i++)
          {

           getline(input_adsorbate, str);
```

```
            cout<<str<<endl;

           }

for(i=0;i<nof;i++)
  {
      int intilizer=0;
         j=0;
        do
        {
          input_adsorbate>>TOA1;

          if(TOA1!="ENDMDL")
            {
               intilizer++;

input_adsorbate>>serial[i][j]>>TOA2[i][j]>>TOA3>>x[i][j]>>y[i][j]>>z[i][j]>>c
harge[i][j]>>mass[i][j]>>TOA4;
             noas[i]=intilizer;
             j++;

         }

        }while(TOA1!="ENDMDL");

       input_adsorbate>>TOA1;

        input_adsorbate>>TOA1;

       input_adsorbate >>TOA1>>
skip[i]>>skip[i]>>skip[i]>>skip[i]>>skip[i]>>skip[i];

  }
input_adsorbate.close();
//Reading frameatoms
for(j=0;j<nofwa;j++)
    {
     input_frame>>TOA2[nof][j]>>x[nof][j]>>y[nof][j]>>z[nof][j];

    }
noas[nof]=nofwa;

input_frame.close();
// RDF calculation starts here
rdfout<<"radius(angstrom)"<<"\t"<<"g(l)"<<endl;
for(i=nof/2;i<nof;i++)
  {
     nosa[i]=0;

    for(j=0;j<nofwa;j++)
       {
```

```
          if(TOA2[nof][j]=='Z')   //Symbol of sitting atom
            {


            s=x[nof][j];
            tt=y[nof][j];
            u=z[nof][j];
            nosa[i]=nosa[i]+1;
            noca[i]=0;

            for(k=0;k<noas[i];k++)
              {


               if( TOA2[i][k]=='C')   //Symbol of counting atom
                 {


                   noca[i]=noca[i]+1;
                  //
cout<<"noca="<<noca[i]<<"\t"<<"nosa="<<nosa[i]<<"\t"<<noas[0]<<"\t"<<i<<endl;
                   del_x = x[i][k]-s;
                   del_y = y[i][k]-tt;
                   del_z = z[i][k]-u;
                   del_x = del_x - Lx *  sgn(del_x)*( (fabs(del_x/Lx))>0.5?
1:0) ;
                   del_y = del_y - Ly *  sgn(del_y)*( (fabs(del_y/Ly))>0.5?
1:0) ;
                   del_z = del_z - Lz *  sgn(del_z)*( (fabs(del_z/Lz))>0.5?
1:0) ;
                   r = sqrt(del_x*del_x+del_y*del_y+del_z*del_z);
                  // cout<<r<<endl;
                   l=(r/bin_size);
                   g[i][l]=g[i][l]+1;
                  //cout<<"g=="<<g[i][l]<<endl;

                 }
              }
           }
           }
          cout<<"noca="<<noca[i]<<"\t"<<"nosa="<<nosa[i]<<endl;
  }

//Now average over all the frames
for(l=0;l<5000;l++)
{
r=double(l*bin_size)+bin_size;
    gsum[l]=0;
    gavg[l]=0.0;
    for(i=nof/2;i<nof;i++)
```

```
        {

gsum[l]=((g[i][l]*(Lx*Ly*Lz))/((4.0*PI*r*r*bin_size)*(nosa[i]*noca[i])));
         gavg[l]=gavg[l]+gsum[l];

       }
     gavg[l]=2*gavg[l]/nof;
     cout<<gavg[l]<<endl;

rdfout<<r<<"\t"<<gavg[l]<<endl;            /******CHANGE HERE FOR SAME ATOM
"nosa*nosa" otherwise "nosa*noca"  **/

}

rdfout.close();

}
float sgn(double x)
{
if(x >0.0)return 1.0 ;
if(x <0.0)return -1.0 ;
return 0.0 ;
}
```